

2



AFOSR-TR. 91 ~~0817~~

# INVESTIGATIONS OF THE OPTICAL AND ELECTRONIC PROPERTIES OF CRYSTALLINE ORGANIC MATERIALS

[illegible]

## FINAL REPORT

**Contract No. AFOSR-87-0273**

DTIC  
ELECTE  
OCT 11 1990  
S B D

**Principal Investigator:**

# Stephen R. Forrest

## Departments of Electrical Engineering and Materials Science

**University of Southern California**

**Los Angeles, CA 90089-0241**

91 1010 077

# REPORT DOCUMENTATION PAGE

Form Approved  
OMB No. 0704-0188

Public reporting burden for this collection of information is estimated to average 1 hour per response, including the time for reviewing instructions, searching existing data sources, gathering and maintaining the data needed, and completing and reviewing the collection of information. Send comments regarding this burden estimate or any other aspect of this collection of information, including suggestions for reducing this burden, to Washington Headquarters Services, Directorate for Information Operations and Reports, 1215 Jefferson Davis Highway, Suite 1204, Arlington, VA 22202-4302, and to the Office of Management and Budget, Paperwork Reduction Project (0704-0188), Washington, DC 20503.

1. AGENCY USE ONLY (Leave blank)		2. REPORT DATE		3. REPORT TYPE AND DATES COVERED FINAL TECHNICAL - 6/15/89-6/14/90	
4. TITLE AND SUBTITLE INVESTIGATIONS OF THE OPTICAL AND ELECTRONIC PROPERTIES OF CRYSTALLINE ORGANIC MATERIALS				5. FUNDING NUMBERS AFOSR-87-0273	
6. AUTHOR(S) STEPHEN R. FORREST					
7. PERFORMING ORGANIZATION NAME(S) AND ADDRESS(ES) UNIVERSITY OF SOUTHERN CALIFORNIA DEPARTMENT OF ELECTRICAL ENGINEERING LOS ANGELES, CA 90089-0241				8. PERFORMING ORGANIZATION REPORT NUMBER	
9. SPONSORING/MONITORING AGENCY NAME(S) AND ADDRESS(ES) AFOSR/NE BOLLING AFB WASHINGTON, DC 20332				10. SPONSORING/MONITORING AGENCY REPORT NUMBER  2306 B1	
11. SUPPLEMENTARY NOTES					
12a. DISTRIBUTION/AVAILABILITY STATEMENT APPROVED FOR PUBLIC RELEASE: DISTRIBUTION UNLIMITED				12b. DISTRIBUTION CODE	
13. ABSTRACT (Maximum 200 words)  We have done extensive investigations of the optical and electronic properties of heterojunctions containing crystalline organic semiconductors. Using the new, ultrahigh vacuum process of organic molecular beam deposition (OMBD), we have grown heterojunctions consisting of organic semiconductors in contact with other organic semiconductors, as well as with inorganic semiconductors. Multiple quantum well structures consisting of two dissimilar organic semiconductors have been grown for the first time, and these structures show evidence for quantum confinement of excitons. Detailed studies of the optical and electronic properties of all heterojunction types are discussed in this report, which is taken from the thesis entitled, "Growth and Characterization of Heterojunctions and Multiple Quantum Well Structures Based on Crystalline Organic Semiconductors" by F. F. So, University of Southern California, 1991.					
14. SUBJECT TERMS				15. NUMBER OF PAGES 280	
				16. PRICE CODE	
17. SECURITY CLASSIFICATION OF REPORT UNCLASSIFIED	18. SECURITY CLASSIFICATION OF THIS PAGE UNCLASSIFIED	19. SECURITY CLASSIFICATION OF ABSTRACT UNCLASSIFIED	20. LIMITATION OF ABSTRACT UL		

**INVESTIGATIONS OF THE OPTICAL AND ELECTRONIC  
PROPERTIES OF CRYSTALLINE ORGANIC MATERIALS**

**FINAL REPORT**

**Contract No. AFOSR-87-0273**

**Principal Investigator:**

**Stephen R. Forrest**

**Departments of Electrical Engineering and Materials Science  
University of Southern California  
Los Angeles, CA 90089-0241**

## Abstract

We have done extensive investigations of the optical and electronic properties of heterojunctions containing crystalline organic semiconductors. Using the new, ultrahigh vacuum process of organic molecular beam deposition (OMBD), we have grown heterojunctions consisting of organic semiconductors in contact with other organic semiconductors, as well as with inorganic semiconductors. Multiple quantum well structures consisting of two dissimilar organic semiconductors have been grown for the first time, and these structures show evidence for quantum confinement of excitons. Detailed studies of the optical and electronic properties of all heterojunction types are discussed in this report, which is taken from the thesis entitled, "Growth and Characterization of Heterojunctions and Multiple Quantum Well Structures Based on Crystalline Organic Semiconductors" by F. F. So, University of Southern California, 1991.

<b>Accession For</b>	
NTIS GRA&I	<input checked="checked" type="checkbox"/>
DTIC TAB	<input type="checkbox"/>
Unannounced	<input type="checkbox"/>
Justification	
By	
Distribution/	
Availability Codes	
Dist	Avail and/or Special
A-1	



## TABLE OF CONTENTS

	page
DEDICATION -----	ii
ACKNOWLEDGEMENTS -----	iii
LIST OF FIGURES -----	iv
LIST OF TABLES -----	xvii
ABSTRACT -----	xviii
 CHAPTERS	
I. INTRODUCTION -----	1
I.1 BACKGROUND -----	1
I.2 GROWTH OF CRYSTALLINE ORGANIC THIN FILMS -----	4
I.3 ORGANIC-ON-INORGANIC HETEROJUNCTIONS -----	6
I.4 FULLY ORGANIC HETEROJUNCTIONS -----	8
I.5 ORGANIC MULTIPLE QUANTUM WELL STRUCTURES -----	10
I.5 THESIS ORGANIZATION -----	11
REFERENCES -----	13
II. GROWTH AND PROPERTIES OF ORGANIC THIN FILMS --	18
II.1 CRYSTAL STRUCTURES AND MATERIAL PROPERTIES -----	18
(A) PTCDA AND NTCDA -----	19
(B) CuPc AND H <sub>2</sub> Pc -----	25
II.2 MATERIAL PREPARATION -----	27

II.3	ORGANIC MOLECULAR BEAM DEPOSITION -----	29
	(A) GROWTH AND SYSTEM DESIGN -----	31
	(B) ORGANIC/INORGANIC MOLECULAR BEAM EPITAXY SYSTEM -----	34
II.4	EFFECTS OF GROWTH PARAMETERS ON MICRO- STRUCTURE -----	38
	(A) EFFECTS OF DEPOSTION RATE -----	38
	(B) EFFECTS OF SUBSTRATE TEMPERATURE -----	40
II.5	ANISOTROPIES IN CRYSTALLINE ORGANIC THIN FILMS GROWN BY OMBD -----	47
	REFERENCES -----	51
III.	ORGANIC-ON-INORGANIC SEMICONDUCTOR HETERO- JUNCTIONS -----	53
III.1	ELECTRICAL CHARACTERISTICS OF OI HETERO- JUNCTIONS -----	57
	(A) DEVICE FABRICATION AND CHARACTERISTICS -----	57
	(B) THERMIONIC EMISSION-SPACE-CHARGE LIMITED MODEL -----	63
III.2	THEORY OF CHARGE TRANSPORT IN OI HETERO- JUNCTIONS -----	67
	(A) OI-HJ POTENTIAL DISTRIBUTION AND THE ENERGY-BAND DISCONTINUITIES -----	69
	(B) CARRIER VELOCITIES -----	94

(C) QUASI-FERMI LEVELS -----	99
III.3 EFFECTS OF ORGANIC THIN FILM COMPOSITION	
ON THE ELECTRICAL CHARACTERISTICS -----	109
(A) THEORY OF SOISAS TECHNIQUE -----	111
(B) OI DIODE FABRICATION -----	116
(C) RESULTS -----	118
(D) DISCUSSION AND CONCLUSIONS -----	122
III.4 DEPENDENCE OF ELECTRICAL CHARACTERISTICS	
OF OI-HJs ON DEPOSITION TEMPERATURE -----	127
III.5 OI PHOTODETECTORS -----	134
(A) DEVICE FABRICATION AND MEASUREMENT -	136
(B) EXPERIMENTAL RESULTS -----	136
(C) SPEED LIMITING FACTORS IN OI PHOTO-	
DETECTORS -----	148
REFERENCES -----	151
IV. CRYSTALLINE ORGANIC SEMICONDUCTOR HETERO-	
JUNCTIONS -----	155
IV.1 INTRODUCTION -----	155
IV.2 MATERIAL PREPARATION AND DEVICE	
FABRICATION -----	158
IV.3 RESULTS -----	160
IV.4 ENERGY BAND DISCONTINUITIES IN ORGANIC HJs	
-----	179
IV.5 CHARGE TRANSPORT IN CRYSTALLINE ORGANIC	

MATERIALS -----	181
(A) HOPPING VERSUS BAND TRANSPORT -----	183
(B) MOBILITY DATA TO SUPPORT THE BAND MODEL -----	185
(C) CHARGE TRANSPORT MECHANISMS IN MATERIALS USED IN THIS WORK -----	187
IV.6 SUMMARY AND CONCLUSIONS -----	188
REFERENCES -----	189
V. ORGANIC MULTIPLE QUANTUM WELLS -----	192
V.1 INTRODUCTION -----	192
V.2 GROWTH AND STRUCTURAL PROPERTIES -----	196
V.3 OPTICAL ABSORPTION AND PHOTOLUMINESCENCE -----	207
(A) OPTICAL ABSORPTION -----	207
(B) PHOTOLUMINESCENCE -----	210
(C) TIME-RESOLVED LUMINESCENCE -----	215
V.4 DISCUSSION -----	217
(A) FRANCK-CONDON SHIFT IN PTCDA -----	217
(B) BLUE SHIFT IN OPTICAL ABSORPTION -----	218
B.1 POLARIZATION EFFECTS -----	218
B.2 EXCITON QUANTUM CONFINEMENT ---	222
(C) REDUCTION OF EXCITON LIFETIME -----	230
V.5 SUMMARY AND CONCLUSIONS -----	233
REFERENCES -----	235

VI. CONCLUSIONS AND FUTURE WORK .....	238
VI.1 CONCLUSIONS .....	238
VI.2 FUTURE WORK .....	241
(A) GROWTH AND STRUCTURAL PROPERTIES .....	241
(B) OF HETEROJUNCTIONS .....	242
(C) NON-LINEAR OPTICAL PROPERTIES .....	244
APPENDIX A .....	250

## List of Figures

Fig. 2.1:	Molecular structures of crystalline organic semiconductors: PTCDA, PTCBI, NTCDA, and CuPc. ....	20
Fig. 2.2:	Two perspective views of a PTCDA unit cell. ....	21
Fig. 2.3:	A perspective view of an NTCDA unit cell. ....	22
Fig. 2.4:	Normal projection of two CuPc molecules. ....	26
Fig. 2.5:	A set up for organic material purification by gradient sublimation. ....	28
Fig. 2.6:	A schematic diagram of the organic molecular beam deposition system. ....	32
Fig. 2.7:	A schematic diagram of the organic/inorganic molecular beam system. ....	35
Fig. 2.8:	X-ray pole figure of the (102) reflection intensity of PTCDA deposited at (a) $> 50 \text{ \AA/s}$ and (b) $2 \text{ \AA/s}$ . ....	39
Fig. 2.9:	Carrier mobility in PTCDA films as a function of deposition rate. ....	41
Fig. 2.10:	Scanning electron micrographs showing the surface morphologies of PTCDA deposited at substrate temperatures of 440 K (a) and at 90 K (b). ....	42
Fig. 2.11:	X-ray diffraction patterns for PTCDA films on Si substrates deposited at (a) 90 K and (b) 293 K. ....	44
Fig. 2.12:	X-ray diffraction patterns for PTCDA films on glass substrates deposited at (a) 90 K and (b) 293 K. ....	45
Fig. 3.1:	A schematic cross-section of an organic-on-inorganic	

	semiconductor diode .....	58
Fig. 3.2:	Current-voltage characteristics for In/PTCDA/p-Si OI diodes and metal-semiconductor Schottky diodes. ....	62
Fig. 3.3:	Band diagram of an organic-on-n-type inorganic semiconductor diode.	
Inset:	Proposed densities of states at the OI interface. ....	65
Fig. 3.4:	Proposed energy band diagram for an organic-on-inorganic semiconductor heterojunction device under (a) forward and (b) reverse bias .....	70
Fig. 3.5:	Current ( $J$ ) versus voltage ( $V_0$ ) characteristics of a 1000 Å thick organic film. ....	72
Fig. 3.6:	(a) Potential distribution versus position within the organic thin film under three applied voltage regimes. (b) The free hole distribution calculated for the film in (a). ....	74
Fig. 3.7:	Component voltages vs applied voltage for a forward biased OI-HJ diode. ....	80
Fig. 3.8:	Component voltage vs reverse applied voltage for the device in Fig. 3.7. ....	82
Fig. 3.9:	(a) Forward current-voltage characteristics of an In/PTCDA/p-Si diode measured at several different temperatures. (b) Saturation current density vs $1/T$ for the diode in (a). ....	84
Fig. 3.10:	Photoemission spectrum of an In/PTCDA/p-Si heterojunction diode.	

Inset:	Band diagram of the OI-HJ showing the allowed emission processes ("a" and "c") and the forbidden, high-energy process "b". -----	88
Fig. 3.11:	The square root of the photocurrent on the long wavelength branch of the response peak in Fig. 3.10 plotted vs photon energy. -----	90
Fig. 3.12:	Density of surface states ( $D_{ss}$ ) vs potential at the Si surface for a CuPc/p-Si heterojunction. -----	91
Fig. 3.13:	Mean carrier velocity ( $\langle v_c \rangle$ ) vs voltage across the substrate for OI-HJ diodes using organic thin films with different mobilities. -----	95
Fig. 3.14:	Quasi-Fermi energy ( $E_{Fp}$ ) vs position within the organic film for several bias regimes. -----	100
Fig. 3.15:	Potential at the inorganic semiconductor surface as a function of voltage across the depletion region for OI-HJ diodes with several different values of barrier energy. -----	103
Fig. 3.16:	Hole concentration (ps) at the OI-HJ interface as a function of voltage for the same parameters used in Fig. 3.15. -----	105
Fig. 3.17:	OI-HJ impedance ( $Z$ , solid lines) and phase angle ( $\theta$ , dashed lines) vs frequency. -----	108
Fig. 3.18:	Calculated C-V data for an OI heterojunction diode with no defect states at the OI interface (dashed line) and for a uniform defect density of states of $2 \times 10^{12}/\text{cm}^2 \text{ eV}$ . -----	115
Fig. 3.19:	Forward-biased current density vs voltage (J-V)	



characteristics of organic/p-Si devices taken at room temperature.	
Inset: Bipolar I-V characteristics of an In/PTCDA/p-Si diode. --	119
Fig. 3.20: Capacitance-voltage (C-V) characteristics near $V_a = 0$ of four OI diodes employing the same organic materials as those discussed in Fig. 3.19. -----	121
Fig. 3.21: Density of interface states ( $D_{ss}$ ) as a function of surface energy ( $\psi_s$ ) in the p-Si band gap for the four diodes in Fig. 3.20. -----	123
Fig. 3.22: Forward current-voltage characteristics for PTCDA/p-Si devices with 2000 Å deposited at different substrate temperatures. -----	129
Fig. 3.23: Carrier mobility vs PTCDA thin film deposition temperature. -----	130
Fig. 3.24: Optical micrographs for (a) 500 Å and (b) 2000 Å thick PTCDA films deposited at room temperature. -----	132
Fig. 3.25: Schematic cross section of an organic-on-inorganic heterojunction photodetector. -----	135
Fig. 3.26: The dark current versus reverse bias voltage of an ITO/PTCDA/p-Si photodetector. -----	137
Fig. 3.27: External quantum efficiency $\eta$ (data points) versus wavelength at different bias voltages of a PTCDA/p-Si photodetector. -----	139
Fig. 3.28: Detector photoresponse vs position. Each line corresponds	

to a measurement taken in steps of 50 $\mu\text{m}$ from an adjacent line. -----	142
Fig. 3.29: Photocurrent vs time of the ITO/PTCDA/p-Si photodetector at 50 V reverse due to 840 nm wavelength laser pulses. ---	144
Fig. 3.30: The magnitude of the diffusion current $I_{\text{diff}}$ in the photoresponse (see Fig. 3.29) vs the depletion layer width. -----	145
Fig. 3.31: Equivalent circuit of organic-on-inorganic (OI) devices. ---	147
Fig. 3.32: Calculated response time vs the thickness for PTCDA film of a PTCDA/Si detector. -----	149
Fig. 4.1: Structural molecular formulae for (a) CuPc, (b) PTCBI, and (c) PTCDA. -----	159
Fig. 4.2: Dark current versus voltage characteristics (solid line) of an ITO/CuPc/PTCDA/In heterojunction shown schematically in the inset. -----	161
Fig. 4.3: Current-voltage characteristics versus temperature of the same device as in Fig. 4.3 under reverse bias. -----	164
Fig. 4.4: Current-voltage characteristics versus temperature of the same device as in Fig. 4.3 under reverse bias. -----	165
Fig. 4.5: Proposed energy band diagrams for p-P heterojunctions consisting of (a) CuPc/PTCDA, (b) CuPc/PTCBI, and (c) PTCDA/PTCBI. -----	167
Fig. 4.6: Activation energy plot of the saturation current density ( $J_s$ ) for CuPc/PTCDA and CuPc/PTCBI heterojunctions. -----	169

Fig. 4.7:	Capacitance (plotted as $1/C^2$ ) versus voltage for a CuPc/PTCDA heterojunction. ....	171
Fig. 4.8:	The photocurrent spectra measured as a function of reverse voltage of CuPc/PTCDA heterojunction diodes. ....	174
Fig. 4.9:	The constituent and combined absorption spectra of CuPc/PTCDA heterojunctions. ....	175
Fig. 4.10:	The absorption spectrum of PTCBI. ....	178
Fig. 4.11:	Proposed crystalline molecular energy level diagram for optical transitions occurring at the CuPc/PTCDA heterointerface plotted as a function of the configuration coordinate, Q. ....	180
Fig. 5.1:	Organic multiple quantum well structure consisting of PTCDA and NTCDA. ....	197
Fig. 5.2:	X-ray diffraction patterns for two quantum well samples (A and B) and one single PTCDA layer sample (C). ....	201
Fig. 5.3:	A schematic diagram showing the setup for birefringence measurements. ....	203
Fig. 5.4:	Birefringence of a 1000 Å PTCDA and a multilayer sample. .....	204
Fig. 5.5:	Schematic diagrams showing the vibronic transitions between singlet states. ....	208
Fig. 5.6:	Typical room temperature optical absorption and low temperature (20 K) photoluminescence spectra of a PTCDA/NTCDA multiple quantum well sample. ....	209

Fig. 5.7:	Exciton line shift as a function of well width. The solid line is the result of variational calculations. -----	211
Fig. 5.8:	Photoluminescence spectra of a 2000 Å thick PTCDA film as a function of temperature. -----	212
Fig. 5.9:	Photoluminescence spectra for PTCDA/NTCDA multiple quantum well samples as a function of layer thickness. ----	214
Fig. 5.10:	Exciton lifetime, $\tau_{ex}$ , as a function of well width. -----	216
Fig. 5.11:	An exciton generated in a PTCDA layer. -----	220
Fig. 5.12:	Integrated luminescence intensity versus layer thickness. -	231
Fig. 6.1:	Luminescence spectra of a 0.4 μm thick PTCDA thin film at 21 K under various various Ar laser pumping intensity. -----	245
Fig. 6.2:	Luminescence peak energy shift as a function of Ar laser pumping intensity for the sample in Fig. 6.1.-----	246
Fig. 6.3:	Schematic diagram showing the two-level model. -----	248
Fig. A.1:	Capacitance measured versus frequency for a horizontal, interdigitated capacitor with PTCDA serving as the dielectric. -----	251
Fig. A.2:	Calculated effective indices at $\lambda = 1.064 \mu\text{m}$ vs PTCDA waveguide thickness.	
Inset:	Coordinate system for a PTCDA waveguide. -----	254
Fig. A.3:	Reflectance at $\lambda = 1.064 \mu\text{m}$ versus incident beam angle for a 1.25 μm thick film on a quartz substrate.	
Inset:	Index of refraction ellipsoid for PTCDA showing the	

relationship between the indices along different thin film	
directions. ....	258

## List of Tables

Table 2.1: Lattice Parameters and energy gaps of several crystalline organic materials. -----	23
Table 2.2: Vacuum specifications and functions in each chamber. --	36
Table 3.1: Typical room temperature reverse-biased characteristics of OI heterojunction diodes. -----	54
Table 3.2: Surface-cleaning sequence for selected semiconductors. -	59
Table 3.3: Ohmic contact metals for several crystalline organic semiconductors. -----	61
Table 3.4: Barrier energies for selected PTCDA-on-inorganic semiconductor diodes using thermionic and diffusion models --	93
Table 3.5: Operating regimes for organic-on-inorganic semiconductor heterojunctions. -----	98
Table 3.6: Characteristics of several organic/p-Si diodes. -----	117
Table 5.1: Properties of organic MQW materials. -----	198
Table 5.2: Parameters used in the variational calculations. -----	228
Table A.1: Reflectivity data for PTCDA thin films. -----	260

## Abstract

Growth of novel heterojunctions and multiple quantum well structures based on crystalline organic semiconductors has been demonstrated by a unique ultra-high vacuum process of organic molecular beam deposition (OMBD). This growth process is capable of fabricating ordered crystalline structures that are free from the requirement that the materials grown be lattice-matched. Hence, relatively strain-free heterostructures using materials with large lattice-mismatch can be realized by the process of OMBD.

We have investigated the charge transport properties of organic-on-inorganic heterojunctions (OI-HJs), including calculating the carrier velocity in the organic film, and the majority carrier quasi Fermi energy. Also, for the first time, the energy band discontinuity of OI-HJs is directly measured by internal photoemission spectroscopy as well as by analysis of the temperature dependence of the current-voltage characteristics.

From studies of the electrical characteristics of OI-HJs based on several crystalline organic compounds, we find that, in some cases, there is a high density of defects at the heterointerface resulting in pinning of the inorganic semiconductor surface Fermi level.

We have also measured the optical and electrical properties of fully organic heterojunctions, and found that the charge transport across the heterojunction is controlled by the energy barrier at the heterointerface, similar to that in inorganic heterojunctions. Finally, the optical properties of organic multiple quantum well structures have been studied, and both the exciton binding energy and the exciton lifetime are found to depend on the well width. These

results can be explained in terms of confinement of excitons in a quantum well. Further, the results of variational calculations are in good agreement with the exciton quantum confinement model.



## Chapter I

### Introduction

#### I.1 Background

Semiconductor heterojunctions (HJs) are contacts between two dissimilar semiconductor materials. The idea of using two heterojunctions for device applications is not new. In the late fifties, Kroemer<sup>1</sup> first proposed to use semiconductor heterostructures for bipolar transistor fabrication, and predicted that the frequency bandwidth can be improved. Later, he<sup>2</sup> also predicted that the threshold current density of injection lasers could be reduced using semiconductor heterostructures. In the early sixties, various efforts were devoted to fabricate semiconductor heterojunctions. For example, attempts were made to grow Ge-Si junctions<sup>3</sup> using an alloying process, and Ge-GaAs<sup>4</sup> using vapor deposition techniques. However, due to the high dislocation density present at the heterointerfaces, useful devices based on semiconductor heterostructures were not available until the early sixties.

Since the advances made in the growth of GaAs/GaAlAs heterostructures by liquid phase epitaxy (LPE),<sup>5</sup> semiconductor heterojunctions have been a subject of intense research. Due to the small lattice mismatch between GaAs and AlAs ( $\Delta a/a = 0.14\%$ ),<sup>6</sup> high quality heterojunctions based on this material system have been achieved. Using this approach, a variety of devices have been fabricated based on semiconductor heterostructures. For example, laser structures consisting of a GaAs emitting layer (small band gap and large index of refraction)

sandwiched between two AlGaAs layers (large band gap and small index of refraction) can be grown by LPE techniques.<sup>6</sup> The so-called double-heterostructure (DH) lasers provide confinement of charge carriers and the optical field in the device, making possible the demonstration of cw semiconductor injection lasers operating at room temperature. Another example is the high bandwidth heterojunction bipolar transistor (HBT)<sup>7,8</sup> in which the minority carrier injection into the emitter is greatly reduced by the potential barrier at the emitter/base heterointerface.

Although semiconductor heterostructures with low defect densities have been grown by LPE, the control of both material composition and layer thickness is difficult to achieve. Due to the rapid progress made in molecular beam epitaxy (MBE)<sup>9</sup> and metal organic chemical vapor deposition (MOCVD)<sup>10</sup> in the mid-seventies, precise control of semiconductor alloy composition, doping concentration, and layer thickness has been made possible. Therefore, it is possible to grow multiple quantum well (MQW) structures<sup>11,12</sup> consisting of alternating, ultra-thin layers of two different semiconductor materials. Quantum well structures have been demonstrated using a number of III-V,<sup>13</sup> II-VI,<sup>14</sup> and IV-IV<sup>15</sup> materials systems. Confinement of carriers in a quantum well gives rise to unusual electronic and optical properties in quantum well structures which cannot be achieved using bulk materials. Due to the modification in the density of states in quantum well structures, the threshold current density of quantum well lasers is significantly reduced.<sup>16</sup> In addition, there are a number of devices fabricated based on quantum well structures such as photodetectors,<sup>17</sup> resonant tunnelling diodes,<sup>18</sup> and spatial light modulators.<sup>19</sup>

In the past decade, heterojunctions and multiple quantum well structures have been limited to inorganic semiconductor materials. Although heterojunction devices have been demonstrated using a large number of inorganic semiconductors, the diversity of their characteristics has been limited due to the fact that the lattice-mismatch between the contacting materials must be small. If the lattice-mismatch exceeds a certain critical value, crystal defects such as dislocations are generated from strain induced at the heterointerface,<sup>20</sup> which degrades the device performance.

In conventional semiconductors, the crystals are bonded together by means of covalent or ionic bonds, and due to the nature of these strong bonds, the strain energy is large when two materials with large lattice-mismatch are brought into contact. On the other hand, crystalline organic materials are bonded together by relatively weak van der Waals forces.<sup>21,22</sup> In this case one would not expect large strains between the contacting materials. Therefore, using such materials, it might be possible to grow relatively strain-free, lattice-mismatched organic-on-inorganic and fully organic heterojunctions based on crystalline organic semiconductors.

Due to the unique structural properties of crystalline organic semiconductor materials, their electronic and optical properties are expected to be different from those of inorganic semiconductors. As a result of the weak van der Waals bonds in the crystals, organic materials are characterized by significant carrier localization<sup>23,24</sup> and a narrow energy bandwidth.<sup>25,26,27</sup> Further, crystalline organic materials often have very little intrinsic mobile charge, and hence conductivity is induced by injection of charge carriers from electrodes,<sup>28,29</sup>

or else generated from the dissociation of excitons.<sup>30,31</sup> On the other hand, optical processes in crystalline organic semiconductors are due to excitonic absorption rather than band-to-band transitions, as is the case for inorganic semiconductors. Therefore, excitons play a very important role in determining the optical and electronic properties in this class of materials.

Another unique feature of crystalline organic materials is their crystal anisotropy. Most crystalline organic materials consists of planar molecules forming stacks, where there is a strong overlap of  $\pi$ -orbitals in the molecular stacking direction while the orbital overlap is generally very weak between stacks.<sup>32</sup> This gives rise to large anisotropies in their electrical and optical properties. For instance, the ratio of electrical conductivities between directions parallel and normal to the substrate plane of 3,4,9,10 perylenetetracarboxylic dianhydride (PTCDA) thin films is found to be  $10^5$ ~ $10^6$ .<sup>33</sup> More recently, we have demonstrated that the difference of refractive indices along two normal directions (or birefringence) in PTCDA thin film waveguides was found to be 0.66,<sup>34</sup> which is the largest value ever reported in the literature for thin films. As a result of the large birefringence in PTCDA thin films, many optical devices such as polarization selecting waveguides and thin film optical isolators can be realized.

## 1.2 Growth of crystalline organic thin films

The first demonstration of growth of ordered crystalline organic thin films on inorganic substrates was reported by Forrest, et al.<sup>35</sup> By vacuum deposition at very high rates ( $> 50 \text{ \AA/s}$ ), ordered PTCDA thin films could be grown on Si or

glass substrates. More recently, Debe and co-workers have demonstrated that the structural ordering of perylene derivative thin films can be improved dramatically by cooling the substrate to low temperatures ( $< 150\text{K}$ ).<sup>36,37</sup> Karl, et al.<sup>38</sup> have also studied the effect of substrate temperature on the growth of PTCDA thin films on single crystal NaCl substrates. Several Japanese groups have been very active in organic thin film growth by molecular beam epitaxy. Most Japanese efforts have focused on growth of organic films on metal dichalcogenide or alkali halide substrates. For instance, Dann and co-workers<sup>39</sup> have grown ultra-thin films of phthalocyanine on KCl substrates, and Hara and co-workers<sup>40,41</sup> have studied the epitaxial growth of copper phthalocyanine thin films by RHEED (reflection high energy electron diffraction) and STM (scanning tunnelling microscopy). Most recently, Tanigaki and co-workers<sup>42</sup> have studied the dependence of the growth of GaPcCl films on vacuum base pressure, and found that single crystal growth can only be achieved with a vacuum base pressure  $< 3 \times 10^{-9}$  Torr. In addition to demonstrating the growth of organic van der Waals solid thin films, epitaxial growth of thin films of inorganic van der Waals materials has also been demonstrated. For example, Koma and co-workers<sup>43,44,45</sup> have grown epitaxial thin films of chalcogenide compounds on both van der Waals solids and GaAs substrates with surface dangling bonds terminated by sulfur atoms. However, most Japanese efforts have been concentrated on the growth of ultra-thin films of thickness less than a few monolayers, and the characterization tools for these thin films have been limited to only RHEED and STM. Thus far, there has been no report on the electrical and optical properties of such ultra-thin film.

The ability to grow high quality crystalline organic thin films is the first

step toward the fabrication of organic-on-inorganic, or fully organic-heterojunctions. Motivated by the work done by Debe, et al.<sup>36</sup> on the low substrate temperature growth of crystalline organic thin films, we have constructed an organic thin film growth system which consists of an ultra-high vacuum growth chamber and a load-lock chamber for sample loading. The key to the so called organic molecular beam deposition (OMBD) technique, which is an ultra-high vacuum growth process similar to molecular beam epitaxy, is to grow crystalline organic films at low substrate temperatures ( $< 120$  K) under ultra high vacuum conditions. In this work, we have grown PTCDA thin films at various substrate temperatures, and studied their crystallinity and surface morphology by means of wide angle x-ray diffraction and scanning electron microscopy. The results of structural analysis indicates that growth at room temperature results in highly disordered films, while growth at low substrate temperatures ( $< 120$  K) results in ordered films with PTCDA molecules stacking at an angle of  $11^\circ$  from the substrate normal. The quality of PTCDA films grown at low substrate temperatures has also been demonstrated by the low losses ( $< 2.5$  dB/cm for channel waveguides) in these thin film waveguides,<sup>46</sup> indicating optical scattering due to crystal defects is small. Since high quality crystalline organic thin films can be grown by OMBD, it is possible to fabricate a variety of heterojunctions based on these materials.

### 1.3 Organic-on-inorganic heterojunctions

Fabrication of organic-on-inorganic (OI) heterojunctions was first reported by Forrest and co-workers.<sup>47</sup> OI heterojunctions have been demonstrated

using a large number of inorganic semiconductor substrates<sup>48</sup> such as Si, GaAs,<sup>49</sup> InGaAs,<sup>50,51</sup> InP,<sup>52</sup> HgCdTe,<sup>53</sup> and InSb. In general, OI devices form rectifying junctions with low reverse leakage currents and high breakdown voltages. For example, OI devices<sup>33</sup> formed by depositing PTCDA films onto 10  $\Omega$ -cm p-Si substrates exhibit rectifying characteristics, with breakdown voltages ( $V_B$ ) as large as 230 V and reverse dark current densities at  $V_B/2$  of  $< 10 \mu\text{A}/\text{cm}^2$ . The electrical characteristics have been analyzed by Forrest, et al.<sup>33</sup> based on the thermionic-emission, space-charge-limited (TE-SCL) current model. In the past, the large breakdown voltages and low reverse currents in OI devices were attributed to the large "apparent barrier height", which is the quantity inferred using the thermionic emission model for metal-semiconductor Schottky barriers. Although the TE-SCL model gives a good approximation to charge transport under some bias regimes, the accuracy of the barrier height at the OI heterointerface obtained based on this model is still subject to question. Therefore, it is important to directly measure the energy band discontinuities at the OI heterointerface. In addition, two other important parameters should be known in order to fully understand the charge transport properties of OI heterojunctions. The first one is the majority carrier quasi-Fermi level (imref), which is used to determine the surface potential of the inorganic semiconductor, a factor crucial for semiconductor surface analysis using techniques such as semiconductor organic-on-inorganic surface analysis spectroscopy (SOISAS).<sup>54,55</sup> Another parameter is the carrier velocity in the organic film, which determines the ultimate speed limitation of OI heterojunction devices. In this work, both of these parameters are calculated, and the results are compared

with experimental data.

Having analyzed the charge transport properties of OI heterojunctions, there are still many unanswered questions regarding the nature of the OI barriers. For example, what determines the barrier energy at the heterointerface? Is it a phenomenon determined by the molecular and atomic potentials contacting at the interface, or is it due to fixed charge induced due to chemical interactions between species from the contacting materials?<sup>56,57</sup> In order to understand the mechanisms for OI energy barrier formation, it is important to know what reactions take place and the nature of defect states at the heterointerface. Here, we study the electrical characteristics of OI heterojunctions employing both dianhydride and phthalocyanine (Pc) compounds, and the results indicate that in the case of OI heterojunctions with Pc compounds, a large number of defects form at the OI heterointerface due to the chemical interactions between species from both the inorganic and organic semiconductors. Hence, in some cases, the surface Fermi level of the inorganic semiconductor is pinned at the defect level, thereby determining the barrier height energy.

#### I.4 Fully organic heterojunctions

Another type of heterojunction we study here is the contact formed between two crystalline organic semiconductors. Fully organic heterojunction devices have been investigated for some time, and most efforts have been focused on organic photovoltaic cells.<sup>58</sup> Recently, there have also been reports on electroluminescent devices using crystalline organic materials.<sup>59</sup> Although new crystalline organic heterojunctions have been demonstrated, no thorough studies



# VeloBind

## PAPER

on charge transport across organic heterojunctions have yet been reported. The lack of detailed studies of the charge transport has led to some misunderstanding in the nature of organic heterojunctions in the literature. For example, some authors<sup>60</sup> have suggested that the rectifying characteristics in organic heterojunctions are due to formation of p-n junctions. As will be shown in this work, this is not necessarily the case. It is, therefore, the purpose of this work to understand the fundamental nature of organic heterojunctions and how charge transport occurs across these junctions.

**DESCRIPTION** 20# COPY BOND  
PLAIN SIDEBIND

**COLOR** WHITE

To study the charge transport properties of organic heterojunctions, we have fabricated n-p-i-s-s devices using three crystalline organic materials, namely, PTCDA, PTCBI, and CuPc. From the results of current-voltage and capacitance-voltage measurements, we find that the charge transport across the organic heterobarrier can be understood in terms of transport theory used to describe the charge transport in organic heterojunctions. In particular, the energy differences between the valence-like bands of the contacting materials have been measured, and the results indicate that hole transport is limited by thermionic emission over the heterojunction energy barrier, similar to that in inorganic semiconductor heterojunctions. Further, band offset energies between the contacting organic materials in these heterojunctions follow a transitive relationship, which gives evidence that defect states at the heterointerfaces do not significantly affect the band offset energies. Since the heterojunction energy barrier is sufficient to control the charge transport across the interface, provided that the charge carrier deionization effect is large compared to the layer thickness in an organic multilayer structure, it is possible to observe the effect of

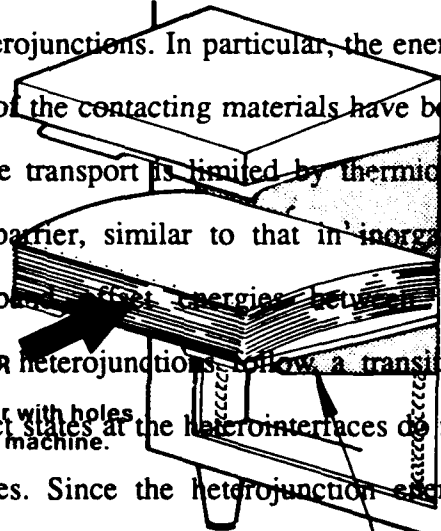
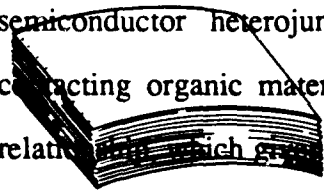
**QUANTITY** 500

**SIZE** 11 x 8 1/2

**PART NO** 4000

**DIRECTIONS:** For optimum results, the VeloBind paper should be loaded in the paper tray with the leading edge (the unpunched side) feeding into the machine first. It is important that the natural curve of the paper is down. Fan and jog the paper prior to loading.

load paper with holes away from machine.



**SOUTHERN CALIFORNIA DISTRICT OFFICE**

5701 SO. EASTERN AVE., SUITE 620  
LOS ANGELES, CALIFORNIA 90040

(213) 721-9898 • FAX (213) 721-2929

**VeloBind**

Offices in Principal Cities

carrier confinement in organic multiple quantum well structures using crystalline organic semiconductors.

### 1.5 Organic multiple quantum well structures

Recently, Lam and co-workers<sup>61</sup> have shown theoretically that crystalline organic multiple quantum well structures based on PTCDA and NTCDA (3,4,7,8 naphthalenetetracarboxylic dianhydride) exhibit large non-linear optical effects. In particular, they predicted that these organic MQW structures should show an intensity dependent absorption and index of refraction at relatively low input powers, which leads to optical bistability. On the other hand, excitons in organic semiconductors are in general thought to be Frenkel-like, i.e., they are localized within a molecule. However, there are also a few reports suggesting that excitons in some aromatic compounds such as anthracene and similar materials are Wannier in nature.<sup>62</sup> Therefore, crystalline organic MQW structures might provide a tool to study the nature of excitons in crystalline organic materials.

Crystalline organic multiple quantum well structures studied here were grown by organic molecular beam deposition. The organic MQW structures consisted of ultra-thin alternating layers of PTCDA and NTCDA with layer thicknesses varying from 10 Å to 200 Å. The results of x-ray diffraction and birefringence measurements indicate that the organic multilayer structures consist of ordered single crystalline-like layers, although the crystal structures of the two materials used are incommensurate. Further, there is an increase of the singlet ground state exciton energy with decreasing layer thickness. The results can be explained in terms of a change in exciton binding energy due to quantum

confinement in a potential well formed by the energy band offsets between the contacting materials. Variational calculations have been done on the well width dependence of the exciton binding energy, and the results are consistent with the experimental data. In order to observe exciton confinement in quantum wells, the luminescence decay times in these organic MQWs have been measured, and there is a decrease in exciton lifetime as the well width decreases. This is also consistent with the exciton quantum confinement picture. The results of the above optical measurements do suggest that the carrier wavefunction does not localize within a molecular site, but extends to the neighboring molecules to such an extent that quantum confinement is observed.

### 1.5 Thesis organization

Most of the work discussed in this dissertation has been previously published by the author (see refs. 34, 46, and 63-73). The dissertation is organized as follows: In Chapter 2, we review the crystal structures and properties of the crystalline organic materials studied in this work, and describe the growth of crystalline organic thin films by organic molecular beam deposition. The theory on charge transport in OI heterojunctions is presented in Chapter 3. In particular, we present the results of calculations on the quasi-Fermi level energy across the OI heterojunction and the carrier velocity in the organic thin film, together with the experimental measurements of the energy band discontinuities. In addition, the effect of organic thin film composition on the electrical characteristics of OI heterojunctions, and the device characteristics of OI photodetectors are also discussed in this chapter. In Chapter 4, we discuss the

fabrication of fully organic heterojunctions and their device characteristics. The growth of organic multiple quantum well structures and their structural properties is discussed in Chapter 5. The optical properties together with the results of variational calculations are also presented in that chapter. Finally, measurements of the large dielectric anisotropies of PTCDA are described in Appendix A.

## References

- <sup>1</sup> H. Kroemer, Proc. IRE **45**, 1535 (1957)
- <sup>2</sup> H. Kroemer, Proc. IEEE **51**, 1782 (1963)
- <sup>3</sup> J. Schewchun and L.Y. Wei, J. Electrochem. Soc. **111**, 1145 (1964)
- <sup>4</sup> R.L. Anderson, Solid State Electron. **5**, 341 (1962)
- <sup>5</sup> H. Kressel and H. Nelson, RCA Rev. **30**, 106 (1969)
- <sup>6</sup> H.C. Casey and M.B. Panish, *Heterostructure Lasers*, (Academic, New York, 1978)
- <sup>7</sup> H. Kroemer, Proc. IEEE **70**, 13 (1982)
- <sup>8</sup> Y. Yamauchi and T. Ishibashi, IEEE Electron Dev. Lett. **EDL-7**, 655 (1986)
- <sup>9</sup> A.Y. Cho and J.R. Arthur, Prog. Solid-State Chem. **10**, 157 (1975)
- <sup>10</sup> R.D. Dupuis and P.D. Dapkus, IEEE J. Quantum Electron. **QE-15**, 128 (1979)
- <sup>11</sup> U. Ekenberg and M. Altarelli, Phys. Rev. **B30**, 3569 (1984)
- <sup>12</sup> G. Bastard and J.A. Brum, IEEE J. Quantum Electron. **QE-22**, 1625 (1986)
- <sup>13</sup> L. Esaki, IEEE J. Quantum Electron. **QE-22**, 1611 (1986)
- <sup>14</sup> J.P. Faurie, IEEE J. Quantum Electron. **QE-22**, 1656 (1986)
- <sup>15</sup> R. Hull, J.C. Bean, and C. Buescher, J. Appl. Phys. **66**, 5836 (1989)
- <sup>16</sup> W.T. Tsang, Semiconductors and Semimetals, ed. R. Dingle, Vol. 24, (Academic, New York, 1987)
- <sup>17</sup> F. Capasso, W.T. Tsang, A.L. Hutchinson, and G.F. Williams, Appl. Phys. Lett. **40**, 38 (1982)
- <sup>18</sup> T.C. Soller, W.D. Goodhue, P.E. Tannenwalid, C.D. Parker, D.D. Peck, Appl. Phys. Lett. **43**, 588 (1983)

- <sup>19</sup> D.A.B. Miller, Appl. Phys. Lett. **54**, 202 (1989)
- <sup>20</sup> J. W. Matthews and A.E. Blakeslee, J. Cryst. Growth **27**, 118 (1974)
- <sup>21</sup> M. Pope and C.E. Swenberg, *Electronic Processes in Organic Crystals* (Oxford, New York, 1982)
- <sup>22</sup> E.A. Silinsh, *Organic Molecular Crystals*, (Spring-Verlag, Heidelberg, 1980)
- <sup>23</sup> L.B. Schein, Chem. Phys. Lett. **48**, 571 (1977)
- <sup>24</sup> Z. Burshtein and D.F. William, Phys. Rev. **B15**, 5769 (1977)
- <sup>25</sup> H. Frolich and G.K. Sewell, Proc. Phys. Soc. London **74**, 543 (1959)
- <sup>26</sup> J.I. Katz, S.A. Rice, S. Choi, and M.T. Vula, J. Chem. Phys. **42**, 733 (1965)
- <sup>27</sup> L.B. Schein and A. R. McGhie, Phys. Rev. **B20**, 1631 (1979)
- <sup>28</sup> P. Mark and W. Helfrich, J. Appl. Phys. **33**, 205 (1962)
- <sup>29</sup> W. Helfrich and W.G. Schneider, Phys. Rev. Lett. **14**, 229 (1965)
- <sup>30</sup> H. Killesreiter and H. Bassler, Phys. Stat. Sol. **B51**, 657 (1972)
- <sup>31</sup> H. Kuhn, J. Chem. Phys. **53**, 101 (1970)
- <sup>32</sup> J.M. Robertson, Rev. Mod. Phys. **30**, 155 (1958)
- <sup>33</sup> S.R. Forrest, M.L. Kaplan, and P.H. Schmidt, J. Appl. Phys. **55**, 1492 (1984)
- <sup>34</sup> D.Y. Zang, F.F. So, and S.R. Forrest, Appl. Phys. Lett. (1991)
- <sup>35</sup> S.R. Forrest, M.L. Kaplan, and P.H. Schmidt, J. Appl. Phys. **56**, 543 (1984)
- <sup>36</sup> K.K. Kam, M.K. Debe, R.J. Poirier, and A.R. Drube, J. Vac. Sci. Technol. **A5**, 1914 (1987)
- <sup>37</sup> M.K. Debe, K.K. Kam, J.C. Liu, and R.J. Poirier, J. Vac. Sci. Technol. **A6**, 1907 (1988)
- <sup>38</sup> M. Mobus, M. Schreck, and N. Karl, Thin Solid Films **175**, 89 (1989)
- <sup>39</sup> A.J. Dann, H. Hoshi, and Y. Maruyama, J. Appl. Phys. **67**, 1371 (1990)

- <sup>40</sup> M. Hara, H. Sasabe, Y. Yamada, and, A.F. Garito, Mat. Res. Soc. Symp. Proc. **159**, 57 (1990)
- <sup>41</sup> M. Hara, H. Sasabe, Y. Yamada, and, A.F. Garito, Jpn. J. Appl. Phys. **28**, L306 (1989)
- <sup>42</sup> M. Tanigaki, Frontier Forum on Organic MBE and STM Symp. Proc. (Wako, Japan, March, 1991)
- <sup>43</sup> A. Koma, K. Saiki, and Y. Sato, Appl. Surf. Sci. **41**, 451 (1989)
- <sup>44</sup> K. Ueno, T. Shimada, K. Saiki, and A. Koma, Appl. Phys. Lett. **56**, 327 (1990)
- <sup>45</sup> K. Ueno, K. Saiki, T. Shimada, and A. Koma, J. Vac. Sci. Technol. **A8**, 68 (1990)
- <sup>46</sup> D.Y. Zang, Y.Q. Shi, F.F. So, S.R. Forrest, and W.H. Steier, Appl. Phys. Lett. **58**, 562 (1991)
- <sup>47</sup> S.R. Forrest, M.L. Kaplan, P.H. Schmidt, T. Venkatesan, and A.J. Lovinger, Appl. Phys. Lett. **41**, 90 (1982)
- <sup>48</sup> P.H. Schmidt, S.R. Forrest, and M.L. Kaplan, J. Electrochem. Soc. **133**, 769 (1986)
- <sup>49</sup> S.R. Forrest, M.L. Kaplan, P.H. Schmidt, and J.M. Parsey, J. Appl. Phys. **58**, 867 (1985)
- <sup>50</sup> S.R. Forrest, P.H. Schmidt, R.B. Wilson, and M.L. Kaplan, Appl. Phys. Lett. **45**, 1199 (1984)
- <sup>51</sup> S.R. Forrest, P.H. Schmidt, R.B. Wilson, and M.L. Kaplan, J. Vac. Sci. Technol. **B4**, 37, (1986)
- <sup>52</sup> S.R. Forrest, M.L. Kaplan, and P.H. Schmidt, J. Appl. Phys. **60**, 2406 (1986)
- <sup>53</sup> S.J. Cheng, L.Y. Leu, S.R. Forrest, C.E. Jones, Appl. Phys. Lett. **54**, 1040

(1989)

<sup>54</sup> S.R. Forrest, M.L. Kaplan, and P.H. Schmidt, J. Appl. Phys. **59**, 513 (1986)

<sup>55</sup> S.R. Forrest, M.L. Kaplan, and P.H. Schmidt, J. Appl. Phys. **60**, 2406 (1986)

<sup>56</sup> J.M. Andrews and J.C. Phillips, Phys. Rev. Lett. **35**, 56 (1975)

<sup>57</sup> W.E. Spicer, I. Lindau, P. Skeath, C.Y. Su, and P. Chye, Phys. Rev. Lett. **44**, 420 (1980)

<sup>58</sup> C.W. Tang, Appl. Phys. Lett. **48**, 183 (1986)

<sup>59</sup> C. Adachi, S. Tokito, T. Tsutsui, and S. Saito, Jpn. J. Appl. Phys. **27**, L713 (1988)

<sup>60</sup> C.W. Tang and S.A. Vanslyke, Appl. Phys. Lett. **51**, 913 (1987)

<sup>61</sup> J.F. Lam, S.R. Forrest, G.L. Tangonan, Phys. Rev. Lett. **66**, 1614 (1991)

<sup>62</sup> P.J. Bounds and W. Siebrand, Chem. Phys. Lett. **75**, 414 (1980)

<sup>63</sup> F.F. So and S.R. Forrest, J. Appl. Phys. **63**, 442 (1988)

<sup>64</sup> F.F. So and S.R. Forrest, Proc. SPIE Conf. on Growth of Compound Semiconductor Structures, Vol. 994 (1988)

<sup>65</sup> F.F. So and S.R. Forrest, Appl. Phys. Lett. **52**, 1341 (1988)

<sup>66</sup> S.R. Forrest and F.F. So, J. Appl. Phys. **64**, 399 (1988)

<sup>67</sup> S.R. Forrest, L.Y. Leu, F.F. So, and W.Y. Yoon, J. Appl. Phys. **66**, 5908 (1989)

<sup>68</sup> F.F. So and S.R. Forrest, IEEE Trans. Electron. Dev. **36**, 66 (1989)

<sup>69</sup> S.R. Forrest, F.F. So, and D.Y. Zang, Proc. of the 16th European Conf. on Optical Comm. Amsterdam, 1990

<sup>70</sup> F.F. So, L.Y. Leu, and S.R. Forrest, SPIE Conf. Proc. Vol. 1285, pp.95 (1990)

<sup>71</sup> F.F. So, S.R. Forrest, Y.Q. Shi, and W.H. Steier, Mat. Res. Soc. Symp. Proc.



Vol. 198, pp.71, 1990

<sup>72</sup> F.F. So and S.R. Forrest, Y.Q. Shi, and W.H. Steier, Appl. Phys. Lett. **56**, 674  
(1990)

<sup>73</sup> F.F. So and S.R. Forrest, Phys. Rev. Lett. May 20, 1991

<sup>74</sup> F.F. So and S.R. Forrest, Electronic Materials Conf. Proc. Boulder, Co. 1991

## Chapter II

### Growth and properties of organic thin films

The crystal structures and the properties of crystalline organic semiconductors are determined by the virtue of the starting materials and growth methods used. In this chapter, we will first discuss crystal structure and how it is related to the material properties, and then we will describe methods used to grow crystalline organic thin films. The effect of deposition parameters on thin film microstructures and material properties will also be discussed. Finally, we will present the theory on crystal anisotropy in crystalline organic materials and the results of dielectric measurements on crystalline organic thin films.

#### II.1 Crystal structures and material properties

Crystalline organic semiconductors are in many ways different from inorganic semiconductors.<sup>1,2</sup> They consist of discrete organic molecules held together by the relatively weak van der Waals force, in contrast to inorganic semiconductors where atoms are held by strong covalent or ionic bonds. Since the interaction between molecules is weak, organic molecular solids are generally soft and have relatively low sublimation temperatures. Further, there are no chemical bonds between molecules, therefore the properties of individual molecules are retained in the solid state to a far greater extent than would be found in non-molecular solids.

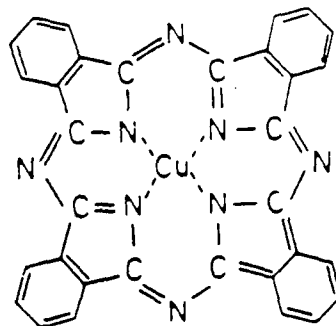
The crystalline organic semiconductors used in this work are: 3,4,9,10 perylenetetracarboxylic dianhydride (PTCDA), 3,4,7,8 naphthalene-

tetracarboxylic dianhydride (NTCDA), 3,4,9,10 perylenetetracarboxylic-bis-benzimidazole (PTCBI), hydrogen phthalocyanine ( $H_2Pc$ ), and copper phthalocyanine (CuPc). The molecular structures of these compounds are shown in Fig. 2.1, and some of the crystal structure data and material properties are also summarized in Table 2.1. One common property of these materials is that they consist of planar molecules which form crystalline stacks. Due to the overlap of  $\pi$ -orbitals between molecules within the stacks, the carrier mobilities of these compounds along the stacking direction are in general high, ranging from  $10^{-2}$   $cm^2/V\cdot s$  for NTCDA to  $> 1$   $cm^2/V\cdot s$  for PTCDA<sup>3</sup>. On the contrary, charge transport between adjacent stacks is inhibited by the lack of orbital overlap, resulting in low carrier mobility in directions transverse to the stacking axis. Therefore, large anisotropies in both the electrical and dielectric properties are anticipated. In this section, we will discuss the crystal structures and the properties of individual compounds in detail.

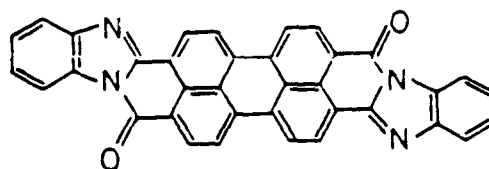
#### (A) PTCDA and NTCDA

Fig. 2.2 shows two views of a unit cell of PTCDA as determined from x-ray crystallographic studies of purified single crystals<sup>4</sup> grown by vapor phase techniques. The crystal has a monoclinic lattice with 2 molecules per unit cell, and the space group is  $P2_1/c(C_{2h}^5)$ . PTCDA has a band gap of 2.2 eV and it absorbs light strongly in the green band of the visible spectrum, giving rise to a deep red color for thin films deposited in vacuum.

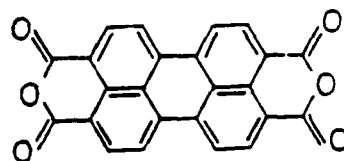
**CuPc**



**PTCBI**



**PTCDA**



**NTCDA**

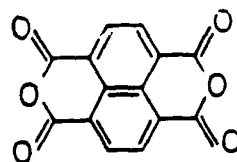


Fig. 2.1 Molecular structures of crystalline organic semiconductors: PTCDA, PTCBI, NTCDA, and CuPc.

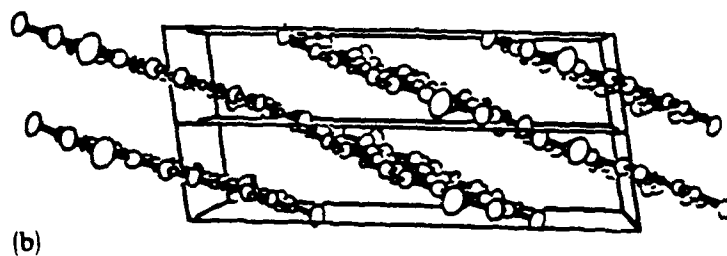
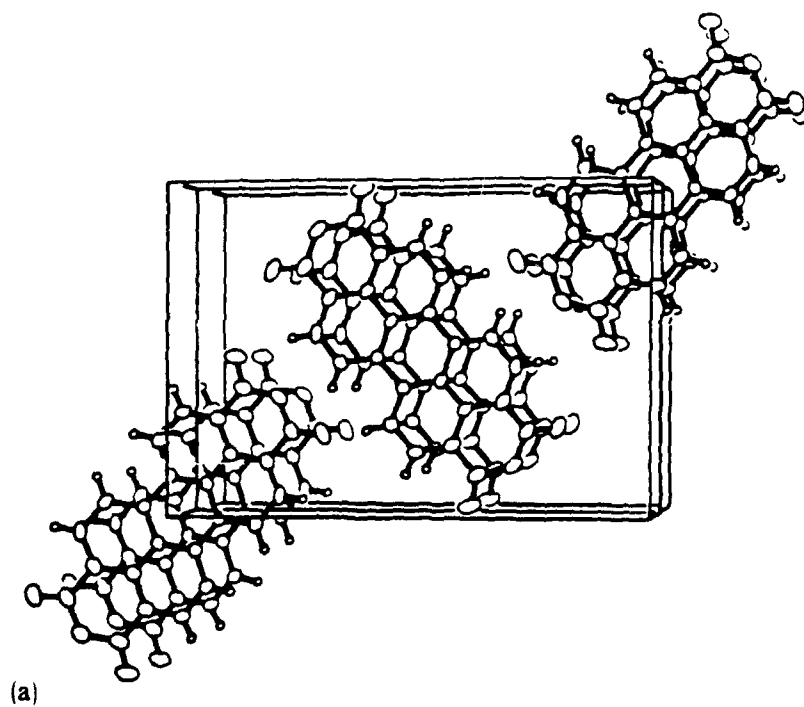


Fig. 2.2 Two perspective views of a PTCDA unit cell.

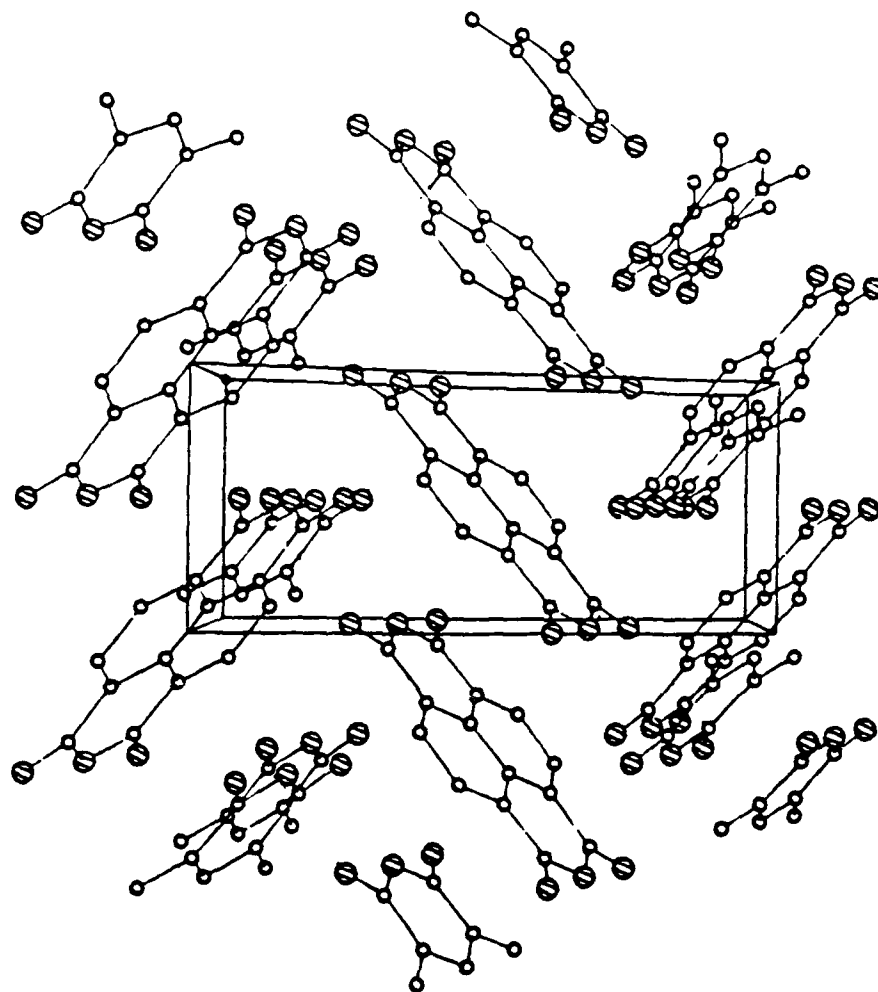


Fig. 2.3 A perspective views of an NTCDA unit cell.

Table 2.1 Lattice parameters and energy gaps of several crystalline organic materials.

Lattice Parameters or Energy Gap	PTCDA	NTCDA	CuPc	H <sub>2</sub> Pc
a (Å)	3.719	7.888	25.92	26.14
b (Å)	11.96	5.334	3.790	3.814
c (Å)	17.34	12.74	23.92	23.97
$\beta$	98.81°	109.04°	90.4°	91.1°
Space group	P2 <sub>1/a</sub> (C <sub>2h</sub> <sup>5</sup> )	P2 <sub>1/a</sub> (C <sub>2h</sub> <sup>5</sup> )	P2 <sub>1/c</sub> (C <sub>2h</sub> <sup>6</sup> )	P2 <sub>1/c</sub> (C <sub>2h</sub> <sup>6</sup> )
Energy gap (eV)	2.2	3.1	2.1	2.6

Molecules in PTCDA films lying in the (102) plane stack at  $11^\circ$  from the substrate normal in such a way that equivalent molecules are directly above one another<sup>4</sup>, with molecules in adjacent stacks rotated  $90^\circ$ . The interplanar spacing within the stack is 3.21 Å, which is even smaller than the interplanar spacing of graphite (3.37 Å). The close intermolecular spacing leads to extensive overlap of  $\pi$ -orbitals, resulting in a higher carrier mobility in PTCDA than in most crystalline organic materials we studied. Due to asymmetry in the crystal structure, extremely large anisotropies in both dielectric and conducting properties have been observed in PTCDA thin films<sup>5,6</sup>. For example, anisotropies in electrical conductivity have been found to be on the order of  $10^6$ , and the difference in indices of refraction ( $\Delta n$ ) along the two orthogonal directions in the crystal is 0.66. Crystal anisotropies will be discussed in detail later in this chapter.

NTCDA molecules are very similar to PTCDA molecules except that the center perylene molecule is replaced by a naphthalene molecule with 2 benzene rings. The NTCDA crystal also has a monoclinic lattice with 2 molecules per unit cell<sup>7</sup>, and it has the same space group as PTCDA. Fig. 2.3 shows a perspective view of an NTCDA unit cell. The NTCDA crystal has a band gap of 3.1 eV, and it absorbs light in the UV region. It is transparent to visible light, and has a very light yellowish color. Molecules stack in a herringbone structure in the crystal with stacks of molecules forming a nested "V" shape. Since adjacent molecules within the stack shift by a distance of about half of the molecular length, the  $\pi$ -orbital overlap is smaller than that of PTCDA, resulting in a lower sublimation temperature of 250°C and a lower carrier mobility of  $10^{-2}$  cm<sup>2</sup>/V-s.



### (B) CuPc and H<sub>2</sub>Pc

The word phthalocyanine (Pc) comes from Greek words *naphtha* and *cyanide* meaning rockoil and dark blue<sup>8</sup>. Pc's are dye compounds that have been known since the beginning of the century. These compounds show exceptional thermal and chemical stability with high sublimation temperatures. Pc's form an extremely versatile chemical system, and at present more than seventy Pc compounds have been identified. Elements from group I<sub>A</sub> to V<sub>B</sub> can all combine with the Pc ring to form metal Pc's (for example, see Fig. 2.1)<sup>8</sup>. Thus an extremely wide range of optical properties in Pc's are anticipated by varying the metal substituent in the ring.

Both CuPc and H<sub>2</sub>Pc are monoclinic crystals belonging to the P2<sub>1/c</sub> space group with two molecules per unit cell<sup>9</sup>. The base centered arrangement of the crystal is shown in Fig. 2.4. The figure also shows the projection of two CuPc molecules in the crystal. The molecular structure of H<sub>2</sub>Pc<sup>10</sup> is similar to that of CuPc except that the center Cu atom is replaced by two hydrogen atoms. When a projection is taken normal to a H<sub>2</sub>Pc molecular plane, none of the atoms in one molecule lie exactly above the atoms in an adjacent molecule in the stack, resulting in a reduced overlap of  $\pi$ -orbitals.

When a copper atom is substituted for the two central hydrogen atoms in the upper molecule, it lies exactly over the nitrogen atom in the molecule below as shown in Fig. 2.4. The intermolecular copper-nitrogen separation is 3.38 Å, which is the closest distance between the two adjacent molecules<sup>10</sup>. The substitution of a copper ion for the two central hydrogen ions in metal-free Pc creates a link between nitrogen atoms on molecules below and above. The results

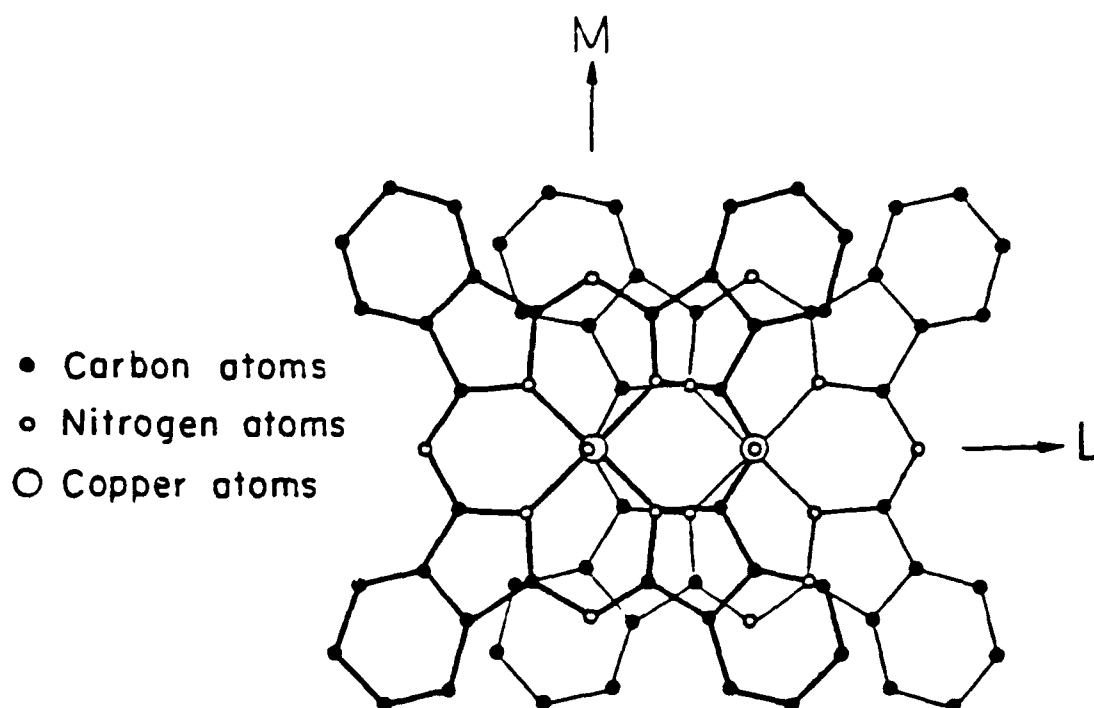


Fig. 2.4 Normal projection of two CuPc molecules. Heavy lines outline the upper molecule; light lines outline the underlying molecule. L and M are the molecular axes of the upper molecule.

of electron spin resonance measurements by Harrison and Assour<sup>10</sup> indicate that there is a considerable overlap between the nitrogen  $\pi$  orbitals and the copper 3d orbitals. Because of the Cu-N orbital overlap, the intermolecular coupling is enhanced, resulting in higher carrier mobility in CuPc than that in H<sub>2</sub>Pc. Indeed, the carrier mobility in CuPc ( $10^{-2}$  cm<sup>2</sup>/V s) is about two orders of magnitude higher than that of H<sub>2</sub>Pc ( $10^{-4}$  cm<sup>2</sup>/V s)<sup>12</sup>.

## II.2 Material preparation

Organic materials that have been used most extensively in this work are all aromatic or phthalocyanine dye compounds. In general, organic dye compounds obtained from commercial manufacturers contain a large quantity of impurities and are not suitable for study and device fabrication. It is therefore important to purify all organic materials prior to deposition. This ensures highly stable and reproducible electrical and optical characteristics of the resulting devices.

Crystalline organic semiconductors are typically purified by zone-refining or gradient sublimation techniques<sup>11,12</sup>. All crystalline organic materials used in this work sublime at atmospheric pressure. In this work, therefore, they were purified by sublimation. All of the materials studied, PTCDA, NTCDA, H<sub>2</sub>Pc, and CuPc are commercially available<sup>13</sup>. Gradient sublimation was done by first putting several grams of starting material (usually in powder form) into the sealed end of a quartz tube as shown in Fig. 2.5. The tube was then evacuated to  $10^{-6}$  Torr by pumping on its open end with the sealed end inserted into a preheated furnace. The source material was kept at 20°C above its sublimation temperature

## TWO STAGE ORGANIC PURIFICATION

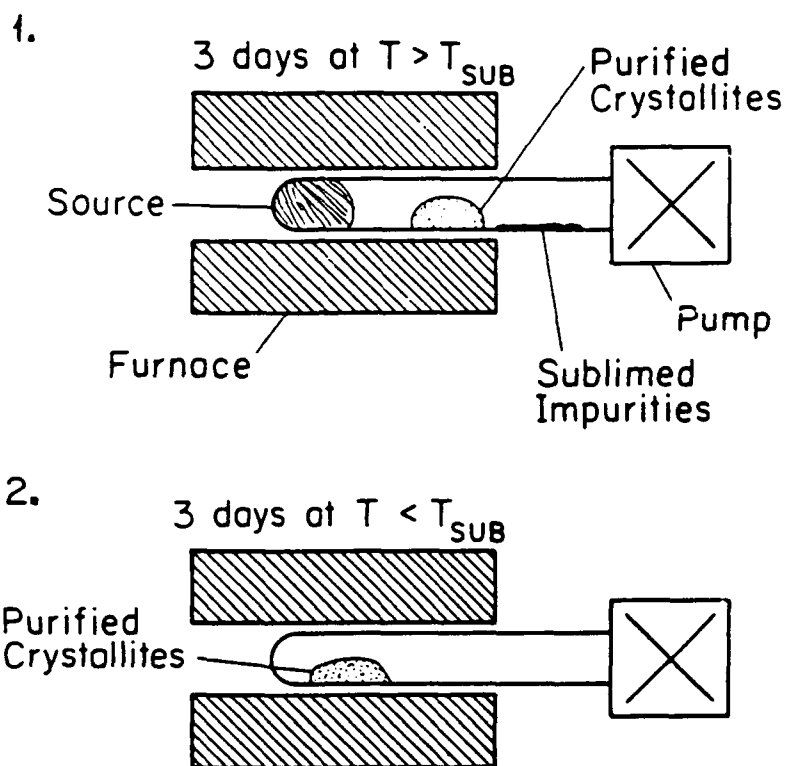


Fig. 2.5 A set up for organic material purification by gradient sublimation.

for 3 days. During this period, organic crystallites usually in whisker form, grew on the inner side wall of the tube in the cold zone of the furnace, while more volatile impurities were evacuated. The impurity residue (mostly carbon black) with higher sublimation temperatures than the source was left in the hot zone of the furnace, and was therefore separated. The organic crystallites were then removed from the tube and repurified for another 3 days at a temperature of 20°C below the source sublimation temperature.

PTCBI was not available commercially. Thus the synthesis of PTCBI<sup>14</sup> was accomplished by mixing 1.96g of pre-purified PTCDA in a 7.5g o-phenylenediamine solution held at 190°C for 4 hours in an oil bath. The fine powdered precipitate was then kept at 45°C for 15 minutes in a mixture containing 560 cc of water, 11g of sodium hydroxide and 11g of sodium hydrosulfate. The whole mixture was then filtered and boiled in a solution of benzoyl chloride and nitrobenzene at 210°C for 5 hours. At this stage, PTCDA was completely converted to PTCBI. The residue was then filtered and dried. Finally, purification by gradient sublimation was carried out for PTCBI according to the procedures described above.

### II.3 Organic molecular beam deposition

Similar to inorganic materials, single crystalline organic materials can be grown from melts with seed crystals using a variety of techniques such as Bridgman and Czochralski growth<sup>12</sup>. Due to the unique nature of van der Waals bonds in crystalline organic semiconductors, the organic semiconductor crystal growth mechanism is expected to be very different from that of inorganic

semiconductors. Thin films of crystalline organic materials grown by vacuum deposition techniques are usually polycrystalline<sup>8</sup> when deposited at room temperature or above. However, under appropriate deposition conditions, highly ordered organic films can be grown on a variety of substrate materials<sup>3,15,16</sup>.

Recent work by Debe and co-workers<sup>17,18</sup> has demonstrated that the microstructure of vapor-deposited perylene dicarboximide thin films is extremely sensitive to the substrate temperature during deposition. At substrate temperatures below 170 K, the surface morphology of the films was found to be very smooth, indicative of a high degree of crystalline order. However, at substrate temperatures above room temperature (up to 400 K), the surface morphology of the deposited films appears to have a whisker-like texture with crystalline filaments oriented randomly on the surface. Recently, Dann, et al.<sup>19</sup> have demonstrated the epitaxial growth of phthalocyanine films on alkali halide substrates by organic molecular beam epitaxy at low substrate temperatures.

More recently, we have also demonstrated<sup>15,16</sup> that, at low substrate temperatures, highly ordered crystalline organic thin films can be grown on a variety of organic and inorganic substrate materials. In fact, combinations of two different van der Waals crystals with vastly different lattice constants have been observed to grow in ordered, multilayer stacks. The so-called quasi-epitaxial growth can be achieved by organic molecular beam deposition (OMBD) -- a process similar to conventional molecular beam epitaxy used to grow semiconductor heterostructures. Since the properties of crystalline organic semiconductors are very sensitive to the presence of impurities<sup>8</sup>, ultra-high vacuum is desirable for growing crystalline organic thin films. In this section, we

will discuss in detail the techniques of organic molecular beam deposition, and the design of the growth system. Also, a second generation inorganic/organic semiconductor molecular beam epitaxy system currently under construction will be briefly described.

#### (A) Growth and system design

The technique of organic molecular beam deposition<sup>20,21</sup> is similar to conventional molecular beam epitaxy (MBE) used to grow inorganic semiconductor materials. The major difference between the two is the substrate temperature used during growth. Conventional MBE techniques usually require substrates to be held at elevated temperatures (500 - 600°C), whereas low substrate temperatures are required for OMBD growth of single crystalline organic films. A schematic diagram of the OMBD system constructed in our laboratory is shown in Fig. 2.6. It consists of a 12" diameter stainless steel ultra-high vacuum growth chamber with a base pressure of  $5 \times 10^{-10}$  Torr, and a small load-lock chamber. The load-lock chamber is used for sample loading without breaking vacuum in the growth chamber. All components used in the growth chamber are ultra-high vacuum compatible. The growth chamber is equipped with a Varian model CS-8 cryopump, a Varian 270 l/s ion pump and a titanium sublimation pump, while the load-lock chamber is pumped by a 50 l/s Leybold turbo pump.

Purified crystalline organic materials are loaded in sublimation cells with a circular exit port which allows for the directional evaporation of organic molecules toward the substrate. These sublimation cells are similar to those used for silicon monoxide evaporation. Resistance heating of sublimation cells was

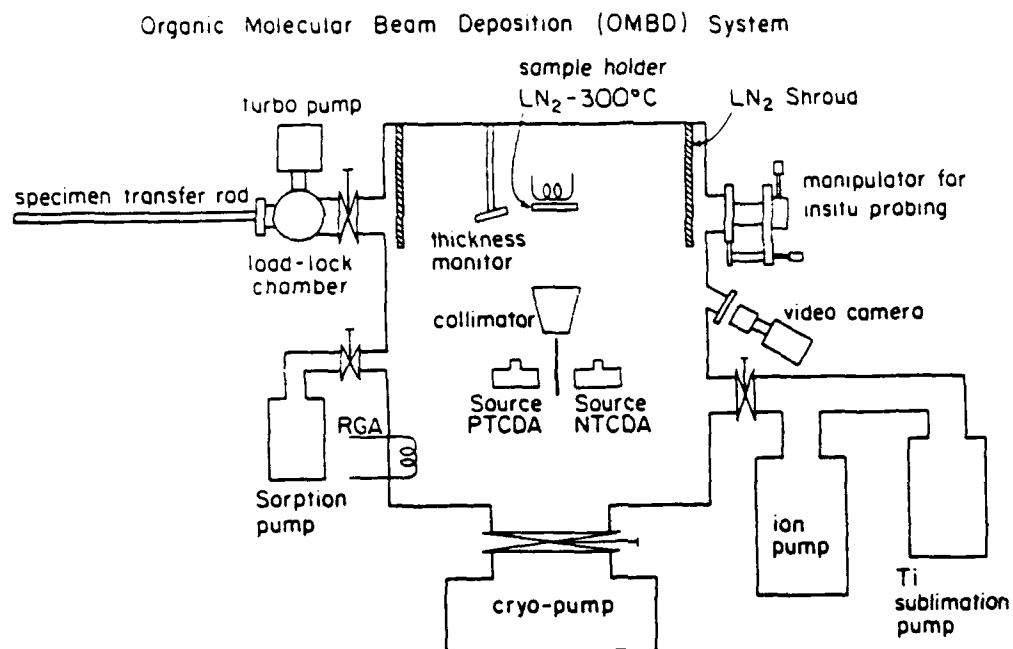


Fig. 2.6 A schematic diagram of the organic molecular beam deposition system.



used to elevate the source temperature to achieve sublimation of organic materials.

Sorption pumps were used to rough the chamber to below 500 mTorr, at which point the cryopump can be used by opening the main gate valve. Within a few minutes, the chamber pressure reaches the  $10^{-7}$  Torr range. Without baking, the chamber pressure reaches  $10^{-9}$  Torr in less than 24 hours. After baking the chamber with heat tapes at about 180°C for two days, the pressure reaches  $10^{-10}$  Torr in 12 hours. Aluminum foil was used to wrap the chamber during baking. It provides for uniform heating and shielding of the chamber. After the desired vacuum level is achieved, the growth chamber is ready for deposition.

Substrates mounted onto an oxygen-free copper sample plate are first loaded into the load lock chamber which is then evacuated by the turbo pump to  $10^{-7}$  Torr. After opening the small gate valve between the load-lock and growth chambers, the sample plate is transferred from the load lock chamber into the growth chamber and hence loaded onto a substrate holder using a magnetically driven transfer rod. The small gate valve is then closed immediately after loading. The growth chamber pressure typically rises into the  $10^{-8}$  Torr range after the gate small valve is closed, but drops to  $1 \times 10^{-9}$  Torr after 15 minutes. The substrate holder is made from oxygen-free copper which can be cooled to low temperatures by flowing liquid nitrogen through channels machined inside the block. In order to achieve uniform growth over a sample area of  $(2.5 \text{ cm})^2$ , the source-to-substrate distance should be about 35 cm. Smaller source-to-substrate distances result in non-uniform growth. On the other hand, larger source-to-substrate distances result in excessive consumption of organic materials.

Prior to growth, the sample block was first cooled down to below 100 K for about 10 minutes. Growth was achieved by heating the sublimation cells (to approximately 450°C for PTCDA and 250°C for NTCDA) to obtain a growth rate of 1 - 5 Å/s, depending on the device structure desired. The organic film thickness and the deposition rate were measured using a quartz crystal thickness monitor which was located next to the substrate holder. To grow organic heterostructures or multiple quantum well structures<sup>15, 16</sup>, growth was achieved by sequential shuttering of the sources. The pressure during growth varied depending on the vapor pressure of the crystalline organic materials used. For NTCDA, the pressure during growth was  $\cong 10^{-8}$  Torr while the pressure during the growth of PTCDA was  $\cong 10^{-7}$  Torr.

#### (B) Organic/inorganic molecular beam epitaxy system

A schematic diagram of the new organic/inorganic semiconductor molecular beam epitaxy system under construction is shown in Fig. 2.7. It has the capability of growing organic materials by OMBD and III-V compounds by gas source molecular beam epitaxy (GSMBE). The system consists of an OMBD chamber, a GSMBE growth chamber, an electron beam evaporation chamber for metal deposition, an analytical chamber for in-situ electrical and optical characterization, and a load-lock chamber for sample loading. All these chambers are attached to a Vacuum Generators R2P2 chamber which is used for delivering samples from one chamber to another within the system. The specifications for each chamber are given in Table 2.2.

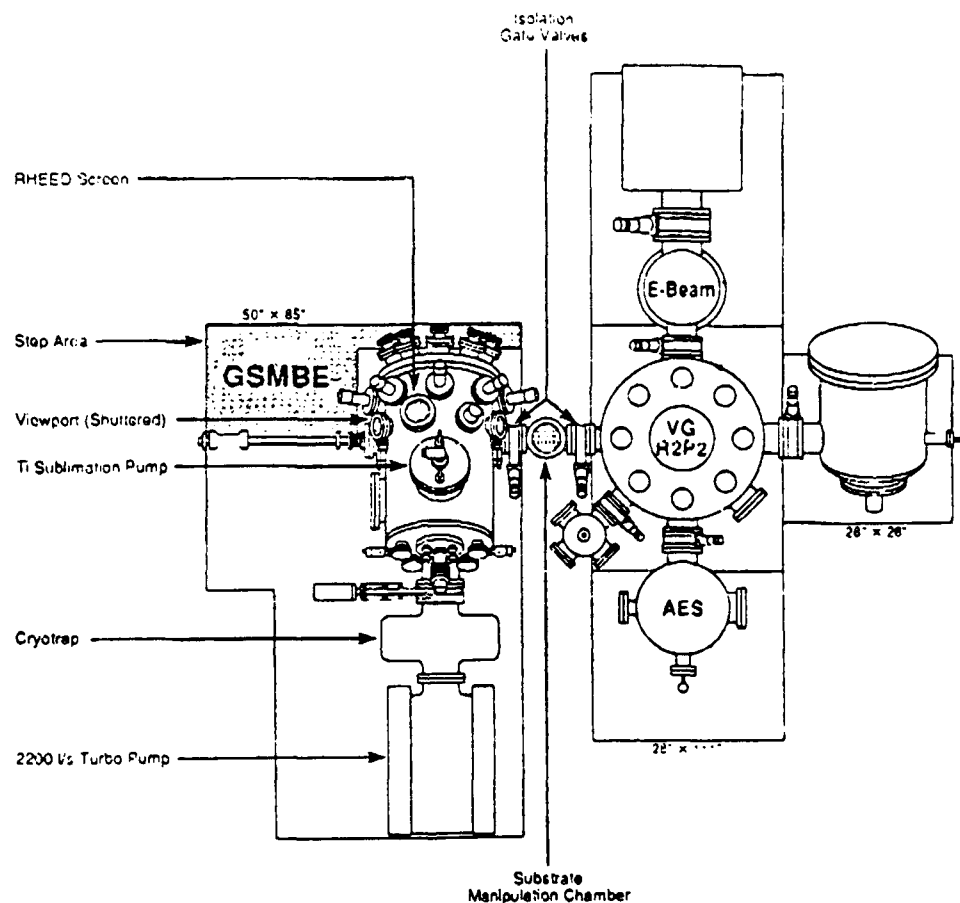


Fig. 2.7 A schematic diagram of the organic/inorganic molecular beam system, including an organic growth chamber, a GSMBE chamber, an analytical chamber for in-situ measurements, a load-lock chamber for sample loading, and a "R2P2" chamber for sample transfer.

Table II.2 Vacuum specifications and functions in each chamber in the organic molecular beam deposition system.

Chambers	OMBD Growth	Analytical	e-beam	R2P2
Functions	organic thin films growth	Electrical and optical characterization	metal contact deposition	sample transfer
Base pressure (Torr)	$6 \times 10^{-11}$	$5 \times 10^{-10}$	$1 \times 10^{-9}$	$1 \times 10^{-9}$
Vacuum pumps	<ul style="list-style-type: none"> <li>• CT-8 cryopump</li> <li>• 270 l/s ion pump</li> <li>• Ti sublimation pump</li> <li>• Cryopanel</li> </ul>	450 l/s ion pump	CT-8 cryopump	CS-8 cryopump
Substrate temperature range (K)	100 K - 900 K	4.2 K - 600 K	300 K - 600 K	room temperature
Hardware	<ul style="list-style-type: none"> <li>• 4 effusion cells</li> <li>• RHEED</li> <li>• RGA</li> <li>• continuous substrate rotation</li> </ul>	<ul style="list-style-type: none"> <li>• probe station</li> <li>• optical ports</li> <li>• ports for installation of XPS and AES</li> </ul>	3-crucible e-beam pocket	extension of 13" into each chamber

The hardware used in the organic growth chamber is listed in Table 2.2. The base vacuum pressure will be  $\cong 10^{-11}$  Torr. One of the unique features of this growth system is that the substrate holder is capable of varying its temperature from about 90 K to 900 K. Sample cooling is achieved by flowing liquid nitrogen through channels inside a copper sample block, whereas heating is achieved using a radiant pyrolytic boron nitride heater. The sample manipulator consists of an ultra-high vacuum, differentially pumped feedthrough resting on an XYZ translation stage. Driven by a stepping motor, the differentially pumped feedthrough provides the necessary continuous sample rotation to achieve uniform growth. The deposition process is monitored using an Inficon IC-6000 thin film process controller in conjunction with Eurotherm temperature controllers which are used to regulate the temperatures of 4 EPI effusion cells. In addition, the growth chamber is equipped with reflection high energy electron diffraction (RHEED) for surface structural analysis during growth. Precision sample rotation provided by the differentially pumped feedthrough is crucial for RHEED alignment.

After growth, samples can be transferred into the e-beam evaporation chamber for contact metal deposition. Finally, in-situ electrical and optical measurements of the final devices can be carried out over a wide temperature range (5 K to 600 K) in the analytical chamber. Since the devices are never exposed to air, such analyses cannot be used for studying the effects of the ambient on the electrical and optical properties of organic thin films.

## II.4 Effects of growth parameters on microstructure

The microstructure of crystalline organic films grown by vacuum deposition is very sensitive to both substrate temperature and deposition rate. In this section, we will discuss how these parameters affect the microstructure and the various properties of the resulting organic thin films.

### (A) Effects of deposition rate

The properties of PTCDA thin films have been found to be very sensitive to deposition rate. Forrest and co-workers<sup>3</sup> have found that thin films of PTCDA deposited at high rates (50-100 Å/s) on substrates held at room temperature show a nearly perfect structural ordering as determined using x-ray diffraction. The most prominent peak at  $2\theta = 27.8^\circ$  in the x-ray diffraction pattern (with Cu K $\alpha$  lines) of PTCDA is the (102) reflection, which corresponds to the interplanar spacing of molecules in the crystal. The overall crystalline ordering in PTCDA can be determined by obtaining the x-ray pole figure for the (102) reflection. This pole figure corresponds to the intensity of the diffraction peak plotted as a function of the sample polar angle relative to the incident x-ray beam. Fig. 2.8(a) shows the x-ray pole figure for the  $2\theta = 27.8^\circ$  line for a film deposited at 50 Å/s. Each contour in the figure corresponds 10% drop in peak intensity. As shown in the figure, PTCDA molecules form stacks oriented at an angle of  $11^\circ$  with respect to the substrate normal, which is a characteristic of single crystalline PTCDA<sup>4</sup>.

Fig. 2.8(b) shows a pole figure for a PTCDA film deposited at 2 Å/s on a substrate at room temperature. In this case, each contour corresponds to only 1% drop in peak intensity. In sharp contrast to Fig. 2.8(a), no preferred orientation is

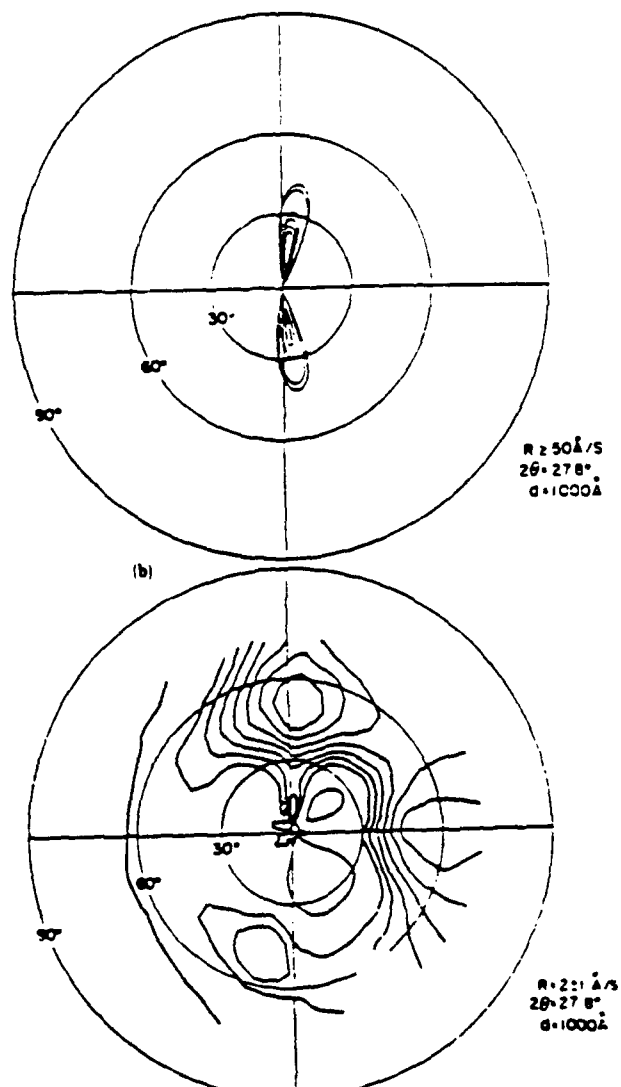


Fig. 2.8 X-ray pole figure of the (102) reflection intensity of PTCDA deposited at (a)  $> 50 \text{ \AA/s}$  and (b)  $2 \text{ \AA/s}$ . Each contour represents a 10% and 2% change in peak intensity for (a) and (b) respectively. These data are taken from Ref. [3]

observed in this sample, indicating molecules deposited under these conditions form randomly oriented stacks.

The effect that the microstructure of PTCDA has on electrical properties is apparent from Fig. 2.9, which has been reprinted from Ref.<sup>3</sup>. For films deposited at 100 Å/s, the carrier mobility along the direction normal to the substrate can be as high as 1.4 cm<sup>2</sup>/V-s, which is one order of magnitude larger than for films deposited at 2 Å/s. These results can be explained in view of the crystalline order of the films: Recall that PTCDA molecules form stacks whose axes lie close to the substrate plane normal. The resulting  $\pi$ -orbital overlap gives rise to high carrier mobility along the stacking direction. For samples deposited at high rates, a high degree of ordering results, which leads to a high carrier mobility along the direction normal to the substrate. However, for samples deposited at low deposition rates, the films are polycrystalline with molecular stacks oriented randomly. In this case, carriers no longer move along the stacking direction, resulting in a decrease in carrier mobility.

#### (B) Effects of substrate temperature

The microstructure of many crystalline organic thin films is also sensitive to substrate temperature during growth. For example, 0.4  $\mu$ m thick PTCDA thin films deposited at room temperature at a rate of 3-5 Å/s consist of a mesh of crystalline filaments approximately 0.2  $\mu$ m long as indicated in the scanning electron micrograph in FIG. 2.10(a). These crystalline filaments are oriented randomly on the surface, and hence the resulting film is polycrystalline. On the other hand, for the same films deposited at 90 K (Fig. 2.10(b)), the surface is smooth, and a uniform single crystalline film is achieved.



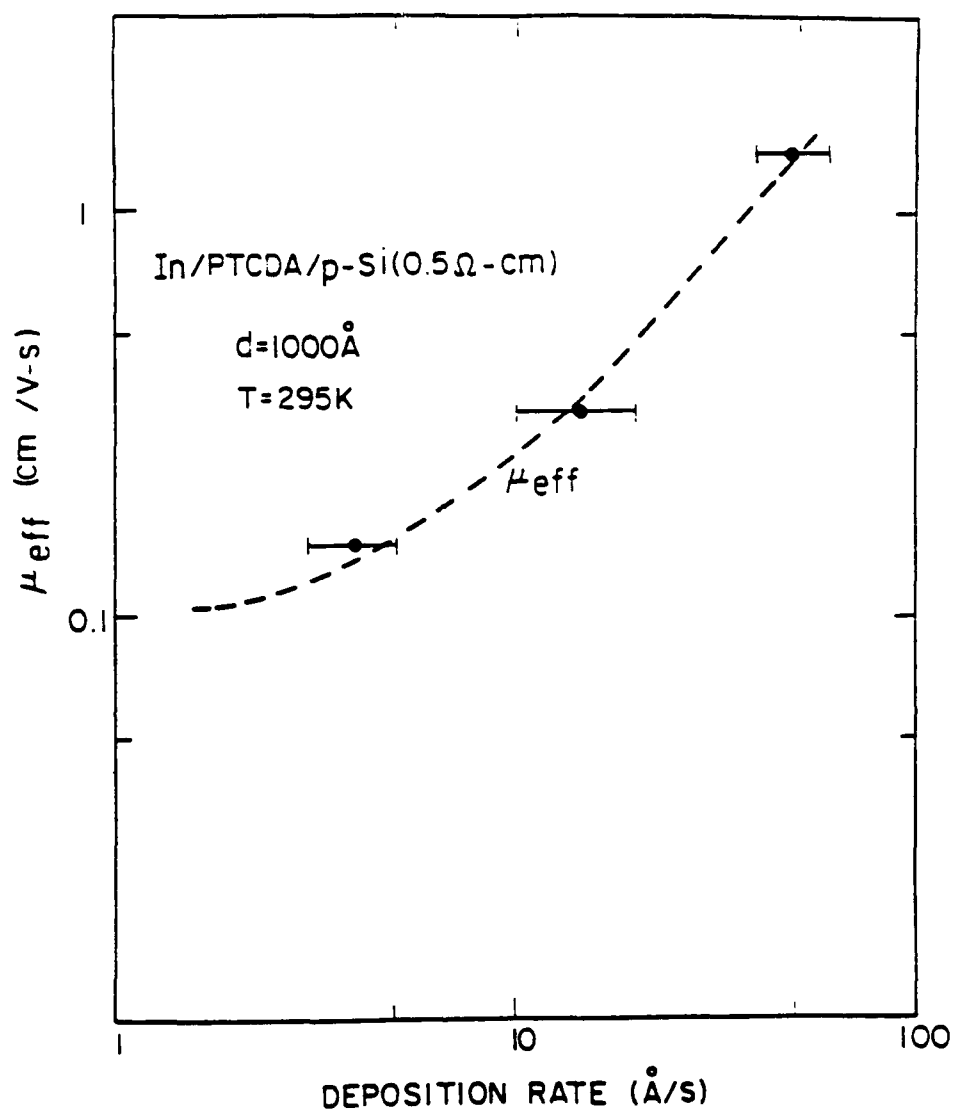


Fig. 2.9 Carrier mobility in PTCDA films as a function of deposition rate. These data are taken from Ref. [3]

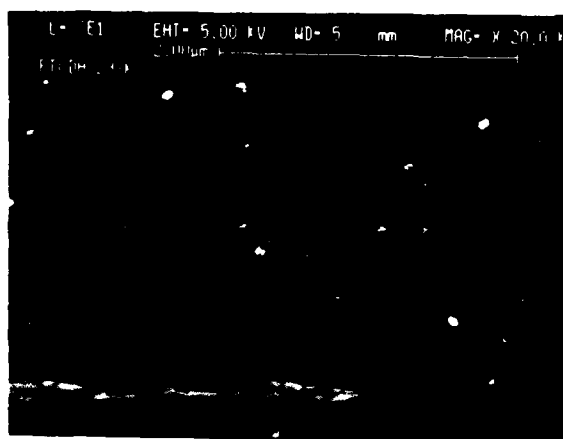
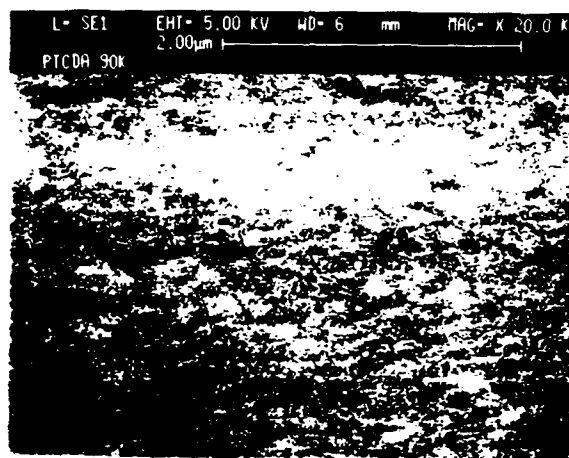


Fig. 2.10 Scanning electron micrographs showing the surface morphologies of PTCDA deposited at substrate temperatures of 440 K (a) and at 90 K (b).

The substrate temperature dependence of the microstructure is also demonstrated from the results of x-ray diffraction. Fig. 2.11 shows the x-ray diffraction patterns for 4000 Å thick PTCDA films deposited on Si wafers at 90 K and 300 K. Figure 2.12 shows the diffraction patterns for PTCDA films deposited under the same conditions on glass substrates. In both figures, the diffraction patterns for the samples deposited at 90 K have been shifted along the y-axis for comparison. The background intensity observed in Figure 2.12 is due to x-ray scattering from the glass substrates. For the samples deposited (on Si and glass) at 300 K, in addition to the most prominent (102) diffraction peak, the (110) peak is also present, indicating the polycrystalline nature of the films. In fact, the (110) peak is observed in all samples deposited at room temperature or above, regardless of the substrate materials used. On the other hand, only one diffraction peak is observed for films deposited on substrates held at 90 K, indicative of the single crystalline nature of the PTCDA films. Note that in both samples with Si and glass substrates, the (102) peak intensity of the samples deposited at low temperature is about 3 times that of the samples deposited at room temperature. The strong diffraction intensity indicates a better structural ordering in the samples deposited at low temperature. For the samples deposited at room temperature, the diffraction intensity is reduced due to structural disorder.

In addition to the improvement in structural ordering, residual strain is developed in organic films deposited at low temperatures, as observed from the diffraction peak broadening in the PTCDA samples deposited at low temperature. The full width at half maximum of the (102) diffraction peak for the samples deposited at low temperature is about twice of that of the samples deposited at

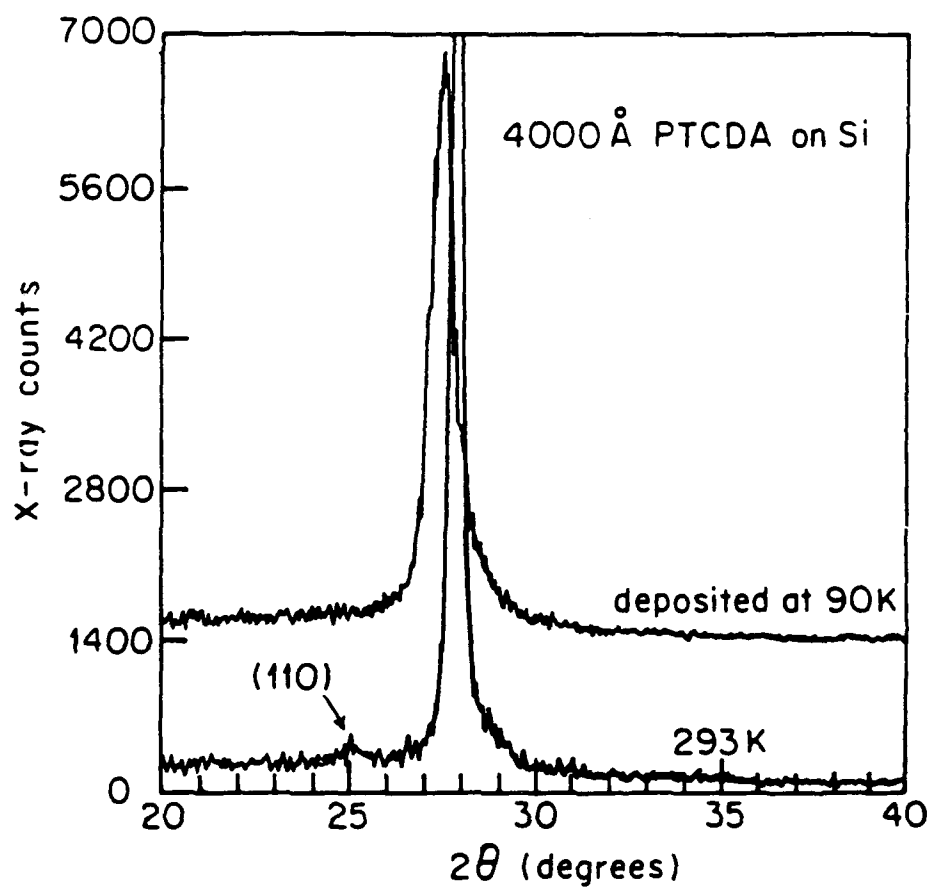


Fig. 2.11 X-ray diffraction patterns for PTCDA films on Si substrates deposited at (a) 90 K and (b) 293 K. The strong diffraction peak is due to (102) reflection.

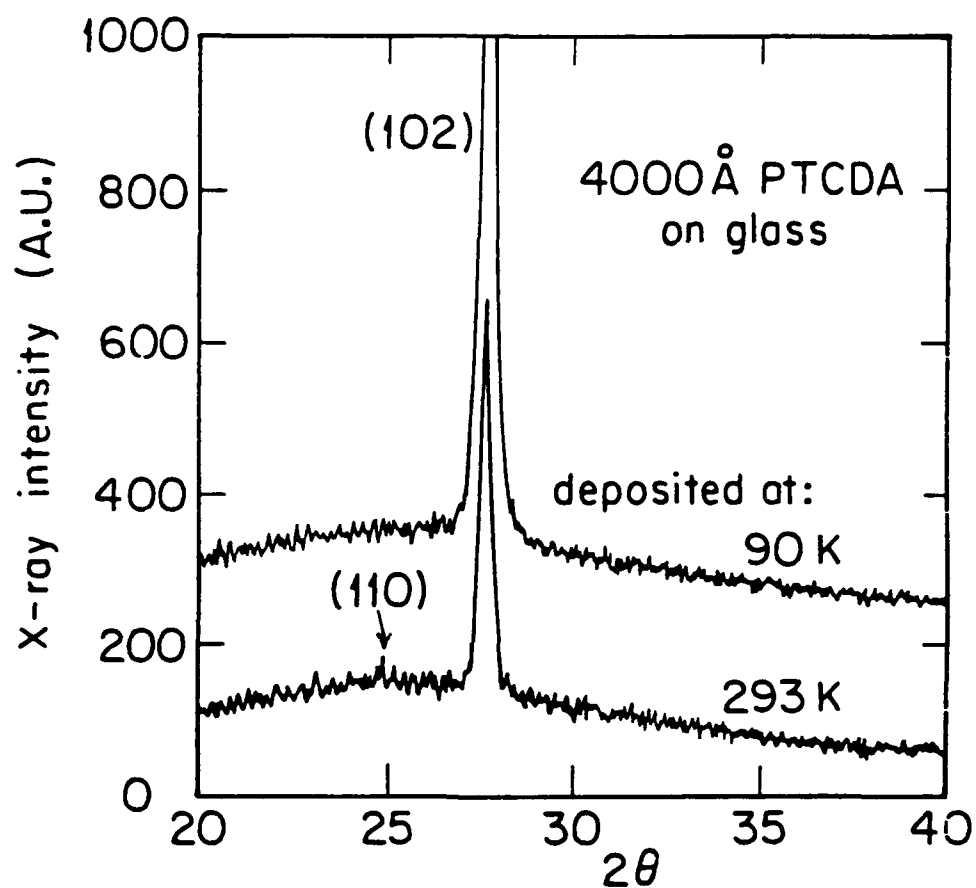


Fig. 2.12 X-ray diffraction patterns for PTCDA films on glass substrates deposited at (a) 90 K and (b) 293 K.

room temperature. Also, there is a slight peak shift in the sample deposited on the Si substrate corresponding to an increase in interplanar spacing of 0.026 Å. Such a shift is not present in the sample deposited on the glass substrate. Both the broadening and shift in the (102) diffraction peak in the samples deposited at low temperature can be explained as follows: Due to the differential thermal expansion in both organic films and substrates, residual stress is developed in the organic films when the sample temperature is brought back to room temperature. Due to the difference in thermal expansion coefficients of Si ( $2.5 \times 10^{-6} \text{ }^{\circ}\text{C}^{-1}$ ) and glass ( $5 \times 10^{-7} \text{ }^{\circ}\text{C}^{-1}$ ), the residual stress in PTCDA films deposited on Si appears to be larger than that in films deposited on glass. This is evident in samples deposited on Si substrates at low temperatures since cracking is sometimes observed in organic films if the sample temperature is increased too rapidly back to room temperature. On the other hand, cracking has not been observed in all samples deposited on glass. As the result of the residual stress in the organic films, inhomogeneous strain causes a slight distortion in the lattice. The fact that the peak shift is not observed in samples deposited on glass substrates also indicates a larger strain in PTCDA films deposited on Si substrates.

Both substrate temperature and deposition rate dependence can be understood in terms of the binding energy of PTCDA molecules in the crystal. Although the size of a PTCDA molecule is large (11 Å x 7 Å), recent calculations<sup>23</sup> on the van der Waals interaction energy between PTCDA molecules indicate that the dimer binding energy is  $\cong 1.35 \text{ eV}$ . Further, the results of the calculations show that there are two local energy minima in the crystal binding energy surfaces. In the PTCDA crystal, the calculated energy

threshold between these energy minima is 20 meV, which is on the order of the room temperature thermal energy of the molecule. Therefore, PTCDA molecules have sufficient thermal energy at room temperature to move on the surface during growth. In fact, the presence of two energy local minima means that given sufficient energy and time (i.e. room temperature thermal energy and low deposition rate), there exists more than one possible orientation of one molecule with respect to another, resulting in irregular stacking, and hence disordered films. As a result, polycrystalline films are often obtained when the substrate temperature is high and the deposition rate is low. On the hand, when films are deposited at low substrate temperatures or high deposition rates, the surface mobility of the molecules is reduced. In this case, the molecules stick in their minimum energy location, thus resulting in perfect stacking.

## II.5 Anisotropies in crystalline organic thin films grown by OMBD

As we have discussed in Section II.1, most crystalline organic semiconductors have large anisotropies due to asymmetries in their crystal structures. Recently, we have measured the dielectric properties of an archetype crystalline organic material --- PTCDA<sup>6</sup>, and found extremely large anisotropies in this material. In this section, we will first calculate the anisotropy of the dielectric properties of PTCDA based on its crystalline structure, and describe the results of the dielectric measurements.

The off-resonance dielectric constant of a material is given by:

$$\epsilon - 1 = \frac{4\pi N q^2 f_j}{m^* (\omega_j^2 - \omega^2)} \quad (2.1)$$

where  $N$  is the number density of the material,  $\omega_j$  is the dipole transition frequency,  $\omega$  is the frequency of the incident electromagnetic radiation,  $q$  is the electronic charge, and  $m^*$  is the electron effective mass. The oscillator strength of the dipole transition from level  $o$  to  $j$  is given by

$$f_j = \frac{2m^* \hbar \omega |x_{oj}|^2}{\hbar^2} \quad (2.2)$$

where  $x_{oj}$  is the electron position expectation value, and  $\hbar$  is the Planck's constant divided by  $2\pi$ . Assuming that the largest contribution to the dipole moment of the molecule is due to  $\pi$ -orbitals, and the electron within a given orbital is completely delocalized, then we can make the approximation that  $f_{j||}/f_{j\perp} \sim |x_{oj||}|^2/|x_{oj\perp}|^2 \sim d^2/L^2$ , where the subscripts  $||$  and  $\perp$  denote the directions along and perpendicular to the molecular stack, respectively. Here,  $d = 3.2 \text{ \AA}$  is the extent of the  $\pi$ -orbital system perpendicular to the molecular plane, and  $L$  is its extent in the plane, which is approximately equal to the length of the perylene molecular core of PTCDA (i.e.,  $L \cong 6.9 \text{ \AA}$ ). Due to the weak interaction between molecules in the directions perpendicular to the molecular stack, this single molecule approximation can be accurately applied to describe the properties of bulk crystals. Hence, provided that there is a perfect crystalline alignment throughout the thin film, we can expect an anisotropy in  $\epsilon$  between directions perpendicular and parallel to the thin film plane (and hence approximately perpendicular and parallel to the molecule stacking axis) to be  $(\epsilon_{||}-1)/(\epsilon_{\perp}-1) \sim d^2/L^2 \sim 0.22$ . This value is only an approximation, since we are assuming that  $m^*$  is isotropic, and



that the dipole moment is due to the delocalized electrons in the extended  $\pi$  system. Nevertheless, it is shown below that this value is close to the measured anisotropy in  $\epsilon$  for highly ordered, quasi-epitaxially grown PTCDA films.

The in-plane dielectric constant of PTCDA films was obtained by measuring the capacitance of interdigitated patterns of metal contacts before and after PTCDA thin film deposition. The details of the measurements of dielectric properties of PTCDA thin films are documented in Appendix A. Following the analysis in the appendix, the in-plane dielectric constant,  $\epsilon_{||}$ , was found to be  $4.5 \pm 0.2$ . The dielectric constant perpendicular to the thin film plane,  $\epsilon_{\perp}$ , was obtained by measuring the capacitance of a parallel plate capacitor consisting of a PTCDA thin film sandwiched between two metal contacts. Using this geometry, it was found that  $\epsilon_{\perp} = 1.9 \pm 0.1$ . From these data we obtain  $(\epsilon_{\perp} - 1)/(\epsilon_{||} - 1) = 0.26$ , which is close to our theoretical estimate of 0.22 for perfectly oriented PTCDA films.

Since  $\epsilon_{\infty} = n^2$ , where  $n$  is the refractive index of the PTCDA film, and  $\epsilon_{\infty}$  is the thin film dielectric constant at optical frequencies, we also expect to observe asymmetries in  $n$  as a result of the ordering in quasi-epitaxially grown PTCDA films. By measuring the coupling angles of PTCDA slab waveguides<sup>16</sup>, the in-plane index  $n_{||}$  was found to be  $2.017 \pm 0.005$ . Determination of  $n_{\perp}$  was done by measuring the reflectivity from the thin film as a function of beam incident angle using several film thicknesses according to the procedures described in Appendix A. The value of  $n_{\perp}$  was found to be  $1.36 \pm 0.01$  at  $\lambda = 1.064 \mu\text{m}$  and  $1.3 \mu\text{m}$ , giving  $\Delta n = n_{||} - n_{\perp} = 0.66$  which is probably the largest value of  $\Delta n$  reported for thin films far from their absorption edge.

It is interesting to compare the asymmetries measured for the dielectric constants and the indices of refraction. Ignoring dispersion between the frequencies at which these parameters were determined, we find that  $\epsilon_{||}/\epsilon_{\perp} = 2.4(n_{||}/n_{\perp})^2 \approx 2$ . This is truly a remarkable agreement given the widely different conditions under which the various measurements were made. Indeed, we see that the low frequency dielectric constant is approximately equal to  $n^2$  for each of the various film directions.

## II.6 Conclusions

In summary, we have discussed the structural properties of crystalline organic semiconductors in terms of the chemical bonding between molecules in the crystal. Due to the unique chemistry of this class of materials, the crystal growth mechanism is different from that for inorganic semiconductors. Crystalline organic thin films have been grown by the process of organic molecular beam deposition, an ultra-high vacuum growth technique similar to convention molecular beam epitaxy for inorganic material growth. Our study on the substrate temperature dependence of growth indicates that disordered films are obtained when deposited at room temperature or above while low substrate temperature growth results in single crystalline-like films. Finally, due to the asymmetries in chemical bond, extremely large anisotropies have been observed for films grown by OMBD.

## References

- <sup>1</sup> M. Pope and C.E. Swenberg, *Electronic Processes in Organic Crystals*, (Oxford University, New York, 1982)
- <sup>2</sup> S.A. Silinsh, *Organic Molecular Crystals*(Springer-Verlag, New York, 1980)
- <sup>3</sup> S.R. Forrest, M.L. Kaplan, and P.H. Schmidt, J. Appl. Phys., **56**, 543(1984)
- <sup>4</sup> A.J. Lovinger, S.R. Forrest, M.L. Kaplan, P.H. Schmidt, and T. Venkatesan, J. Appl. Phys., **55**, 476(1984)
- <sup>5</sup> F.F. So and S.R. Forrest, J. Appl. Phys., **63**, 442(1988)
- <sup>6</sup> D.-Y. Zang, F.F. So, and S.R. Forrest, To be published in Appl. Phys. Lett.
- <sup>7</sup> A. Jayaraman, M.L. Kaplan, and P.H. Schmidt, J. Chem. Phys., **82**, 1682 (1985)
- <sup>8</sup> J. Simon and J.-J. Andre, *Molecular Semiconductors* (Springer, Berlin, 1985)
- <sup>9</sup> R.S. Kirk, Molecular Crystals, **5**, 211(1968)
- <sup>10</sup> S.E. Harrison and J.M. Assour, J. Chem. Phys., **40**, 365(1964)
- <sup>11</sup> N. Karl and K.H. Probst, Mol. Cryst. Liq. Cryst., **11**, 155(1970)
- <sup>12</sup> F. Gutmann and L.E. Lyons, *Organic Semiconductors* (Wiley, New York, (1967)
- <sup>13</sup> Aldrich Chemical Co., Milwaukee, WI 53233
- <sup>14</sup> T. Maki and H. Hashimoto, Bull. Chem. Soc. Jpn. **25**, 411(1952)
- <sup>15</sup> F.F. So, S.R. Forrest, Y.Q. Shi, and W.H. Steier, Appl. Phys. Lett., **56**, 674(1990)
- <sup>16</sup> D.Y. Zang, Y.Q. Shi, F.F. So, S.R. Forrest, and W.H. Steier, Appl. Phys. Lett., Feb., 1991
- <sup>17</sup> M.K. Debe, K.K. Kam, J.C. Liu, and R.J. Poirier, J. Vac. Sci. Technol.

A6, 1907(1988)

<sup>18</sup> K.K. Kam, M.K. Debe, R.J. Liu, and R.J. Poirier, J. Vac. Sci. Technol.

A5, 1914(1987)

<sup>19</sup> A.J. Dann, H. Hoshi and Y. Maruyama, J. Appl. Phys., **67**, 1371(1990)

<sup>20</sup> F.F. So, Y.Q. Shi, S.R. Forrest, and W.H. Steier, Materials Research

Society Conference Proceedings, 1990

<sup>21</sup> F.F. So, L.Y. Leu, and S.R. Forrest, SPIE Conference Proceedings,

1990

<sup>22</sup> S.R. Forrest, L.Y. Leu, F.F. So, and S.R. Forrest, J. Appl. Phys., **66**,

5908(1989)

<sup>23</sup> Y.J. Zhang and S.R. Forrest, Unpublished work.

## Chapter III

### Organic-on-Inorganic Semiconductor Heterojunctions

The study of semiconductor heterojunctions has been a topic of great interest due to their ubiquitous use in numerous optical and electronic devices.<sup>1</sup> Indeed, the advent of optoelectronic devices employing multiple quantum well and heterojunction structures<sup>2,3</sup> has led to entirely new classes of physical phenomena. This has resulted in the development of devices which perform highly complex and novel functions impossible to achieve with homogeneous bulk semiconductor materials.

Recently, investigations of a new class of heterojunctions, i.e., organic-on-inorganic semiconductor heterojunctions (OI-HJs), have attracted some interest<sup>4,5</sup> due to both the unusual nature of these contacts, as well as to the potential new devices to which these heterojunction contacts can be applied. In particular, crystalline molecular semiconductors exhibit rectification characteristics similar to ideal p-n junctions when vacuum-deposited onto inorganic semiconductor substrates.<sup>6</sup> OI-HJ's have been demonstrated using a variety of inorganic semiconductor materials<sup>7</sup> such as Si, Ge, GaAs,<sup>8</sup> InP,<sup>9</sup> InGaAs,<sup>10</sup> GaSb, InSb, and HgCdTe<sup>11</sup>. The electrical characteristics of OI heterojunction diodes with several representative inorganic semiconductor materials are listed in Table 3.1. As shown in the table, the reverse current-voltage characteristics (low reverse dark currents and high breakdown voltages)

Table 3.1 Typical room temperature reverse-biased characteristics of OI heterojunction diodes.

Inorganic substrate material	Substrate doping ( $\text{cm}^{-3}$ )	Organic material	Breakdown voltage ( $V_B$ )	Dark current density at $V_B/2$ ( $\mu\text{A}/\text{cm}^2$ )
p-Si	$1.5 \times 10^{15}$	PTCDA	240	3
n-Si	$5.5 \times 10^{15}$	PTCDA	100	4000
p-Ge	$5 \times 10^{14}$	PTCDA	170	$20 \times 10^3$
p-GaAs	$2 \times 10^{16}$	PTCDA	10	4
n-GaAs	$3 \times 10^{15}$	DIME-PTCDI	30	40
n-InP	$1.5 \times 10^{15}$	PTCDA	120	3000
n-CdTe	$\sim 10^{13}$	PTCDA	>2000	<1
p- $\text{Hg}_{0.7}\text{Cd}_{0.3}\text{Te}$	$5 \times 10^{15}$	CuPc	8	5000
n-InSb	$3 \times 10^{16}$	PTCDA	5	7000

of OI semiconductor contacts are in most cases superior to those of Schottky contacts using the same inorganic semiconductor materials.

The recent demonstration of quasi-epitaxial growth of crystalline organic thin films<sup>12,13</sup> described in Chapter 2 is particularly exciting since it suggests that van der Waals bonds are sufficiently flexible to allow lattice-mismatched materials to form ordered structures without inducing a high density of defects. This is in contrast to inorganic semiconductor heterojunction systems consisting of mismatched combinations of materials, such as InP and InGaAsP. Thus, high quality organic films can be grown on various inorganic substrate materials, and new opportunities for engineering heterostructures consisting of a wide range of materials without regard to the lattice-matching conditions provides exciting possibilities in the field of optoelectronics.

In addition, the large anisotropies in dielectric properties,<sup>14</sup> low loss in the infrared spectral region, large optical non-linearities,<sup>15</sup> and unique electronic properties of many organic semiconductors<sup>16</sup> suggest uses for such organic-inorganic structures in many optoelectronic device applications. These include many recently demonstrated organic-on-inorganic semiconductor devices. For example, OI InP-based field effect transistors have been fabricated<sup>17</sup> with an extrinsic transconductance of 80 mS/mm. No drain current drift has been observed in such devices, in contrast to InP metal-insulator-semiconductor FETs where drain current is very unstable with time.<sup>18</sup> OI photodetectors have also been fabricated and an external quantum efficiency as high as 85 % has been demonstrated. With the proper design of device parameters,<sup>19</sup> OI photodetectors are capable of operating at high bandwidth ( $> 1$  GHz). The characteristics of these

devices will be discussed later in this chapter. Further, very low loss optical waveguides using crystalline organic semiconductors ( $< 2$  dB/cm in channel waveguides) have been demonstrated.<sup>20</sup> This latter finding opens up new opportunities for integrated photonic devices, such as waveguide-coupled detectors and waveguide-coupled phototransistors.

More recently, a new technology to photolithographically pattern and passivate OI heterostructures<sup>21</sup> has been developed in our laboratory. Passivation of OI heterojunction devices was achieved via deposition of  $\text{SiO}_2$  onto organic thin films using a low temperature chemical vapor deposition process.<sup>22</sup> Reliability tests made at elevated temperatures indicate that the passivated OI devices are stable over extended periods of time. Since some crystalline organic semiconductors are stable up to  $350^\circ\text{C}$ , the processing technology of patterning OI devices is compatible with the fabrication processes of most III-V and II-VI compound semiconductor devices. Thus, the development of passivation technology has made a major breakthrough to bring forth OI devices for practical applications.

To fully utilize these OI heterojunction devices, a thorough understanding of their charge transport properties is essential. Therefore in this chapter, we will analyze the charge transport properties of OI-HJs theoretically, and compare the results with experimental data. The organization of this chapter is as follows: We will first review the fabrication and the characteristics of OI devices in Section III.1. The thermionic emission-space charge limited (TE-SCL) current model developed by Forrest et al. will be discussed. In Section III.2, we will present the complete theory on charge transport in OI heterojunctions, including the potential



distribution, the carrier velocities in organic films, and the quasi-Fermi level energy across the OI heterostructure bulk. Both ohmic as well as space-charge-limited conduction regimes of the organic thin film are considered. Measurement of the valence band discontinuity energy at the OI heterointerface between several organic/inorganic semiconductor pairs will also be presented. In Section III.3, the dependence of the electrical characteristics of OI heterojunction devices on organic thin film composition, and the effect of the presence of organic thin films on inorganic semiconductor surfaces will be discussed. In Section III.4, the effect of organic thin film deposition temperature on the electrical characteristics of OI-HJs will be studied, and their characteristics will be explained in terms of the structural properties of the organic thin films. Finally, the fabrication of OI heterojunction photodetectors and their device characteristics are presented in Section III.5.

### III.1 Electrical Characteristics of OI Heterojunctions

#### (A) Device fabrication and characteristics

The fabrication of the first organic-on-inorganic heterojunction diodes was reported in 1982 by Forrest and co-workers.<sup>23</sup> A schematic cross-section of an organic-on-inorganic semiconductor diode is shown in Fig. 3.1. The first step in the fabrication of OI heterojunction diodes is purification of the organic material (see Chapter 2). The semiconductor substrate material must also be prepared by cleaning its surface. For most semiconductor materials, a thorough solvent cleaning is first carried out, followed by an oxide-removing etch, such as

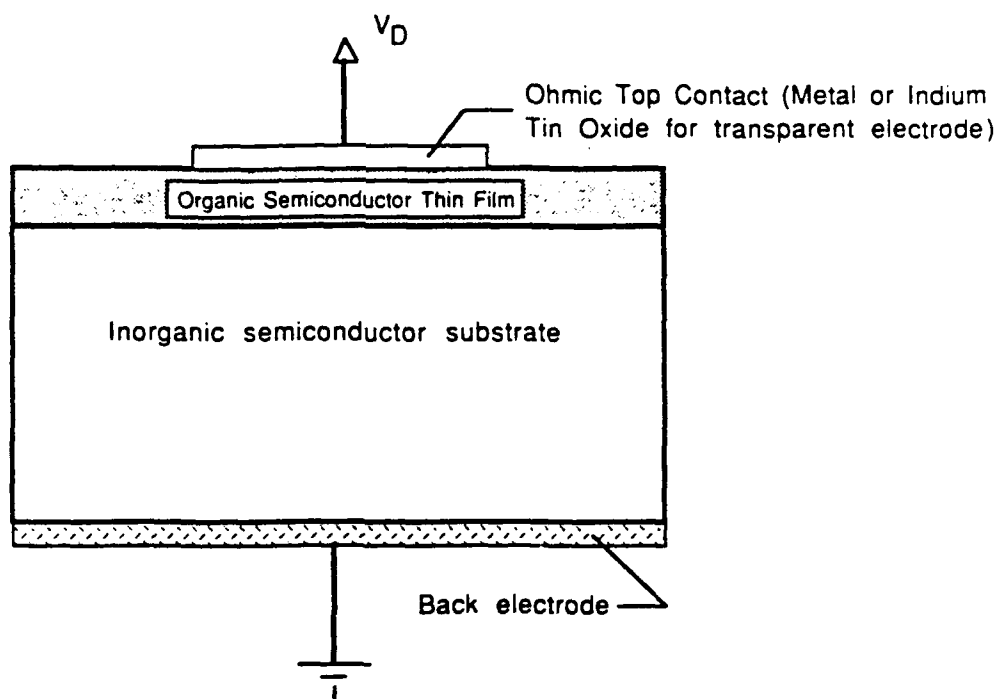


Fig. 3.1 A schematic cross-section of an organic-on-inorganic semiconductor diode.

Table 3.2 Surface-cleaning sequence for selected semiconductors

Semiconductor <sup>a</sup>	1:4 HF:H <sub>2</sub> O (30 s)	HNO <sub>3</sub> (conc) (10 s)	30% H <sub>2</sub> O <sub>2</sub>
Si	X		
GaAs	X		30 s
InP	X	X	
In <sub>0.53</sub> Ga <sub>0.47</sub> As	X		2 min
InSb	X		2 min <sup>b</sup>

<sup>a</sup> Surface treatments all follow a thorough organic solvent cleaning. All acid exposure steps were followed by a 5 minute rinse in deionized water. Samples were inserted in a vacuum for organic film deposition immediately following the last water rinse and blow dry.

<sup>b</sup> Exposure to 10% H<sub>2</sub>O<sub>2</sub> solution for this sample.

exposure of the sample to a dilute HF solution. However, in some materials, particularly InP and related compounds and HgCdTe, it has been found that the contact barrier can be significantly enhanced by exposure of the surface to an oxidant such as  $\text{HNO}_3$  or  $\text{H}_2\text{O}_2$  following the solvent surface-cleaning procedure. A summary of surface preparation conditions used for several semiconductors is given in Table 3.2.

Immediately following surface cleaning, the semiconductor substrate is loaded into a vacuum chamber which is then pumped down to a vacuum level lower than  $10^{-6}$  Torr, and a metal ohmic contact is then deposited onto the bottom substrate surface. Next, a 1000 Å - 2000 Å thick organic film is deposited onto the pre-cleaned top wafer surface at vacuum levels similar to those employed for deposition of the metallic contact. The thickness of the organic film is monitored during deposition with a standard oscillating crystal monitor. After the organic film has been deposited, an ohmic top metal contact pad 3000-4000 Å thick is deposited onto the organic thin film surface through a shadow mask. Table 3.3 shows the ohmic metal contacts used for several crystalline organic compounds. Electrical measurements are made using a standard wafer probe station; soft Au wire probes are used to avoid damage to the devices.

Table 3.3 Ohmic contact metals for several crystalline organic semiconductors

Organic semiconductor	PTCDA	NTCDA	DIME-PTCDI	CuPc	H <sub>2</sub> Pc	PTCBI
Ohmic contact metal	In, Ti	In	In	Au	Au, In	Ag, In

Figs. 3.2 (a) and (c) show typical room temperature current-voltage (I-V) characteristics of In/PTCDA/p-Si/In devices with various substrate resistivities. Here, the PTCDA film thicknesses were 2000 Å, and the substrates had nominal resistivities of 10 Ω-cm [Fig. 3.2 (a)] or 0.5 Ω-cm [Fig. 3.2 (b)]. These figures are reproduced from Ref. 4. In these devices, indium was used for the top (as well as the substrate) electrode since it produced stable and low-resistance contacts when deposited on PTCDA films. The resulting devices formed a rectifying junction similar to an ideal p-n junction with breakdown voltage ( $V_B$ ) as large as 20 V and reverse dark current densities at  $V_B/2$  of  $\leq 10 \mu\text{A}/\text{cm}^2$ . For these devices, high breakdown voltages observed indicate the characteristics of avalanche breakdown in the substrate<sup>24</sup> rather than in the organic film. The forward characteristics indicate an exponential dependence of current on voltage for  $I \leq 100 \mu\text{A}$ , along with a low series resistance. At higher forward currents, the forward characteristics deviate from the exponential dependence.

For comparison to the PTCDA/p-Si devices, we show the room temperature I-V characteristics of Ag/p-Si Schottky barrier diodes [Figs. 3.2 (c) and 3.2 (d)] with identical substrate resistivities as those used in the OI diodes.

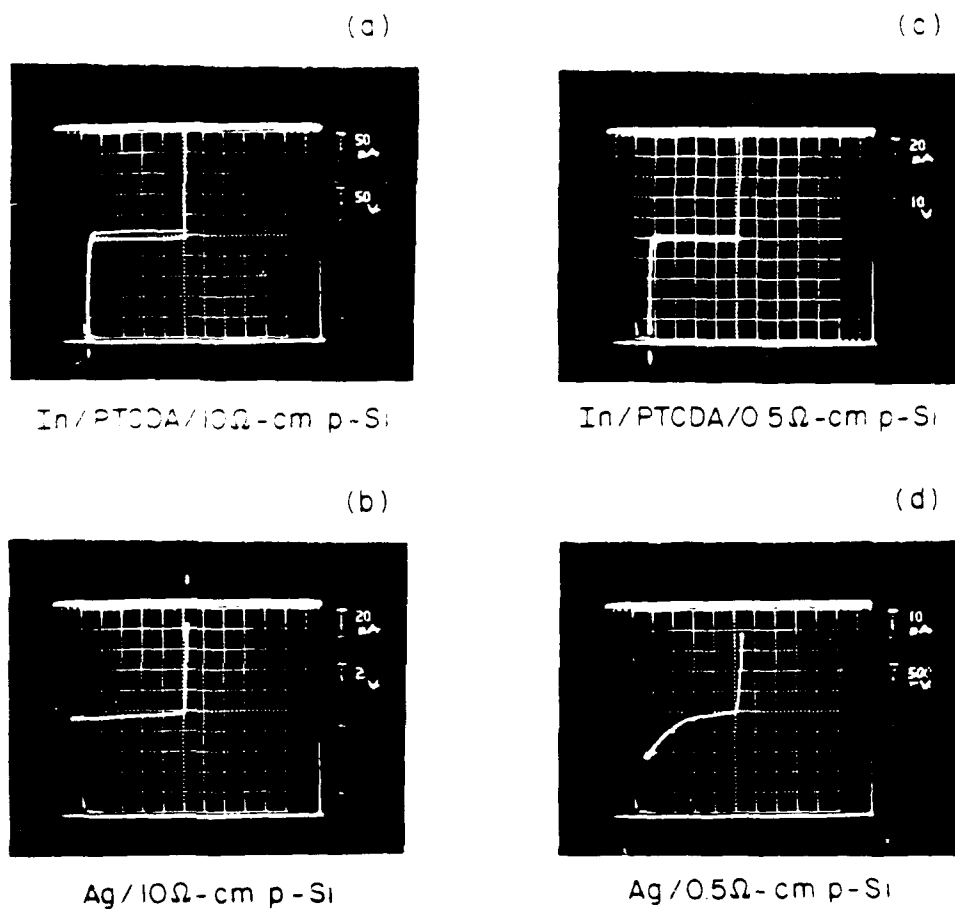


Fig. 3.2 (a) Current-voltage characteristics for In/PTCDA/10 Ω cm p-Si OI diode. (b) Same as (a) for Ag/10 Ω cm p-Si Schottky diode. (c) Same as (a) using 0.5 Ω cm p-Si substrate. (d) Same as (a) for Ag/0.5 Ω cm p-Si Schottky diode.

Here, Ag was used for Schottky barrier formation due to the relatively large barrier energy obtained on p-Si,<sup>24</sup> yet the I-V characteristics of these devices are inferior to the PTCDA/p-Si devices. These Ag/p-Si Schottky diodes have high reverse dark currents and breakdown voltages between 4 and 11 V for the 10  $\Omega$ -cm p-Si substrate, and from 1.5 to 2.5 V for the 0.5  $\Omega$ -cm p-Si substrate. These breakdown voltages are less than one-tenth of those obtained using PTCDA as the contact material, and it is apparent that OI devices are far better than the Schottky diodes when used with the same substrate materials.

(B) Thermionic emission-space-charge limited model

The earliest analyses on the transport properties of organic-on-inorganic heterojunction devices were done by Forrest and co-workers.<sup>4</sup> Their treatment considered the organic thin film as an ohmic conductor in the low injection current regime. Hence, in this regime the charge transport of OI-HJs is similar to a metal-semiconductor Schottky diode, i.e., the current is limited by thermionic emission of charge carriers over the energy barrier at the OI interface. At high injection levels, the current density is limited by space-charge effects in the organic film, and the I-V characteristics are no longer dominated by thermionic emission. From the thermionic emission region of the I-V characteristics, one can obtain a value of barrier height  $\phi_B$  based on Schottky barrier transport theory. Instead of identifying it as the barrier height as in the case of a Schottky diode, they carefully called it the "apparent barrier height". Nevertheless, the thermionic emission-space charge limited current model they developed can satisfactorily

describe the experimental I-V data obtained for OI-HJ devices. In this section, we will summarize their treatment and compare it with experimental results.

The band diagram of an OI-HJ at equilibrium is shown in Fig. 3.3 which has been reprinted from Ref. 25. This diagram shows the contact between PTCDA and an n-type semiconductor with band gap energy  $\epsilon_g$ . The PTCDA "band gap" of 2.2 eV extends from the top of the highest occupied molecular orbital (HOMO) to the lowest unoccupied molecular orbital (LUMO).<sup>25</sup> Crystalline organic materials differ markedly from conventional, inorganic semiconductors such as Si and GaAs in that the organic LUMO and HOMO densities of states (DOS's) are considerably smaller, and the total bandwidth (from the bottom of the HOMO to the top of the LUMO) is on the order of a few tenths of an eV.<sup>26</sup> In PTCDA, the total bandwidth is only 0.9 eV, as inferred from optical absorption data. Also shown in Fig. 3.3 is a thin interfacial layer of thickness  $\delta_{ss}$  and densities of defects states  $D_{ss}$  and  $D_{so}$  in both organic and inorganic semiconductors.

The predominant mechanism for carrier transport across this heterointerface is thermionic emission. The current density is given by:

$$J_T = J_{os} [\exp(qV_D/kT) - 1] \quad (3.1)$$

where  $J_T$  is the total current density,  $q$  is the electronic charge,  $kT$  is the Boltzmann energy at absolute temperature  $T$ ,  $J_{os}$  is the saturation current density, and  $V_D$  is the voltage dropped across the inorganic semiconductor substrate. In the early treatment by Forrest et al.,<sup>4</sup> the OI heterojunction diode was treated like



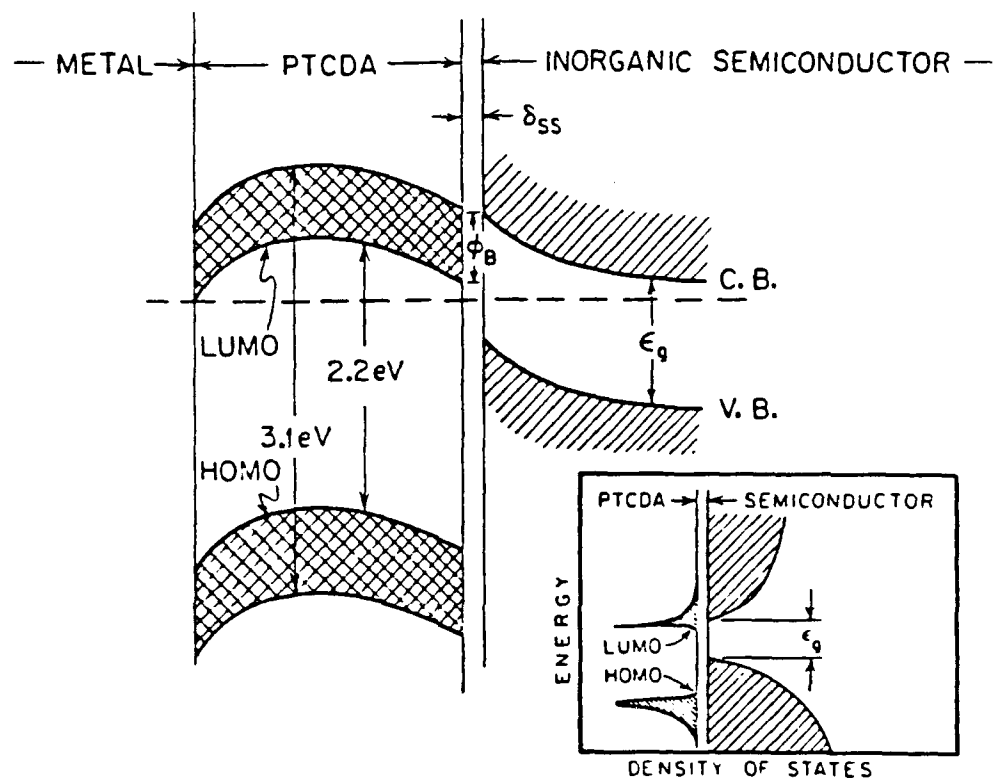


Fig. 3.3 Band diagram of an organic-on-n-type inorganic semiconductor diode. Various notation and features of this diagram are discussed in the text.  
Inset: Proposed densities of states at the OI interface.

a Schottky metal-semiconductor contact. In this case, the saturation current is given by:

$$J_{os} = A^*T^2 \exp[-q\phi_B / kT], \quad (3.2)$$

where  $A^*$  is the Richardson constant of the inorganic semiconductor substrate and  $\phi_B$  is the apparent energy barrier between the organic and inorganic materials. This apparent barrier height is similar to the conduction band discontinuity energy at an inorganic semiconductor heterojunction or the energy barrier at a metal-semiconductor junction<sup>24</sup>; its exact value might be subject to question, depending on the applicability of the Schottky thermionic emission model in OI-HJs.

Eq. (3.1) is constrained by the requirement that the total applied voltage ( $V_a$ ) be given by:

$$V_a = V_o + V_{ss} + V_D \quad (3.3)$$

where  $V_o$  is the voltage across the organic film and  $V_{ss}$  is the voltage across the interface region. Further, we define the ideality factor (or  $n$ -value) via:

$$V_{ss} = (n-1)V_D \quad (3.4)$$

Combining Eq. (3.4) and Eq. (3.1), we obtain

$$J_T = J_{os} [\exp(V_D'/nkT) - 1]. \quad (3.5)$$

where  $V_D'/n = V_D$ . Thus,  $n$  depends explicitly on the ratio of the voltage drop across the interface region to the voltage across the substrate. In the absence of interface charge, and for  $\delta_{ss} = 0$ , we obtain  $V_{ss} = 0$  and  $n = 1$ .

Transport of charge across the organic layer is limited at high current density by space-charge injection from the ohmic metal contact. In this regime, it can be shown that:

$$J_T = \frac{9}{8} \kappa_o \mu_p \frac{V_o^2}{d^3}, \quad (3.6)$$

where  $\kappa_o$  is the permittivity of the organic material,  $d$  is its thickness, and  $\mu_p$  is the hole mobility. Knowing the correct values  $d$  and  $\kappa_o$ , simultaneous solution of Eq. (3.5) and (3.6) can thus be used to calculate the forward and reverse current characteristics of OI diodes, and the carrier mobility in the organic film can be obtained.

### III.2 Theory of Charge Transport in OI Heterojunctions

In the previous section, we have discussed the thermionic emission-space charge limited (TE-SCL) current model developed by Forrest et al. to describe the charge transport in OI heterojunctions. Although this model gives a good approximation to charge transport in OI-HJs under some bias regimes, the accuracy of the "apparent barrier height" at the OI heterojunction obtained based on the thermionic emission model has never been tested. Therefore, it is essential that the energy band discontinuities at the heterointerface be accurately determined in order that the mechanisms of charge transport across the energy barriers is fully understood. Knowledge of the energy band discontinuities is of particular interest since a technique has been proposed whereby the surfaces of inorganic semiconductors; such as InP, GaAs and Si, can be electrically studied

for the existence of surface states via a surface admittance technique called semiconductor organic-on-inorganic surface analysis spectroscopy (SOISAS).<sup>27,28</sup>

Similar to the thermionic emission theory for Schottky barriers, the TE-SCL model assumes the majority-carrier quasi-Fermi level ( $\text{imref}$ ) for OI-HJs is flat across the semiconductor bulk under forward bias. Under reverse bias, the surface  $\text{imref}$  in a Schottky barrier is pinned at a value determined by its barrier height. It is not certain in an OI-HJ how the  $\text{imref}$  position varies under different bias regimes, and therefore it is the purpose of this work to analyze the  $\text{imref}$  position in an OI-HJ diode, which is the basis of the SOISAS technique.

In this Section, we will calculate the potential distribution across all regions of the OI-HJ [Part (A)]. This treatment takes into consideration (i) both ohmic and space-charge limited (SCL) current regimes in the organic thin film, and (ii) the effects of diffusion and drift in the thin-film and substrate. The results obtained are then used to determine the OI-HJ valence band discontinuity energy between PTCDA and various inorganic semiconductors which has not been possible using "apparent" barrier energies as discussed in the previous section. Data from several experimental tests of this theory are presented. In Part (B), we calculate the carrier velocities across the OI-HJ barrier. This is useful in understanding both the temporal response of the OI-HJ, as well as in determining the majority carrier quasi-Fermi level across the diode bulk, as is done in Part (C). In Part (D), we present conclusions concerning the implications of these results.

#### (A) OI-HJ Potential Distribution and the Energy-Band Discontinuities

In the thermionic emission-space charge limited model discussed in the previous section, there are two charge transport regimes. Under low injection levels, the current is limited by thermionic emission over the OI heterobarrier, while under high injection levels, the current is limited by space-charge effects in the organic film. However, in analyzing the charge transport properties of OI-HJs, the current through the organic layer is assumed to be space-charge limited regardless of the injection level [see Eq. (3.6)]. Although such an assumption gives a good approximation to the current transport under the high bias regime, at low bias voltages the organic layer should behave like an ohmic conductor, and the use of Eq. (3.6) is not appropriate. Here, we will analyze the charge transport through the organic layer considering both ohmic and space-charge-limited regimes simultaneously.

Fig. 3.4 shows a band diagram of an isotype OI-HJ diode (assuming a p-type substrate) with a valence band discontinuity energy of  $\Delta E_v$ . The potential distribution and the electric field (E) within the organic film are determined as a function of position (x) using Gauss' Law. Thus, assuming single carrier (hole) injection:

$$\frac{dE}{dx} = \frac{q[p(x) - p_0]}{\kappa_o} \quad (3.7)$$

where  $\kappa_o$  is the permittivity of the organic thin film,  $p_0$  is the free hole concentration, and  $p(x)$  is the total hole concentration consisting of the sum of  $p_0$

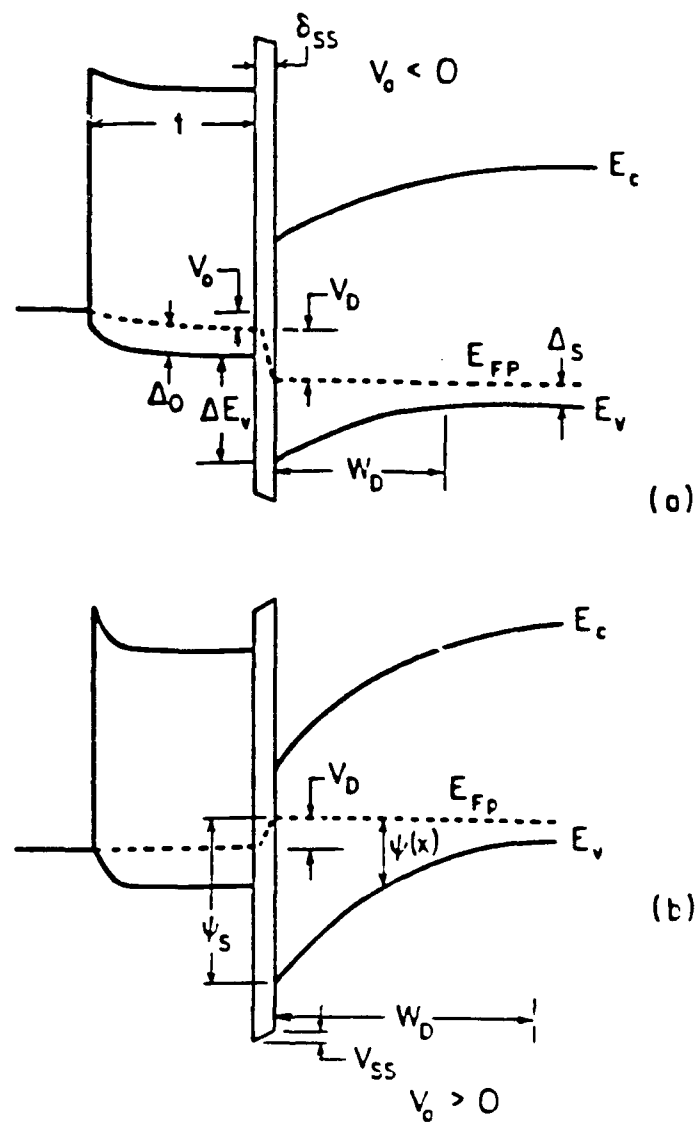


Fig. 3.4 Proposed energy band diagram for an organic-on-inorganic semiconductor heterojunction device under (a) forward and (b) reverse bias.

and holes injected ( $p_{inj}$ ) from the contact at  $x = 0$ . Assuming a constant mobility ( $\mu_p$ ) at small  $E$ , the current density within the film is:

$$J = qp(x)\mu_p E(x) , \quad (3.8)$$

which, via charge conservation, is independent of position (assuming no charge trapping). These equations have the following solution<sup>29</sup> for the voltage dropped ( $V_o$ ) across an organic film of thickness  $t$ :

$$\frac{q^3 p_o^3 \mu_p^2 V_o}{\kappa_o J^2} = u_t^2 - u_t - \ln(1 - u_t) \quad (3.9)$$

where

$$J = \frac{q^2 p_o^2 \mu_p t}{\kappa_o [-u_t - \ln(1 - u_t)]} \quad (3.10)$$

and

$$u_t = p_o/p(t) \quad (3.11)$$

is inversely proportional to the hole density at  $x = t$ . To solve Eqs. (3.9) and (3.10), we first choose a value of  $J$  from which the parameter,  $u_t$ , is determined via Eq. (3.10). This is substituted into Eq. (3.9), from which the voltage across the thin film,  $V_o$ , is calculated. The results of this calculation are shown in Fig. 3.5, where  $J$  is plotted as a function of  $V_o$  for organic thin films with hole mobilities of  $\mu_p = 0.01 \text{ cm}^2/\text{V-s}$  and  $0.1 \text{ cm}^2/\text{V-s}$ , a free hole concentration of  $5 \times 10^{14} \text{ cm}^{-3}$ , and a film thickness of  $1000 \text{ \AA}$ . These values are typical of an OI diode using PTCDA as the organic layer. In the figure, the ohmic transport regime at  $V_o < V_x \equiv 0.02 \text{ V}$  ( $\mu_p = 0.01 \text{ cm}^2/\text{V-s}$ ) is distinguishable from the SCL regime at higher voltages. That is, at  $V_o < V_x$ ,  $J \propto V_o$ , whereas at  $V_o > V_x$ , then  $J$

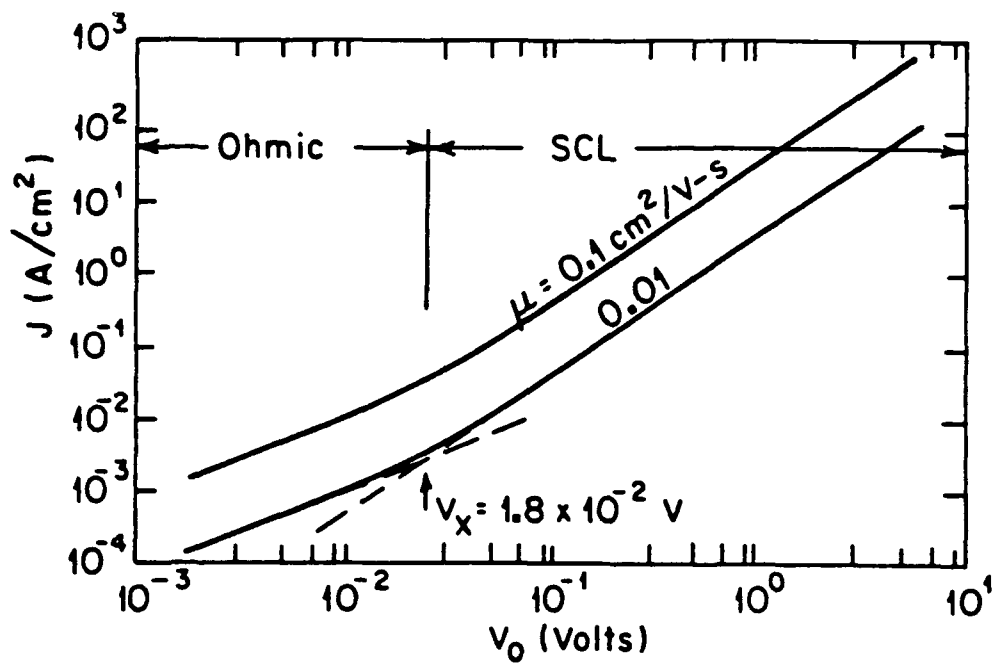


Fig. 3.5 Current ( $J$ ) versus voltage ( $V_0$ ) characteristics of a  $1000 \text{ \AA}$  thick organic film. The two curves correspond to films with mobilities of  $0.1$  and  $0.01 \text{ cm}^2/\text{V s}$ . Regions corresponding to ohmic and space-charged-limited (SCL) transport regimes are shown.



$\propto V_0^2$ . This plot is in good agreement with the J-V characteristics of metal/PTCDA/metal devices reported by Forrest et al.<sup>4</sup> The important aspect of this plot is the low current density ( $J \leq 2 \text{ mA/cm}^2$  for  $\mu_p = 0.01 \text{ cm}^2/\text{V-s}$ ) at which ohmic to SCL transport transition takes place. Thus, at small forward voltages, and even at modest reverse biases for "leaky" OI diodes with small barrier diffusion potentials  $\phi_{Bp}$ , the position of the hole quasi-Fermi level in the organic thin film is determined extrinsically by the amount of charge injected from the contacts ( $p_{inj}$ ), rather than from the equilibrium concentration of carriers ( $p_0$ ).

To calculate the potential distribution  $[\psi(x)]$  throughout the thin film, we replace  $V_0$  by  $\psi(x) \leq V_0 = \psi(t)$  in Eq. (3.9), and solve for  $u(x) < u_t$ . Then  $x$  is found using [cf. Eq. (3.10)]:

$$\frac{q^2 p_0^2 \mu_p x}{\kappa_0 J} = -u(x) - \ln[1 - u(x)] \quad (3.12)$$

A plot of  $\psi(x)$  is shown in Fig. 3.6(a) for the same film parameters as those used in Fig. 3.6, with  $\mu_p = 0.01 \text{ cm}^2/\text{V-s}$ . Note that  $\psi(x)$  is shown for three different voltages,  $V_0$ , corresponding to the ohmic, transition and SCL regimes. In the transition regime,  $V_0 \cong V_x$ . As expected, in the ohmic regime the potential increases nearly linearly with distance from the metal contact at  $x = 0$  to the OI heterointerface at  $x = t$ . However, even in the ohmic regime, there is some non-linearity in  $\psi(x)$  near  $x = 0$  due to charge injection effects. In the SCL regime, the potential increase is nearly quadratic with distance, indicating a substantial amount of injected charge.

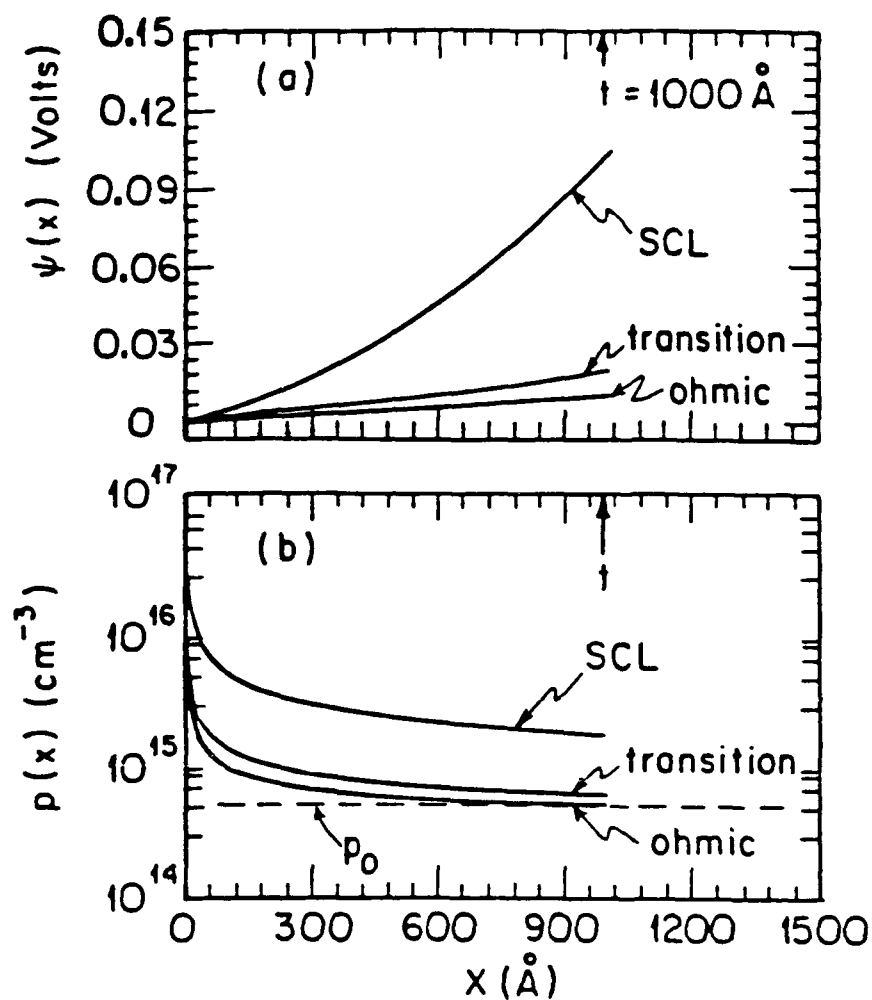


Fig. 3.6 (a) Potential distribution versus position within the organic thin film under three applied voltage regimes. The mobility of the 1000 Å thick film is  $0.01 \text{ cm}^2/\text{V s}$ . (b) The free hole distribution calculated for the film in (a). Here,  $P_0$  corresponds to equilibrium hole concentration.

To determine the charge distribution as a function of  $x$ , the value of  $u(x)$  for a given  $\psi(x)$  and  $J$  is substituted into Eq. (3.11), which is then solved for  $p(x)$ . The results are shown in Fig. 3.6(b) for the same three regimes considered in Fig. 3.6(a). As expected, the charge piles up near the metallic cathode, and decreases with distance toward the OI heterointerface where it reaches a minimum value of  $p(t)$ . In the ohmic regime,  $p(t) \equiv p_0$ . For SCL transport,  $p(t)$ , which is the sum of the injected ( $p_{inj}$ ) and background ( $p_0$ ) carrier concentrations, can be considerably larger than  $p_0$ .

The current at the organic side of the heterojunction (at  $x = t$ ) is given by:

$$J(t) = J = q[p_s(V_D) - p_s(0)]\langle v_c \rangle, \quad (3.13)$$

where  $p_s(V_D)$  is the hole density at the OI interface corresponding to the lowest point in the valence band maximum at the inorganic semiconductor surface (Fig. 3.4). Also,  $V_D$  is the voltage drop across the inorganic substrate. Equation (3.13) suggests that current injected from the substrate into the organic thin film is limited by the rate at which carriers are transported toward the contacts. This limit is determined by the mean carrier velocity,  $\langle v_c \rangle$ , within the organic film, and at low  $V_0$  is approximately given by:

$$\langle v_c \rangle = v_{co} = V_0 \mu_p / t. \quad (3.14)$$

Equation (3.14) is the drift velocity in the ohmic regime where diffusion is neglected (see below), and once again assumes  $\mu_p$  is independent of  $E$ . At higher voltages, it is more appropriate to use the full expression for the mean carrier velocity, viz:

$$\langle v_c \rangle = \frac{1}{l} \int_0^l v_c(x) dx = \frac{1}{l} \int_0^l \mu_p(x) E(x) dx \quad (3.15)$$

We note that the above treatment considers only drift. However, diffusion becomes important at  $V_o \leq kT/q$ . Since  $V_x$  is approximately equal to the thermal, or diffusion potential, this suggests that diffusion is important under some (low voltage) diode operating conditions. When diffusion of holes in the organic layer is significant, the drift velocity is replaced by:

$$\langle v_c \rangle = (D_{po}/\tau_{po})^{1/2} = (\mu_p kT/q\tau_{po})^{1/2} \quad (3.16)$$

where  $D_{po}$  and  $\tau_{po}$  are the diffusion constant and lifetimes of holes within the organic thin film, respectively. From the speed of response measurements of OI photodetectors (will be discussed in detail in Sec. III.5), it has been found that  $\tau_{po} < 10^{-7}$  s in PTCDA, suggesting a minimum carrier velocity due to diffusion through the organic thin film of 500 cm/s for  $\mu_p = 1 \text{ cm}^2/\text{V s}$ .

The current on the inorganic side of the heterojunction is given by:

$$J = qD_{ps} \left( \frac{qpE}{kT} - \frac{dp}{dx} \right), \quad (3.17)$$

where  $D_{ps}$  is the diffusion constant for holes in the inorganic semiconductor substrate, and  $E$  is the electric field. This equation is solved using Eq. (3.13) along with:

$$p(x) = N_{vs} \exp[-q\psi(x)/kT], \quad (3.18)$$

where  $\psi(x)$  is the energy difference between the valence band maximum and the substrate quasi-Fermi level (Fig. 3.4), and  $N_{vs}$  is the effective valence band density of states for the inorganic material.

Combining Eqs. (3.13), (3.17), and (3.18) gives:

$$J = \frac{qN_{vs}\langle v_c \rangle}{1 + \langle v_c \rangle / v_d} \exp(-q\phi_{Bp} / kT) [\exp(-qV_D / kT) - 1] \quad (3.19)$$

Here,  $\phi_{Bp}$  is the diffusion potential due to the OI-HJ barrier, and  $v_d$  is the inorganic semiconductor diffusion velocity given by:

$$v_d = D_{ps} \left[ \int_t^{W_D+t} \exp\left(\frac{q[\phi_{Bp} - \psi(x)]}{kT}\right) dx \right]^{-1}, \quad (3.20)$$

where,  $W_D$  is the depletion region width.

We now express the barrier diffusion potential,  $\phi_{Bp}$  in terms of the valence-band discontinuity  $\Delta E_v$ . For isotype heterojunctions:

$$\Delta E_v = q\phi_{Bp} + \Delta_s - \Delta_o \quad (3.21)$$

where  $\Delta_s$  and  $\Delta_o$  are the energy differences between the equilibrium Fermi levels in the bulk of the semiconductor substrate and organic thin film, respectively. That is, for the inorganic material:

$$\Delta_s = -kT \ln (p_s / N_{vs}) \quad (3.22)$$

where  $p_s$  is the equilibrium hole concentration. Similarly, for the organic material:

$$\Delta_o = -kT \ln (p_o/N_{vo}), \quad (3.23)$$

where  $N_{vo}$  is the effective valence band density of states in the organic materials.

Equation (3.21) implies that, under certain conditions,  $\phi_{Bp}$  is bias dependent. Since the equilibrium carrier concentration,  $p_o$ , in the organic layer is relatively small in many crystalline organic compounds, then under conditions of large injected currents where  $p_{inj} \gg p_o$ , the value of  $\Delta_o$  can change significantly from its equilibrium value. As  $\Delta E_v$  is an intrinsic property of the HJ which is unaffected by the presence of injected charge, we therefore conclude that  $\phi_{Bp}$  must also be bias dependent. In fact, when  $p_{inj} \gg p_o$ ,  $\Delta_o$  must decrease, thereby inducing a corresponding decrease in  $\phi_{Bp}$ . This effect is very pronounced in OI diodes, whereas in Schottky devices it is negligible due to the large free carrier concentration in the metal contact. Thus, Eq. (3.22) is similar to that which is obtained in the case of Schottky barriers,<sup>30</sup> with the exception that for OI devices,  $\phi_{Bp}$  can be voltage dependent under strong, forward biased current injection. Also,  $\langle v_c \rangle$  is used in place of  $v_c$ , i.e., the "collection" velocity of the metal contact. Nevertheless, if  $\phi_{Bp}$  is measured under low injection conditions, the valence band discontinuity energy (or conduction band discontinuity,  $\Delta E_c$ , in the case of n-type substrates) can be inferred using  $p_o$ .

Equation (3.19) is also similar to the results obtained for thermionic emission over the OI barrier, except that the exponential prefactor for TE limited currents used in the Schottky thermionic emission model is simply  $A^*T^2$ , where  $A^*$  is the Richardson constant. If  $J_{SB}$  is the current due to thermionic emission over a Schottky-like OI barrier, and recognizing that in most cases  $\langle v_c \rangle/v_d \ll 1$ , then

$$J/J_{SB} = \langle v_c \rangle (2\pi m^* / kT)^{1/2} \quad (3.24)$$

where  $m^*$  is the effective mass of holes in the inorganic substrate. Taking  $\langle v_c \rangle = 10^3$  cm/s,  $m^* = m_0$  (where  $m_0$  is the electron rest mass), and  $T = 300$  K, we obtain  $J/J_{SB} \cong 3.7 \times 10^{-4}$ . As the forward bias is increased,  $\langle v_c \rangle$  is also increased [Eq. (3.15)]. In this case,  $J/J_{SB}$  approaches 1, implying that the conduction mechanism under strong forward injection approaches that of an ideal Schottky diode. Under such conditions, the organic material becomes degenerate due to the presence of a high density of injected charge, and hence its behavior approximates that of a metal contact. Indeed, the ratio  $J/J_{SB}$  is a qualitative measure of the validity of the use of the Schottky approximation in analyzing OI diode transport. Clearly, this approximation fails at low current injection, where  $\langle v_c \rangle$  becomes small.

Using these current-voltage relationships, we can calculate the potential distribution across the entire OI diode, assuming that there is no significant charge trapping in the device volume. In this case, Eqs. (3.10) and (3.19) are equal, and the applied voltage is given by

$$V_a = nV_D + V_o, \quad (3.25)$$

where  $nV_D = V_D + V_{ss}$  [see Eq. (3.4)]. Note that the  $n$ -value determines the exponential voltage dependence of the current under forward bias.

In Fig. 3.7 we plot the various forward-biased component voltages as a function of  $V_a$ , assuming two values of OI barrier height. Other parameters used in this calculation are similar to those in Fig. 3.6. Also, we take  $n = 1.5$ ,  $T =$

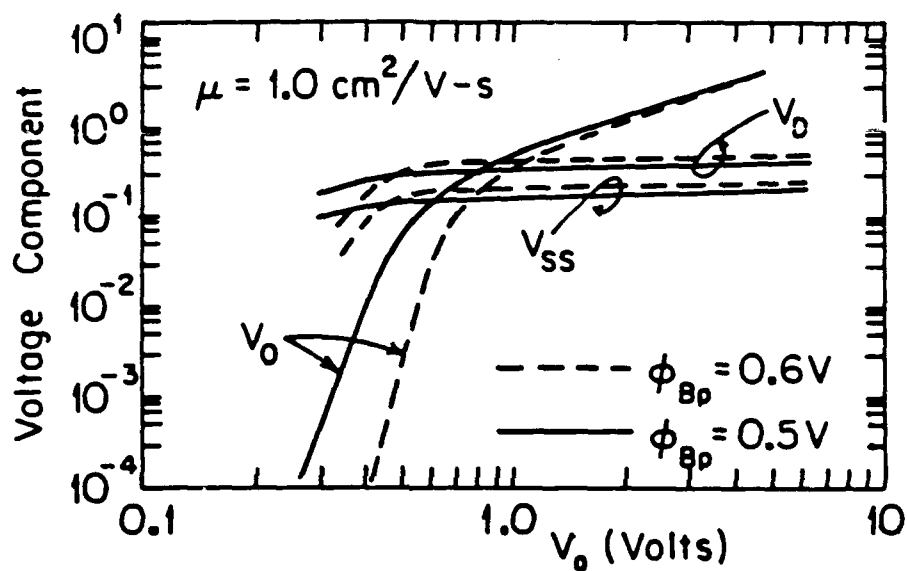


Fig. 3.7 Component voltages vs applied voltage for a forward biased OI-HJ diode, assuming two different barrier potentials of 0.6 and 0.5 V. Here,  $V_D$ ,  $V_{SS}$ , and  $V_o$  correspond to the voltage across the substrate depletion region, interfacial region, and thin film, respectively. A film thickness of 1000 Å is assumed.



300K,  $N_{vs} = 2 \times 10^{19} \text{ cm}^{-3}$  for p-Si, and  $\langle v_c \rangle$  is given by the greater of Eq. (3.15) or (3.16), which is a function of the voltage drop across the organic thin film. As expected, at low forward bias, the voltage is predominantly dropped across the inorganic substrate [see Eq. (3.5)]. At higher voltages, SCL transport through the organic layer dominates, leading to a larger voltage drop across the organic thin film. The shift between ohmic and SCL transport in the film is evidenced by the change in slope in the curves at the value of  $V_a$  where all the voltage components are approximately equal. Below this transition point, we expect the J-V characteristic to depend exponentially on  $V_a \equiv V_D$  as indicated by Eq. (3.19). At higher voltages,  $V_a \equiv V_O$ , and in this case  $J \propto V_a^2$ , typical of SCL transport. Note that the transition from TE to SCL dominated currents occurs at lower values of  $V_a$  as the OI barrier height is decreased. This results since the current through the device is larger at a given voltage as the barrier height is lowered [cf. Eq. (3.19)].

Fig. 3.8 shows the various reverse voltage components for the device with  $\phi_{Bp} = 0.5 \text{ V}$ . Under the reverse bias,  $V_O$  and  $V_{ss}$  are considerably smaller than  $V_D$  due to the small leakage current characteristic of OI-HJ structures, and a large fraction of the applied voltage is dropped across the inorganic substrate. This accounts for the widely observed phenomena that the characteristics of OI diodes under low forward and reverse bias are dominated by the inorganic semiconductors. Also, note that the voltage drop across the interfacial layer ( $V_{ss}$ ) increases linearly with voltage and saturates at the reverse bias where the surface potential ( $\psi_s$ ) is equal to the band gap (see Fig. 3.4).

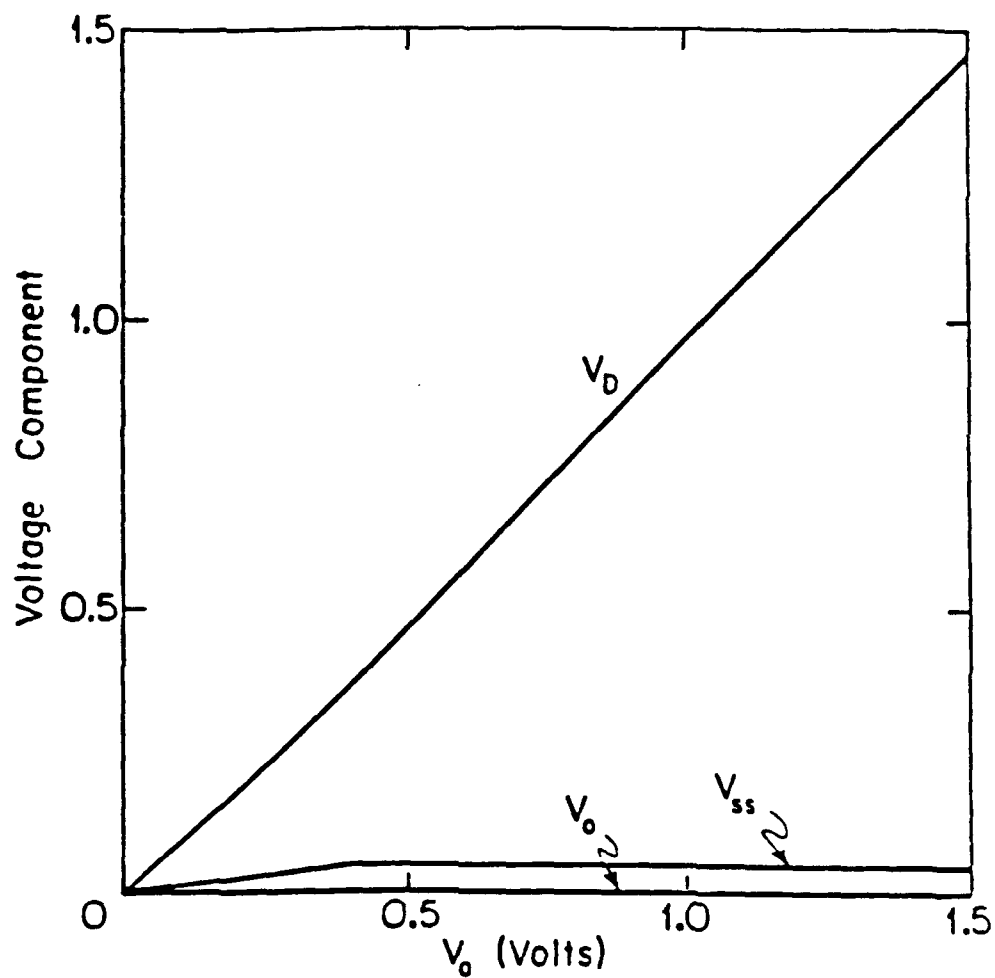


Fig. 3.8 Component voltage vs reverse applied voltage for the device in Fig. 3.7.

The validity of the assumptions leading to the expression for current density [Eq. (3.19)] needs to be tested. This is particularly important since the magnitude of  $J/J_{SB}$  in Eq. (3.24) is significantly less than one, such that large errors in determining the barrier energy from the forward current-voltage characteristics can be incurred. To distinguish between the diffusion and thermionic models, we note that the total saturation current density,  $J_s$ , is given by:

$$J_s = J_0 \exp(-q\phi_{Bp}/kT) \quad (3.26)$$

where  $J_0$  is equal to either the prefactor in Eq. (3.19), or in the case of pure thermionic emission,  $J_0 = A^*T^2$ . Thus, a plot of  $\log(J_s)$  vs.  $1/T$  should be nearly exponential, with small deviations due to the weak temperature dependence of  $J_0$ . The slope of this plot gives the barrier energy, and the intercept with the  $\log(J_s)$  axis yields  $\log(J_0)$ .

In Fig. 3.9(a) is shown the temperature dependence of the forward biased J-V characteristics of an In/PTCDA/p-Si device [cf. Fig. 4, Ref. 6]. From the intercept of these curves with the  $V_a = 0$  axis, we obtain the saturation current as a function of  $T$ , which is replotted in Fig. 3.9(b). The saturation current density is thermally activated, and a least squares fit to the data--as indicated by the solid line--gives  $\phi_{Bp} = 0.56 \pm 0.02$  V, and  $J_0 = 1700$  A/cm<sup>2</sup>. This value for the barrier height is significantly smaller than the "apparent" values obtained using the Schottky thermionic emission model, where  $\phi_{Bp} = 0.75$  V is typical for these diodes. Furthermore,  $J_0 = A^*T^2 = 9 \times 10^6$  A/cm<sup>2</sup> for p-Si Schottky diodes, which is several orders of magnitude larger than the value of  $J_0$  actually obtained. Returning to Eq. (3.19), we see that for  $\langle v_c \rangle / v_d \ll 1$ , then  $J_0 = qN_{vs}\langle v_c \rangle$ . Using  $J_0$

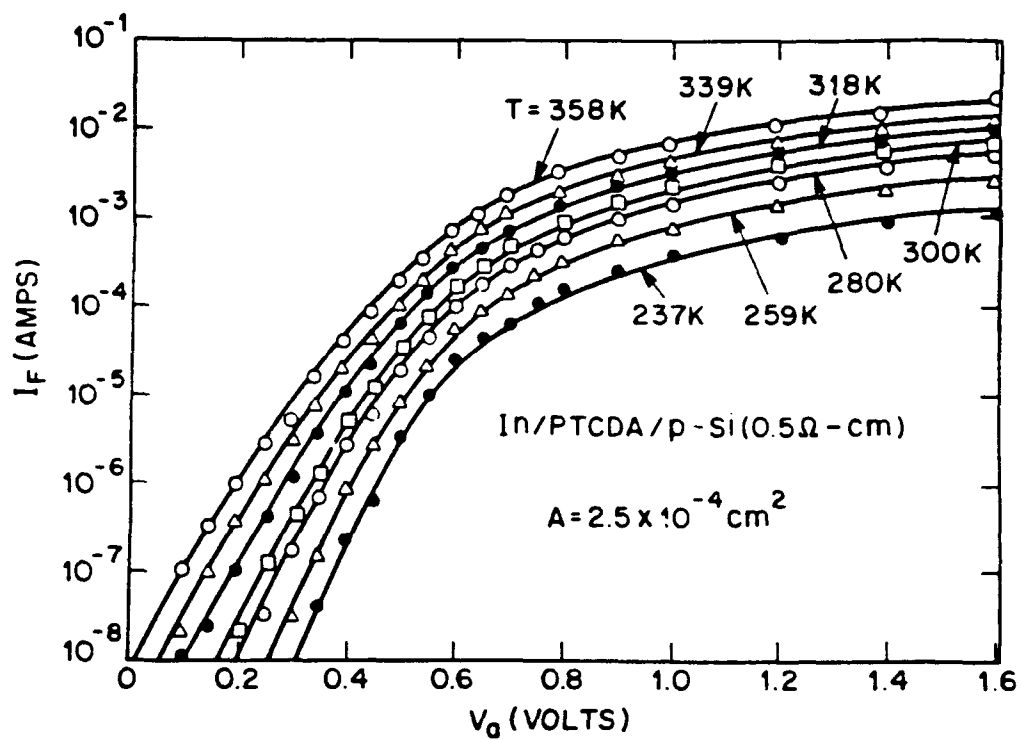


Fig. 3.9 (a) Forward current-voltage characteristics of an In/PTCDA/p-Si diode measured at several different temperatures. The PTCDA thickness is 2000 Å.

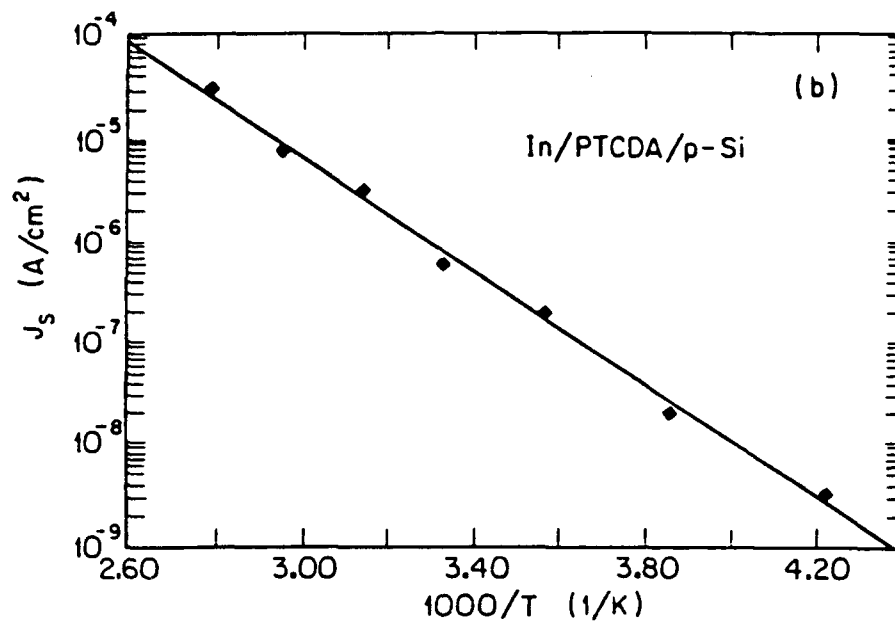


Fig. 3.9 (b) Saturation current density vs  $1/T$  for the diode in (a). The solid line represents a best fit to the data, and give a barrier diffusion potential of  $\phi_{Bp} = 0.56$  V, and an intercept with the  $J_s$  axis of  $J_0 = 1700$  A/cm<sup>2</sup>.

$= 1700 \text{ A/cm}^2$ , and  $N_{VS} = 2 \times 10^{19} \text{ cm}^{-3}$  for p-Si, then  $\langle v_c \rangle = 450 \text{ cm/s}$ . This is in satisfactory agreement with the lower limit value of  $500 \text{ cm/s}$  estimated using carrier lifetime data and the diffusion constant in the organic layer [Eq. (3.16)]. This result is therefore in strong support of the model of current transport across the OI-HJ barrier limited by both diffusion and drift [Eq. (3.19)]. Using  $\phi_{BP} = 0.56 \pm 0.02 \text{ V}$  along with Eq. (3.21), a valence band discontinuity energy for PTCDA/p-Si devices of  $\Delta E_c = (0.48 \pm 0.02) \text{ eV}$  is obtained. To our knowledge, this represents the first such measurement of an energy band discontinuity in crystalline organic/inorganic semiconductor heterojunctions.

The values for  $\phi_{BP}$  obtained through the use of Eq. (3.19) are still subject to errors induced by approximations used in developing the transport model. In particular, although there is no direct evidence of a high density of surface charge (this will be discussed in Sec. III.3), one would expect that such interfacial defects could affect the measurement of  $\Delta E_v$  using J-V analysis, and a direct measurement of  $\Delta E_v$  is necessary. Therefore,  $\Delta E_v$  was also measured via internal photoemission.<sup>31</sup>

In Schottky<sup>32</sup> or isotype heterojunction<sup>33</sup> barriers, free majority carriers can be photoexcited over the barrier by sub-bandgap energy photons. The photocurrent ( $I_{ph}$ ) induced per photon absorbed is given by:<sup>34</sup>

$$I_{ph} \propto (h\nu - \Delta E_v)^2, \quad (3.27)$$

where  $h$  is Planck's constant, and  $\nu$  is the frequency of the incident light. To directly measure  $\Delta E_v$  in OI-HJ devices, the photoemission current spectrum for a PTCDA/p-Si diode was investigated. For this experiment, the diode was fabricated in the same manner as that used in obtaining the data in Fig. 3.9. This

diode was placed perpendicular to a chopped (1 kHz) monochromatic light source incident via the substrate such that light with  $h\nu$  greater than the band-gap of Si was filtered out before reaching the diode active area at the OI interface. To further suppress the signal due to the fundamental absorption in Si, a second Si wafer was placed between the light source and the OI diode. The bandgap<sup>4</sup> of PTCDA is 2.2 eV, such that no direct absorption in the organic material is expected in this experiment.

The photoresponse as a function of light energy and wavelength is shown in Fig. 3.10. In obtaining these data, the OI diode was operated at  $V_a = 0$ . A maximum response is observed in the photoemission spectrum at 0.57 eV. No signal is observed between the energy of this peak and the band edge of Si. The peak height did not change with temperature (varied from 20°C to 100°C) or light chopping frequency (varied from 100 Hz to 2 kHz). Furthermore, the peak was unaffected by strong white light illumination (or bleaching) incident on the thin film surface. Finally, an In/PTCDA/indium-tin-oxide device was also fabricated and illuminated in the same wavelength region as the In/PTCDA/p-Si sample. The former device, however, had no photoresponse peak as that shown in Fig. 3.10, indicating that the peak is not due to a photoemission process in the PTCDA itself. These observations, coupled with the relatively high intensity of the signal, rule out the possibility that the peak is due to a high density of traps in the semiconductor bulks, or at the OI-HJ interface.

We attribute this response to the photoemission of carriers from the highest occupied molecular orbital (or HOMO) in PTCDA to the valence band maximum in p-Si over the interface barrier energy. Note, however, that the

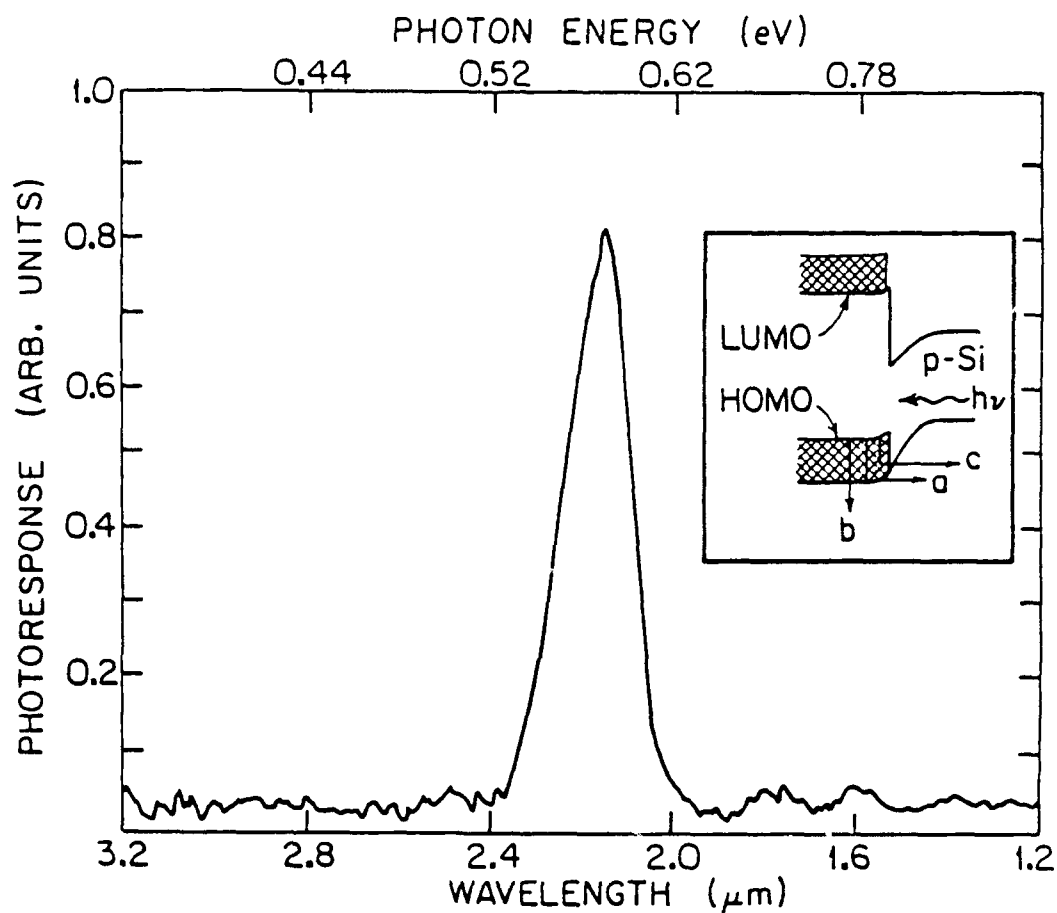


Fig. 3.10 Photoemission spectrum of an In/PTCDA/p-Si heterojunction diode. Inset: Band diagram of the OI-HJ showing the allowed emission processes ("a" and "c") and the forbidden, high-energy process "b". The crosshatched regions refer to width of the organic bands.



signal shown in Fig. 3.10 is considerably different than that predicted for photoemission, where we expect a monotonic increase in  $I_{ph}$  with energy. The dip in the OI-HJ photoemission data at high energy can be understood in terms of the band diagram in the inset of Fig. 3.10 where the widths of the organic energy bands are indicated by the cross-hatched regions. Unlike Schottky diodes or inorganic semiconductor heterojunctions, molecular semiconductors are characterized by relatively narrow energy bands. Optical absorption experiments have shown that the total HOMO plus LUMO (lowest unoccupied molecular orbital) bandwidth is 0.9 eV for PTCDA. If we now assume that the valence bandwidth is on the order of  $\Delta E_v$ , then the peak absorption occurs at photon energies comparable to this barrier height (process "a" and "c" in the inset of Fig. 3.10). As the photon energy increases, however, the transitions are forbidden in the organic material as a result of the narrow bandwidth (process "b"), and hence a decrease in  $I_{ph}$  with increasing  $h\nu$  is observed. Finally, for  $h\nu < \Delta E_v$ , the photon has insufficient energy for photoemission to occur.

From these arguments, the photocurrent on the long-wavelength side of the peak should follow Eq. (3.27). Thus, in Fig. 3.11 we plot  $(I_{ph})^{1/2}$  versus photon energy ( $h\nu$ ), and find that the dependence is linear along nearly the entire long-wavelength edge. The intercept of these data with the energy axis gives  $\Delta E_v = (0.50 \pm 0.01)$  eV--a value consistent with that obtained from the J-V analysis.

Accurate determination of the barrier height as provided above has important implications as to the interpretation of the mechanisms affecting the formation of OI-HJ contact barriers. For example, as discussed in the beginning

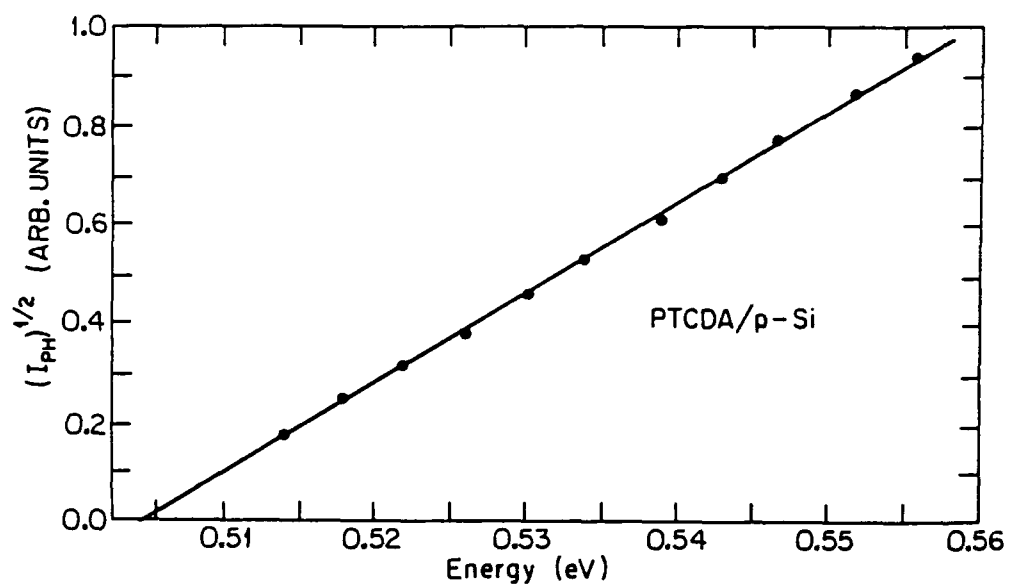


Fig. 3.11 The square root of the photocurrent on the long wavelength branch of the response peak in Fig. 3.10 plotted vs photon energy. The intercept of the straight line fit to the data with the  $(I_{ph})^{1/2} = 0$  axis give  $\Delta E_v = (0.50 \pm 0.01)$  eV.

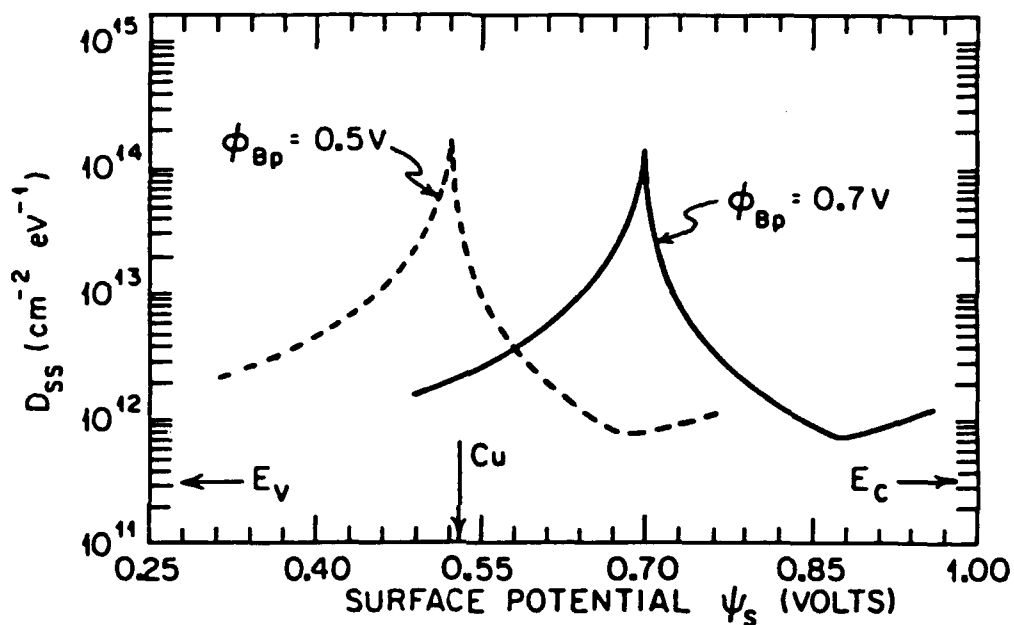


Fig. 3.12 Density of surface states ( $D_{ss}$ ) vs potential at the Si surface for a CuPc/p-Si heterojunction. The solid line refers to data using a barrier height of 0.7 V. The dashed line is for this same data except that  $\phi_{Bp} = 0.5$  V estimated using the OI-HJ current model. The arrow labeled "Cu" corresponds to the position of the Cu acceptor defect level in bulk Si. Also,  $E_c$  and  $E_v$  refer to the conduction and valence band extrema in Si respectively.

of this section, measurements of the density of interface states using the SOISAS technique are affected by the value of the OI-HJ barrier energy. In Fig. 3.12 is shown the density of states in equilibrium with a p-Si substrate ( $D_{ss}$ ) as a function of energy in the Si bandgap for a Cu-phthalocyanine/p-Si OI-HJ. The solid line corresponds to the data assuming an apparent barrier height of 0.70 V as determined from thermionic emission theory, and the dashed line is this same data replotted assuming a barrier height of 0.50 V, which would be obtained from Eq. (3.6), assuming the hole velocity in Cu-phthalocyanine (CuPc) is approximately the same as that in PTCDA.<sup>35</sup> Thus, the position of the trap density curve is linearly related to the barrier energy.

We note that the large peak value for  $D_{ss}$  CuPc/p-Si OI-HJs has been attributed<sup>36</sup> to reactions between these two materials at the heterointerface, resulting in free Cu at the Si surface. The reaction between CuPc and p-Si substrates at the OI heterointerface will be discussed in detail in Sec. III.3. The corrected data appear to support this model, since the peak in  $D_{ss}$  nearly coincides with the Cu acceptor defect energy of 0.52 eV above the valence band maximum in Si.<sup>37</sup> The position of this Cu defect is indicated by the vertical line in Fig. 3.12. Hence, knowledge of the actual, rather than the apparent values for  $\phi_B$  is central to our understanding of the OI-HJ barrier.

For purposes of comparison, OI-HJ energy barrier heights measured assuming both thermionic emission and diffusion-limited transport models are given in Table 3.3. These data are for PTCDA-based OI-HJ diodes only, and are taken from Ref. 4. Also included in the table are values of  $\Delta E_v$  for selected OI-HJs as inferred from the diffusion model values of  $\phi_{Bp}$  using Eq. (3.21).

Table 3.4 Barrier energies for selected PTCDA-on-inorganic semiconductor diodes using thermionic and diffusion models.

Inorganic substrate	Majority-carrier type	$J/J_{th}$	$q\phi_{Bp}$ (TE)	$q\phi_{Bp}$ (diffusion)	$\Delta E_v^b$ (eV)
Si	n	$2.0 \times 10^{-4}$	$0.61 \pm 0.01$	$0.39 \pm 0.01$	.....
	p	$1.4 \times 10^{-4}$	$0.75 \pm 0.02$	$0.56 \pm 0.02$	$0.50 \pm 0.02$
Ge	p	$6.6 \times 10^{-5}$	$0.55 \pm 0.03$	$0.30 \pm 0.03$	$0.25 \pm 0.04$
GaSb	p	$1.2 \times 10^{-4}$	0.60	0.37	$0.29 \pm 0.04$
	n	$3.9 \times 10^{-5}$	ohmic	ohmic	.....
GaAs	n	$5.2 \times 10^{-5}$	0.64	0.39	.....
	p	$1.4 \times 10^{-4}$	0.75	0.52	$0.43 \pm 0.05$
InP	n	$5.5 \times 10^{-5}$	0.55	0.30	.....

<sup>a</sup> Values at  $T = 300$  K, with  $\langle v_c \rangle = 500$  cm/s.

<sup>b</sup>  $\Delta E_v$  for p-type substrates only. For these calculations  $m^* = m_0$  for PTCDA.

The value for p-Si is measured; whereas for other materials,  $\Delta E_v$  is calculated using  $\phi_{Bp}$  obtained from Ref. 4 and reproduced here. Doping of p-Si and p-GaSb:  $5 \times 10^{14}$  cm<sup>-3</sup>; p-Ge:  $5 \times 10^{14}$  cm<sup>-3</sup>; and p-GaAs:  $2 \times 10^{16}$  cm<sup>-3</sup>.

### (B) Carrier Velocities

The carrier velocity  $\langle v_c \rangle$  in the thin film is determined using Eqs. (3.15) and (3.16). The results for forward-biased devices are given in Fig. 3.13. Here, the velocity is plotted for several values of thin film hole mobility ranging from 0.01 to 1 cm<sup>2</sup>/V-s, and for two values of  $\phi_{BP}$  as indicated in the figure. It is apparent that the carrier velocity strongly depends on voltage,  $V_D$ , with increasing exponentially when  $V_D \geq 0.3$  V. Velocities as high as 10<sup>5</sup> cm/s are expected for thin films with high mobilities, and for diodes with barrier heights of 0.50 V. The dependence of these curves on  $V_D$  is a result of the increase of  $V_o$  with voltage,  $V_o$ , when  $V_o > kT/q$ . At low voltage, the electric field in the thin film is small, such that diffusion dominates. In this case,  $\langle v_c \rangle$  is given by Eq. (3.16), where  $\tau_s = 1.0$   $\mu$ s was assumed in these calculations. As  $V_D$  increases beyond 0.3 V, the voltage drop across the organic thin film increases due to the transition into to the SCL current regime. The velocity at a given voltage decreases as the barrier height increases due to the reduced forward current, hence resulting in a lower voltage drop across the organic thin film.

The above treatment assumes a constant hole mobility in the organic crystal, independent of the magnitude of the applied electric field. The relatively high mobility of holes arises from the large overlap of electronic wavefunctions in the  $\pi$ -orbitals of adjacent molecules in a crystalline stack. At very high electric fields, it is expected<sup>38,39</sup> that the mobility will decrease and the carrier velocity will saturate due to generation of phonons. Such processes depend on temperature, crystallinity, and film purity, and need to be taken into consideration, especially under large forward bias.

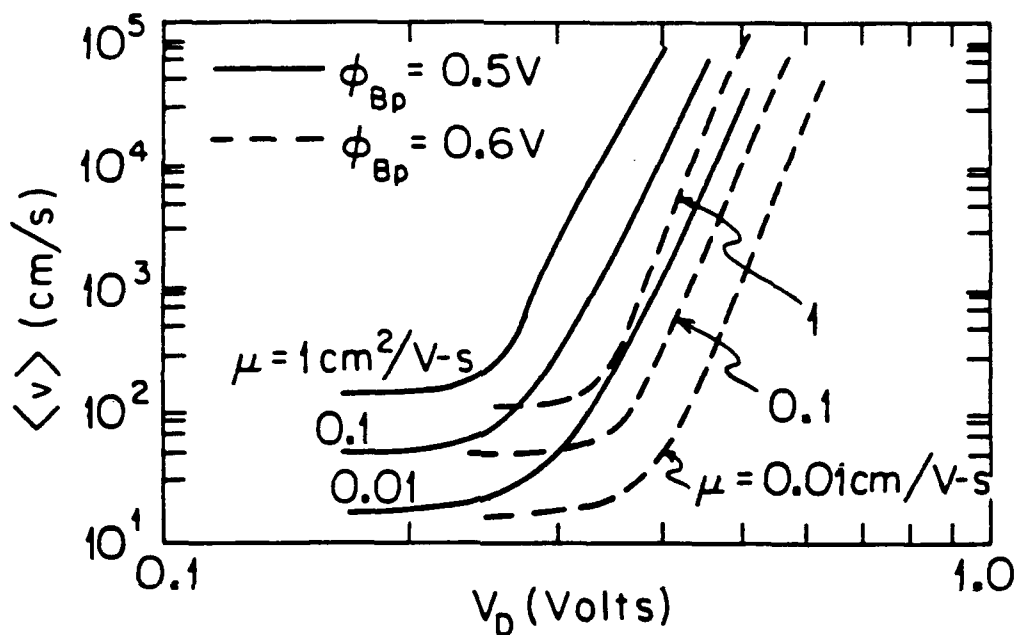


Fig. 3.13 Mean carrier velocity ( $\langle v_c \rangle$ ) vs voltage across the substrate for OI-HJ diodes using organic thin films with different mobilities, and assuming barrier heights of 0.5 and 0.6 V. For these curves, a film thickness of 1000 Å and a hole lifetime of 1 μs are assumed.

Under reverse bias, the electric field in the thin film is small, such that the drift velocity is much smaller than the diffusion velocity [Eq. (3.16)] for all but the smallest values of  $\phi_{BP}$ . Hence, under reverse bias,  $\langle v_c \rangle$  varies from 100 cm/s to approximately 2000 cm/s, depending on the mobility and lifetime of holes in the organic layer. For these conditions the film will respond to even low frequency signals as if it were a leaky dielectric in a metal-insulator-semiconductor (MIS) capacitor. However, due to the high conductivity of the thin film compared with that of glassy insulators such as  $\text{SiO}_2$ , it is not possible to strongly invert the surface of the OI diode. As greater reverse voltages are applied such that the Fermi level at the OI interface is brought to well above the center of the inorganic semiconductor band gap, the minority carriers (electrons) arriving from the semiconductor bulk are either swept across the organic film and collected at the metal contact, or else they recombine with injected holes arriving at the OI interface from the metal contact. In either case, this leakage current density is determined by the rate at which minority carriers are generated within the inorganic semiconductor.

Turning now to the carrier velocity in the inorganic substrate, Eq. (3.20) must be solved to obtain the diffusion velocity,  $v_d$ . Assuming that the doping density in the substrate ( $N_A$ ) is uniform, the potential  $\psi(x)$  (see Fig. 3.4) is parabolic. Thus:

$$\psi(x) = qN_A (W_D - x + t)^2 / 2\kappa_s + \Delta_s / q \quad (3.28)$$

where  $\kappa_s$  is the semiconductor permittivity. Substituting this into Eq. (3.20) gives:<sup>30</sup>



$$v_d \equiv D_{ps} / 2L_D = \mu_{ps} kT / 2qL_D \quad (3.29)$$

where  $600 \text{ cm}^2/\text{V-s}$  is the hole mobility in the (Si) inorganic material, and  $L_D \sim 1000 \text{ \AA}$  is the Debye screening length.<sup>24</sup> From this expression, we obtain  $v_d \sim 10^6 \text{ cm/s}$  at room temperature.

One additional characteristic velocity of the OI diode is the hole drift velocity in inorganic semiconductor, which limits the rate at which holes can transit the depletion region under reverse bias. For most cases, this approaches the saturation velocity of holes in p-type semiconductors, which is typically  $(5 - 10) \times 10^6 \text{ cm/s}$ .

Thus we find that under nearly all bias regimes, the OI diode satisfies the condition that  $\langle v_c \rangle / v_d \ll 1$ . Furthermore, due to the large range over which  $\langle v_c \rangle$  can vary for a small change in bias near  $V_D = 0$ , we have the circumstance that the OI diode changes its behavior from "Schottky-like" under large forward bias, to a "MIS-like" regime under small forward and reverse voltages. Under large reverse voltage, the device enters a "heterojunction-like" regime whereby minority carrier generation in the semiconductor substrate is balanced by recombination at the OI interface, thereby preventing charge inversion. The "heterojunction" regime also allows for Zener, or avalanche breakdown to occur at the largest applied reverse voltages.<sup>4</sup>

The characteristics of these various modes of OI-HJ operation are summarized in Table 3.5. In the table,  $p_s$  refers to the density of holes at the OI interface, which is calculated in Part C. The last column labelled "Organic Conductivity"

gives a qualitative description of the current-transporting nature of the organic thin film in each of the various bias regimes. More discussion of this unusual character of the OI-HJ is presented in Part (D).

Table 3.5 Operating regimes for organic-on-inorganic semiconductor heterojunctions.

Regime	Voltage range <sup>a</sup>	Current density	$\langle v_c \rangle$ (cm/s)	$p_s$	Organic conductivity
Schottky	$-V_a \gg \phi_B$	$J \gg J_s$	$10^4$ - $10^6$	$\gg p_0$	SCL
MIS	$ V_a  \leq E_g$	$J \leq J_s$	$\sim 100$ - $10^4$	$\leq p_0$	leaky insulator
HJ	$V_B < V_a \leq \phi_B$	$J \sim J_s$	$100$ - $10^3$	$\ll p_0$	ohmic

<sup>a</sup> Positive voltage refers to reverse bias for p-type substrates.

(C) Quasi-Fermi Levels

To calculate the position of the quasi-Fermi level (or imref) within the organic thin film, we employ:

$$E_{Fp}(x) - E_{v0} = kT \log [N_{v0}/p(x)], \quad (3.30)$$

where  $N_{v0}$  is the valence band effective density of states [c.f., Eq. (3.23)], and  $E_{v0}$  is the energy of the valence band maximum (or HOMO) in the organic film. In Fig. 3.14,  $E_{Fp}(x) - E_{v0}$  is plotted as a function of  $x$ , where  $p(x)$  is obtained with the aid of Eqs. (3.9)-(3.11). This function dips toward the valence band maximum at the metal anode [i.e.,  $E_{Fp}(0) \rightarrow E_{v0}$ ], increasing to a nearly constant value as the OI interface is approached. By examining the position of the imref at  $x = t$ , we see that while  $V_0$  increases from 5 mV in the ohmic regime to 100 mV in the SCL regime (Fig. 3.6),  $E_{Fp}(t) - E_{v0}$  changes by only 30 meV. That is, the relationship between the imref position at the OI interface, and the voltage applied to the thin film ( $V_0$ ), is sublinear. Furthermore, under reverse bias, the conduction mechanism within the thin film is nearly always ohmic in nature, suggesting that  $V_0$  is generally less than 10 mV for all bias levels of interest. It can therefore be concluded that under reverse, or even moderately large ( $\leq 0.7V$ ) forward biases, the imref position at the organic side of the OI-HJ is only a weak function of voltage dropped across the layer. This is consistent with assertions<sup>27</sup> that the occupancy of traps in equilibrium with the thin film does not change significantly with bias, and hence their contribution to total diode admittance is generally small.

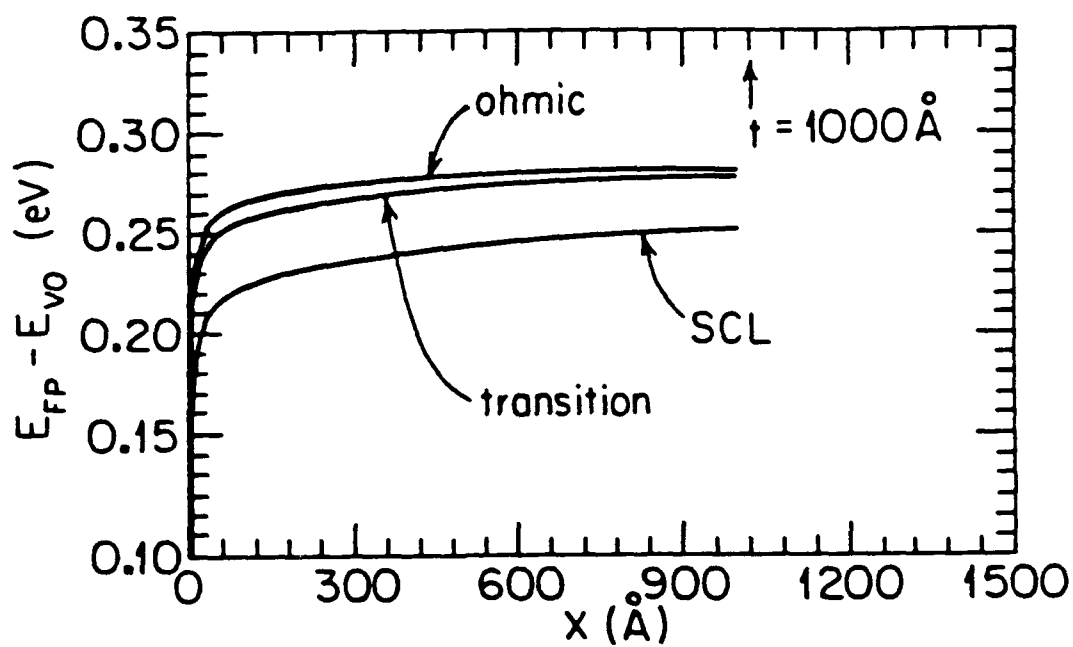


Fig. 3.14 Quasi-Fermi energy ( $E_{FP}$ ) vs position within the organic film for several bias regimes. Parameters used in this calculation are the same as those in Fig. 3.7.

To calculate the imref in the inorganic substrate, we assume that the doping is uniform, in which case the potential distribution,  $\psi(x)$ , is given by Eq. (3.29). Substituting Eq. (3.29) into Eq. (3.17), and using Eq. (3.30) (with  $N_{vs}$  substituted for  $N_{v0}$ ) one then obtains:

$$\begin{aligned} E_{Fp}(x) - qV_D \\ = kT \ln \left( 1 - \frac{\exp(-\beta) D(\theta/\beta) \exp(\theta^2 \beta) [1 - \exp(qV_D / kT)]}{v_d / \langle v_c \rangle + D(\sqrt{\beta})} \right) \end{aligned} \quad (3.31)$$

where the normalized position is  $\theta = (W_D + t - x)/W_D$ , and<sup>40</sup>

$$\begin{aligned} D(\sqrt{\beta}) &= \exp(-\beta) \int_0^{\sqrt{\beta}} \exp(t^2) dt \\ &= \sqrt{\beta} \exp(-\beta) \sum_{n=0}^{\infty} \frac{\beta^n}{(2n+1)n!} \end{aligned} \quad (3.32)$$

Here  $\beta$  is the band bending parameter, given by:

$$\beta = -q[\psi(W_D) - \psi(t)]/kT. \quad (3.33)$$

To determine  $E_{Fp}$  at the semiconductor surface, Eq. (3.31) is solved at  $\theta = 1$ , giving:

$$\begin{aligned} E_{Fp}(t) - qV_D \\ = kT \ln \left( \frac{v_d / \langle v_c \rangle + D(\sqrt{\beta}) \exp(qV_D / kT)}{v_d / \langle v_c \rangle + D(\sqrt{\beta})} \right) \end{aligned} \quad (3.34)$$

This is similar to the result obtained for Schottky barrier diodes<sup>30</sup>, except that  $\langle v_c \rangle$  is the mean carrier velocity in the organic layer rather than the collection velocity in the metal, and  $V_D$  is used in place of  $V_a$ .

It is apparent that the magnitude of  $v_d/\langle v_c \rangle$  determines the functional dependence of  $E_{Fp}$  on voltage. For example, under small forward bias where  $V_D < 0$ , and where  $v_d/\langle v_c \rangle$  is large [as is the case for most OI diodes--see Part (B)], Eq. (3.34) reduces to  $E_{Fp}(t) - qV_D = 0$ . That is, the imref is flat throughout the substrate, independent of voltage, thereby allowing the majority carrier imref in p-type diodes to sweep through the lower half of the band gap with  $V_a$ . Under reverse bias,  $V_D > 0$ , implying that  $E_{Fp}(t) - qV_D = 0$  as long as the second term in the numerator of Eq. (3.34) is smaller than  $v_d/\langle v_c \rangle$ . For small reverse biases, this is indeed the case in OI diodes.

Now, we can calculate the potential at the inorganic side of the OI-HJ as a function of  $V_D$  using the values determined for  $\langle v_c \rangle$  in Part (B). The surface potential (Fig. 3.4) is just

$$q\psi(t) = q\psi_s = E_{Fp}(t) + q\phi_{Bp}. \quad (3.35)$$

In Fig. 3.15,  $\psi_s$  is plotted versus  $V_D$  for both forward ( $V_D < 0$ ) and reverse ( $V_D > 0$ ) bias. This function is determined for several barrier heights. For comparison, the imref of a Schottky barrier device with  $v_c \sim 10^6$  cm/s is also shown in the figure. Returning to Eq. (3.34) for Schottky diodes,  $v_d/\langle v_c \rangle \approx 1$  and the second term in the numerator dominates at almost all applied voltages, thus resulting in the surface imref being "pinned" to its value at  $V_D = 0$  under reverse bias. As shown in Fig. 3.15, the surface potential for a Schottky barrier diode is essentially constant under reverse bias, as expected from diffusion and thermionic emission theory.<sup>30</sup> On the other hand,  $\psi_s$  decreases linearly with  $V_D$  under forward bias. For this reason, the Schottky diode is useful for exploring traps which are located

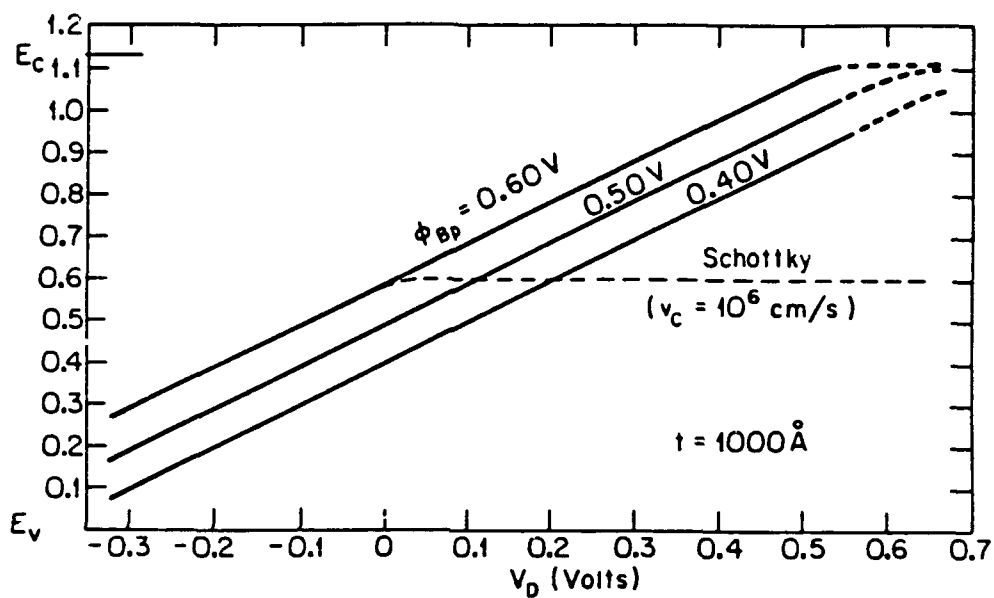


Fig. 3.15 Potential at the inorganic semiconductor surface as a function of voltage across the depletion region for OI-HJ diodes with several different values of barrier energy. The surface potential for a Schottky barrier diode (with barrier energy 0.6 eV) is shown for comparison.

between the equilibrium Fermi level and the majority carrier band edge, as has been suggested by Barret and co-workers.<sup>41,42</sup> This is due to the ability to "scan" the imref through the trap energies by changing the applied voltage, and hence altering the net trap occupancy.

In the case of the OI diode, the carrier velocity,  $\langle v_c \rangle$ , is several orders of magnitude less than  $v_d$ . Thus, the surface potential varies linearly with  $V_D$  in both forward and reverse bias over nearly the entire band gap of the inorganic semiconductor, as shown in Fig. 3.15. This result is largely independent of hole mobility within the organic film, as long as the mobility is in the range typical of crystalline organic solids<sup>43</sup> (i.e.,  $\mu_p < 10 \text{ cm}^2/\text{V-s}$ ). However, if the barrier height is sufficiently small, the surface potential cannot be brought near to the minority carrier band edge due to the increased leakage currents. Under forward bias, the behavior of the surface potential is similar to that of the Schottky barrier device, i.e., it decreases linearly with applied voltage.

Finally, Fig. 3.16 is a plot of the free hole concentration in the inorganic material at the OI interface [see Eq. (3.18)]. The same parameters employed in Fig. 3.14 are also used in this figure. The surface charge concentration is seen to vary over 14 decades as the potential changes from a forward bias of -0.5 V (where  $p_s \cong 10^{15} \text{ cm}^{-3}$ ), to a reverse bias of 0.5 V (with  $p_s = 1 \text{ cm}^{-3}$ ). The surface charge density can be understood directly in terms of the carrier velocity. For example, under strong forward bias  $\langle v_c \rangle$  is large, resulting in a hole transit time which is small compared with  $\tau_{po}$ . In this case,  $p_s$  must be very large. However, as  $\langle v_c \rangle$  is reduced,  $\tau_{po}$  becomes small with respect to the transit time, thereby depleting the thin film of injected charge near the OI interface.



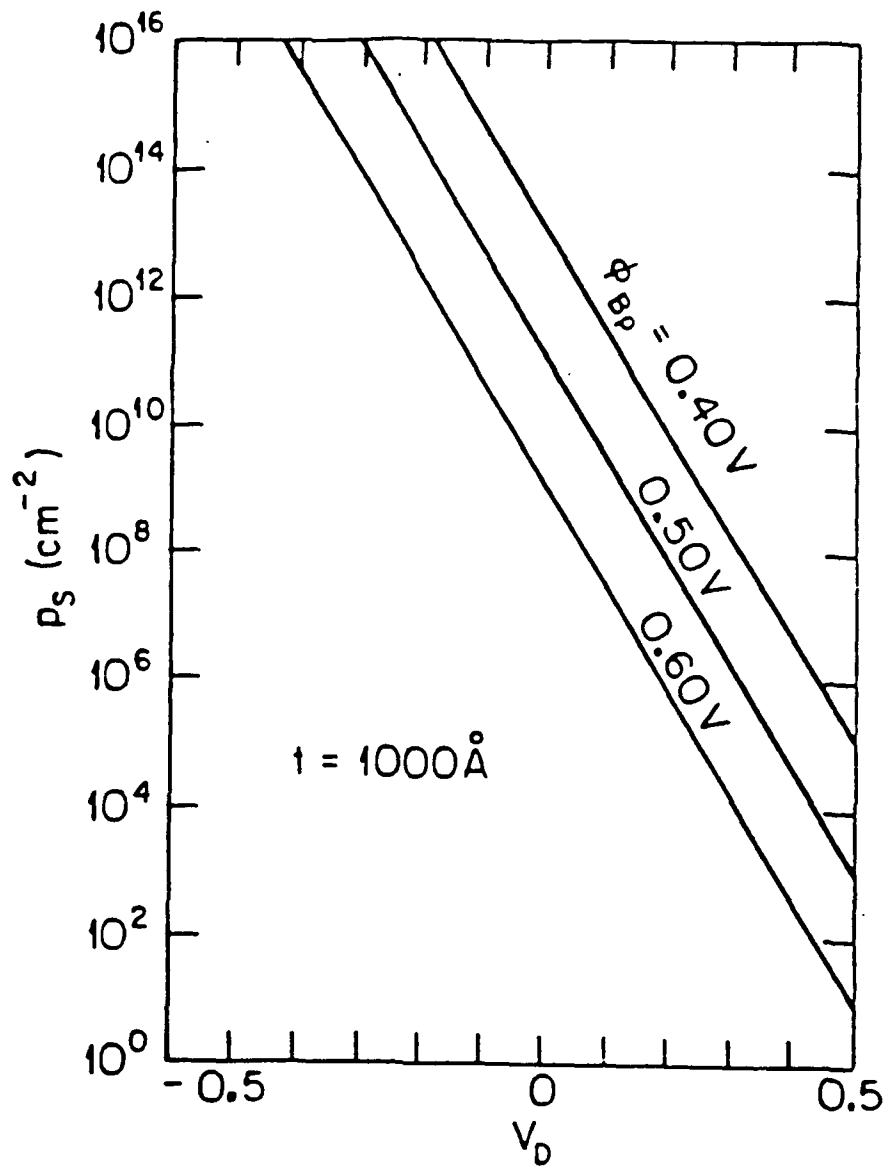


Fig. 3.16 Hole concentration ( $p_s$ ) at the OI-HJ interface as a function of voltage for the same parameters used in Fig. 3.15.

#### (D) Discussion and Conclusions

A significant result of this work is that the transport theory presented in Part (B) results in an expression for diffusion-limited current in OI-HJ diodes from which an accurate barrier energy, and hence  $\Delta E_v$ , for these novel heterojunctions can be determined. Several experimental results have also been presented which corroborate the theoretical treatment. In addition, we have shown that the majority carrier quasi-Fermi level in OI-HJ diodes is flat throughout the bulk of the inorganic semiconductor substrate for both forward and reverse bias voltages, in contrast to Schottky barrier diodes where the surface  $\mu_{ref}$  is bent towards the metal Fermi level under reverse bias. Thus, applying a bias to the OI-HJ causes the majority carrier  $\mu_{ref}$  to sweep through nearly the entire semiconductor bandgap. Provided that the density of surface states at the OI-HJ is small ( $10^{12} \text{ cm}^{-2} \text{ eV}^{-1}$ ), these states will be thermalized as  $E_{Fp}$  is lowered below the trap energy, and thus will contribute to diode admittance.<sup>27,28</sup> A higher surface state density can result in Fermi level pinning at the OI interface, this point will be discussed in detail in the next section.

The dependence of the quasi-Fermi level on voltage results from the relatively low carrier velocities, and carrier concentrations in the organic thin film. By calculating both  $E_{Fp}$  and  $\langle v_c \rangle$  as a function of  $V_D$ , we find that the OI-HJ has unique electrical properties as compared with conventional inorganic semiconductor devices. For example, near  $V_D \cong 0$ , there is only a small voltage drop across the organic film, and the organic film can be considered similar to a

leaky insulator. Thus, the device at low voltages behaves like a MIS capacitor whose impulse response is limited by the thin film dielectric relaxation time,  $\tau_{\text{diel}} = \kappa_0/\sigma$ . Here,  $\sigma$  is the conductivity of the film, and is typically  $\sigma \sim 10^{-5}$  S/cm. Using<sup>4</sup>  $\kappa_0 = 0.37 \times 10^{-12}$  F/cm, we obtain  $\tau \cong 37$  ns. Hence, under reverse or low forward voltages, the OI-HJ diode varies from a resistive response at  $f < 1/2\pi\tau_{\text{diel}} \cong 5$  MHz (depending on the inorganic semiconductor depletion capacitance,  $C_D$ ) to a reactive response at higher frequencies. The impedance and phase versus frequency characteristics of a typical OI diode operated in the MIS regime is illustrated in Fig. 3.17, assuming a conductance for the OI-HJ barrier ( $g_D$ ) of 2 or 200  $\mu\text{S}$ . The latter value corresponds to a "leaky" OI-HJ with a low barrier potential,  $\phi_{\text{BP}}$ . In this case, the organic film can be approximated by a resistor-capacitor network in series with a resistor due to the HJ, whose characteristic time is  $\tau_{\text{diel}}$ . As the network becomes reactive ( $\theta > 45^\circ$ ), then  $|Z| \propto 2\pi fC$ , which decreases inversely with frequency. For less leaky barriers (e.g.,  $g_D = 2 \mu\text{S}$ ), the network is in series with capacitance  $C_D$ , and hence becomes reactive at frequencies lower than  $2\pi\tau_{\text{diel}}$ .

Under large forward bias, the diode performs analogous to a Schottky diode. In this case, a large charge density ( $p_{\text{inj}}$  or  $n_{\text{inj}}$ ) is injected from the substrate and metal contacts into the thin film such that  $n_{\text{inj}}$  or  $p_{\text{inj}} \gg p_0$ . Here, conduction in the organic material becomes extrinsically space-charge-limited. This effectively "pulls" the Fermi energy to the organic band edge, hence making the organic material degenerate. With the exception that the resistance of the thin film in this regime is a non-linear function of voltage, in most other respects the film behaves as if it were an ohmic metal contact forming a Schottky barrier with

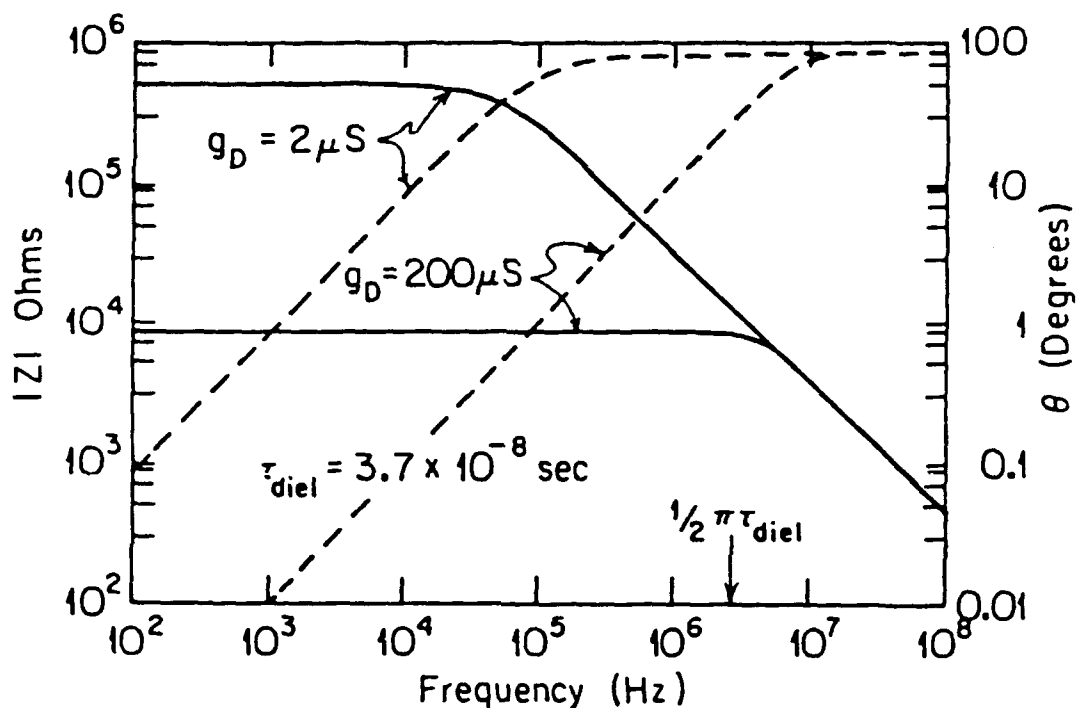


Fig. 3.17 OI-HJ impedance ( $Z$ , solid lines) and phase angle ( $\theta$ , dashed lines) vs frequency. A dielectric relaxation time of 37 ns is assumed for organic thin film. These functions are calculated for two values of barrier conductance:  $g_D = 2$  and  $200 \mu S$ , the latter value corresponding to a "leaky" diode. Also, a depletion region capacitance of  $C_D = 5 \text{ pF}$  is assumed.

the substrate. In the Schottky regime, the carrier velocity  $\langle v_c \rangle$  can be as high as  $10^4$ - $10^5$  cm/s. With a film thickness of 100 Å, a response time of between 10 and 100 ps would result.

Finally, a third "heterojunction" regime is obtained under moderate to large reverse bias voltages. The poor insulating properties of the organic material prevent the OI-HJ interface from being strongly inverted. Hence, under reverse bias this charge must either recombine at the interface, within the bulk of the film, or diffuse to the ohmic metal contact made to the film surface. As the bias is further increased, large electric fields are developed in the semiconductor substrate, leading to eventual bulk breakdown in the inorganic material. Note that when large breakdown currents are developed, charge transport is once more limited by space-charge effects in the organic material, similar to conditions of large forward bias.

### III.3 Effects of Organic Thin Film Composition on the Electrical Characteristics of OI-HJs

In the previous section, we have developed a theory of charge transport in OI-HJs based on a known value of barrier height  $\phi_B$ . On the other hand, the factors that determine the OI energy barrier formation and the magnitude of the barrier are not yet well understood. In metal-semiconductor Schottky barrier formation, interface states play a crucial role, and can often determine the barrier heights of many Schottky diodes based on both Si and III-V compounds.<sup>44,45</sup> Therefore, in order to understand the energy barrier formation in OI-HJs, it is

important to know what reaction takes place at the OI heterointerface and the defect state formation on the inorganic semiconductor surface. Hence, a study of the effect of different organic species on the inorganic semiconductor surface will perhaps shed some light on the OI energy barrier formation.

In the past, most crystalline organic materials used for OI-HJs study are either perylene-based or naphthalene-based compounds. With the exception of the polymeric OI heterojunctions,<sup>46</sup> there have been no reports of OI-HJs having been formed outside this narrow class of aromatic dianhydride dye compounds. This has limited the usefulness of OI-HJs as well as the progress made in understanding the mechanisms involved in their formation. Here, we describe the fabrication of OI barrier diodes using phthalocyanine-based compounds (Pc's) deposited on p-Si substrates. The Pc compounds are a technologically important class of crystalline organic compounds due to their potential uses in photovoltaic devices<sup>47,48</sup> and non-linear optics applications.<sup>15</sup> The two Pc compounds used in this work, namely, CuPc and H<sub>2</sub>Pc, are particularly interesting in that one has a metal ligand ion and the other one is metal-free. By studying the electrical characteristics of the OI-HJs based on these two Pc's, the effect of the presence of the metal ion in the Pc molecule (see Fig. 2.1) on OI heterojunction energy barrier formation can be determined. In fact, our SOISAS (organic-on-inorganic surface analysis spectroscopy) results<sup>28</sup> suggest that the presence of the relatively weakly bound central ligand atoms in the Pc molecular core might be responsible for a significantly higher density of surface states induced at the OI heterojunctions. In addition, our results indicate that the deposition of CuPc induces the highest density of surface states yet observed in OI diodes, which can

be explained in terms chemical bonding of Cu to Si surface atoms at the OI interface. These observations indicate defect states at the OI interface play an important role in determining the OI heterointerface energy barrier height.

In this section, we will review the theory of SOISAS technique used for semiconductor surface analysis and describe the fabrication procedures for OI diodes. Next, both the current-voltage (I-V) and capacitance-voltage (C-V) characteristics of the resulting devices are discussed. Finally, the SOISAS results obtained are discussed in terms of the reaction between the organic materials and the underlying substrate at the OI heterointerface.

#### (A) Theory of SOISAS technique

The SOISAS technique using PTCDA-based OI diodes<sup>28</sup> has been used to analyze the defect states of inorganic semiconductor surfaces. The ability of this technique to probe the surface properties of semiconductor wafers is due to the inert nature of PTCDA molecules on inorganic semiconductor surfaces. Therefore, we apply the same technique to study the reactions between organic and inorganic semiconductors at the OI heterointerface. Here, we will present a summary of the SOISAS technique developed by Forrest and co-workers.<sup>27</sup>

The interface state measurement technique can be understood in terms of the energy band diagram of the OI interface in Fig. 3.1. The diagram shows a distribution of interface states,  $D_{ss}$ , is in equilibrium with the inorganic semiconductor, while the distribution  $D_{so}$ , is in equilibrium with the organic thin film. These states are physically separated by an interfacial layer of thickness  $\delta_{ss}$ . The charge balance of such a heterojunction is given by:

$$Q_{oi} + Q_{ss} + Q_s = 0 \quad (3.36)$$

where  $Q_{oi}$  and  $Q_{ss}$  are the mobile and fixed charges at the OI heterointerface, respectively, and  $Q_s$  is the semiconductor substrate space charge. Following the analysis on metal-insulator-semiconductor junctions<sup>49,50</sup> modified for the case of OI diodes, we obtain using Gauss' Law:

$$Q_{oi} = -\kappa_i(dV_{ss}/\delta_{ss}). \quad (3.37)$$

Here,  $\kappa_i$  is the permittivity of the boundary layer and  $d$  is the thickness of the organic film. Substituting Eq.(3.36) into Eq.(3.37) and taking the derivative with respect to the applied voltage gives

$$\frac{dV_{ss}}{dV_a} = \frac{\delta_{ss}}{\kappa_i} \left( \frac{dQ_{ss}}{dV_a} + \frac{dQ_s}{dV_a} \right). \quad (3.38)$$

Now, the derivative of the fixed interface charge in Eq. (3.37) can be rewritten as

$$\frac{dQ_{ss}}{dV_a} = \frac{\partial Q_{ss}}{\partial V_o} \frac{\partial V_o}{\partial V_a} + \frac{\partial Q_{ss}}{\partial V_D} \frac{\partial V_D}{\partial V_a}, \quad (3.39)$$

with

$$\frac{\partial Q_{ss}}{\partial V_o} = -qD_{so} \quad (3.40)$$

and

$$\frac{\partial Q_{ss}}{\partial V_D} = -qD_{ss} \quad (3.41)$$

As has been discussed in Sec. III.2(C), when voltage is applied across the OI heterojunction barrier, the surface potential  $\psi_s$  [see Fig. 3.4] of the majority



imref is swept through the entire band gap, allowing the emission of interface trapped charge into the conduction band of the substrate from states  $D_{ss}$  and into the bands of the organic film from  $D_{so}$ . This trap charge density gives rise to the additional capacitance in the device. Thus, the capacitance deviation from that of the ideal (trap-free) diode due to interface charge is simply

$$\delta C = \frac{\partial Q_{ss}}{\partial V_o} + \frac{\partial Q_{ss}}{\partial V_D} = -q(D_{so} + D_{ss}) \quad (3.42)$$

where  $Q_{ss}$  is the total interface state charge. It can then be shown that the interface state densities are given by:<sup>27</sup>

$$D_{ss} = \frac{dg_{TE}}{\sigma_p} D_{so} = \frac{\kappa_i}{q\delta_{ss}} \left[ 1 + \frac{dg_{TE}}{\sigma_p} - \frac{\partial V_a}{\partial V_D} + \frac{\kappa_s \delta_{ss}}{\kappa_i W(V_D)} \right], \quad (3.43)$$

which can be found as a function of applied voltage  $V_a$  as long as  $\partial V_a / \partial V_D$  is measurable for a particular sample. Here  $g_{TE}$  is the conductance due to thermionic emission over the OI barrier,  $\delta_p$  is the conductivity of the organic material, and  $W(V_D)$  is the depletion layer width at  $V_D$  which can be found from the following equations:

$$|N_D - N_A| = \frac{2}{q\kappa_s A^2} \frac{dV_D}{d(1/C_D^2)}, \quad (3.44)$$

and

$$W = \kappa_s A / C_D. \quad (3.45)$$

which is the C-V characteristics of a sample with known uniform free carrier concentration. Here,  $|N_D - N_A|$  is the free carrier concentration and  $C_D$  is the

capacitance due to the depletion layer of the inorganic semiconductor substrate, and  $A$  is the area of the ohmic contact.  $\partial V_a / \partial V_D$  is easily found from the C-V characteristics of a sample with known, uniform free carrier concentration,  $N_D$ . In this case:

$$\frac{\partial V_D}{\partial V_a} = - \left( \frac{q \kappa_s N_D A^2}{2} \right) \frac{d(1/C_D)^2}{dV_a} \quad (3.46)$$

Essentially, this equation gives the deviations of the C-V data for a given sample from ideal (trap-free) value.

If Eqs. (3.43) and (3.46) are used and  $d$  is kept small, a measurement of the C-V characteristics yields  $D_{ss}(\psi_s)$ , where  $\psi_s = V_D - \phi_B$  for  $\psi_s < \epsilon_g/q$ . It should be emphasized that the free carrier concentration in the semiconductor must be uniform both in the bulk region such that  $N_D$  is easily obtained for a particular sample at voltages high enough that the depletion region edge is sufficiently far from the semiconductor surface i.e.,  $|V_a| \gg \epsilon_g/q$ . Under this condition, the measurement of  $N_D$  is not affected by the presence of interface charge. Fig. 3.18 (reproduced from Ref. 27) shows the calculated C-V characteristics for an ideal sample with no defect states at the OI interface and for one with a surface state density ( $D_{ss}$ ) of  $2 \times 10^{12}/\text{cm}^2$  eV distributed uniformly across the energy band gap. A marked distortion of these data from the ideal C-V characteristics is apparent. For the sample free from surface defect states,  $C_D$  decreases smoothly with increasing reverse bias voltage. On the other hand, there is a step near 0 V as well as a shift with respect to the ideal C-V data. Thus,  $D_{ss}$  can be obtained from the C-V data using Eq. (3.43).

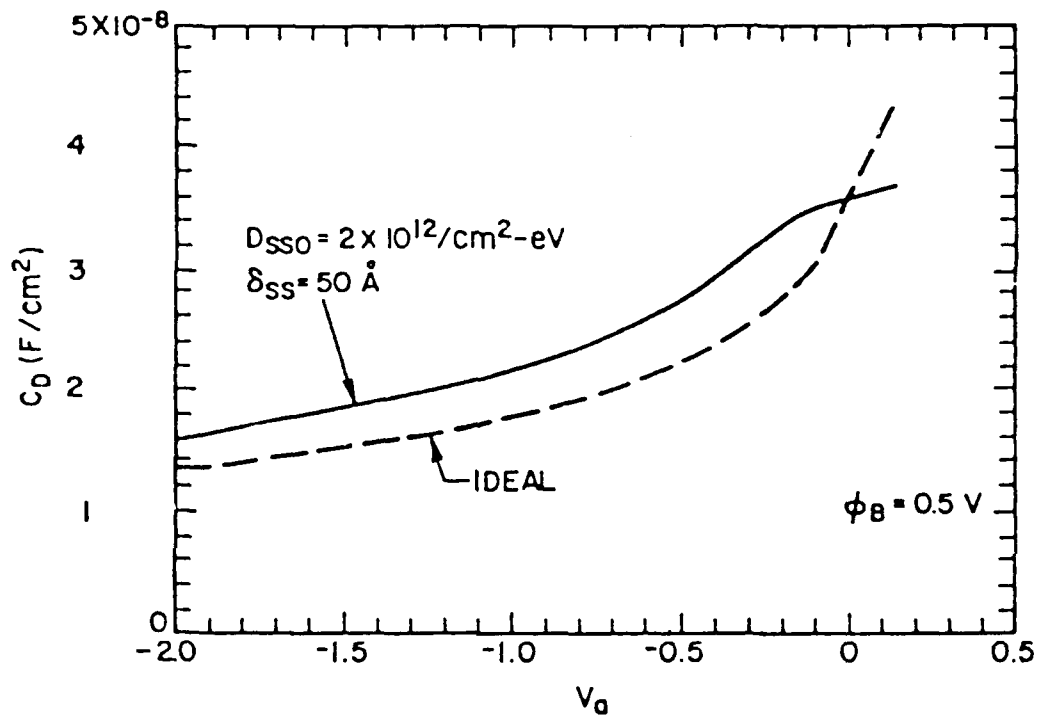


Fig. 3.18 Calculated C-V data for an OI heterojunction diode with no defect states at the OI interface (dashed line) and for a uniform defect density of states of  $2 \times 10^{12}/\text{cm}^2 \text{ eV}$ .

## (B) OI diode fabrication

The devices studied in this work were fabricated as follows: First, it was necessary to identify appropriate metals useful in forming ohmic contacts to the various organic thin films. For this purpose, a symmetrical metal/organic/metal thin film device was fabricated by depositing an approximately 2000 Å thick metallic layer onto a pre-cleaned glass substrate. This was immediately followed by the deposition via vacuum sublimation of approximately 1000 Å of the pre-purified organic film across the entire metal/substrate surface at room temperature. The vacuum prior to thin film deposition was  $< 2 \times 10^{-6}$  Torr, and the deposition rate was 10 - 15 Å/s. Finally, contact dots using the same metal as that used for the full area back contacts were deposited through a shadow mask placed onto the organic thin film. To test whether the metal formed a blocking (Schottky) or ohmic contact, the I-V characteristics were tested by applying a potential between the top and back metal electrodes. Only those metals which exhibited linear I-V characteristics over a range of at least  $-0.2 \text{ V} < V < 0.2 \text{ V}$ , and whose specific resistance was nominally less than  $5 \times 10^{-3} \Omega\text{-cm}^2$  were used as the ohmic contact metals in this work.

Once the ohmic contact metal and deposition parameters were established, the OI diode was fabricated using (100) p/p<sup>+</sup> epitaxial Si wafers. The resistivity of the epitaxial p-layer was roughly 5 Ω-cm. Details of the fabrication of OI diodes has been discussed in Sec. III.1. After back contact deposition, the top wafer surface was degreased and then dipped for 1 minute in a 1:1 deionized (DI) water: 30% HF solution to remove surface oxides. The wafer was then thoroughly rinsed in DI water, blown dry in filtered nitrogen, and quickly inserted into the

vacuum system for a full surface organic thin film deposition. Typically, between 100 Å and 1000 Å thick films were deposited at room temperature. The final step was to deposit the 270 µm diameter ohmic metal dot contact using a procedure similar to that used in fabricating the metal/organic/metal test structures. Specific layer thicknesses and contact metals used in the study are listed in Table 3.6. Fine gold wire probes of 30 µm in diameter were used for all electrical measurements of OI diodes.

Table 3.6 Characteristics of several organic/p-Si diodes.

	PTCDA	NTCDA	CuPc	H <sub>2</sub> Pc
Thickness (Å)	1000	150	300	200
Ohmic contact metal	In	In	Au	In
$\phi_B$ (V)	$0.56 \pm 0.02$	$0.50 \pm 0.02$	$0.50 \pm 0.02$	$0.55 \pm 0.02$
n	$1.45 \pm 0.1$	$2.4 \pm 0.1$	$3.2 \pm 0.02$	$2.0 \pm 0.01$
$(D_{ss})_{max}$ (cm <sup>-2</sup> eV <sup>-1</sup> )	$2 \times 10^{12}$	$2 \times 10^{12}$	$2 \times 10^{14}$	$8 \times 10^{12}$

### (C) Results

Typical bipolar current-voltage (I-V) characteristics of an In/PTCDA/p-Si diode are shown in the inset of Fig. 3.19. As shown in the figure, the OI diode characteristics exhibit exponentially increasing forward current characteristics at low bias voltages, consistent with the diffusion model discussed in Sec. III.2(A). Very low reverse-bias leakage currents and large avalanche breakdown voltages ( $V_B > 200$  V for PTCDA/Si diodes) are commonly observed in OI-HJs, as shown in the inset. At higher voltage, the rate of increase in current decreases due to space-charge injection into the organic thin film [see Sec. III.1]. The characteristics of the OI diodes using the four organic materials investigated are qualitatively similar as shown in Fig. 3.19. To analyze the I-V characteristics of these OI-HJs, the diffusion model described in Sec. III.2(A) is used here. The diode ideality factors (*n*-value) can be determined from the slopes of the I-V curves in Fig. 3.19 [see Eq. (3.5)], and the barrier heights of OI-HJs can be obtained from Eq. (3.19). To determine the pre-exponential factor in Eq. (3.19), the same mean carrier velocity (500 cm/s) is used for PTCDA, NTCDA, and CuPc due to their small difference in carrier mobilities and lifetimes. On the other hand, the carrier mobility in H<sub>2</sub>Pc is known<sup>51</sup> to be about two orders of magnitude lower than that in CuPc, and a hole velocity of 50 cm/s is assumed for H<sub>2</sub>Pc. The *n*-values and the barrier heights for the OI diodes using four organic materials under investigation are listed in Table 3.6. It is apparent that the lowest *n*-value and highest barrier are 1.45 and 0.55 V, respectively, for PTCDA. On the other hand, *n*-values as high as 3.2 for CuPc are obtained indicating a high density of OI heterointerface states [see Eq. (3.4)]. However, due to the low

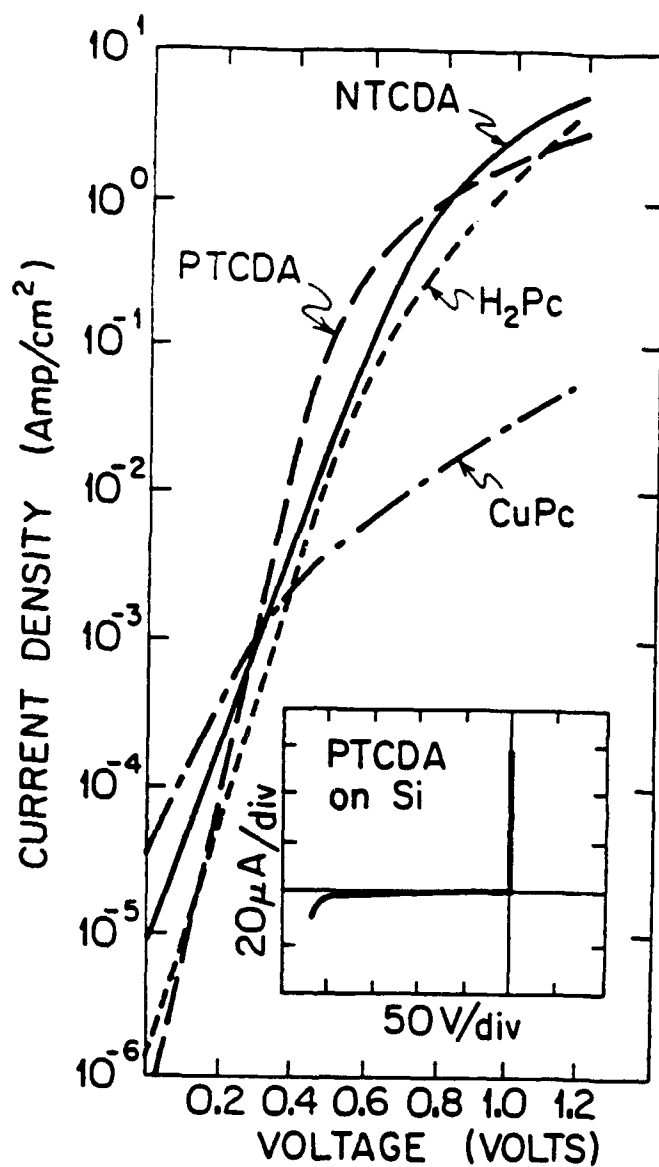


Fig. 3.19 Forward-biased current density vs voltage (J-V) characteristics of organic/p-Si devices taken at room temperature. For J-V data for PTCDA, NTCDA, H<sub>2</sub>Pc, and CuPc-based devices are shown. Inset: Bipolar I-V characteristics of an In/PTCDA/p-Si diode.

forward bias at which the current through CuPc becomes space charge-limited, the  $n$ -value thus obtained is subject to significant error. Further, we point out that the barrier heights measured from the I-V characteristics of devices with  $n$ -values significantly greater than 1, as in the case of CuPc and NTCDA, should not be considered to be accurate. That is, the  $\phi_B$  value obtained from I-V data is reasonably accurate only if the density of interface states and thin film resistivity is small. As pointed out in Section III.1 [Eq. (3.4)], a high interface state density will result in  $n \gg 1$ . We therefore suspect that the CuPc/p-Si interface has a considerably higher number of defects than that observed for the more ideal PTCDA/Si interface.

The details of the interface state density can be more quantitatively understood via analysis of the 1 MHz capacitance-voltage (C-V) characteristics shown in Fig. 3.20. These characteristics are measured over the range  $0.2 \text{ V} > V_a > -5 \text{ V}$ , where  $V_a > 0$  indicates forward bias. Over this voltage range, the conductance of the OI diode is smaller than the susceptance which is nearly purely capacitive.<sup>27</sup> It is apparent that the C-V characteristics of the dianhydride-containing compounds (PTCDA and NTCDA) are qualitatively different than those obtained for the phthalocyanines. For example, the data for PTCDA and NTCDA indicate a smooth, monotonic decrease in capacitance with increasing reverse voltage. This is characteristic of OI diodes with a low density of interface states and uniform substrate doping. In contrast, the curves for both H<sub>2</sub>Pc and CuPc show a small but pronounced step near  $V_a = 0 \text{ V}$ . Features of this nature have been shown in Fig. 3.18 to be due to the existence of a high density of charged defect states at the OI interface which tend to screen the externally



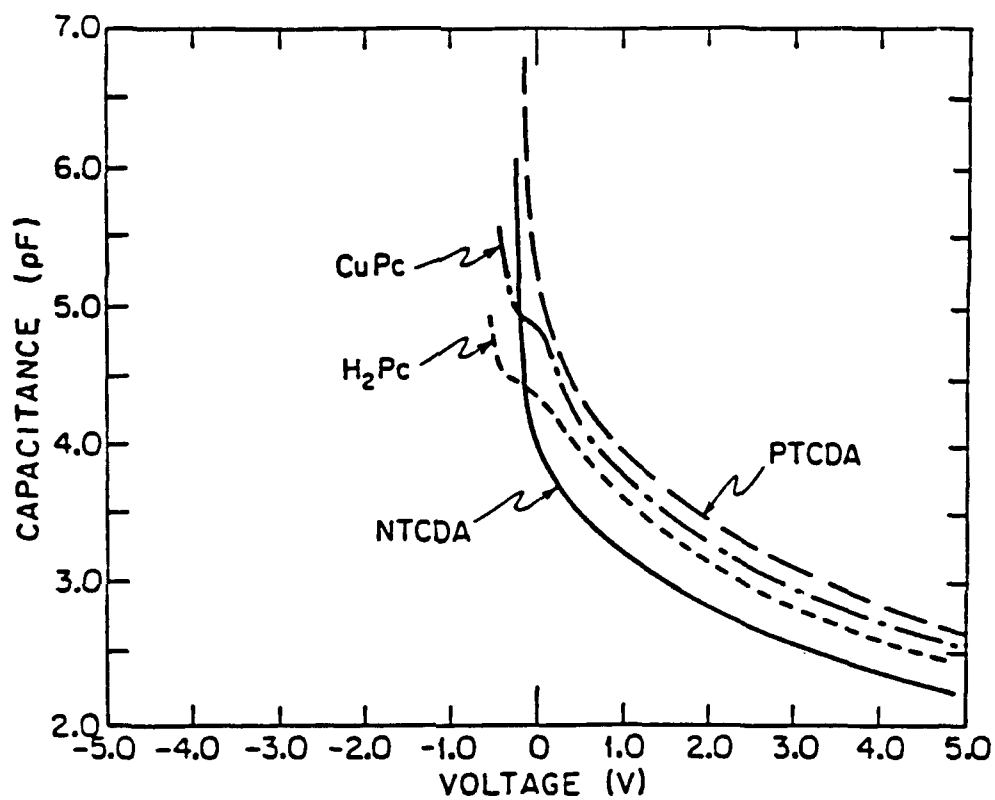


Fig. 3.20 Capacitance-voltage (C-V) characteristics near  $V_a = 0$  of four OI diodes employing the same organic materials as those discussed in Fig. 3.19.

applied potential from the semiconductor bulk. Indeed, using the SOISAS analysis discussed in Part (A), these data can be used to quantitatively determine the distribution of charged interface states ( $D_{ss}$ ) within the inorganic semiconductor bandgap.

In Fig. 3.21 we show the results of such analysis for the four OI diodes studied. The relative differences between the anhydrides and the Pc's are readily apparent. For example, the surface state densities of the former compounds are at a relatively low value of approximately  $10^{12} \text{ cm}^{-2}\text{eV}^{-1}$ , whereas the CuPc sample has a very pronounced peak in surface state density at 0.5 eV above the valence band maximum. This peak is nearly two orders of magnitude higher than the background values of  $10^{12} \text{ cm}^{-2}\text{eV}^{-1}$ . Although a similar peak exists for the H<sub>2</sub>Pc sample, its magnitude is considerably less than that observed for CuPc.

#### (D) Discussion and Conclusions

One potential mechanism which explains the existence of the high surface state density observed at the CuPc/p-Si interface involves reactions between water and CuPc. Adsorption of water molecules onto the semiconductor surface can readily occur via diffusion through the  $\sim 30 \text{ \AA}^2$  gaps between adjacent Pc stacks. The water molecule diffusion into the organic thin film can occur when the OI diodes are exposed to the laboratory environment. Note that it has already been found that exposure of CuPc/metal Schottky barrier devices to oxygen<sup>52</sup> and hydrogen<sup>53,54</sup> has a significant influence on their electrical characteristics. Once at the OI interface, the water molecule can react with CuPc to form H<sub>2</sub>Pc and CuO. Such a reaction might occur via:

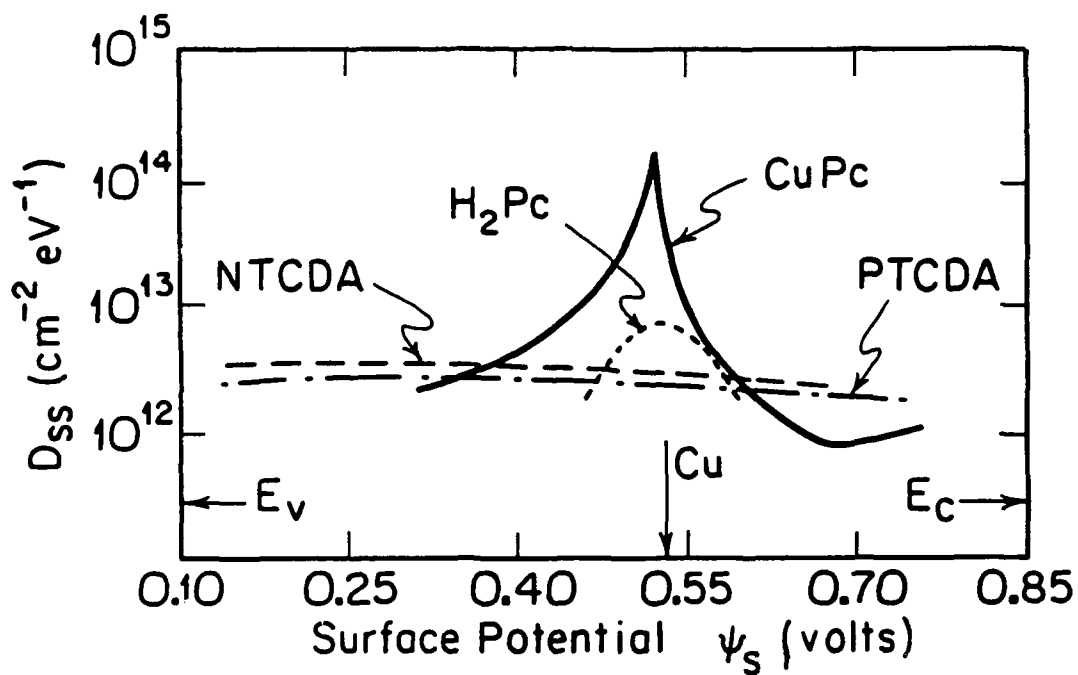


Fig. 3.21 Density of interface states ( $D_{ss}$ ) as a function of surface energy ( $\psi_s$ ) in the p-Si band gap for the four diodes in Fig. 3.20. The energy is with respect to the conduction ( $E_c$ ) and ( $E_v$ ) band edges of the Si substrate.



Given the Gibb's free energies ( $\Delta G^\circ$ 's) of CuO and H<sub>2</sub>O and assuming the difference in  $\Delta G^\circ$ 's between H<sub>2</sub>Pc and CuPc is approximately equal to the free energy difference between H-N and Cu-N bonds, then  $\Delta G^\circ = -66.2$  kcal/mole for the above reaction. Since  $\Delta G^\circ < 0$ , the possibility for the above reaction to occur is favorable. The CuO molecules thus formed can diffuse through the thin surface SiO<sub>2</sub> and participate in the following reaction:



Here,  $\Delta G^\circ = -143$  kcal/mole, indicating that this reaction, too, is probable. It should be noted that a similar mechanism was proposed by Fan and Faulkner<sup>48</sup> to account for the change of the electrical characteristics of the Al/H<sub>2</sub>Pc Schottky barrier diode exposed to atmosphere. They suggested that the change in short-circuit photocurrent in the diodes was due to oxidation of the Al electrode. In the case of Au/CuPc/Si, however, it is unlikely that Au is oxidized and, therefore, the top metal contact should be stable in the laboratory environment. On the other hand, the silicon surface readily forms a native oxide. Hence, free copper atoms and Cu-O-Si complexes can be formed at the CuPc/Si interface, giving rise to the high surface state density near the mid-gap energy. These states have the effect of pinning the surface Fermi level at the charge density maximum. Fermi-level pinning due to mid-gap states is also commonly observed in some metal/semiconductor Schottky diodes<sup>55,56</sup> where the barrier heights are determined by the interface defect levels. To our knowledge this is the first case in which a crystalline organic semiconductor has been found to perturb the OI

interface to the extent that the energy barrier is pinned at the extrinsically induced defect levels.

An analogous sequence of reactions can also occur in the case of  $H_2Pc$ , whereby the molecule is oxidized, liberating hydrogen which then forms Si-OH complexes at the  $SiO_2/Si$  interface. Such complexes can exist in a charged state which, in turn, pins the Fermi level. Although the details of such reactions are not yet established, we emphasize here that, in general, the surface state densities at the mid-gap energy observed for the Pc's significantly exceeds that observed for the dianhydrides (Fig. 3.21) suggesting that surface reactions are taking place in the former class of compounds. The mechanisms proposed in Eqs. (3.45) and (3.46) indicate that these reactions are energetically favorable.

Integrating the area under the peak in Fig. 3.21, we estimate that the total number of surface states, at the CuPc/Si interface is  $\sim 5 \times 10^{11}/cm^2$ . Since a CuPc molecule has an area of  $\sim 100 \text{ \AA}^2$ , the number of CuPc molecules that are contributing to the reactions postulated by Eqs. (3.47) and (3.48) is about 0.5%. This model suggests that the surface state density of the Pc/Si interface is sensitive to the environment. On the other hand, in the case of PTCDA and NTCDA, the C = O bond in the anhydride groups, as well as the core C = C bonds are extremely stable (with bond energies of -532 kcal/mole for the C = O bond, for example). Hence, it is unlikely that reactions will occur between these compounds and the underlying Si or  $SiO_2$  surface. For this reason, we have been unable to detect a large density of surface states after the deposition of these latter thin film materials. In fact, the "background" surface state density that is observed for the dianhydride samples may be due to the presence of a thin native oxide

film rather than having been induced by the deposition of the organic compound. For example, typical values of  $D_{ss}$  observed at the native oxide/Si interfaces have been found<sup>45</sup> to be on the order of  $10^{12}/(\text{cm}^2 \text{ eV})$ . It should be noted that this value is about the same for grown ultra-thin oxides whose  $D_{ss}$  value is generally higher than for thicker thermally grown oxides.<sup>57,58</sup> In contrast, earlier work has shown that the background surface state densities measured for InP and related compounds<sup>28</sup> can be as low as  $8 \times 10^{11}/(\text{cm}^2\text{-eV})$ , indicating a highly non-destructive contact using PTCDA on many semiconductor substrates.

In conclusion, we have shown that an entirely new class of stable, crystalline aromatic dye compounds--the phthalocyanines--form rectifying barriers when vacuum-deposited onto inorganic semiconductor substrates such as Si. This result extends the range of optical and electronic properties of the organic materials which can be utilized in novel organic-on-inorganic semiconductor heterojunction devices. We find that the electrical characteristics of the Pc-based OI devices are consistent with previous theories used to describe the performance of dianhydride-based structures. Thus, the devices exhibit exponentially increasing I-V characteristics under forward bias, whereas the reverse-bias attainable is limited only by avalanche breakdown in the underlying inorganic semiconductor material.

Unlike the anhydrides, however, the Pc's (and, in particular, CuPc) appear to interact strongly with the inorganic semiconductor surface. This interaction results in a high density of interface states which pin the surface Fermi energy in the inorganic semiconductor band gap, thereby determining the magnitude of the OI barrier energy. Thus, OI barriers are similar to metal/semiconductor Schottky

barriers in that interface states play an important role in determining the barrier energy. While this extrinsic phenomenon may also be responsible for determining the OI barrier height for the anhydrides, it has not yet been possible to observe a surface state spectrum which might support the existence of strong organic-inorganic chemical interactions and bond exchange, as has been proposed for the phthalocyanines.

### III.4 Dependence of Electrical Characteristics of OI-HJs on Organic Thin Film Deposition Temperature

As described in Chapter 2, the crystallinity of organic films is very sensitive to the substrate temperature at which the films are deposited. When films are deposited at low substrate temperatures ( $< 120$  K) or high deposition rate ( $> 50$  Å/s), molecules stack in a highly ordered fashion. On the other hand, disordered films result when they are deposited at elevated temperatures or low deposition rates. As discussed in Section III.1, the electrical properties of organic films in the OI diodes can be determined via the study of the current-voltage (I-V) characteristics. We, therefore, investigated the electrical properties of PTCDA films deposited on Si substrates at various temperatures, and the results are explained in terms of the structural properties of the organic thin films.

To fabricate OI diodes, indium was first deposited onto the back side of p-Si substrates (with substrate resistivity of  $5\ \Omega\ \text{cm}$ ), then the wafers were degreased by standard organic solvents. The surface oxide was removed by dilute HF solution as described in Section III.1. Next, PTCDA films with thicknesses ranging from  $500\ \text{\AA}$  to  $4000\ \text{\AA}$  were deposited at a rate of  $5\text{-}10\ \text{\AA/s}$  onto the top

wafer surface followed by indium contact deposition through a shadow mask onto the organic films. The metal contact area was  $5.5 \times 10^{-4}$  cm. Electrical measurements of the OI heterojunction diodes were carried out using fine gold wire probes.

Fig. 3.22 shows the forward current-voltage (I-V) characteristics for OI devices with 2000 Å thick PTCDA films deposited at different substrate temperatures. For the sample with the organic film deposited at 90 K, the forward current has an exponential dependence on voltage due to diffusion current across the OI heterointerface in the low bias voltage regime, and then exhibits a roll off in current due to space-charge-limited current at large bias voltages [see Eqs. (3.5) and (3.6)]. For the sample with PTCDA deposited at 443 K, the forward current has no exponential dependence for the entire voltage range studied. Such an early roll off at low bias voltages is an indication of low carrier mobility in the organic film. Using Eqs. (3.5) and (3.6), the fits to the experimental I-V data are also shown by the solid lines in Fig. 3.22. From these fits, we find that the carrier mobility in the organic films decreases from 0.16 cm<sup>2</sup>/V-s for the sample deposited at 90 K to  $2 \times 10^{-4}$  cm<sup>2</sup>/V-s for the sample deposited at 443 K.

Fig. 3.23 shows the carrier mobility for PTCDA films of different thicknesses deposited at various temperatures. Note that the carrier mobility is highest for films deposited at 90 K, and decreases as the deposition temperature increases, except for the 500 Å sample. As shown in Fig. 3.23, there is no difference in carrier mobility between the 500 Å thick samples deposited at 90 K and 293 K. For the 500 Å sample deposited at 443 K, however, the carrier



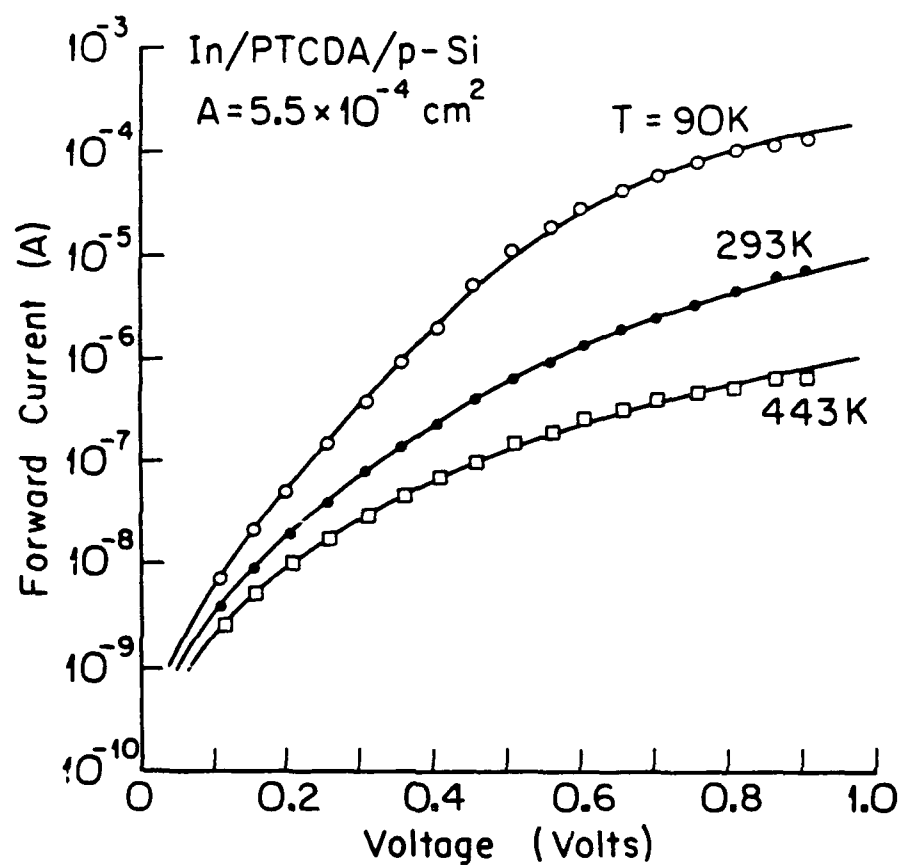


Fig. 3.22 Forward current-voltage characteristics for PTCDA/p-Si devices with 2000 Å deposited at different substrate temperatures. The solid lines are the fits to the data using parameters described in the text.

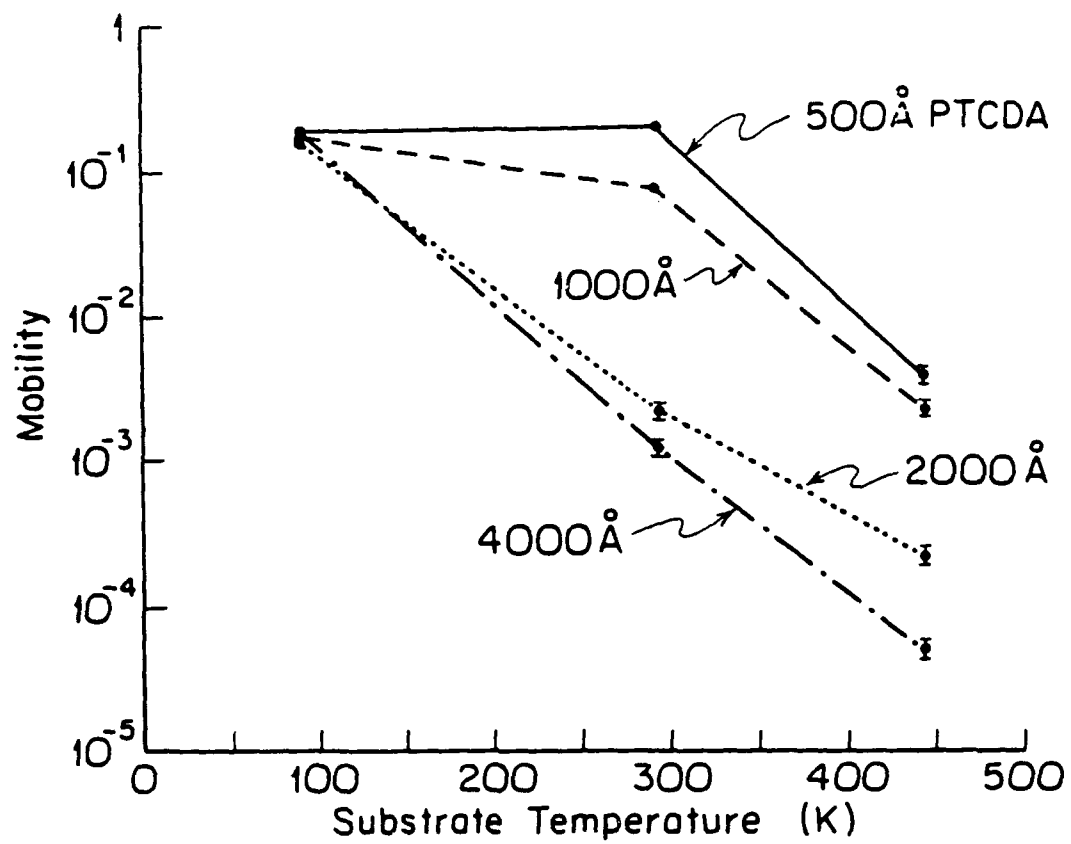


Fig. 3.23 Carrier mobility vs PTCDA thin film deposition temperature. The mobility values are obtained from the fits to the I-V characteristics of OI-HJs shown in Fig. 3.22.

mobility decreases by about 2 orders of magnitude compared to the samples deposited at lower temperatures. A similar trend is also observed in the 1000 Å sample where there is only a small difference in mobility between the samples deposited at 90 K and 293 K. On the other hand, the carrier mobilities of the thicker samples (2000 Å and 4000 Å) deposited at 90 K and 293 K differ by about 2 orders of magnitude, indicating that by lowering the substrate temperature to 90 K, there is a significant improvement in carrier mobility in the organic films.

The results of the mobility measurements of organic films can be explained in terms of their structural properties. As discussed in Chapter 2, for PTCDA films deposited at low temperatures or high deposition rates, molecules form stacks tilted at an angle of  $11^\circ$  from the normal. Charge carriers in the organic films can therefore move along the stacking direction, giving rise to high carrier mobility in the films. On the other hand, films deposited at elevated temperatures are polycrystalline with randomly oriented molecular stacks, and carriers no longer move along the stacking direction, resulting in reduction of carrier mobility by almost 4 orders of magnitude.

In addition to the substrate temperature dependence on the carrier mobility in organic films, the mobility also has a thickness dependence for films deposited at elevated temperatures (293 K and 443 K). Except for the films deposited at 90 K, as the thickness of the film increases, the mobility decreases. Such a thickness dependence is also seen in the optical micrographs of PTCDA films deposited at room temperature as shown in Fig. 3.24. For example, for the 500 Å thick film sample deposited at room temperature, no surface texture is observed, indicating a

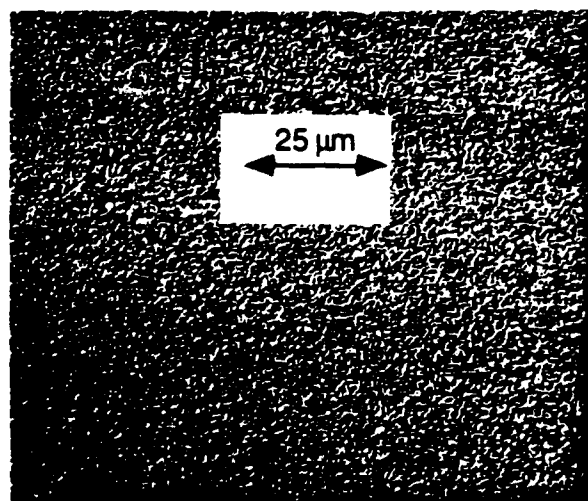
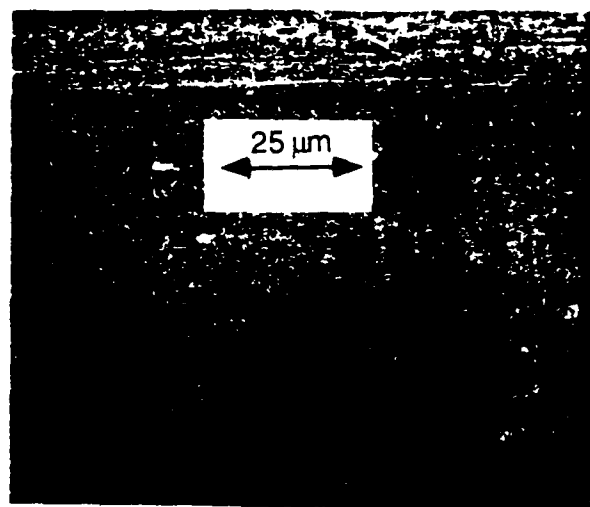


Fig. 3.24 Optical micrographs for 500 Å (top) and 2000 Å (bottom) thick PTCDA films deposited at room temperature.

strong structural ordering in the films which accounts for the high carrier mobility. On the other hand, for the 2000 Å thick film deposited at room temperature, Considerable surface texture is observed indicating the polycrystalline nature of the films which gives rise to a reduction in carrier mobility.

The film thickness dependence on the structural properties can be explained in terms of the van der Waals interaction energy of PTCDA molecules. Recall from Chapter 2 that there is an energy threshold of 20 meV (i.e., slightly less room temperature thermal energy) in the PTCDA crystal binding energy surfaces. When PTCDA is deposited at room temperature, there are some molecules which do not have sufficient energy to surmount the energy threshold and stay at the global minimum, resulting in perfect ordering in certain areas of the sample. A fraction of the molecules, however, have sufficient thermal energy to move on the crystal surface. This results in faulty stacking habits. As this process continues, the number of sites with perfect ordering decreases, and more surface molecules stack irregularly. As the film grows thicker, the structural ordering continues to degrade. On the other hand, such a problem is not encountered for films deposited at low temperature. In this case, molecules do not have sufficient thermal energy to wander around on the crystal surface, and hence always stay at the global energy minimum, resulting in perfect structural ordering and large carrier mobility.

### III.5 OI Photodetectors

In previous sections, we have discussed various aspects of the electrical characteristics of OI-HJ devices. In particular, rectifying heterojunction devices formed by depositing PTCDA on p-Si have been shown to have high breakdown voltage and extremely low reverse dark current ( $< 2 \mu\text{A}/\text{cm}^2$  at  $V_B/2$ ). These characteristics are ideal for fabrication of optoelectronic devices such as photodetectors. Fabrication of OI photodetectors lets us explore the possibility of using OI-HJs for optoelectronic device applications. By studying their characteristics, we can gain a better understanding of the OI device parameters such as carrier velocity.

In this Section, we report on the fabrication and characterization of PTCDA/p-Si based OI-HJ photodetectors. The structure of an OI photodetector, shown in Fig. 3.25, is very similar to the OI-HJs discussed previously, except that indium-tin-oxide (ITO) is used as the top contact material. ITO is used because it also makes a low resistivity, transparent ohmic contact to PTCDA. This greatly simplifies the device structure since light illumination can be incident via the contact window, and back illumination is not necessary. Quantum efficiencies as high as 85% and optical response times of 5 ns have been found for these heterojunction detectors. With an optimum device geometry, a 3-dB roll-off frequency of higher than 1 GHz can be achieved. In addition, the results of our speed of response measurements indicate that the diffusion velocity in the organic layer is the dominant factor limiting the operating frequency of optimized OI detectors.

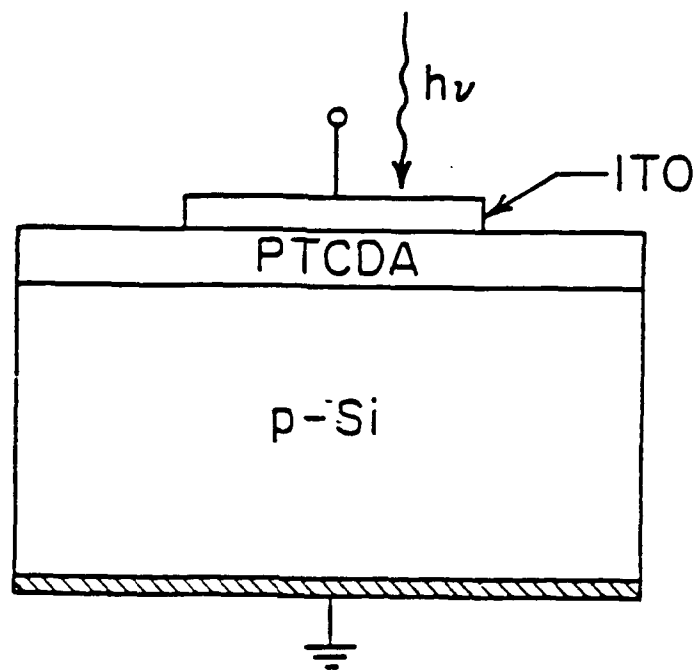


Fig. 3.25 Schematic cross section of an organic-on-inorganic heterojunction photodetector.

#### (A) Device Fabrication and Measurement

To fabricate OI detectors, (100) 2  $\Omega$ -cm p-Si substrate was first degreased with organic solvent, followed by an oxide etch with a dilute HF solution. Indium was deposited onto the back substrate surface as an ohmic contact to the inorganic semiconductor. Pre-purified PTCDA was vacuum-deposited to a thickness of 1500 Å onto the Si top surface at room temperature. Transparent ITO window contacts were sputtered onto the organic film surface at room temperature in a  $10^{-3}$  Torr Ar pressure. The pressed powder ITO targets used for sputtering consisted of 91%  $\text{In}_2\text{O}_3$  and 9% SnO. Typically, a sheet resistance of 100  $\Omega/\square$  is obtained by this technique. The ITO film had a thickness of approximately 2000 Å, and an index of refraction of 2.0 at a wavelength of 6328 Å.

For electrical measurements, 50  $\Omega$  coaxial probes were used to make contact to the ITO window layer. For quantum efficiency measurements, light output from a monochromator was coupled to the OI detector through an optical fiber, and the detector response was measured using a lock-in amplifier. The speed of response measurement was done using a 3 mW GaAs pulsed laser diode (emitting at 840 nm) with an optical pulse fall time <100 ps as the light source. Illumination was incident via the contact window for both quantum efficiency and speed of response measurements.

#### (B) Experimental Results

Typical reverse-biased dark current characteristics for the ITO/PTCDA/p-Si photodetector with an area of  $2.2 \times 10^{-3} \text{ cm}^2$  are shown in Fig. 3.26 (filled



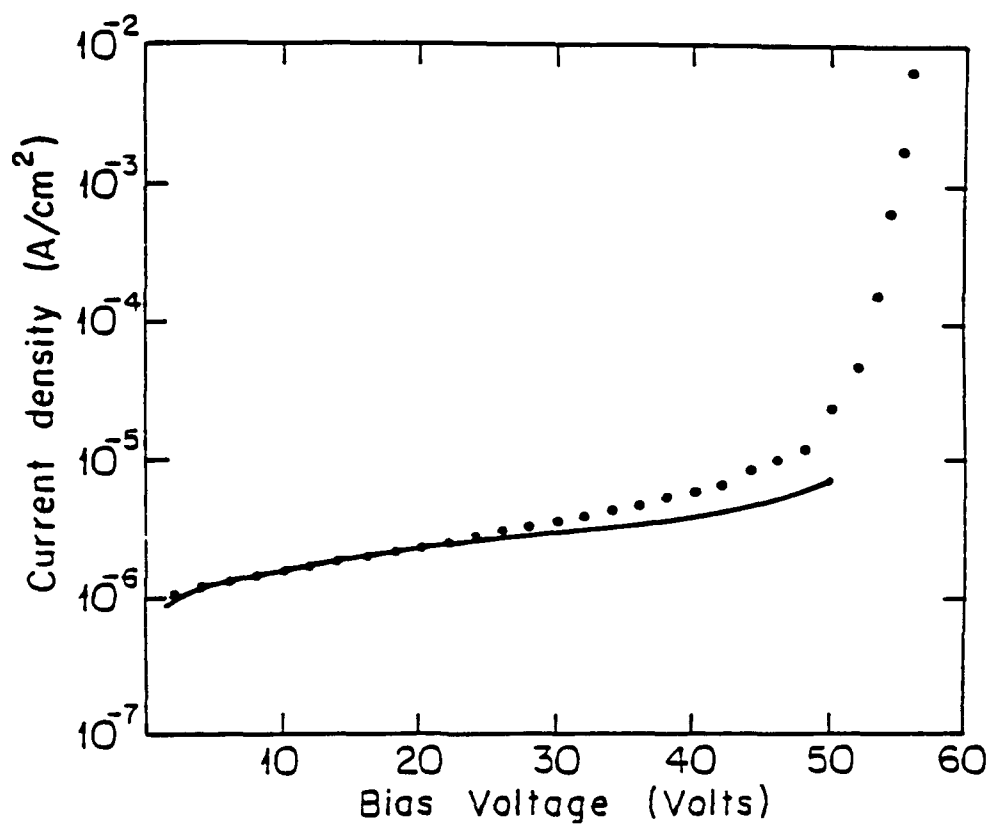


Fig. 3.26 The dark current versus reverse bias voltage of an ITO/PTCDA/p-Si photodetector. Circles indicate experimental data, and the solid line is a theoretical fit.

circles). The detector undergoes avalanche breakdown in the Si substrate at about 55 V. This breakdown voltage is consistent with the Si doping concentration of  $7 \times 10^{15} \text{ cm}^{-3}$ . The dark current density is  $< 3 \times 10^{-6} \text{ Acm}^{-2}$  at half the breakdown voltage. It has been shown that generation and recombination current is often dominant<sup>4</sup> when an OI diode is reverse biased. In this case, we expect the dark current density to follow<sup>24</sup>:

$$J_D = qn_i WM/\tau_{\text{eff}} \quad (3.49)$$

where  $n_i$  is the intrinsic carrier concentration of Si,  $\tau_{\text{eff}}$  is the effective minority carrier recombination time,  $M$  is the carrier multiplication factor obtained by measuring photocurrent versus voltage,  $q$  is the electronic charge, and  $W$  is the depletion region width obtained from capacitance-voltage measurements. Using Eq (3.49), a good fit to the experimental data up to  $> 30 \text{ V}$  is obtained as shown by the solid line in Fig. 3.26. The deviation between the fit and the data at higher voltages is attributed to dark current generation due to other mechanisms such as carrier recombination via trap levels<sup>4</sup> at the OI interface.

The external quantum efficiency measured at several different reverse biases of the detector is shown (data points) in Fig. 3.27. A maximum external quantum efficiency ( $\eta$ ) of 85% is obtained at 650 nm at a reverse-bias of 10 V. The short wavelength cutoff in the spectral response is due to optical absorption in PTCDA. Since PTCDA has an energy gap<sup>4</sup> of 2.2 eV, it is only transparent to light with wavelength ( $\lambda$ ) larger than 0.60  $\mu\text{m}$ . The long-wavelength cutoff at  $\lambda > 1.1 \mu\text{m}$  is due to the transparency of the Si substrate to light with  $\lambda$  greater than the band-gap cutoff wavelength.

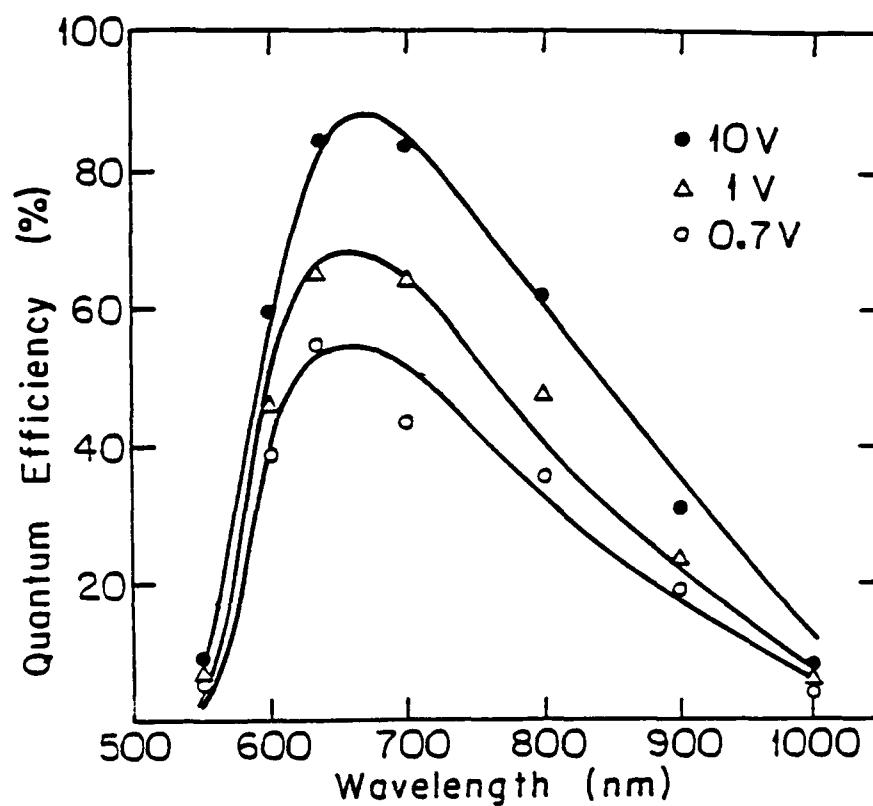


Fig. 3.27 External quantum efficiency  $\eta$  (data points) versus wavelength at different bias voltages of a PTCDA/p-Si photodetector. The solid lines show the calculated  $\eta$  following the analysis given in the text.

A theoretical fit to the experimental data is also shown (solid lines) in Fig. 3.27. In the calculation, the total photocurrent density ( $J_{ph}$ ) is assumed to consist of two components: (i) the drift current due to carriers generated within the depletion region on the Si side of the heterojunction, and (ii) the diffusion current due to carriers generated outside the depletion layer, and which subsequently diffuse into the reverse-biased junction. The strong bias dependence of  $\eta$  is due to the change of the depletion region width in response to the change in applied voltage. To calculate the contribution of carrier diffusion to the photocurrent, the diffusion depth is given by  $L_D = \sqrt{D_n \tau_n}$ , where  $D_n$  is the electron diffusion coefficient, and  $\tau_n$  is the electron lifetime. Taking the electron mobility<sup>24</sup> in Si to be  $1000 \text{ cm}^2/\text{V}\cdot\text{s}$ ,  $D_n$  is found to be  $25 \text{ cm}^2\text{s}^{-1}$  at room temperature. The electron lifetime is estimated to be 160 ns from the diffusion tail in the speed of response data (see below). Thus  $L_D$  is approximately  $20 \text{ }\mu\text{m}$ . Note that the transmittance of the stack of ITO/PTCDA/Si layers as well as the absorption<sup>4</sup> of PTCDA have also been taken into account in generating the fit. The predicted quantum efficiency is in good agreement with the experimental data at all voltages and wavelengths shown in the figure.

To determine the electric field distribution in the OI photodiode, the photoresponse was measured as a function of position around the diode area, as shown in Fig. 3.28. For this experiment, an  $8 \text{ }\mu\text{m}$  diameter,  $\lambda = 820 \text{ nm}$  light spot was scanned across the  $550 \text{ }\mu\text{m}$  diameter top ITO contact with a reverse-bias of 15 V applied to the diode. Each line in the y-direction is stepped by  $50 \text{ }\mu\text{m}$  from the adjacent line. The photoresponse is found to be uniform across the ITO window, and decreases rapidly to zero as the light spot moved away from the

contact edge. The spatial sensitivity data can be used to infer the diffusion length of electrons in the photodetector. We can assume that the distance over which the photoresponse falls to zero for a beam scanned across the diode diameter is due to a combination of the scan beam width and the diffusion length. Now, the scan beam diameter is approximately  $8\text{ }\mu\text{m}$ , and the sensitivity is found to fall to zero within approximately  $40\text{ }\mu\text{m}$  of the diode edge. Thus, we conclude that the electron diffusion length is approximately  $20 - 30\text{ }\mu\text{m}$ , which is consistent with our previous estimate made from the carrier lifetime and diffusion coefficient. From the results of this experiment, we conclude that the electric field lines, and hence the depletion region in an OI diode, are confined within the area directly underneath the contact pad.

The speed of response of the detector at 50 V reverse bias to a pulsed optical signal is shown in Fig. 3.29. Both the rise and fall times consist of a fast component followed by a slower, exponentially decaying tail. The fast rise and fall times are less than 5 ns, and the slow tail has a characteristic time of about 200 ns. The amplitude of this tail decreases with increasing voltage, suggesting that it is due to the diffusion of electrons from the undepleted Si into the reverse-biased depletion region at the heterojunction. The penetration depth<sup>59</sup> of light at 840 nm in Si is  $10\text{ }\mu\text{m}$ , which is considerably larger than the depletion width ( $3.2\text{ }\mu\text{m}$ ) at 50 V. Hence a significant fraction of carriers are expected to be generated in the undepleted region. When the light pulse is turned off, a fraction of the excess minority carriers diffuse toward the depletion region where they are collected, giving rise to the tail in the response. As the voltage is increased, the width of the depletion layer is also increased. This results in less absorption in the

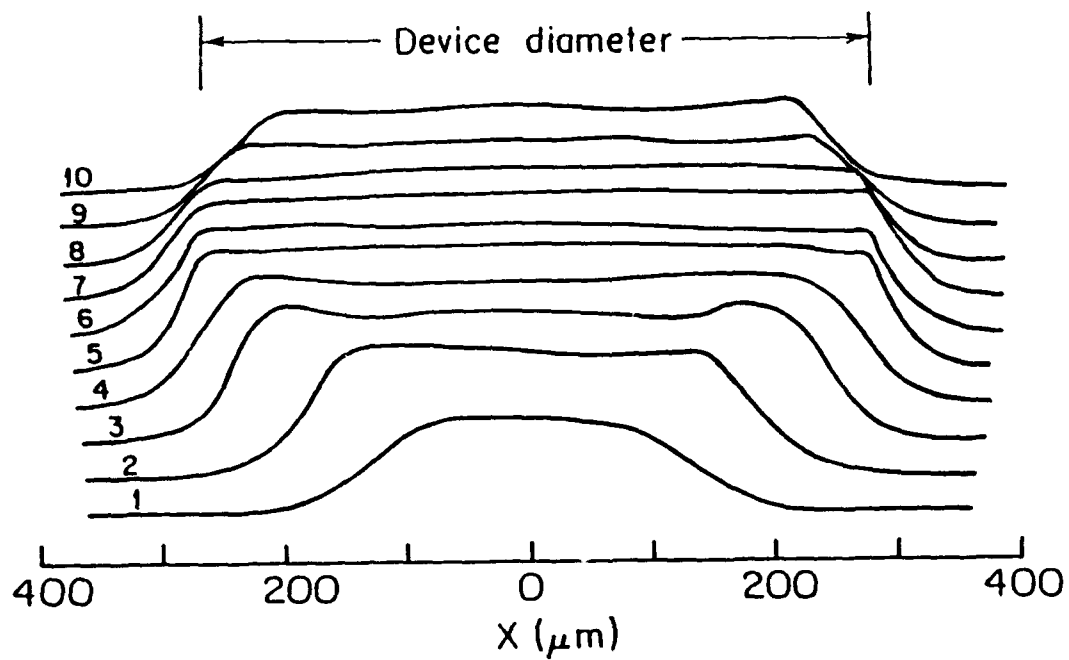


Fig. 3.28 Detector photoresponse vs position. Each line corresponds to a measurement taken in steps of  $50 \mu\text{m}$  from an adjacent line.

undepleted region, and hence a concomitant reduction of the magnitude of the diffusion tail photocurrent ( $J_{\text{diff}}$ ).

It can be shown that the contribution to the photocurrent due to diffusion is given by:

$$J_{\text{diff}} = \beta \exp(-\alpha W) \quad (3.50)$$

Here,  $\alpha$  is the absorption coefficient of Si at 840 nm, and  $\beta$  is a voltage-independent constant which depends on  $\alpha$ ,  $\tau_n$  and  $D_n$ . A plot of  $\log(J_{\text{diff}})$  versus depletion width is shown in Fig. 3.30, and the slope of the fit to the data gives an absorption coefficient of  $1130 \text{ cm}^{-1}$  which is in close agreement with the published value at 840 nm. To eliminate the diffusion tail in the PTCDA/p-Si detector, the depletion width at breakdown can be increased by decreasing the substrate doping concentration. For example, with a Si substrate carrier concentration of  $1 \times 10^{15} \text{ cm}^{-3}$ , the depletion width<sup>24</sup> at breakdown is  $15 \text{ }\mu\text{m}$ , and therefore most of the carriers would be generated within the depletion region. Alternatively, the diffusion tail can be eliminated using direct band gap semiconductors such as  $\text{In}_{0.53}\text{Ga}_{0.47}\text{As}$  where  $\alpha > 10^4 \text{ cm}^{-1}$  is typical for light of energy greater than the band gap energy of 0.75 eV.

The fast rise and fall times (5 ns) of the detector shown in Fig. 3.29 are determined by several factors. Among the contributions are :

- (i) Carrier transit time across the depletion region. For a depletion width of about  $3 \text{ }\mu\text{m}$  and reverse bias voltage of 50 V, the maximum electric field exceeds  $1 \times 10^5 \text{ V/cm}$  such that photo-generated holes reach their saturation velocity<sup>24</sup> ( $v_s$ ) of

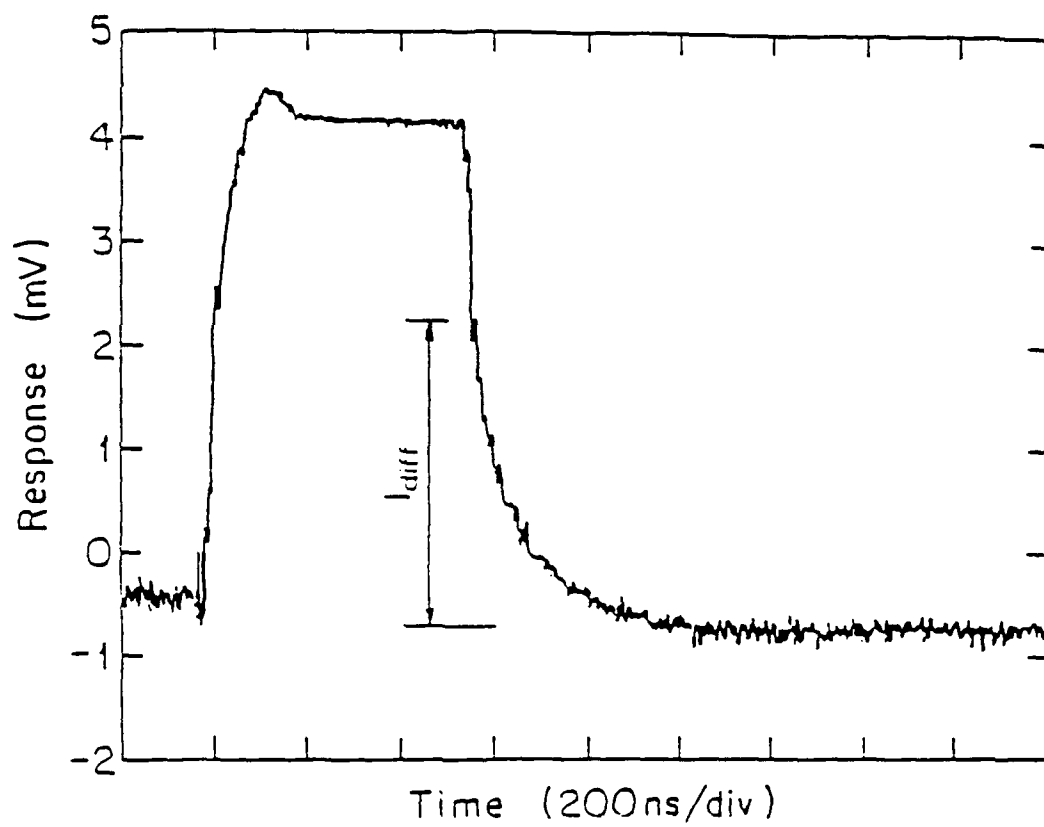


Fig. 3.29 Photocurrent vs time of the ITO/PTCDA/p-Si photodetector at 50 V reverse due to 840 nm wavelength laser pulses.



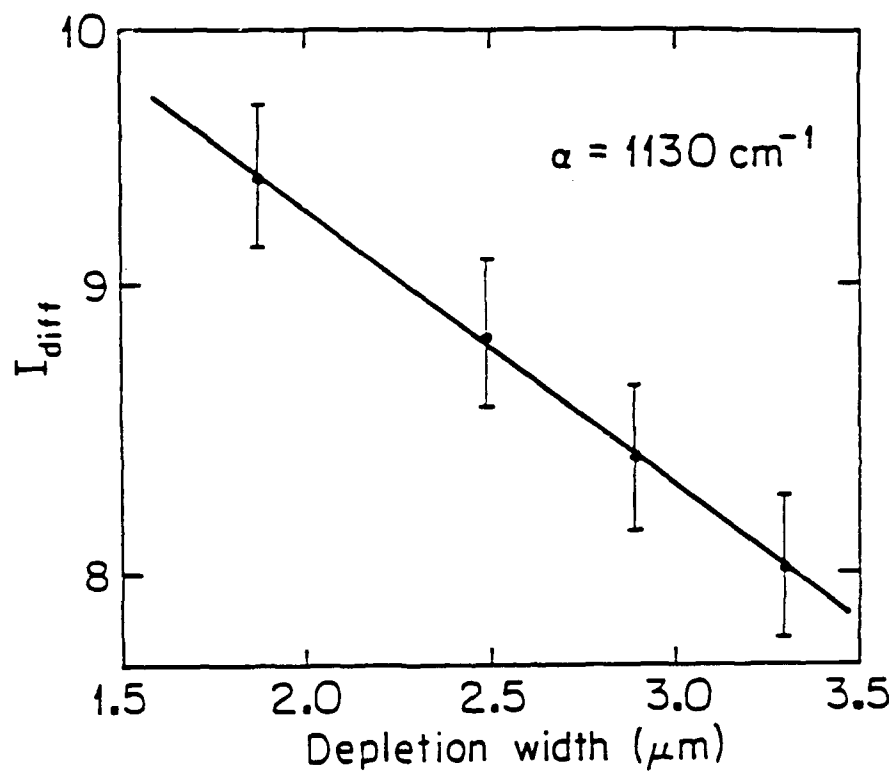


Fig. 3.30 The magnitude of the diffusion current  $I_{\text{diff}}$  in the photoresponse (see Fig. 3.29) vs the depletion layer width. The slope of the fit to the data is approximately equal to the absorption coefficient of Si at 840 nm.

$6 \times 10^6$  cm/s. Thus the transit time is  $< 100$  ps, which is too small to account for the measured 5 ns response.

(ii) RC time constant. The equivalent circuit of an OI diode<sup>4</sup> can be represented by a series combination of two parallel RC networks in series with the substrate resistance as shown in Fig. 3.31. At high frequency, the conductances are much smaller than the corresponding susceptances, and the circuit is capacitive. The total RC time constant is thus  $\tau_{RC} = RC_T$ , where  $C_T$  is the series capacitance of the organic and depletion layers,  $R$  is the sum of the load resistance of  $50 \Omega$ , and the Si substrate resistance of about  $20 \Omega$ . The permittivity<sup>4</sup> of PTCDA is  $0.37$  pF/cm, and the thin film thickness is  $1500 \text{ \AA}$ . Hence,  $C_o$  is  $55$  pF for the device area of  $2.2 \times 10^{-3} \text{ cm}^2$ . At a reverse bias of  $50 \text{ V}$ ,  $C_D$  is  $8$  pF. Therefore  $C_T = 7$  pF, giving  $\tau_{RC} = 0.5$  ns, which is significantly less than the diode fast rise and fall times.

(iii) Transit time of carriers across the organic thin film. The transit time,  $\tau_o$ , can be due to carrier drift or diffusion. The drift field in the organic film is calculated using  $E = J_{ph}/\sigma$ , where  $\sigma$  is the conductivity of the organic material. For  $J_{ph} = 0.04 \text{ Acm}^{-2}$ , the electric field [see Sec. III.2(A)] is  $1000 \text{ V/cm}$ . Taking the carrier mobility<sup>4</sup> to be  $0.1 \text{ cm}^2/\text{V-s}$ , the drift velocity is about  $100 \text{ cm/s}$ . The drift time across a film of thickness of  $1500 \text{ \AA}$  is therefore about  $150 \text{ ns}$ --a value which is too long to account for the fast rise and fall times. A final important mechanism for carrier transport across the thin film is diffusion. The electron diffusion velocity across the organic film of thickness  $d$  is  $\langle v \rangle = d/\tau_o$ , where  $\tau_o$  is the diffusion time for electrons. If we assume that the diffusion time in the organic

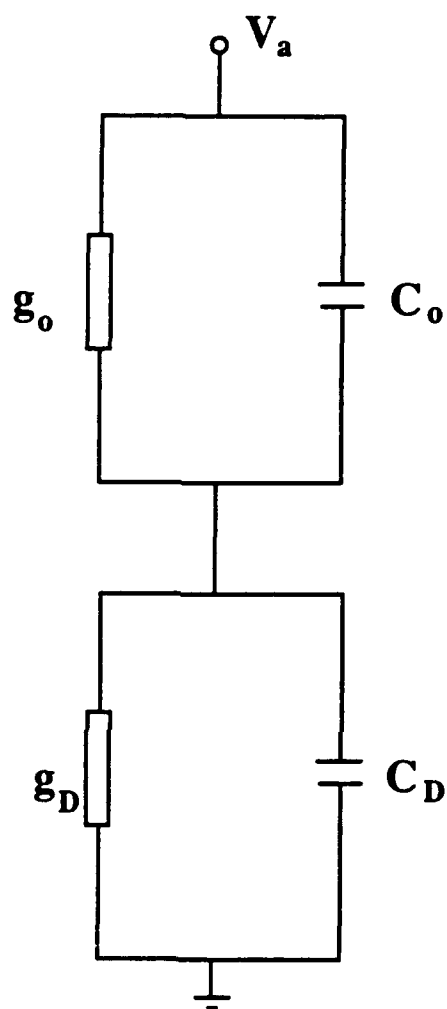


Fig. 3.31 Equivalent circuit of organic-on-inorganic (OI) devices. Here,  $g_D$  and  $g_o$  are the conductance of the depletion layer of the inorganic substrate and organic film, respectively, and  $C_D$   $C_o$  their respective capacitances.

film is limiting the fast rise and fall times, a rise time of 5 ns implies that the average carrier diffusion velocity in the organic film is 3000 cm/s.

### (C) Speed limiting factors in OI photodetectors

In order to estimate the minimum response time expected for PTCDA/p-Si detectors, the calculated dependence of the speed of response on PTCDA thickness is plotted in Fig. 3.32. Here,  $\tau_o$  and  $\tau_i$  are the transit times of carriers across the organic film and the depletion layer (of width,  $W$ ) of the inorganic semiconductor substrate respectively, and  $\tau_{RC}$  is the RC time constant. Now,  $\tau_i$  is obtained using  $\tau_i = W/v_s$ . For the figure,  $W$  is taken to be 4  $\mu\text{m}$ . Hence,  $\tau_i = 70$  ps, which is independent of the organic layer thickness,  $d$ . Recall from the discussion of  $\tau_{RC}$  above, the total capacitance decreases as the organic film thickness increases, resulting in a decrease of RC time constant. Also,  $\tau_o$  is obtained by assuming a diffusion velocity in the organic layer of 1000 cm/s. Hence,  $\tau_o$  is expected to increase linearly with the thickness of PTCDA as shown. This is clearly the dominant response speed limiting mechanism over a wide range of layer thicknesses,  $d$ . Stable and reliable OI diodes can be fabricated with an organic film thickness  $< 100 \text{ \AA}$ . Therefore, with an optimum device geometry which consists of a thin organic layer and small device area, a 3 dB roll-off frequency of higher than 1 GHz can be achieved. It is expected that the use ultra-high purity organic materials<sup>60</sup> in OI photodetectors can reduce  $\tau_o$  even further, resulting in considerable improvement in the frequency response.

One important aspect we learned about these OI detectors is that the photocurrent is only generated in the region beneath the contact pad, which is due

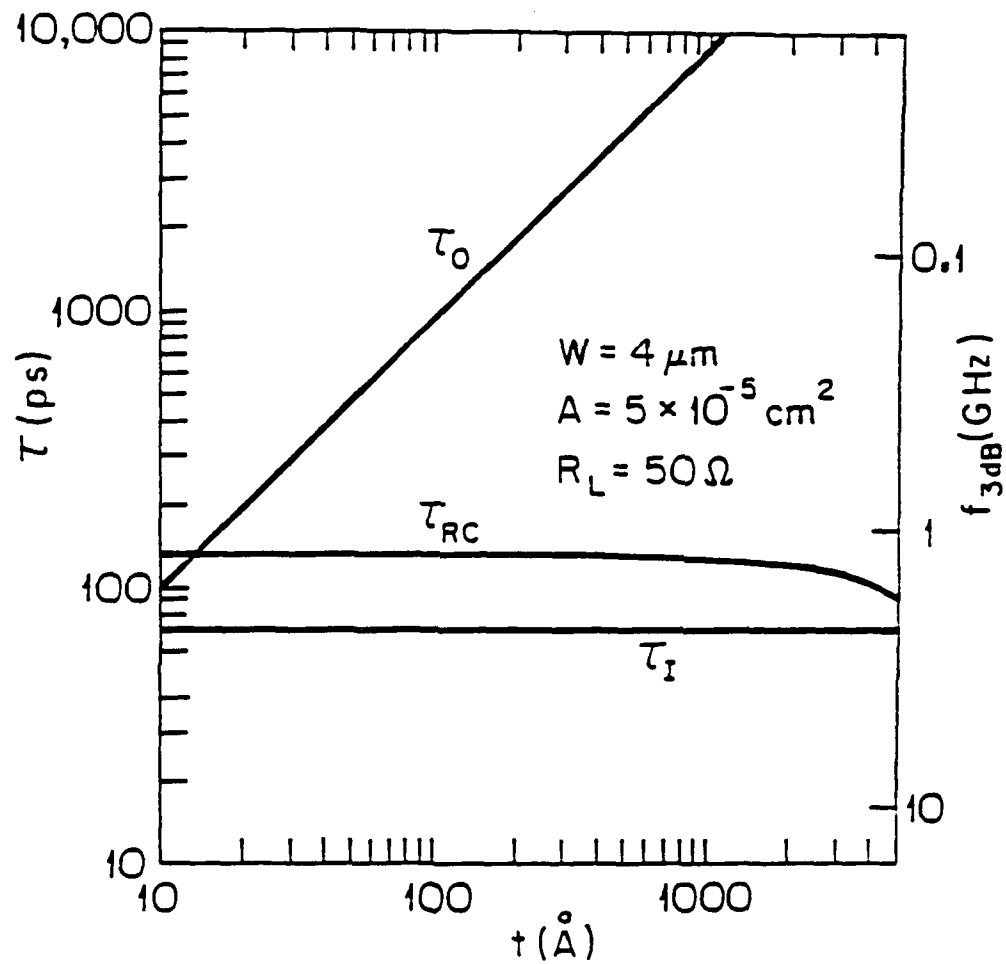


Fig. 3.32 Calculated response time vs the thickness for PTCDA film of a PTCDA/Si detector. Here,  $\tau_{RC}$  is the RC time constant, and  $\tau_0$  and  $\tau_i$  are the carrier transit times across the organic film and depletion layers, respectively.

to the large anisotropy in conductivity in PTCDA films. For highly ordered PTCDA films, the anisotropy is typically  $10^4 - 10^6$ , and the highest conductivity is perpendicular to the plane of the film. Since the field lines are uniformly distributed in the region right under the ohmic contact, there is no edge effect under large reverse bias voltages, giving rise to generally large breakdown voltages in OI devices. These properties plus the fact that OI devices can be lithographically patterned and passivated<sup>21</sup> make them very attractive to be used in various optoelectronic device applications.

## References

- <sup>1</sup> F. Capasso and G. Margaritondo, Eds., *Heterojunction Band Discontinuities: Physics and Device Applications* (North-Holland, Amsterdam, 1987).
- <sup>2</sup> R. Dingle, Ed., *Semiconductors and Semimetals*, Vol. 24 (Academic, New York, 1987)
- <sup>3</sup> G. Bastard and J.A. Brum, IEEE J. Quantum Electron. **QE-22**, 1625 (1986)
- <sup>4</sup> S.R. Forrest, M.L. Kaplan, and P.H. Schmidt, J. Appl. Phys., **55**, 1492 (1984).
- <sup>5</sup> M. Ozaki, D. Peebles, B.R. Weinberger, A.J. Heeger, and A.G. MacDiarmid, J. Appl. Phys., **51**, 4252 (1980).
- <sup>6</sup> S.R. Forrest, M.L. Kaplan, and P.H. Schmidt, J. Appl. Phys., **56**, 543 (1984).
- <sup>7</sup> P.H. Schmidt, S.R. Forrest, and M.L. Kaplan, J. Electrochem. Soc. **133**, 769 (1986)
- <sup>8</sup> S.R. Forrest, M.L. Kaplan, P.H. Schmidt, and J.M. Parsey, J. Appl. Phys., **58**, 867 (1985).
- <sup>9</sup> S.R. Forrest, M.L. Kaplan, P.H. Schmidt, and J.V. Gates, Appl. Phys. Lett. **57**, 2892 (1985)
- <sup>10</sup> S.R. Forrest, P.H. Schmidt, R.B. Wilson, and M.L. Kaplan, Appl. Phys. Lett. **45**, 1199 (1985)
- <sup>11</sup> S.J. Chang, L.Y. Leu, S.R. Forrest, and C.E. Jones, Appl. Phys. Lett. **54**, 1040 (1989)
- <sup>12</sup> F.F. So, S.R. Forrest, Y.Q. Shi, and W.H. Steier, Appl. Phys. Lett., **56**, 674 (1990).
- <sup>13</sup> F.F. So, S.R. Forrest, Y.Q. Shi, and W.H. Steier, Materials Research Society

Symposium Proceedings Vol.198, 71 (1990)

- <sup>14</sup> D.Y. Zang, F.F. So, and S.R. Forrest, Submitted to Appl. Phys. Lett.
- <sup>15</sup> D.J. William, Ed., Nonlinear Optical Properties of Organic and Polymer Materials, (Washington D.C., American Chemical Society, 1983)
- <sup>16</sup> M. Pope and C.E. Swenberg, *Electronic Processes in Organic Crystals*, (Oxford, New York, 1982)
- <sup>17</sup> C.L. Cheng, S.R. Forrest, M.L. Kaplan, P.H. Schmidt, and B. Tell, Appl. Phys. Lett., **47**, 1217 (1985)
- <sup>18</sup> J.G. Johnson, S.R. Forrest, C.R. Zeisse, and G. Nguyen, Appl. Phys. Lett. **52**, 495 (1988)
- <sup>19</sup> F.F. So and S. R. Forrest, IEEE Trans. Electron. Dev. **36**, 66 (1989)
- <sup>20</sup> D.Y. Zang, Y.Q. Shi, F.F. So, S.R. Forrest, and W.H. Steier, Appl. Phys. Lett. **58**, 562 (1991)
- <sup>21</sup> V. Prabhakar, S.R. Forrest, J.P. Lorenzo, and K. Vaccaro, IEEE Photonics Technol. Lett., **2**, 724 (1990)
- <sup>22</sup> B.R. Bennet, J.P. Lorenzo, K. Vaccaro, and A. Davis, J. Electrochem. Soc. **134**, 2517 (1987)
- <sup>23</sup> S.R. Forrest, M.L. Kaplan, P.H. Schmidt, T. Venkatesan, and A.J. Lovinger, Appl. Phys. Lett., **41**, 708 (1982)
- <sup>24</sup> S.M. Sze, Physics of Semiconductor Devices, 2nd Ed., (Wiley, New York, 1981)
- <sup>25</sup> S.R. Forrest, M.L. Kaplan, and P.H. Schmidt, Ann. Rev. Mater. Sci., **17**, 189 (1987)
- <sup>26</sup> S. A. Silinsh, *Organic Molecular Crystals*, (Springer-Verlag, New York,



1980).

- <sup>27</sup> S.R. Forrest and P.H. Schmidt, J. Appl. Phys. **59**, 523 (1986)
- <sup>28</sup> S.R. Forrest, M.L. Kaplan, and P.H. Schmidt, J. Appl. Phys. **60**, 2406 (1986)
- <sup>29</sup> M. Lampert and P. Mark, *Current Injection in Solids*, (Academic, New York, 1970)
- <sup>30</sup> C.R. Crowell and M. Beguwala, Solid-state Electron., **14**, 1149 (1971)
- <sup>31</sup> F.F. So and S.R. Forrest, Appl. Phys. Lett. **52**, 1341 (1988)
- <sup>32</sup> C.R. Crowell, W.G. Spitzer, L.E. Howarth, and E.E. LaBate, Phys. Rev., **127**, 2006 (1962)
- <sup>33</sup> M.A. Haase, M.A. Emanuel, S.C. Smith, J.J. Coleman, and G.E. Stillman, Appl. Phys. Lett., **50**, 404 (1987)
- <sup>34</sup> R.H. Fowler, Phys. Rev. **38**, 45 (1931)
- <sup>35</sup> P. Devaux and P. Quedec, Phys. Lett. **28A**, 537 (1969)
- <sup>36</sup> F.F. So and S.R. Forrest, J. Appl. Phys. **63**, 442 (1988)
- <sup>37</sup> A.G. Milnes, *Deep Impurities in Semiconductors* (Wiley, New York, 1973)
- <sup>38</sup> W. Warta, R. Stehle, and N. Karl, Appl. Phys. **A36**, 163 (1985)
- <sup>39</sup> W. Warta and N. Karl, Phys. Rev. **B32**, 1772 (1985)
- <sup>40</sup> This is known as Dawson's integral; see M. Abramowitz and I Stegun, *Handbook of Mathematical Functions* (Dover, New York, 1965), pp. 298.
- <sup>41</sup> C. Barret and A. Vapaille, J. Appl. Phys. **50**, 4217 (1979).
- <sup>42</sup> C. Barret, F. Chekir, and A. Vapille, J. Phys. C **16**, 2421 (1983)
- <sup>43</sup> F. Gutman and L.E. Lyons, *Organic Semiconductors* (Wiley, New York, 1967).
- <sup>44</sup> J.M. Andrews and J.C. Phillips, Phys. Rev. Lett. **35**, 56 (1975)

- <sup>45</sup> W.E. Spicer, I. Lindau, P. Skeath, C.Y. Su, and P. Chye, Phys. Rev. Lett. **44**, 420 (1980)
- <sup>46</sup> M. Ozaki, D. Peebles, B.R. Weinberger, A.J. Heeger, and A.G. MacDiarmid, J. Appl. Phys. **51**, 4252 (1980)
- <sup>47</sup> C.W. Tang, Appl. Phys. Lett. **48**, 183 (1986)
- <sup>48</sup> R.O. Loutfy, J.H. Sharp, C.K. Hsiao, and R. Ho, J. Appl. Phys. **52**, 548 (1981)
- <sup>49</sup> H.C. Card and E.H. Rhoderick, J. Phys. D **4**, 1589 (1971)
- <sup>50</sup> H.C. Card and E.H. Rhoderick, J. Phys. D **4**, 1602 (1971)
- <sup>51</sup> S.E. Harrison and J.M. Assour, J. Chem. Phys. **40**, 365 (1964)
- <sup>52</sup> N. Yamamoto, S. Tonomura, and H. Tsubomura, J. Appl. Phys. **52**, 5705 (1981)
- <sup>53</sup> F.R. Fan and L.R. Faulkner, J. Chem. Phys. **69**, 3334 (1978)
- <sup>54</sup> F.R. Fan and L.R. Faulkner, J. Chem. Phys. **69**, 3341 (1978)
- <sup>55</sup> R. Rahimi and H.K. Henisch, Appl. Phys. Lett. **38**, 896 (1981)
- <sup>56</sup> H.K. Henisch, *Semiconductor Contacts*, (Oxford, New York, 1984)
- <sup>57</sup> J. Maserjian and N. Zamani, J. Appl. Phys. **53**, 559 (1982)
- <sup>58</sup> S.K. Lai, Electrochem. Soc. Proc. **81-5**, 416 (1981)
- <sup>59</sup> E.D. Palik, *Handbook of Optical Constants of Solids*, (Orlando, FL, Academic, 1985, pp.547)
- <sup>60</sup> W. Warta, R. Stehle, and N. Karl, Appl. Phys. A **36**, 163 (1985)

## Chapter IV

### Crystalline Organic Semiconductor Heterojunctions

#### IV.1 Introduction

Semiconductor heterojunctions (HJs) provide many unique and useful functions for optoelectronic device applications. Among HJ devices, examples include field-effect and bipolar transistors, lasers, photodetectors and a wide range of devices based on multiple quantum wells.<sup>1,2</sup> Although the characteristics of single HJs depend on the properties of the contacting semiconductor materials, the diversity of these characteristics has been limited by requiring that the contacting materials be lattice-matched. If this condition is ignored, strains induced between crystalline layers are relieved by inducing dislocations or other imperfections which, if present in high densities, degrade both the optical and electronic properties of the HJ device.

On the other hand, organic molecular crystals are bonded by relatively weak van der Waals forces between adjacent molecules.<sup>3,4</sup> Hence, provided that it is possible to fabricate high quality heterojunctions consisting of one or more crystalline organic materials, one would not expect there to be large strains induced between layers.<sup>5,6</sup> Recently, highly mismatched layers of dichalcogenide films<sup>7,8</sup> as well as crystalline organic thin films<sup>9,10,11</sup> have been grown in a van der Waals- (or quasi-) epitaxial structure onto a variety of substrate materials by molecular beam epitaxy, indicating that van der Waals bonds are sufficiently

flexible to allow lattice-mismatched combinations to form epitaxial structures without inducing a high density of defects. Thus, organic heterojunctions also provide a means for relaxing the strict requirements of lattice-matching which currently underlies HJ growth.

Of perhaps deeper significance is the role that fully organic HJs can play in our developing a more complete, fundamental understanding of semiconductor contacts in general. At present, there is considerable controversy surrounding the models used to predict band offsets at inorganic HJs. In particular, the role that charge redistribution plays in determining the offset energy at inorganic semiconductor HJs is as yet unresolved.<sup>12</sup> Since the carrier wavefunctions in organic semiconductors are localized over only a few adjacent molecules, in such systems there can be no significant charge transfer effects which determine band offset energies. Hence, if we can identify suitable crystalline organic compounds which do not contain a high density of electronic defects, these materials combinations can provide simplified systems which might be studied to select between various HJ theories.

Recently, several organic heterojunction devices have been investigated. Harima, et al.<sup>13</sup> reported on a p-n junction photovoltaic cell consisting of Au/ZnPc (500 Å)/TPyP (400 Å)/Al in which ZnPc (zinc phthalocyanine) is p-type, and TPyP [5,10,15,20-tetra (3-pyridyl) porphyrin] is n-type. They observed a better spectral match to the solar spectrum than corresponding, single-layer Schottky-type cells. Tang<sup>14</sup> reported a two-layer, fully crystalline organic photovoltaic cell composed of CuPc (copper phthalocyanine) and PTCBI (3,4,9,10 perylenetetracarboxylic-bis-benzimidazole) in which a relatively large

fill factor and power conversion efficiency were observed. Most recently, organic heterojunction electroluminescent devices have also been reported by several authors.<sup>15,16,17</sup> In particular, Adachi, et al.<sup>18</sup> have fabricated organic electroluminescence devices consisting of an electron transport layer (a triphenylamine derivative), a hole transport layer (an oxadiazole derivative) and an emitting layer. These devices showed an enhancement in emission efficiency due charge carrier confinement in the emitting layer. Although new crystalline organic devices have been fabricated and reported, no thorough studies on charge transport across organic heterojunctions have yet been made.

In this chapter, we study the optical and electronic properties of a p-P, isotype CuPc/PTCDA (3,4,9,10 perylenetetracarboxylic dianhydride) HJ. CuPc is well known as a p-type semiconductor whose electrical characteristics are controlled by traps exponentially distributed within the bandgap.<sup>19,20</sup> PTCDA is also p-type.<sup>5</sup> No evidence has been found for a high density of traps in this latter material. From the electrical characteristics of this HJ, we find that the charge transport across the organic heterobarrier can be understood in terms of transport theory used to describe the behavior of inorganic heterojunctions. In particular, the energy difference between the valence-like bands of both organic materials has been measured, and we find that hole transport is limited by thermionic emission over this barrier, similar to that in inorganic semiconductor heterojunctions. Furthermore, band offsets between these materials and PTCBI are reported, with the result that the offset energies in this system of three HJs follow a transitive relationship.<sup>21</sup>

This chapter is organized as follows: In Sec. IV.2, we discuss the organic heterojunction preparation and device fabrication, and in Sec. IV.3 we present the current, capacitance and photoresponse-versus-voltage characteristics of the organic semiconductor heterojunctions. These data are analyzed using the charge transport theory for inorganic HJs. We develop an energy band picture for these novel organic devices in Sec. IV.4. In Sec. IV.5, we will review various charge transport models for organic molecular crystals, and then discuss the validity of the band picture used organic HJs. Finally, a summary and the significance of this work is presented in Sec. IV.6.

#### IV.2 Material Preparation and Device Fabrication

The molecular structural formulae for CuPc, PTCDA and PTCBI are shown in Fig. 4.1. Both CuPc and PTCDA were obtained commercially<sup>22</sup>, and were purified by temperature gradient sublimation in vacuum for 3 days prior to use in diode structures.<sup>23</sup> On the other hand, PTCBI was synthesized from PTCDA and o-phenylenediamine.<sup>24</sup> Details of organic material purification and synthesis have been discussed in Chapter 2.

To fabricate organic heterojunction devices, it was necessary to identify appropriate materials useful in forming ohmic contacts to the organic thin films. For this purpose, symmetrical metal (or ITO)/organic/metal thin film devices were fabricated by vacuum deposition on a glass substrate. Only those materials which exhibited linear current-voltage characteristics over a range of at least  $-0.2 \text{ V} < V < 0.2 \text{ V}$  with specific resistance less  $5 \times 10^{-3} \Omega\text{-cm}^2$  were used as for ohmic contacts in this work. Based on the results of the testing described above, it

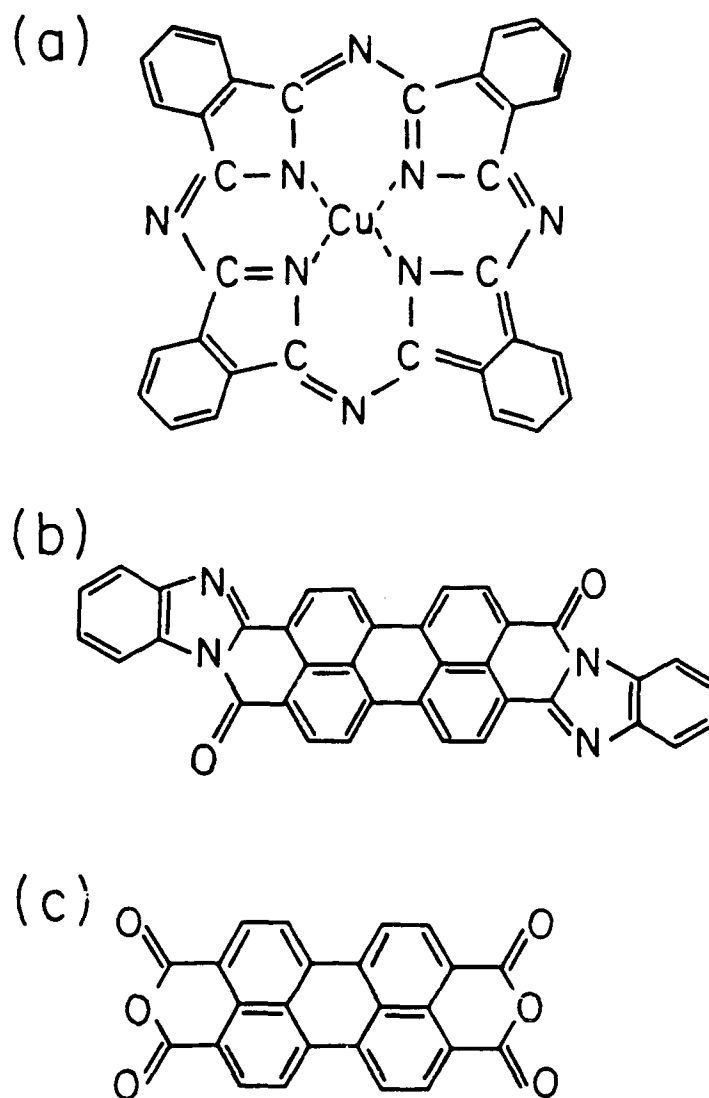


Fig. 4.1 Structural molecular formulae for (a) CuPc, (b) PTCBI, and (c) PTCDA.

was found that CuPc and PTCDA form an ohmic contact to ITO, PTCDA forms an ohmic contact to In, and Ag is used with PTCBI. Thus, in fabricating a typical CuPc/PTCDA HJ structure, 100 Å - 800 Å CuPc was first deposited at room temperature in at  $10^{-6}$  Torr at a rate of 5 - 10 Å/s onto a transparent, ITO-coated glass substrate. This was followed by room temperature deposition of approximately the same thickness of PTCDA on the top of the CuPc film. Before the deposition of the PTCDA layer, the CuPc film was exposed to air for approximately 30 minutes. The deposition rate of the PTCDA was also 5 - 10 Å/s. Top contact was made to the PTCDA film by deposition of In through a shadow mask. An analogous procedure was used in fabricating CuPc/PTCBI and PTCDA/PTCBI HJs.

#### IV.3 Results

Since CuPc and PTCDA make ohmic contacts with the ITO and In electrodes respectively, we infer that the rectification shown in the bipolar current-voltage (J-V) characteristics (solid line) in Fig. 4.2 is due to the energy barrier at the junction between the CuPc and PTCDA layers. For this  $5.7 \times 10^{-4}$  cm<sup>2</sup> device, which consists of 350 Å PTCDA deposited on top of 250 Å of CuPc, forward bias is achieved when the PTCDA is negative with respect to the CuPc layer.

Breakdown under reverse bias varies from -0.5 V to -5 V across a wafer. Here, all bias polarities are referred to the ITO contact. Furthermore, the forward characteristics begin to degrade (i.e. series resistance increases) after 5-10 hours in room atmosphere. The rectification effect observed in Fig. 4.2 is due to the



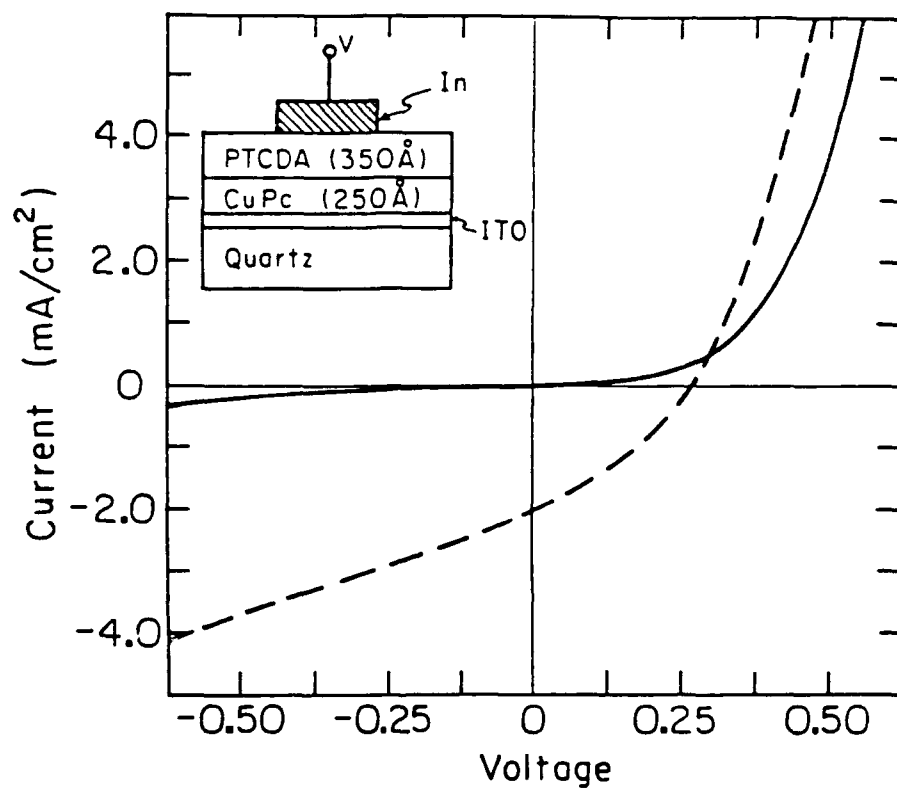


Fig. 4.2 Dark current versus voltage characteristics (solid line) of an ITO/CuPc/PTCDA/In heterojunction shown schematically in the inset. Also shown are the characteristics under white light illumination (dashed line).

doping of the CuPc in the HJ region by exposure to oxygen during the deposition process (Sec. IV.2). It has been widely observed, both in our studies and elsewhere<sup>25,26,27</sup>, that CuPc which has not been O<sub>2</sub>-doped is highly insulating. Hence, we speculate that the increase in series resistance with time is due to the slow diffusion of the O<sub>2</sub> away from the heterointerface and into the bulk PTCDA and CuPc films. An analogous increase in film resistivity has been observed in CuPc films which are returned to a vacuum environment after previously having been doped.<sup>40</sup> An alternative explanation is that the increased resistance may be a result of moisture being absorbed into the CuPc near the heterointerface. Also shown in the figure are the J-V characteristics under white light illumination (dashed line) with a power density of approximately 10 mW/cm<sup>2</sup>. Under reverse bias, the responsivity increases approximately linearly with voltage. As will be shown below, this is due to increased carrier collection efficiency for carriers generated in the CuPc. That is, the depletion region width in the CuPc layer increases with reverse bias. Under forward bias there is a small photovoltaic effect, with the HJ having a short circuit current of  $J_{sc} = 2.0 \text{ mA/cm}^2$ , and an open circuit voltage of  $V_{oc} = 260 \text{ mV}$ . The fill-factor for this device is only 0.35, and is limited by the high series resistance and poor collection efficiency of the forward-biased CuPc. We are uncertain as to why the photocurrent in the forward-biased diode results in an increased current at  $J > 400 \text{ } \mu\text{A/cm}^2$ . One possible explanation is that the energy barrier at the CuPc/PTCDA heterojunction is reduced under illumination as a result of the accumulation of a high density of photogenerated charge in this region, or from the large series resistance in the

film bulk (see below). Series resistance would tend to decrease the relative voltage drop across the HJ as the current is increased due to illumination.

To understand these J-V characteristics in greater detail, both the forward and reverse-biased characteristics as a function of temperature are shown in Fig. 4.3 and Fig. 4.4, respectively. The symmetry of these curves suggests that the energy barrier in the heterointerface region between CuPc and PTCDA is similar to that shown in Fig. 4.5(a). Here, the "band gaps" of CuPc and PTCDA are 1.7 eV and 2.2 eV, respectively.<sup>5,28</sup> This band gap refers to the minimum energy difference between the highest occupied and lowest unoccupied molecular orbitals (i.e. HOMO and LUMO, respectively). Since both CuPc and PTCDA are p-type materials, current flow is limited in this region by thermionic emission of holes over the valence band discontinuity energy barrier of height  $\Delta E_v$ . Within the bulk of the two material layers, charge transport is largely determined by series resistance. We note, however, that care must be taken in the interpretation of band diagrams as those shown in Fig. 4.5 since the analogy between molecular and inorganic semiconductors might not be a rigorous one in all cases, as will be discussed in Sec. IV.5. Assuming the charge transport in the organic materials used in this work can be described by the band theory used in inorganic semiconductors, and there are no interface states at the HJ (which may not be rigorously true in all cases), following the treatment of Chang,<sup>29</sup> then continuity of the electric displacement across the heterojunction implies that the current density is given by:

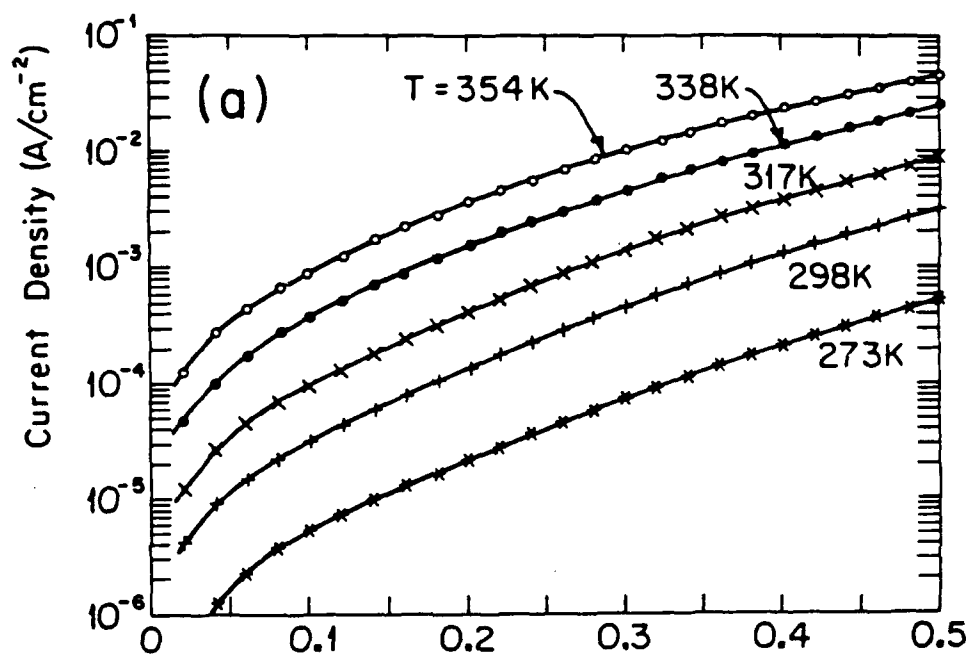


Fig. 4.3 Current-voltage characteristics versus temperature of a CuPc/PTCDA heterojunction under forward bias.

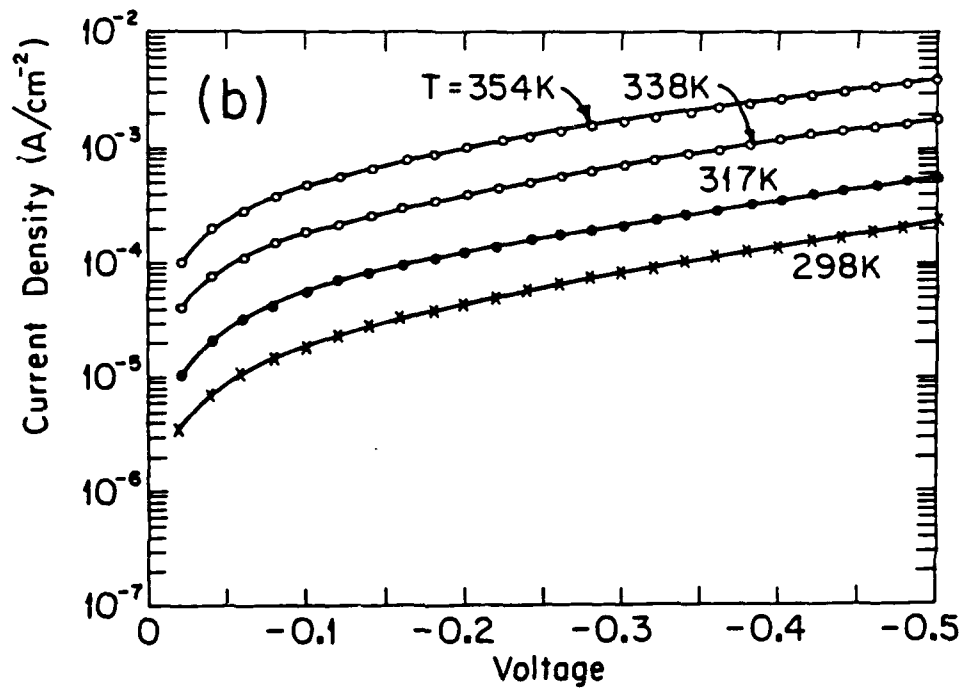


Fig. 4.4 Current-voltage characteristics versus temperature of the same device as in Fig. 4.3 under reverse bias.

$$J = qN_{A2}(kT/2\pi m_2^*)^{1/2} \exp(-qV_{D2}/kT) \\ \times [\exp(qV_2/kT) - \exp(-qV_1/kT)] \quad (4.1a)$$

or

$$J = J_s [\exp(qV_2/kT) - \exp(-qV_1/kT)] \quad (4.1b)$$

Here, variables with subscripts 1 and 2 refer to PTCDA and CuPc, respectively. Further,  $q$  is the electronic charge,  $kT$  is the Boltzmann energy at temperature  $T$ ,  $m^*$  is the effective hole mass,  $N_A$  is the density of acceptors in the HOMO band,  $V_{D2}$  is the diffusion potential on the CuPc side of the heterobarrier, and  $V_i$  ( $i = 1, 2$ ) is the voltage component dropped across the two sides of the HJ. The relationship between  $\Delta E_v$ ,  $V_{D1}$  and  $V_{D2}$  is given by:

$$\Delta E_v = qV_{D1} + qV_{D2} + kT \log(N_{A1}N_{v2}/N_{A2}N_{v1}), \quad (4.2)$$

where  $N_v$  is the effective density of states at the HOMO band edge. From Eq. (4.5) it is apparent that the J-V characteristics do not saturate under either forward or reverse bias since the applied potential decreases the energy barrier in both cases. However, due to the asymmetry of the charge distribution at the HJ, the division of the applied voltage between  $V_1$  and  $V_2$  results in a concomitant asymmetry in the J-V characteristics. It can be shown that the relationship between  $V_1$  and  $V_2$  is given by:<sup>29</sup>

$$\epsilon_1 N_{A1} / \epsilon_2 N_{A2} = \\ \frac{V_{D2} - V_2}{\frac{kT}{q} [\exp(q(V_{D1} - V_1)/kT) - 1] - (V_{D1} - V_1)} \quad (4.3)$$

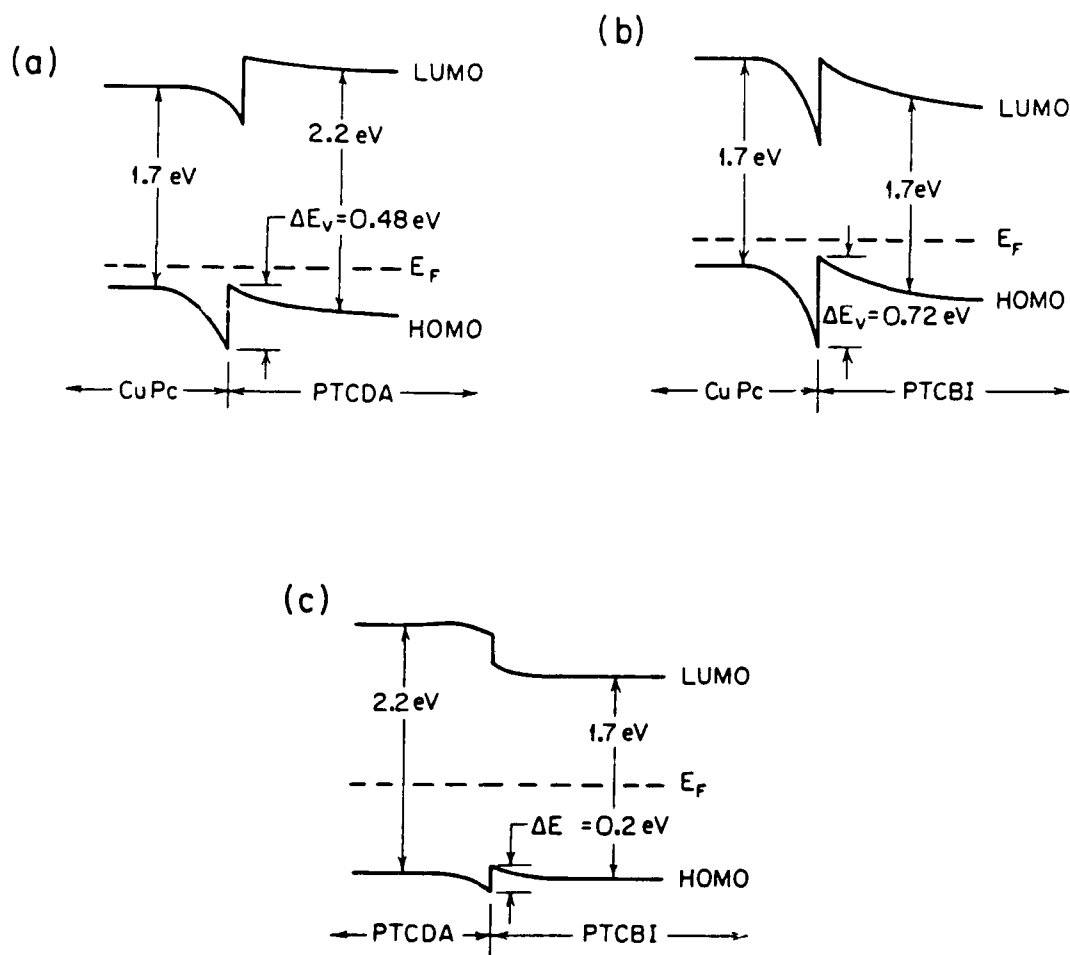


Fig. 4.5 Proposed energy band diagrams for p-P heterojunctions consisting of (a) CuPc/PTCDA, (b) CuPc/PTCBI, and (c) PTCDA/PTCBI.

where  $\epsilon$  is the semiconductor dielectric constant.

To obtain the relationship between the applied voltage ( $V_a$ ) and  $V_i$ , we need to calculate the voltage dropped across the bulks of materials 1 and 2 by a simultaneous solution of Eq. (4.1) and:

$$J = V_R / AR_s \quad (4.4).$$

Here,  $A$  is the diode area,  $V_R$  is the total voltage dropped across the bulk layers, and  $R_s$  is the total series resistance of the two layers. Further:

$$V_a = V_1 + V_2 + V_R, \quad (4.5)$$

where  $V_a$  is the applied voltage.

Charge transport across heterobarriers cannot, in general, be adequately modelled by assuming only thermionic emission. Indeed, past work on inorganic HJs has shown that both image-induced barrier lowering and tunneling<sup>29</sup> can lead to significant departures from Eq. (4.5). To account for these other transport processes, it is convenient to introduce the  $n$ -value, such that in forward bias we can rewrite Eq. (4.5) as:

$$J_F = BT^{1/2} \exp(-qV_{D2}/kT) [\exp(q(V_a - V_1 - R_sAJ_F)/nkT)] \quad (4.6)$$

where  $B^2 = q^2 N_{A2}^2 k^2 / 2\pi m_2^*$ . Examination of Eqs. (4.1) and (4.6) indicates that the current density under both forward and reverse bias (as  $V_2 \rightarrow 0$ ) is thermally activated with energy  $qV_{D2}$ .

In Fig. 4.6,  $J_s$  is plotted versus  $1/T$  for a CuPc/PTCDA device, where the values of  $J_s$  are obtained by extrapolation of the reverse and forward-biased data in Fig. 4.6 to 0 V. The slopes (and hence activation energies) obtained under



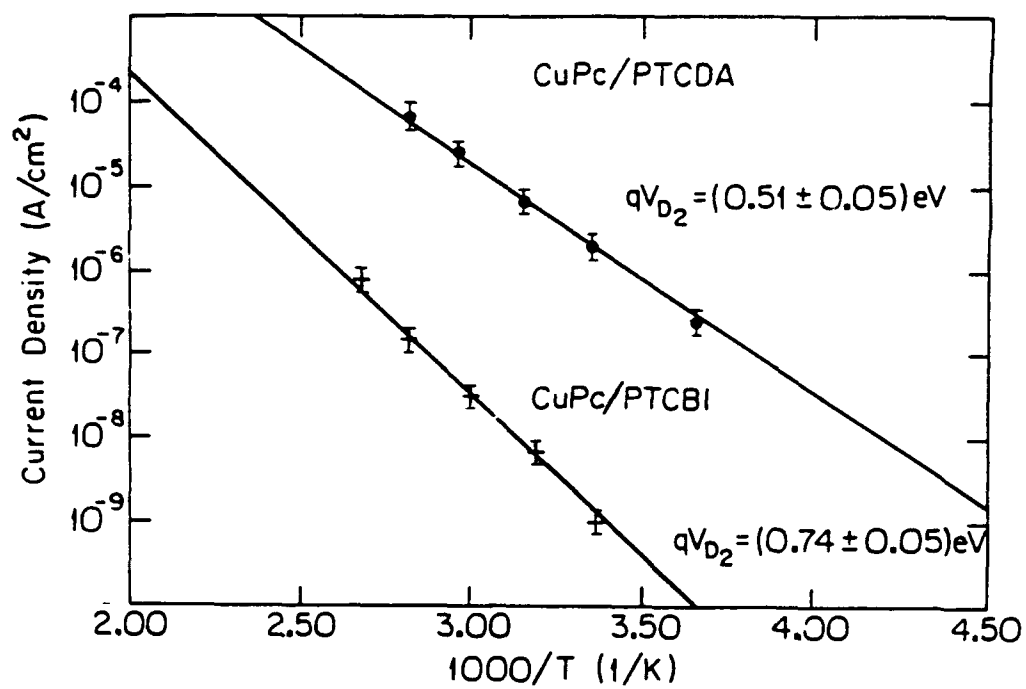


Fig. 4.6 Activation energy plot of the saturation current density ( $J_s$ ) for CuPc/PTCDA and CuPc/PTCBI heterojunctions.

both bias directions are the same, yielding  $V_{D2} = (0.51 \pm 0.05) \text{ V}$ . As will be shown below,  $N_{A1} = 7 \times 10^{17} \text{ cm}^{-3} \gg N_{A2} = 5 \times 10^{14} \text{ cm}^{-3}$ . In this case, using Eq. (4.3) we obtain  $V_{D1} = 0.01 \text{ V}$  or,  $V_D = V_{D1} + V_{D2} = (0.52 \pm 0.05) \text{ V}$ .

From a fit to the forward-biased characteristics, we obtain  $n = (1.5 \pm 0.4)$  at  $T = 273 \text{ K}$ . Note that due to the large curvature in the J-V characteristics near  $V_a = 0$  (Figs. 4.3 and 4.4), there is considerable inaccuracy in our estimate of  $n$ . Nevertheless, since  $n > 1$ , this indicates that processes other than thermionic emission are, in part, responsible for charge transport in the HJ region. Finally, from both plots in Figs. 4.3 and 4.4, we infer  $R_s A = (2.0 \pm 0.2) \times 10^2 \Omega\text{-cm}^2$ . If we assume that  $A$  is determined by the metal dot contact area of  $5.7 \times 10^{-4} \text{ cm}^2$ , we obtain a total series resistance of  $R_s = 350 \text{ k}\Omega$ . This high resistance, which gives rise to the short exponential region in the J-V data, has been confirmed by direct measurement of the conductance at a measurement frequency of  $1 \text{ kHz}$  using an HP4194 impedance analyzer, where it was found that  $R_s$  ranged between  $200 \text{ k}\Omega$  and  $400 \text{ k}\Omega$ , depending on how long the sample was exposed to the laboratory environment. This resistance is too large to be due to the bulk resistivity of PTCDA (which typically has a mobility of  $0.1 \text{ cm}^2/\text{V-s}$  and a hole density of  $5 \times 10^{14} \text{ cm}^{-3}$ ). On the other hand, polycrystalline CuPc (thin films of CuPc are expected to be polycrystalline under the deposition condition used) has a mobility of  $\sim 10^{-3} \text{ cm}^2/\text{V-s}$ .<sup>29</sup> Taking an equilibrium hole concentration in the CuPc bulk of  $10^{14} \text{ cm}^{-3}$ , a  $250 \text{ \AA}$  thick CuPc film has a resistance of roughly  $200 \text{ k}\Omega$ , which is reasonably close to observation.

The capacitance-voltage (C-V) characteristics (measured at  $1 \text{ kHz}$ ) of a reverse-biased HJ is shown in Fig. 4.7, where  $1/C^2$  is plotted versus  $V_a$ . Due to

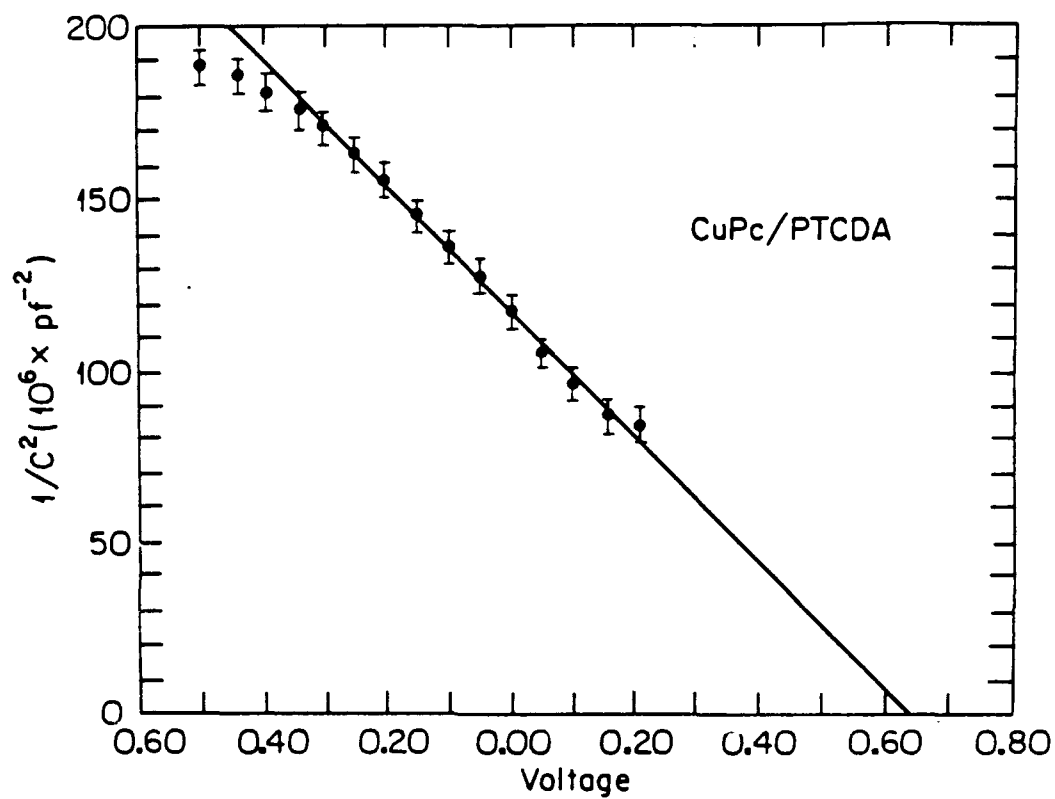


Fig. 4.7 Capacitance (plotted as  $1/C^2$ ) versus voltage for a CuPc/PTCDA heterojunction.

the low carrier concentration ( $\sim 5 \times 10^{14} \text{ cm}^{-3}$ ) of PTCDA this thin layer is completely depleted even at 0 V. Thus, the voltage dependence of the capacitance arises from depletion of holes from the CuPc layer. When measured as a function of frequency ( $f$ ), we find that  $C$  decreases rapidly at  $f \geq 10 \text{ kHz}$ . This indicates that the free hole density in CuPc arises from thermal excitation of carriers from deep traps with applied voltage. As the measurement frequency increases, the holes are unable to respond to changes in the Fermi level induced by the a.c. voltage, and hence are not observed. This phenomenon of hole trapping at deep levels exponentially distributed within the energy gap has been widely observed for CuPc.<sup>19</sup> From the linear relationship between  $1/C^2$  and  $V_a$ , and assuming a dielectric constant of  $\epsilon = 3.5$  typical of CuPc, we obtain a hole trap concentration of  $N_{A1} = 7 \times 10^{17} \text{ cm}^{-3}$  for CuPc, consistent with measurements reported elsewhere for Pc thin films.<sup>30</sup> These traps provide a "reservoir" for holes which become free once the Fermi energy is raised above the deep ( $\text{O}_2$  induced) hole trap energy as the reverse bias is increased.

We note that although large series resistances such as observed for our sample can systematically affect the values obtained<sup>31</sup> for  $C$ , we estimate that this effect causes no more than a 2% error at  $f = 1 \text{ kHz}$ . This is well within the other sources of error (such as in the determination of diode area) encountered in the experiment.

The intercept of the straight line extrapolated to  $1/C^2 = 0$  is equal to  $nV_{D2} = (0.65 \pm 0.05) \text{ V}$ . Taking  $n = 1.5$ , we obtain  $V_{D2} = (0.45 \pm 0.15) \text{ V}$ , which is consistent with  $V_{D2}$  inferred from the  $I$ - $V$  data.

In Figure 4.8 we plot the reverse-biased photocurrent as a function of wavelength for several voltages. Light was incident on the sample through the ITO window. Also shown at the bottom are the excitonic absorption band regions of CuPc and PTCDA. It is clear that light absorption and subsequent free carrier generation occurs in both the CuPc and PTCDA layers, although only the carrier collection efficiency in the CuPc layer is influenced by the applied voltage. For reference, the absorption spectra of bulk PTCDA and CuPc, and of the CuPc/PTCDA HJ (also illuminated via the CuPc) are shown in Fig. 4.9. Taking the relative absorption spectra of PTCDA and CuPc as  $A_p(\lambda)$  and  $A_c(\lambda)$ , respectively, then the PTCDA layer transmission is given by  $T_p(\lambda) = 1 - A_p(\lambda)$ , with a similar expression for CuPc. Provided that the HJ sample contains no new spectroscopic features than those obtained in the two bulk constituents, we should thus expect the HJ absorption spectrum to follow

$$A_{HJ}(\lambda) = 1 - T_p(\lambda)T_c(\lambda). \quad (4.7)$$

Indeed, this is found to be the case as shown by the dashed line in Fig. 4.9, which fits the observed spectrum over the wavelength range of  $290 < \lambda < 820$  nm. Also labelled in the figure are the singlet transitions for the two materials. Thus,  $P_{0,0}$  refers to transitions in PTCDA between the lowest crystalline singlet vibronic (or exciton) ground and first excited states, whereas  $P_{0,1}$  is a transition from the ground state to the second excited vibronic state, etc. More discussion of this will be given in Sec. IV.4. In these data, transitions  $P_{0,1}$  and  $P_{0,2}$  are not resolved, although we have found them to be clearly apparent in other more detailed spectral studies of PTCDA.

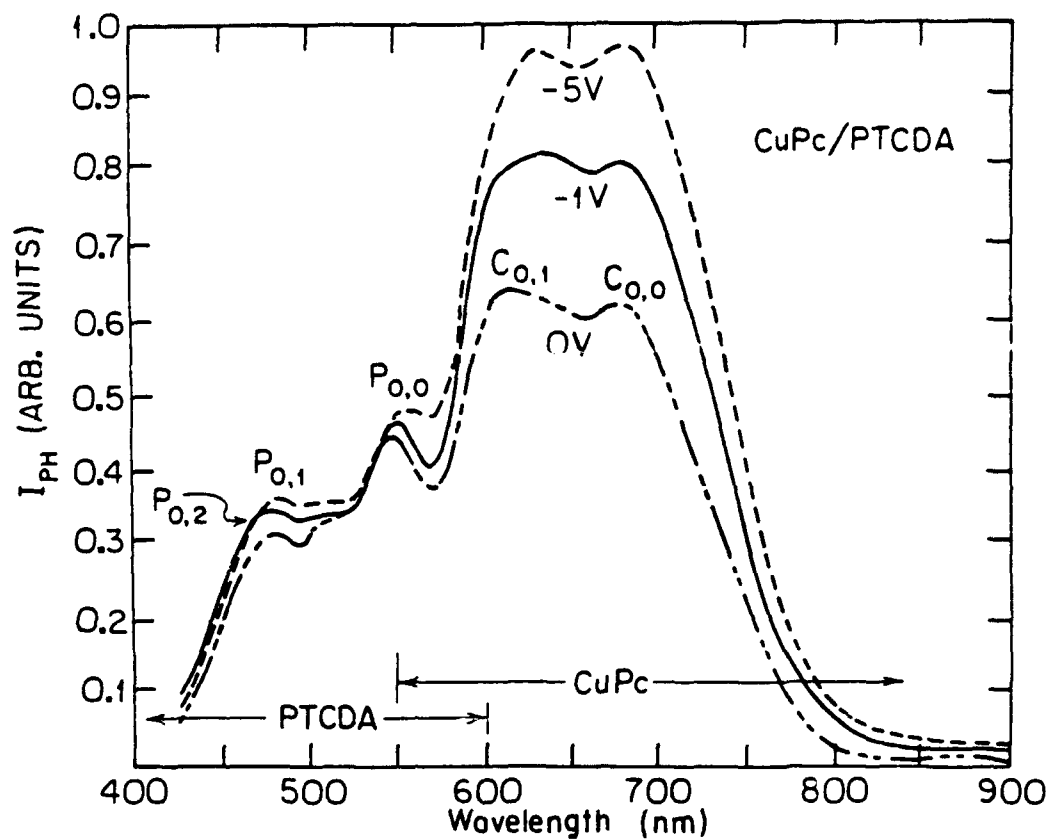


Fig. 4.8 The photocurrent spectra measured as a function of reverse voltage of CuPc/PTCDA heterojunction diodes. The various peaks labeled  $P_{0,0}$ ,  $P_{0,1}$ , etc. correspond to peaks in the absorption spectra shown in Fig.4.9.

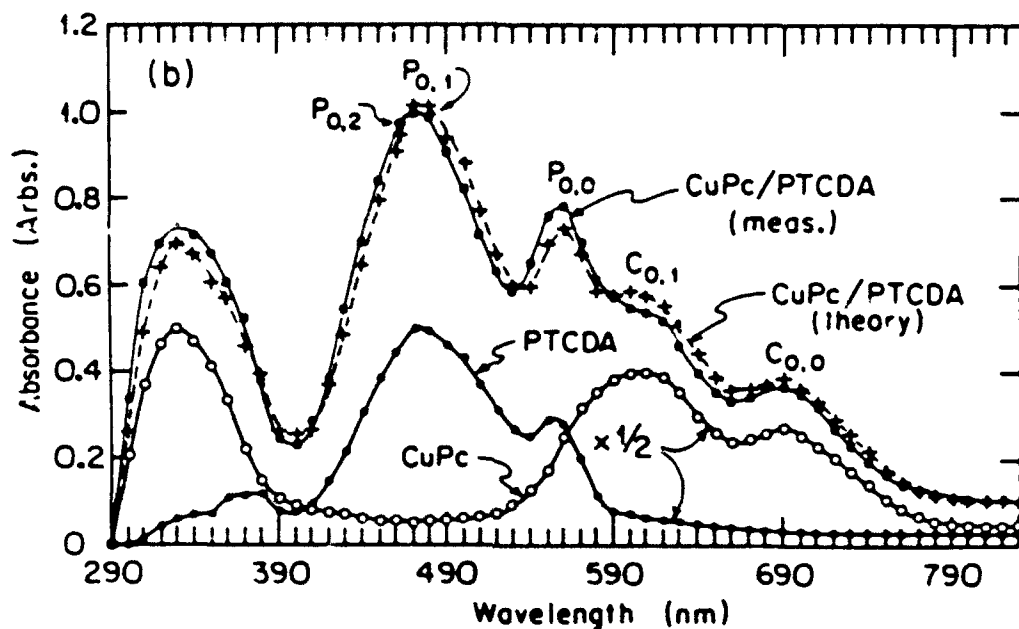


Fig. 4.9 The constituent and combined absorption spectra of CuPc/PTCDA heterojunctions. A fit to the data of the combined spectrum is also shown (dashed line). Peaks labelled P and C correspond to those exciton lines associated with PTCDA and CuPc, respectively. Subscripts 0,0 and 0,1 refer to singlet transitions between the two lowest molecular vibronic levels (0 and 1) in the ground and first excited states (see Fig. 4.11).

By comparison with Fig. 4.8, all of these spectral features are observed in the photocurrent spectrum, although the charge collection efficiency in CuPc appears to be considerably enhanced over that of PTCDA. The voltage dependence of these data is thus interpreted as due to increased carrier collection efficiency in CuPc resulting from depletion of this layer under reverse bias. That is, photon absorption in both PTCDA and CuPc results in the generation of excitons. These excitons diffuse through the material until they collide with the heterointerface. At this site, the exciton dissociates<sup>32</sup>, and the electron and hole are subsequently swept apart by the electric field, and are collected. Since PTCDA is completely depleted at  $V = 0$ , the carriers absorbed in this region are collected prior to recombination. On the other hand, C-V data indicate that the CuPc, with its higher charge concentration, is only depleted near the HJ unless a reverse bias is applied. Hence, as  $V_a$  is increased in the reverse direction, the carrier collection efficiency in the CuPc is increased as a result of the applied electric field which separates the free carriers prior to recombination at the high density of trap sites in this material.

Measurements similar to those described above have also been made on both CuPc/PTCBI and PTCDA/PTCBI HJs. Thus, in Fig. 4.6 we show the dependence of  $J_s$  on  $1/T$  for the CuPc/PTCBI sample, and find that the diffusion potential is  $V_{D2} = (0.74 \pm 0.05)$  V. Furthermore, this is consistent with C-V measurements, where  $V_{D2} = (0.69 \pm 0.10)$  V is found. The symmetry of this HJ inferred from the J-V characteristics is similar to that of CuPc/PTCDA: i.e. the valence band edge of CuPc lies below that of PTCBI. (Fig. 4.5b).



We note that previous work has suggested that the CuPc/PTCBI materials combination is rectifying since PTCBI is an n-type semiconductor<sup>14</sup>, thus forming a p-n junction with CuPc. However, the polarity required for forward and reverse bias of Au/PTCBI Schottky barrier devices indicates that PTCBI is p-type (with a hole concentration of approximately  $10^{14} \text{ cm}^{-3}$ ), similar to its relative, PTCDA.

Finally, a PTCDA/PTCBI HJ has also been characterized by analysis of the room temperature J-V characteristics. It is found that the barrier height between these two materials is small, thus leading to a large leakage current under both forward and reverse bias, even at very small applied voltage. The observation of a small offset is also consistent with our conclusion that PTCBI is p-type. If it were n-type, it would form an energy barrier at the p-n junction roughly equal to the semiconductor band gap energy ( $\sim 2 \text{ eV}$ ), which is not observed. As a result of the small band offset, it is difficult to estimate the magnitude of the energy barrier between these two materials. Nevertheless, from the value obtained for  $J_s$  this sample, we obtain  $\Delta E_v = (0.2 \pm 0.1) \text{ eV}$ . From the symmetry of the weakly rectifying HJ contact, we infer that the valence band edge of PTCDA lies below that of PTCBI. (Fig. 4.5c).

The lowest singlet exciton energy of PTCBI is  $E_g = 1.7 \text{ eV}$ , as inferred from the approximate position of the long wavelength cutoff in the absorption spectrum shown in Fig. 4.10. Using the data, we summarize the results obtained in this study for these three HJ systems by the band diagrams shown in Fig. 4.5. Note that the absorption spectrum obtained for PTCBI is consistent with that inferred from the data of Tang<sup>14</sup> who measured only the combined CuPc/PTCBI

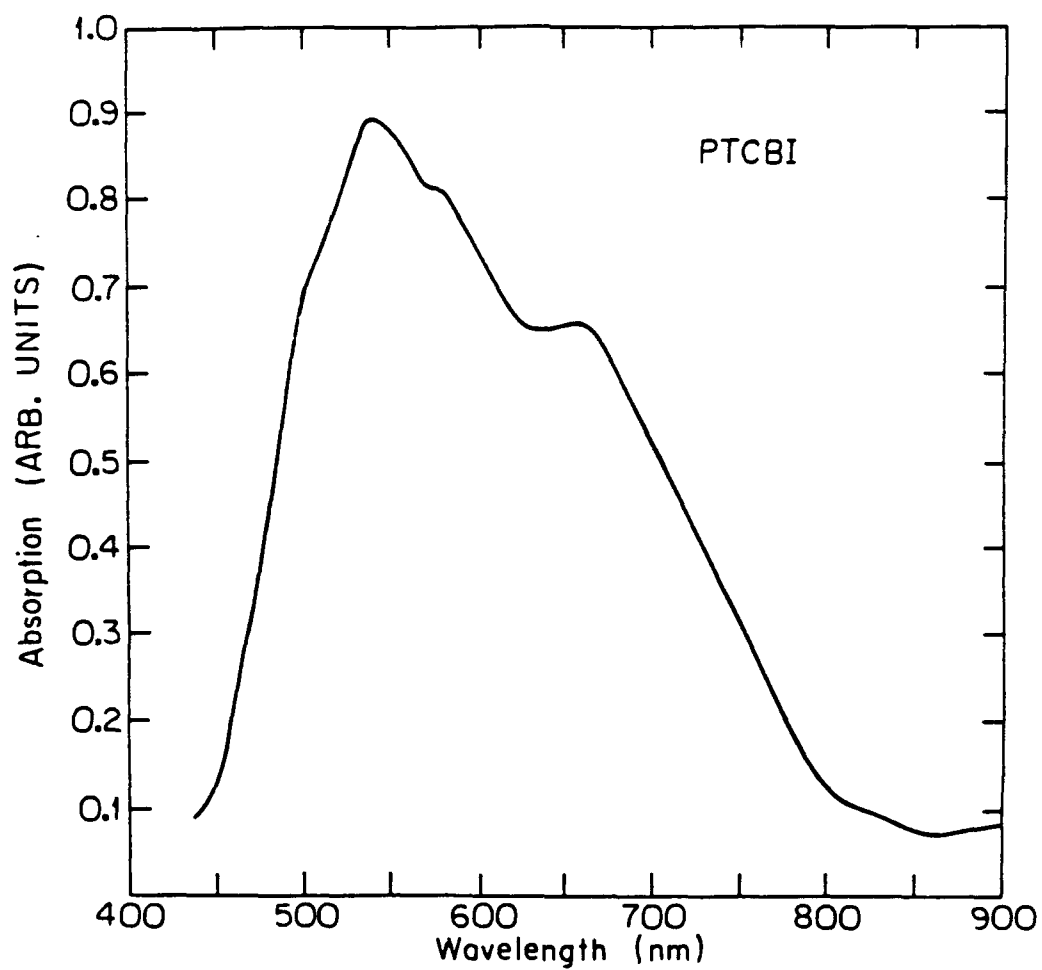


Fig. 4.10 The absorption spectrum of PTCBI.

spectrum. Indeed, our combined spectrum is qualitatively similar to that of Tang, indicating that our synthesized product for this material is of similar composition.

#### IV.4 Energy band discontinuities in organic HJs

The current, capacitance and photocurrent characteristics of a p-P CuPc/PTCDA HJ have been measured and suggest a band picture near the heterointerface resembling that shown in Fig. 4.5a. The valence band offset energy for this material combination can, in principal, be found using Eq. (4.6), provided that the density of states,  $N_v$  is known. Typically, there is approximately one state per molecule; hence  $N_v \sim 10^{21} \text{ cm}^{-3}$  is not uncommon.<sup>19,30</sup> Furthermore, if we assume that the free, or detrapped charge at equilibrium is roughly equal for CuPc<sup>19</sup> and PTCDA<sup>5</sup>, then the last term in Eq. (4.6) becomes very small. This results in a nominal valence band offset energy equal to  $qV_D$ . We note, however, that in terms of understanding transport across the HJ, such assumptions need not be made since it is only the diffusion potential which is responsible for governing charge transport in this region.

In terms of gaining a physical understanding of the HJ system, however, the distinction between  $V_D$  and  $\Delta E_v$  becomes important. As noted above, the band pictures suggested in Fig. 4.5 must be cautiously applied to systems where the electronic overlap between adjacent molecules is relatively small compared with inorganic semiconductors. An alternative, crystalline molecular vibronic level diagram<sup>33</sup> for the HJ is shown in Fig. 4.11, indicating the various HOMO and LUMO bands as a function of configuration coordinate,  $Q$  (where the

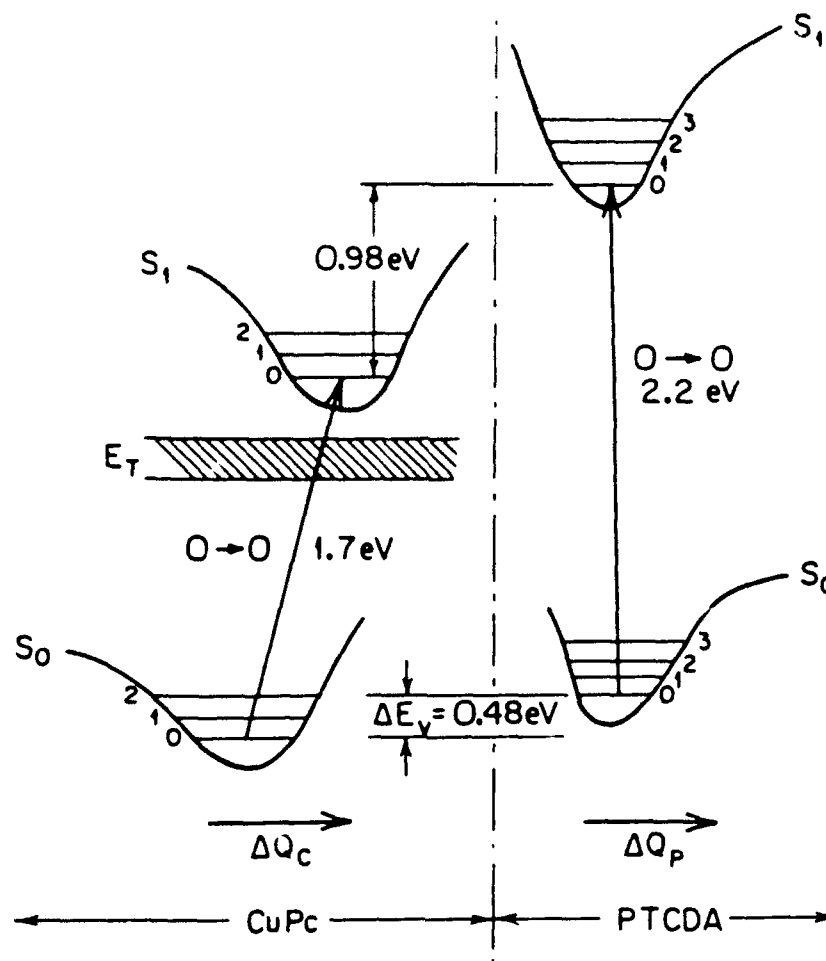


Fig. 4.11 Proposed crystalline molecular energy level diagram for optical transitions occurring at the CuPc/PTCDA heterointerface plotted as a function of the configuration coordinate,  $Q$ . Here  $S_0$  and  $S_1$  refer to ground and first excited singlet states, respectively. The light lines between states (labelled 0,1,2,3) schematically indicate molecular vibronic levels. The band labelled  $E_T$  corresponds to a trap level observed in CuPc.

subscripts C and P refer, as usual, to CuPc and PTCDA, respectively). Both the ground states ( $S_0$ ) and first excited singlet states ( $S_1$ ) are resolved into their separate crystalline vibronic levels (labelled 0, 1, 2, etc.) which are responsible for the observed structure in the molecular absorption spectra. Here, the molecular ground singlet state energies ( $S_0$ ) of CuPc and PTCDA are shown to be offset by an "activation energy",  $\Delta E_v$ . Consistent with our preceding analysis, the low energy absorption edges correspond to transitions between the crystalline 0 vibronic level in the ground and excited states. Also,  $\Delta E_v$  represents the energy required to transfer a charge from a CuPc to a PTCDA molecule across the heterointerface. We also note the existence of a high density of defects at a mean energy  $E_T$  within the forbidden gap of CuPc. No such level is observed in PTCDA.

Comparison of the three HJ systems studied in this work, and summarized in Fig. 4.5 indicates that the offset energies are associated by a transitive relationship. That is, if we define  $\Delta E_{vC,P} = E_{vC} - E_{vP}$ , where  $E_{vC}$  ( $E_{vP}$ ) refers to the valence band energy of CuPc (PTCDA), then we have the following approximate relationship governing the offsets of the three material pairs:

$$\Delta E_{vC,P} = \Delta E_{vC,B} - \Delta E_{vB,P} \quad (4.8)$$

where  $E_{vB}$  is the valence band energy of PTCBI.

#### IV.5 Charge transport in crystalline organic materials

Since the late fifties, there has been an interest in the mechanisms for charge transport in crystalline organic materials. Although the transport properties

of many crystalline organic solids, such as naphthalene, anthracene, perylene and durene have been studied extensively, there has been no satisfactory theoretical model available to provide a good understanding of the charge transport mechanisms in these materials. It is the purpose of this section to discuss the different charge transport models used in organic molecular crystals, and hence gain a qualitative understanding of the transport properties of the materials used in this work. In this section, we will first review the transport properties of the most common crystalline organic materials, and discuss the validity of the hopping and band models used in various crystalline organic materials, including those employed in this work.

Up to the present time, there has been considerable controversy regarding the charge transport mechanisms in crystalline organic materials. Available carrier mobility data do not seem to be consistent with either the band theory model<sup>34</sup> or the hopping model.<sup>35</sup> More recently, Warta and Karl<sup>36</sup> have made low temperature and high field mobility measurements on ultra-high purity naphthalene and perylene crystals, and their results seem to provide the first evidence for a band model description of charge transport in molecular crystals. In the following, we will describe both the hopping model and the band model in detail, and explain why these models fail to explain the early mobility data obtained for organic crystals. Next, we will summarize the results of the recent mobility measurements by Warta and Karl,<sup>36</sup> and describe how these data can be understood in terms of the framework of the standard band theory used in inorganic semiconductors.

#### (A) Hopping versus band transport

It is commonly believed that the presence of translational symmetry in a crystal is a sufficient condition for applying the band theory in solids. As we shall see later, this is not necessarily true in the case of molecular crystals. For the band model to be a good representation, the electron-phonon coupling must be small compared to the intermolecular electron coupling.<sup>37</sup> In other words, the mean free path of the charge carrier should be long compared to the crystal lattice periodicity. Under this condition, the charge carrier is considered to be delocalized. For organic crystals, theoretical calculations indicate that the charge carrier bandwidth is comparable to the room temperature thermal energy  $kT$ .<sup>38</sup> For materials with small energy bandwidth ( $W < kT$ ), Frohlich and Sewell<sup>39</sup> have shown that the carrier mobility  $\mu$  is related to the bandwidth,  $W$ , by:

$$\mu = \frac{q\lambda}{kT} \frac{aW}{h} \quad (4.9)$$

Here,  $h$  is the Planck's constant,  $a$  is the lattice spacing, and  $\lambda$  is the carrier mean free path. For typical organic crystals such as anthracene and naphthalene,  $\mu = 1 \text{ cm}^2/\text{V-s}$  at room temperature, and  $W \sim 10^{-2} \text{ eV}$ .<sup>26</sup> In this case, Eq. (4.9) gives  $\lambda = 5 \text{ \AA}$ , which is on the order of the intermolecular spacing. It should be noted that the values of  $W$  used in the literature are subject to question because they are all based on the results of theoretical calculations with no experimental data yet available. Nevertheless, the above analysis clearly shows that charge carriers are scattered on every molecular site in the lattice. In other words, they are actually strongly localized rather than delocalized, as it is assumed in the band picture. Such carrier localization is inconsistent with band theory since electron motion

cannot be adequately described by a wave vector,  $k$ . Carrier localization leads one to question the validity of the band model in organic crystals, and the hopping model is a natural alternative.

On the other hand, data on crystalline organic materials such as anthracene, naphthalene, and perylene indicate that the carrier mobility is independent of temperature near room temperature.<sup>40</sup> By cooling the samples to temperatures below 50 K, carrier mobility in naphthalene increases by a factor of 2 compared to its room temperature value. This weak temperature dependence of carrier mobility is inconsistent with the hopping model. In the hopping model, the electron wavefunction is assumed to be localized at a particular site which is accessible by electron hopping from adjacent sites. Hopping motion of localized charge carriers occurs when the thermal energy fluctuations are large compared with the electronic exchange interaction. It is expected, therefore, that the mobility should increase with increasing temperature since the presence of phonons increases the hopping rate. In the hopping model, the temperature dependence of the carrier mobility can be written as:<sup>41</sup>

$$\mu \approx T^{-m} \exp(-E_h/kT) \quad (4.10)$$

where  $m \approx 1$ , and  $E_h$  is the hopping activation energy depending on the values of polaron binding energy and phonon energy. A thermally activated behavior is therefore characteristic of hopping motion at low temperatures, and the term  $T^{-m}$  dominates at high temperatures. Such a temperature dependence is not observed in any available mobility data for molecular crystals such as naphthalene,



anthracene, and  $\text{As}_2\text{S}_3$ .<sup>42</sup> Further, hopping models predict the electric field dependence<sup>43</sup> of the mobility to be:

$$\mu \sim \exp(qFa/2kT) \quad (4.11)$$

where  $F$  is the electric field. Measurements at high fields<sup>42</sup> and low temperatures demonstrated that  $\mu$  is independent of  $F$ , and the results are inconsistent with Eq. (4.11). Based on the above considerations, the hopping model has been unsuccessful in describing the experimental mobility data.

#### (B) Mobility data to support the band model

Using ultra-high purity naphthalene crystals, Warta and Karl<sup>36</sup> have recently reported the low temperature, high electric field mobility data for these materials. They found that the hole mobility exceeds  $100 \text{ cm}^2/\text{V-s}$  at temperatures below 40 K, and reaches a maximum value of  $400 \text{ cm}^2/\text{V-s}$  at 4.2 K. These mobility data are the highest ever reported for organic molecular crystals, indicative of the high quality of the materials used. In addition, the hole velocities increase linearly with electric field at temperatures below 36 K, and tend to saturate at  $v_d = 1.8 \times 10^6 \text{ cm/s}$  at high fields ( $> 10 \text{ kV/cm}$ ). More recently, velocity saturation at high fields has also been observed in other organic crystals such as anthracene<sup>44</sup> and perylene.<sup>45</sup> Warta and Karl<sup>36</sup> suggested that the carrier velocity saturation is due to hot carrier effects, and velocity saturation is established by the balance between energy gain from the field and energy loss to emission of optical phonons. This is similar to the argument used by Shockley<sup>46</sup>

to explain carrier velocity saturation in inorganic semiconductors. Further, their carrier velocity data were fit to Shockley's expression:<sup>46</sup>

$$v_d = \mu_o E \sqrt{2} \left\{ 1 + \left[ 1 + \frac{3\pi}{8} \left( \frac{\mu_o E}{u_L} \right)^2 \right]^{1/2} \right\}^{-1/2} \quad (4.12)$$

where  $u_L$  is the speed of longitudinal lattice waves in the crystal and  $\mu_o$  is the low field mobility. At high fields,  $v_d$  is proportional to  $\sqrt{E}$ , as observed in the mobility data.

To justify the use of the band model, Warta and Karl<sup>36</sup> did an estimate of the carrier mean free path in naphthalene. Using  $\mu = 360 \text{ cm}^2/\text{V-s}$  at 19 K, and taking the bandwidth  $W = 40 \text{ meV}$ , they estimated that the mean free path  $\lambda$  was at least eight lattice constants. Therefore, they concluded that the large value of mean free path supports the band model description for the low temperature mobility data.

On the other hand, based on the room temperature mobility data of naphthalene, the estimate of  $\lambda$  turns out to be smaller than the lattice constant. This inconsistency suggests that a different transport mechanism exists at high temperatures. Warta and Karl<sup>36</sup> pointed that, since there is no change in temperature dependence of  $\mu$  from the low-temperature to high-temperature regime, the band model description for the low temperature mobility data might be extended to explain the high temperature data as well. Their argument is as follows: Knowing that the valence bandwidth is about 40 meV, a fraction of carriers reaches states with higher effective mass as temperature is increased. Therefore, as the temperature increases, the average value of the effective mass

increases, giving rise to errors in evaluation of  $\lambda$ . In addition, due to the crystal symmetry in these crystalline organic materials, the effective conduction band (or valence) consists of multiple bands with narrow bandwidths, and interband scattering can also affect the effective mobility value. Therefore, the band picture appears to provide a convincing description of the charge transport in aromatic organic crystals.

(C) Charge transport mechanisms in materials used in this work

Of the three crystalline organic materials used in this work, very little is known about the transport properties of PTCDI. It is expected, however, that the transport properties of PTCDI are very similar to those of PTCDA because of the similarity in their molecular structures. The room temperature hole mobility of PTCDA is  $1.4 \text{ cm}^2/\text{V}\cdot\text{s}$ . This is about the same as that found in naphthalene and perylene. If we were to get an estimate of  $\lambda$  for PTCDA from Eq. (4.9), we have to know the value of bandwidth,  $W$ . However, the hole bandwidth in PTCDA is  $0.5 \text{ V}$  according to the results of internal photoemission measurements of PTCDA/p-Si heterojunctions, and we can no longer use Eq. (4.9) to estimate  $\lambda$  because  $W \gg kT$ . On the other hand, since the internal photoemission process in OI-HJs is due to intra-band transitions in the organic material, band transport is an appropriate description of the transport mechanism in PTCDA. Further, the results of optical measurements on organic multiple quantum well samples indicate that the carriers in PTCDA are delocalized in the lattice with  $\lambda > 10 \text{ \AA}$ ,<sup>11</sup> implying band-like transport is a probable picture. Finally, the fact that we can apply the theory for inorganic HJs to describe the transport properties of organic

HJs is also consistent with the band-like transport picture. Similar arguments can be used for PTCBI and CuPc, and therefore the band model is more appropriate to use than the hopping model to describe the charge transport properties of the crystalline organic materials studied here.

#### IV. 6 Summary and conclusions

In summary, the layering of more than one crystalline organic semiconductor results in HJs with good rectification properties. These structures have proven useful in understanding these novel HJ systems. In addition, an energy offset between the ground (HOMO) state and excited (LUMO) state levels is formed at the heterointerface. This offset, or activation energy, is sufficiently large to control the charge transport across the interface in a manner analogous to that encountered at inorganic semiconductor HJs. Therefore, provided that the charge carrier delocalization effect is large compared to the layer thickness in a multilayer heterostructure, quantum confinement of carriers can perhaps be achieved in multilayer structures based on certain crystalline organic semiconductors. This can open up a new area of quantum well physics and devices. Indeed, the growth of organic multiple quantum well structures and their optical properties will be discussed in the next chapter.

## References

- <sup>1</sup> H. Kroemer, J. Appl. Phys. **20**, 9 (1981)
- <sup>2</sup> F. Capasso and G. Margaritondo, eds. *Heterojunction Band Discontinuities: Physics and Device Applications*, North-Holland, Amsterdam (1987)
- <sup>3</sup> F. Gutmann and L.E. Lyons, *Organic Semiconductors*, Wiley, New York, 1967
- <sup>4</sup> M. Pope and C.E. Swenberg, *Electronic Processes in Organic Crystals*, Oxford, New York, 1982
- <sup>5</sup> S.R. Forrest, M.L. Kaplan and P.H. Schmidt, J. Appl. Phys. **55**, 1492 (1984)
- <sup>6</sup> S.R. Forrest and F.F. So, J. Appl. Phys. **64**, 399 (1988)
- <sup>7</sup> K. Saiki, K. Ueno, T. Shimada, and A. Koma, J. Cryst. Growth **95**, 603 (1989)
- <sup>8</sup> K. Ueno, T. Shimada, K. Saikim, and A. Koma, Appl. Phys. Lett. **56**, 327 (1990)
- <sup>9</sup> A.J. Dann, H. Hoshi, and Y. Maruyama, J. Appl. Phys. **67**, 1371 (1990)
- <sup>10</sup> M. Hara, H. Sasabe, A. Yamada, and A.F. Garito, Japan. J. Appl. Phys. **28**, L306 (1989)
- <sup>11</sup> F.F. So, S.R. Forrest, Y.Q. Shi, and W.H. Steier, Appl. Phys. Lett. **56**, 674 (1990)
- <sup>12</sup> J. Tersoff, Phys. Rev. **B30**, 4874 (1984)
- <sup>13</sup> Y. Harima and K. Yamashita, Appl. Phys. Lett. **45**, 1144 (1984)
- <sup>14</sup> C.W. Tang, Appl. Phys. Lett. **48**, 183 (1986)
- <sup>15</sup> C.W. Tang and S.A. Vanslyke, Appl. Phys. Lett. **51**, 913 (1987)
- <sup>16</sup> C. Adachi, S. Tokito, T. Tsutsui and S. Saito, Japan. J. Appl. Phys. **27**, L269 (1988)
- <sup>17</sup> C. Adachi, S. Tokito, T. Tsutsui and S. Saito, Japan. J. Appl. Phys. **27**, L713,

- (1988)
- <sup>18</sup> C. Adachi, T. Tsutsui, and S. Saito, Appl. Phys. Lett. **55**, 1489 (1989)
- <sup>19</sup> A. Sussman, J. Appl. Phys. **38**, 2738 (1967)
- <sup>20</sup> C. Hamann, Phys. Stat. Sol. **26**, 311 (1968)
- <sup>21</sup> H. Kroemer, J. Vac. Sci Technol. **B2**, 433 (1984)
- <sup>22</sup> Aldrich Chemical Co., Milwaukee, WI 53233
- <sup>23</sup> S.R. Forrest, M.L. Kaplan and P.H. Schmidt, Ann. Rev. Mat. Sci. **17**, 189 (1987)
- <sup>24</sup> T. Maki and H. Hashimoto, Bull. Chem. Soc. Japan. **25**, 411 (1952)
- <sup>25</sup> H. Laurs and G. Heiland, Thin Solid Films, **149**, 129 (1987)
- <sup>26</sup> J. Simon and J.-J. Andre, *Molecular Semiconductors*, Springer-Verlag, Berlin (1985)
- <sup>27</sup> A.Twarowski, J. Chem. Phys. **77**, 5840 (1982)
- <sup>28</sup> P.E. Fielding and F. Gutmann, J. Chem. Phys. **26**, 411 (1957)
- <sup>29</sup> L.L. Chang, Solid-State Electron. **8**, 721 (1965)
- <sup>30</sup> A. Sussman, J. Appl. Phys. **38**, 2748 (1967)
- <sup>31</sup> J.D. Wiley and G.L. Miller, IEEE Trans. on Electron Dev. **22**, 265 (1975)
- <sup>32</sup> R.F. Chaiken and D.R. Kearns, J. Chem. Phys. **45**, 3966 (1966)
- <sup>33</sup> S.R. Forrest, L.Y. Leu, F.F. So, and W.Y. Yoon, J. Appl. Phys. **66**, 5908 (1989)
- <sup>34</sup> O.H. LeBlanc, J. Chem. Phys. **35**, 1275 (1961)
- <sup>35</sup> W. Siebrand, J. Chem. Phys. **41**, 3574 (1964)
- <sup>36</sup> W. Warta and N. Karl, Phys. Rev. **B32**, 1172 (1985)
- <sup>37</sup> Z. Burshtein and D.F. Williams, Phys. Rev. **B15**, 5769 (1977)

- <sup>38</sup> E.A. Silinsh, *Organic Molecular Crystals*, (Spring-Verlag, New York, 1980)
- <sup>39</sup> H. Frolich and G.K. Sewell, Proc. Phys. Soc. London **74**, 643 (1959)
- <sup>40</sup> L.B. Schein, Chem. Phys. Lett. **48**, 571 (1977)
- <sup>41</sup> I. Vilfan, Phys. Status Solid **B59**, 351 (1973)
- <sup>42</sup> L.B. Schein and A.R. McGhie, Phys. Rev. **B20**, 1631 (1977)
- <sup>43</sup> L.B. Schein and A.R. McGhie, Chem. Phys. Lett. **62**, 356 (1979)
- <sup>44</sup> K. Bitterling and F. Willig, Phys. Rev. **B35**, 7973 (1987)
- <sup>45</sup> N. Karl, J. Crystal Growth **99**, 1009 (1990)
- <sup>46</sup> W. Shockley, Bell Syst. Tech. J. **30**, 990 (1951)

## Chapter V

### Organic Multiple Quantum Wells

Recent developments in crystal growth techniques such as molecular beam epitaxy (MBE) and metal-organic vapor deposition (MOCVD) have allowed fabrication of semiconductor heterostructures which are smooth down to an atomic layer with excellent composition control. Using semiconductor materials with compatible crystal structures, it is possible to grow multiple quantum well structures (MQWs) consisting of alternating ultra-thin layers. Examples of these structures have been grown using a number of III-V,<sup>1</sup> II-VI,<sup>2</sup> and IV-IV<sup>3</sup> materials. Quantum confinement of carriers gives rise to unusual electronic and optical properties in MQWs<sup>4</sup> which cannot be achieved using bulk materials. In the past decade, numerous semiconductor devices such as lasers,<sup>5</sup> photodetectors,<sup>6</sup> resonant tunnelling diodes,<sup>7</sup> and optical modulators<sup>8</sup> have been demonstrated based on MQW structures.

Although multiple quantum well structures can be made using various combinations of materials, epitaxial growth is limited to materials with small or no lattice-mismatch.<sup>9</sup> In contrast, organic crystals, as discussed in Chapter 2, are bonded together by the relatively weak van der Waals forces,<sup>10</sup> which allows for the layering of materials of widely differing crystal lattices whose strain energy is insufficient to create lattice defects. Recently, heteroepitaxial growth of both organic and inorganic van der Waals solids has been demonstrated by molecular beam epitaxy (or van der Waals epitaxy) regardless of their lattice incompatibility. Forrest and co-workers<sup>11</sup> first demonstrated highly ordered



3,4,9,10 perylenetetracarboxylic dianhydride (PTCDA) thin film growth on glass substrates in 1984. Debe, et al.<sup>12</sup> have studied low temperature growth of perylene derivative films. Karl, et al.<sup>13</sup> have recently studied the growth of PTCDA films on NaCl substrates. Several Japanese groups have also been very active in the area of van der Waals epitaxy. For instance, Koma and co-workers have demonstrated the growth of chalcogenide films on both van der Waals solids<sup>14</sup> and semiconductor surfaces.<sup>15</sup> Dann and co-workers<sup>16</sup> have grown ultra-thin phthalocyanine films on alkali halide substrates, and Hara and others<sup>17</sup> have studied the epitaxial growth of organic films by RHEED (reflection high energy electron diffraction) and scanning tunnelling microscopy (STM). Although a number of publications have come from the Japanese efforts, the thickness of van der Waals bonded thin films grown by MBE has been limited to a few monolayers, and characterization of such ultra-thin films has been limited to techniques such as RHEED and STM. Further, useful devices are unlikely to be made based on thin films of only a few monolayers in thickness.

Recently, we have demonstrated the growth of ordered crystalline organic thin films by the ultrahigh vacuum process of organic molecular beam deposition (OMBD).<sup>18</sup> The so-called "quasi-epitaxial" growth of organic thin films has been achieved on a variety of substrate materials including inorganic semiconductors such as InP and Si. In addition, ordered organic thin films can be grown on non-crystalline substrates such as fused quartz, glass and polymers.<sup>19</sup> We have also grown high quality films of PTCDA up to more than one micron in thickness, and useful devices can be fabricated based on such films. Our recent demonstration of the first crystalline organic optical rib waveguides<sup>19</sup> with low loss ( $\sim 2.5$  dB/cm)

indicates that this material is very promising for optical device fabrication. Thus, new opportunities for engineered heterostructures consisting of a wide range of organic material combinations layered without regard to lattice-match provide exciting possibilities in the field of photonics.

More recently, organic MQW structures based on PTCDA and NTCDA have been theoretically shown to have large non-linear optical effects by Lam, Forrest and Tangonan.<sup>20</sup> Although these organic materials do not have  $\chi^{(2)}$  effects due to the inversion symmetry of the monoclinic lattice, the organic MQW structures are predicted to have strong nonlinear optical effects due to  $\chi^{(3)}$ . Essentially, Lam and co-workers<sup>20</sup> predicted that ordered, quasi-epitaxially grown organic MQWs should show an intensity dependent absorption and index of refraction at relatively low input powers which lead to an intrinsic bistability at optical intensities as low as 100 W/cm<sup>2</sup> for wavelengths at the excitonic absorption band edge.

Optical absorption processes in the visible and near-infrared spectral regions in crystalline organic semiconductors are fundamentally different from those of inorganic semiconductors since the electronic transitions of organic semiconductors are primarily due to the generation of excitons. Excitons in most organic crystals are thought to be Frenkel-like, although there are a few reports suggesting that excitons in anthracene and similar materials are Wannier<sup>21,22</sup> in nature. Therefore, it is important to determine the characteristics of excitons in the archetype compound PTCDA in order to understand their optical and electronic properties. Crystalline organic semiconductor heterojunctions (HJs) have been discussed in Chapter 4, and their electrical and optical properties

indicate that the HJ band offsets control the flow of charge carriers between the contacting semiconductors in a manner<sup>23,24</sup> similar to inorganic heterostructures. Thus, MQW structures based on PTCDA and 3,4,7,8 naphthalenetetracarboxylic dianhydride (NTCDA) provide the ideal tools for a study of the nature of excitons in crystalline organic semiconductors. Since the optical absorption bands of PTCDA and NTCDA do not overlap, any change in absorption in these materials will easily be observed in such layered structures.

In this chapter, we describe the growth and the properties of PTCDA/NTCDA MQWs. Both the results of x-ray and birefringence measurements indicate ordered thin film multilayer structures are obtained by OMBD growth, although the crystal structures of the two materials are incommensurate. In addition, an increase of the singlet ground state exciton energy with decreasing PTCDA layer thickness has been observed. The results can be understood in the context of a change in exciton binding energy due to quantum confinement in a potential well<sup>25,26</sup> formed by the energy band offsets between the contacting materials. The results of variational calculations on the well width dependence of exciton binding energy are in good agreement with experimental data. In addition, results of time-resolved photoluminescence measurements indicate the exciton lifetime decreases with decreasing PTCDA/NTCDA layer thickness. This phenomenon is explained in terms of a shrinkage in exciton volume in the MQWs,<sup>27,28</sup> as a result of quantum confinement of charge carriers.

The organization of this chapter is as follows: In Sec. V.2, we describe the growth PTCDA/NTCDA MQW structures by organic molecular beam deposition,

followed by structural measurements by x-ray diffraction and birefringence techniques. Next, we present the results of photoluminescence and optical absorption measurements on these organic MQW samples in Sec. V.3. The results obtained in Sec. V.3, in particular, the optical absorption and time-resolved luminescence data, will be discussed in Sec. V.4 in the context of exciton quantum confinement. The results of our variational calculations on exciton binding energy in organic QW structures are also presented. Finally, we present conclusions and discuss the significance of this work in Sec. V.5.

## V.2 Growth and Structural Properties

Growth of the organic multiple quantum well structures was accomplished by organic molecular beam deposition. The structures of the organic MQW samples investigated consist of ultra-thin, alternating layers of PTCDA and NTCDA, with each layer thickness varying from 10 Å to 200 Å. A schematic diagram of a PTCDA/NTCDA MQW is shown in Fig. 5.1. Table 5.1 shows the crystal structure parameters and the properties of these two materials. As shown in the table, both materials have a monoclinic lattice structure with two molecules per unit cell. In the quantum well structure, PTCDA is the well material with an energy gap of 2.2 eV, and NTCDA is the potential barrier layer with an energy gap of 3.1 eV. The properties of the two materials employed here have been discussed in Chapter 2.

In our experiments, optical quality quartz or glass slides are used as the substrates. To achieve good surface morphology and sharp interfaces, substrates

MOLECULAR SEMICONDUCTOR  
MULTILAYER STRUCTURE

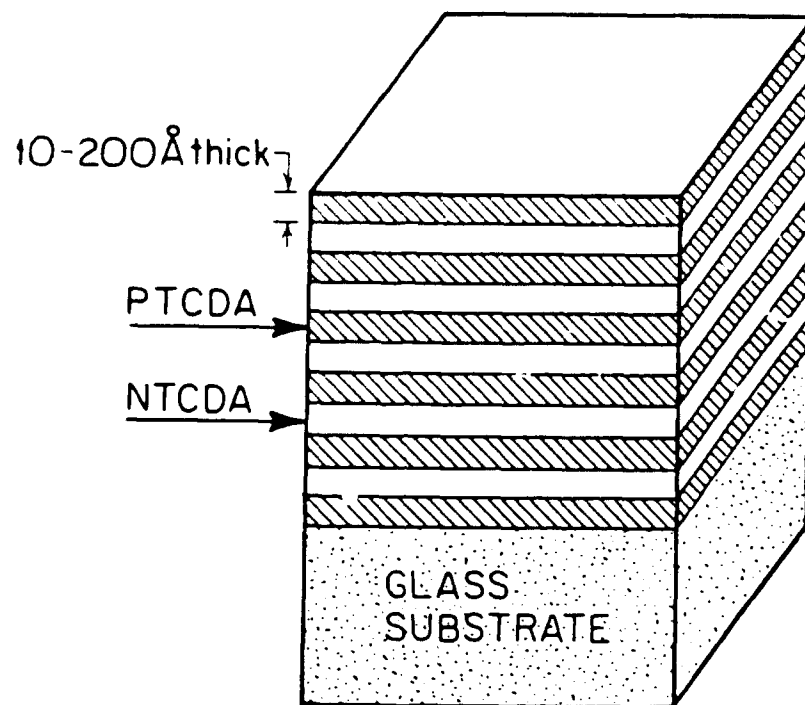


Fig. 5.1 Organic multiple quantum well structure consisting of PTCDA and NTCDA.

Table 5.1 Properties of organic MQW materials.

Property	PTCDA	NTCDA
Crystal structure	monoclinic	monoclinic
a (Å)	3.719	7.888
b (Å)	11.956	5.334
c (Å)	17.338	12.743
$\alpha$	90	90
$\beta$	98.81	109.04
Interplanar spacing (Å)	3.21	3.506
Molecules per unit cell	2	2
$E_g$ (eV)	2.2	3.1

were kept at temperatures below 100 K during growth. To grow organic MQW structures, optical quality glass or quartz substrates were first cleaned using standard organic solvents, and then they were immediately loaded into the growth chamber with a base pressure in the  $10^{-9}$  -  $10^{-10}$  Torr range through the load-lock chamber described in Chapter 2. After the growth chamber reached the base pressure once again, the samples were cooled down to below 100 K by flowing liquid nitrogen through the oxygen-free copper sample block. The sample temperature was monitored by a thermocouple inserted into the center of the sample block. Prior to growth, the samples were kept at low temperatures for about 10 minutes.

Growth was then achieved by resistance heating of the sublimation cells ( $450^{\circ}\text{C}$  for PTCDA and  $250^{\circ}\text{C}$  for NTCDA) to obtain a deposition rate of 0.2 - 1 Å/s, depending on the layer thicknesses. Both the layer thickness and the deposition rate were measured using a Temescal quartz crystal thickness monitor. Multilayer structure growth was achieved by carefully shuttering the sources. Both PTCDA and NTCDA have fairly low vapor pressures. Typically, the pressure during growth of PTCDA was  $\sim 10^{-7}$  Torr while for NTCDA it was  $10^{-8}$  Torr. After deposition, the samples were warmed slowly to room temperature over a period of 3 - 4 hours while they were still in vacuum. This process avoids cracking which might occur if the samples are rapidly warmed.

A series of samples were grown which consisted of alternating layers of PTCDA and NTCDA, and whose layer thicknesses were varied from 10 Å to 200 Å. Unless otherwise specified, the total thickness of each multilayer sample was 400 Å. For crystallographic structure analysis, x-ray measurements were done

using a Rigaku wide angle diffractometer. Figure 5.2 shows the x-ray diffraction patterns of PTCDA/NTCDA multilayer samples with layer thicknesses of 10 Å (20 periods, sample A) and 200 Å (7 layers of PTCDA and 6 layers of NTCDA, sample B). For comparison, the diffraction pattern of a 500 Å thick, single layer PTCDA film (sample C) is also shown. Here, the diffraction peak at  $27.8^\circ$  corresponds to the (102) reflection of the PTCDA crystal while the diffraction peak at  $12.7^\circ$  corresponds to the (110) reflection of the NTCDA crystal. Since the diffraction peaks of single-layer PTCDA and NTCDA<sup>29</sup> samples are found at the same angles as the corresponding peaks for all the multilayer samples, this suggests that the strain in the crystal is too small (less than 0.6%) to measurably affect the molecular interplanar spacings (3.21 Å for PTCDA and 3.506 Å for NTCDA), as expected for van der Waals crystals. Note that the same diffraction peaks are observed for samples of layer thicknesses as small as 10 Å (3 molecular layers), indicating that crystalline ordering is retained in this sample. However, the diffraction intensities of the multilayer samples are weaker than for the single layer samples. Since the PTCDA layers are separated by NTCDA layers of different lattice constant (which is not an integer multiple of that of PTCDA), the scattered waves from separated, thin PTCDA layers are not in phase, hence reducing the total diffraction intensity. In addition, the full widths at half maxima of the diffraction peaks increase with decreasing layer thickness. The broadening in the diffraction peak is attributed to the small layer thicknesses characteristic of the multilayer samples since significant broadening in diffraction peaks is commonly observed when the layer thickness is below 1000 Å.<sup>30</sup>



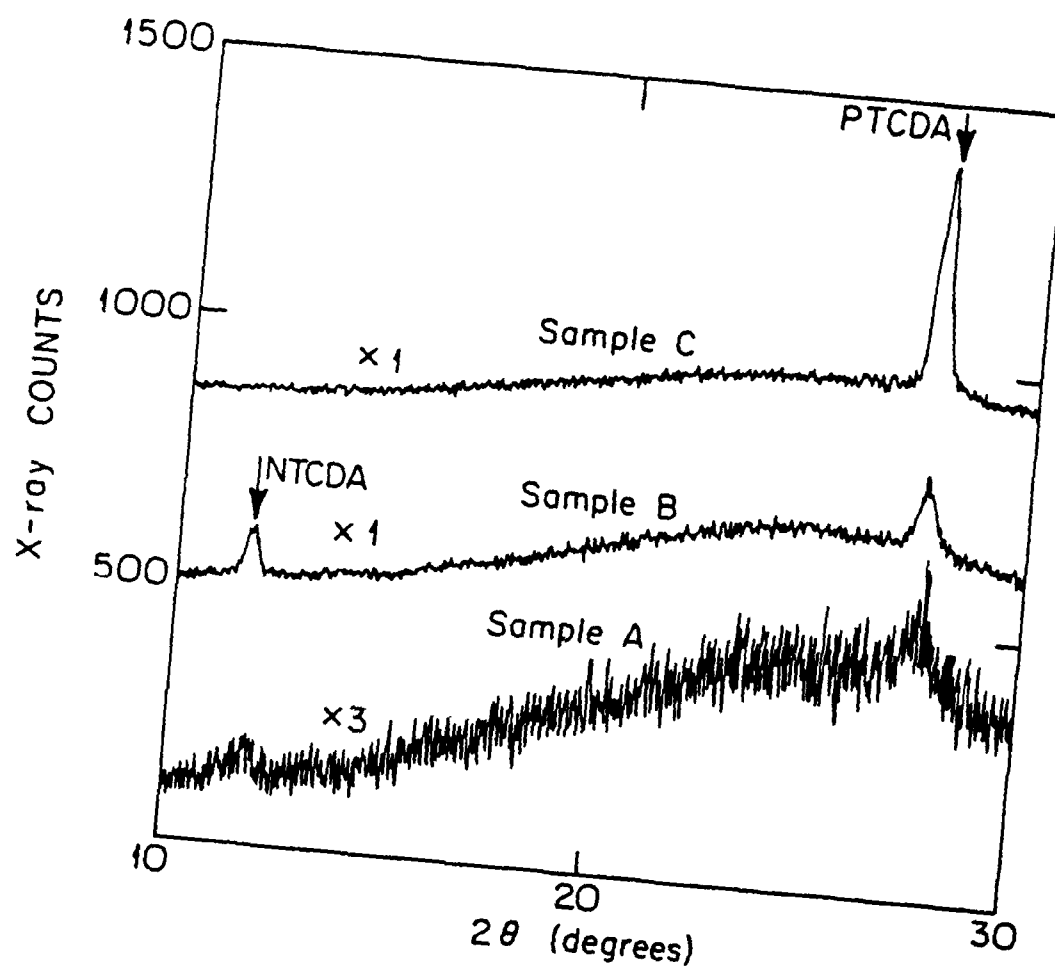


Fig. 5.2 X-ray diffraction patterns for two quantum well samples (A and B) and one single PTCDA layer sample (C). The diffraction patterns of samples B and C are offset by 500 and 800 counts, respectively, for clarity. The background intensity is due to the x-ray scattering of the glass substrate.

The ordering of the multilayer structures can also be studied by measuring their birefringence. This was accomplished by inserting the samples between crossed polarizers and measuring the transmitted light intensity while the plane of the sample was rotated about its normal axis which was oriented parallel to the beam. Here, a He-Ne laser was used as the light source, and a Si detector was used to measure the transmitted light. Note that it is important to shield the stray light from the detector as the transmitted intensity is below a microwatt. The setup for the birefringence measurements is shown in Fig. 5.3. For a birefringent crystal, the transmitted intensity is:

$$I(\theta) = I_0 \sin^2(2\theta) \sin^2(\Delta n \pi d / \lambda). \quad (5.1)$$

Here,  $\theta$  is the angle of rotation,  $\Delta n$  is the difference in refractive indices between the ordinary and extraordinary rays,  $d$  is the thickness of the crystal, and  $\lambda = 633$  nm for the He-Ne laser line.

Figure 5.4 is a plot of a transmitted light intensity as a function of  $\theta$  for a multilayer sample, as well as a single (1000 Å) layer film of PTCDA. The transmitted light intensity variation is in good agreement with Eq. (5.1), indicating that the PTCDA thin film is birefringent, as expected for such an anisotropic crystal. Indeed, recent measurements<sup>31</sup> on the refractive indices of PTCDA thin film waveguides indicate that PTCDA has a birefringence ( $\Delta n$ ) of 0.66, which is the largest value ever reported for thin film materials. Note that the transmission maxima, which occur at 90° intervals, do not have the same amplitude due to small misalignments in the optics. For the single layer sample, it was found that the orientation of the extraordinary and ordinary axes does not

### EXPERIMENTAL SETUP FOR BIREFRINGENCE MEASUREMENT

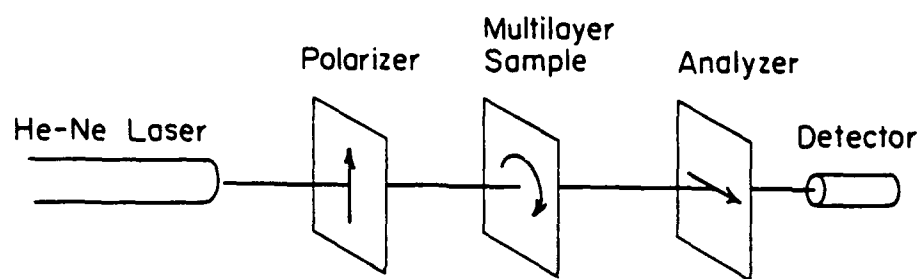


Fig. 5.3 A schematic diagram showing the setup for birefringence measurements.

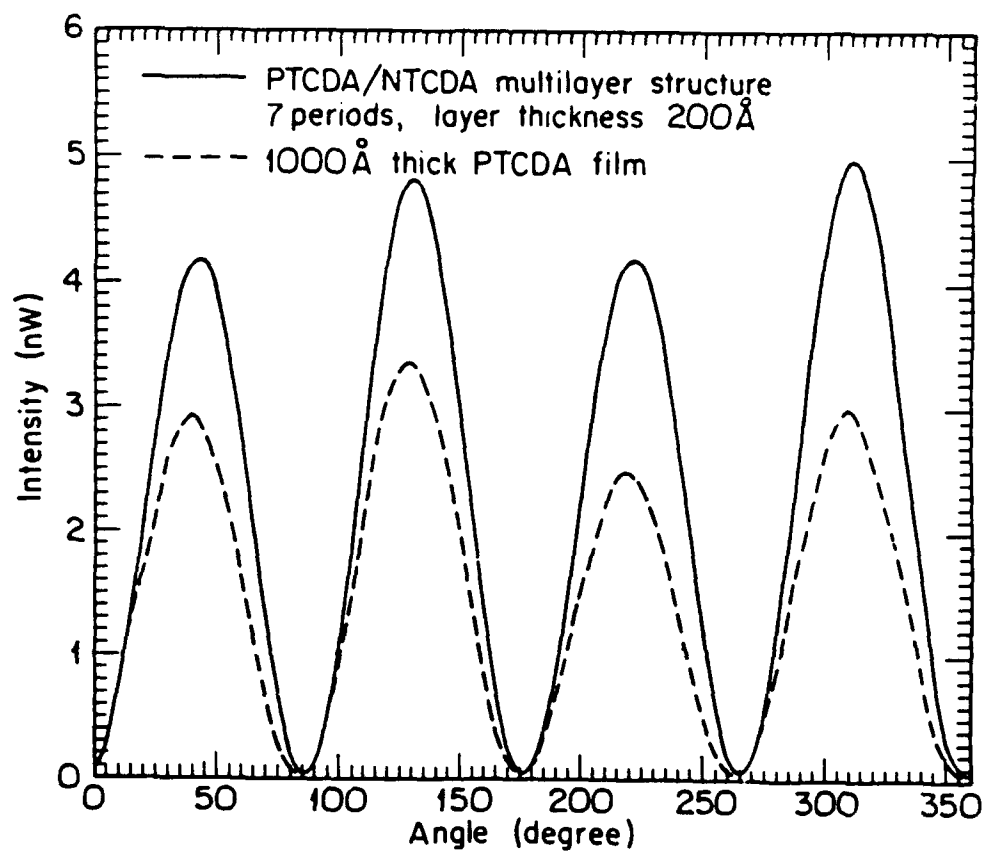


Fig. 5.4 Birefringence of a 1000 Å PTCDA and a multilayer sample.

vary across a 2 cm sample to within the tolerance of our measurement ( $\pm 2^\circ$ ), indicating a surprisingly high degree of spatial lateral ordering of the molecular stacks. The optical axis of the PTCDA film was determined by tilting the sample plane with respect to the beam, and adjusting the orientation at which no transmission through the crossed polarizers is observed. By this means the optical axis was found to be  $10^\circ$ - $12^\circ$  off the substrate normal. Recall from Chapter 2 that x-ray pole figure measurements indicate PTCDA molecules form stacks at an angle of  $11^\circ$  from the normal, which is consistent with the orientation of the optical axis of the PTCDA thin film. Therefore, from the results of birefringence and x-ray measurements, we infer that the optical axis of the film is along the molecular stacking direction.

To study the birefringence of the multilayer sample, we first investigated the birefringence of a single layer NTCDA sample grown under identical conditions as those used for the multilayer samples. Using similar procedures described above for single PTCDA layer birefringence measurements, it was determined that the optical axis of the NTCDA film is normal to the sample surface. Hence, any birefringence measured in the multilayer sample is due only to PTCDA. Fig. 5.4 also shows the birefringence of a multilayer sample (sample B), and it is qualitatively similar to single films of PTCDA. Here, the birefringence of sample B is due to the total PTCDA layer thickness of 1400 Å. According to Eq. (5.1),  $I(\theta)$  for the multilayer sample should be about twice that of the 1000 Å thick single layer sample if all of the PTCDA layers in the former structure are perfectly aligned. Here, the amplitudes of the maxima of the multilayer sample are about  $1.6 \pm 0.1$  times that of the single layer sample,

indicating molecules in the separated PTCDA layers have the same orientation. By determining the orientation of the optical axis of the sample, it was found that the principle planes of different layers coincide even though they are separated by the NTCDA layers. These data suggest that ordering between the individual (separated) PTCDA layers exists, as well as between the NTCDA layers. Similar to the single layer sample, the optical axis of the PTCDA layers in the multilayer sample is also tilted at an angle of  $11^\circ \pm 1^\circ$  from the substrate normal. The constant spatial orientation of the optical axes across lateral distances  $\sim 2$  cm for this sample indicate that ordering also exists across large distances along the multilayer sample surface. Thus, there must be a strong molecular interaction between PTCDA and NTCDA molecules in order to be able to grow such a quasi-heteroepitaxial structure between two organic layers even though the crystal structures are incommensurate.

Quasi-epitaxial growth of a PTCDA/NTCDA multilayer structure can be qualitatively visualized as follows: As PTCDA molecules arrive on the initial single crystalline NTCDA surface, they slowly deposit until a full monolayer is grown. According to recent van der Waals bond energy calculations<sup>32</sup> the PTCDA/NTCDA bond energy is smaller than the PTCDA/PTCDA and NTCDA/NTCDA bond energies. Therefore the strain energy at the PTCDA/NTCDA interface is expected to be small. Further, at low substrate temperatures, PTCDA molecules have sufficient surface mobility on the NTCDA surface to minimize the overall crystal energy, resulting in a single crystalline growth of PTCDA. This process requires that some PTCDA molecules on the

NTCDA surface shift from their original positions, and hence, low energy dislocations are generated at the NTCDA/PTCDA interface.

Once a monolayer growth of PTCDA is achieved, the further deposition of molecules permits growth in the natural crystal habit of PTCDA. Thus, a single crystalline layer of PTCDA is grown on the top of NTCDA by the mechanism described above, even though these materials are lattice-mismatched. Due to the inversion symmetry in the PTCDA lattice, an NTCDA layer can also be quasi-epitaxially grown on the PTCDA surface, and is aligned to some degree with the bottom NTCDA layer, thus preserving the crystalline ordering of the entire multilayer structure.

### V.3 Optical Absorption and Photoluminescence

#### (A) Optical absorption

Optical absorption measurements were done at room temperature using a spectrophotometer. The room temperature optical absorption and low temperature (20 K) photoluminescence spectra of a 5 period symmetric PTCDA/NTCDA organic MQW sample with an individual layer thickness of 40 Å is shown in Fig. 5.5. The characteristic absorption spectra of both PTCDA and NTCDA are present, and the absorption bands are due to exciton generation in the corresponding crystalline layers. In general, optical absorption in crystalline organic materials are due to  $\pi$ - $\pi^*$  electronic excitations from the ground singlet state ( $S_0$ ) to different vibronic states in the first excited state ( $S_1$ ) as shown in Fig. 5.6. Note that the absorption bands observed here are relatively broad because of

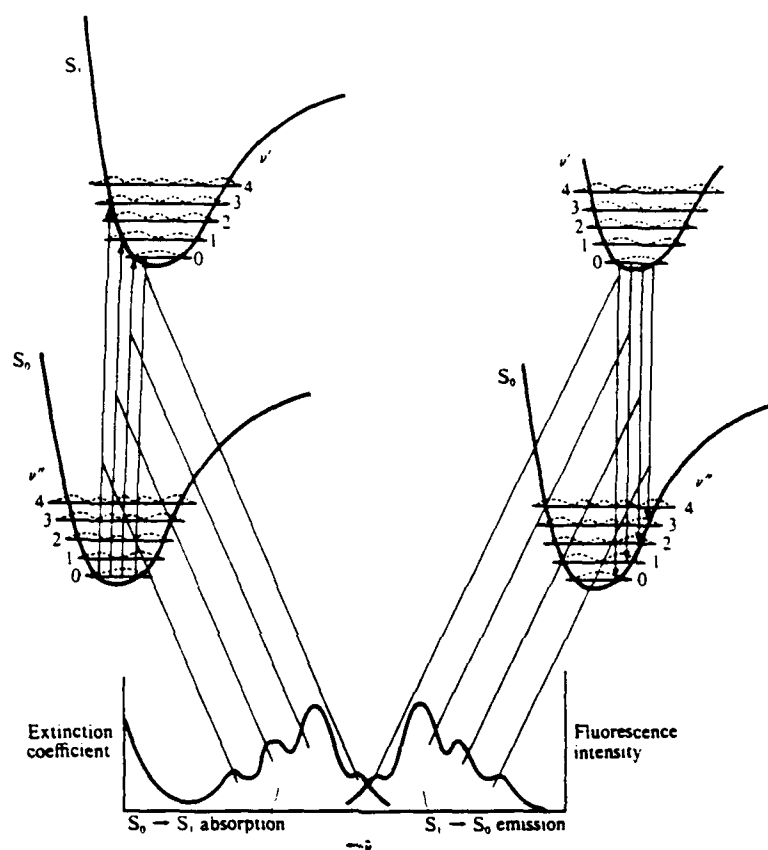


Fig. 5.5 Schematic diagrams showing the vibronic transitions between singlet states. Optical absorption (left) is due to excitations from the lowest vibronic level in the  $S_0$  state to various vibronic levels in the  $S_1$  state. Fluorescence (right) is due to transitions between the lowest level in the  $S_1$  state to the various vibronic levels in the  $S_0$  state. [Reprinted from M. Pope and C.E. Swenberg, *Electronic Processes in Organic Crystals*, (Oxford, New York, 1982)]



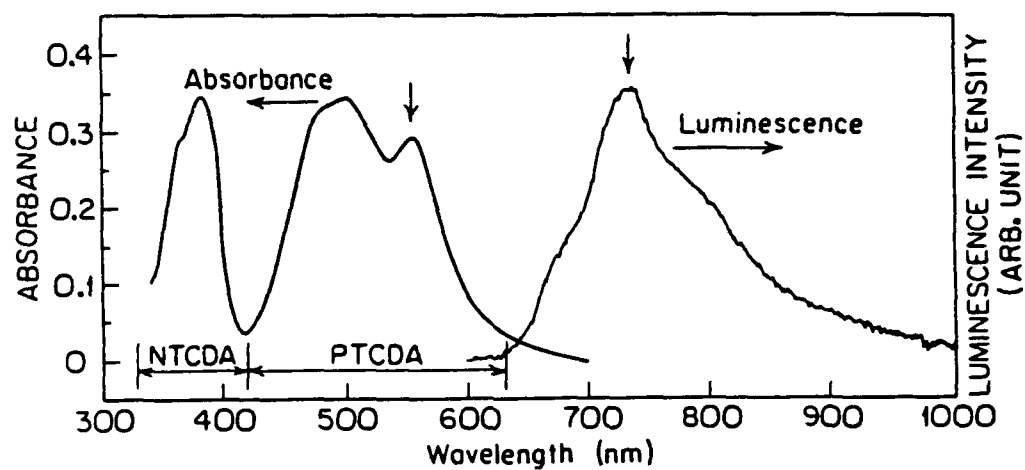


Fig. 5.6 Typical room temperature optical absorption and low temperature (20 K) photoluminescence spectra of a PTCDA/NTCDA multiple quantum well sample.

the strong exciton-phonon interaction characteristic of organic crystals. From the lowest energy cutoffs of the spectra, the "energy gaps" are determined to be 2.2 and 3.1 eV for PTCDA and NTCDA, respectively. We have found that the lowest energy singlet exciton absorption peak in PTCDA (indicated by the arrow) shifts to higher energy as the layer thickness is decreased, as shown by the data points in Fig. 5.7. No apparent shifts in the higher energy exciton lines were observed, possibly as a result of the broad nature of these lines.

#### (B) Photoluminescence

Photoluminescence measurements of both organic multiple quantum well and bulk samples were done using the 515 nm emission line from a cw Ar<sup>+</sup> laser. The excitation power was about 10 mW. The luminescence signal was measured using a S-1 type photomultiplier tube used in conjunction with a lock-in amplifier and a chopper. A double-pass 0.75 m Spex monochromator driven by a computer controlled stepping motor was used in this experiment as well as in the time-resolved luminescence measurements. Samples were mounted on a cold head of a cryostat, and the sample temperature was measured using a Si diode sensor. Fig. 5.8 shows luminescence spectra for a 2000 Å PTCDA single layer sample taken at various temperatures. Note that there is no significant difference in the luminescence spectra if the 488 nm Ar<sup>+</sup> line is used as the excitation source. We identify two major emission bands for the spectrum taken at 21 K, one with a maximum at 720 nm and the other one at 800 nm. Since luminescence signals at these two wavelengths have lifetimes of less than 10 ns, these emission bands can be attributed to transitions from different vibronic levels of the first excited

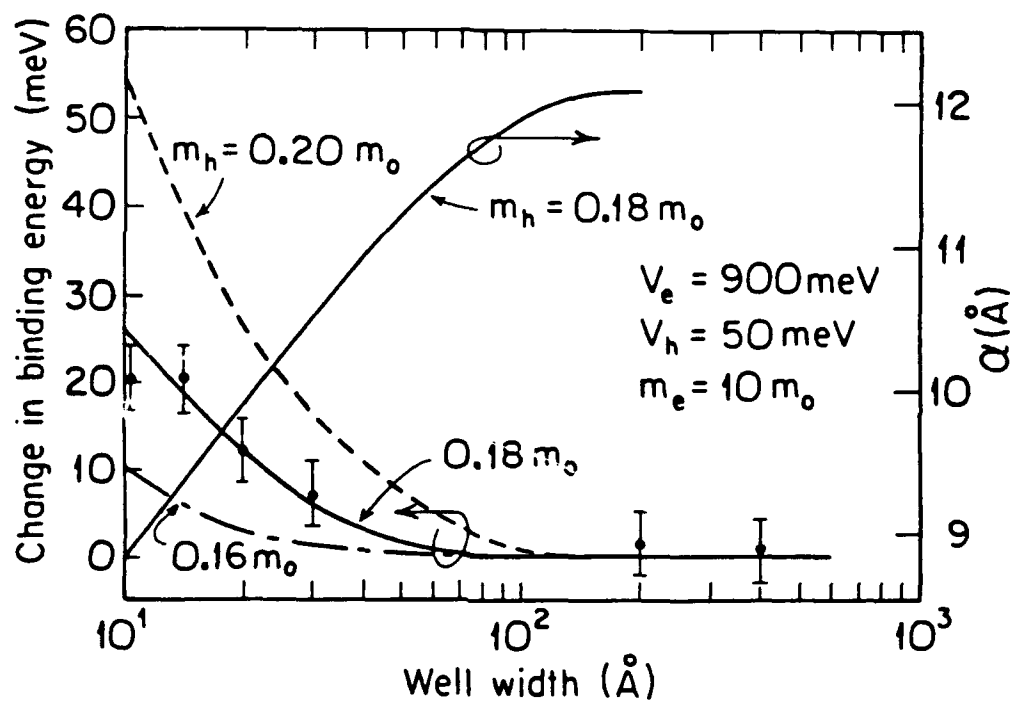


Fig. 5.7 Exciton line shift as a function of well width. The solid line is the result of variational calculations. Also, the variational parameter,  $\alpha$ , is shown in the figure.

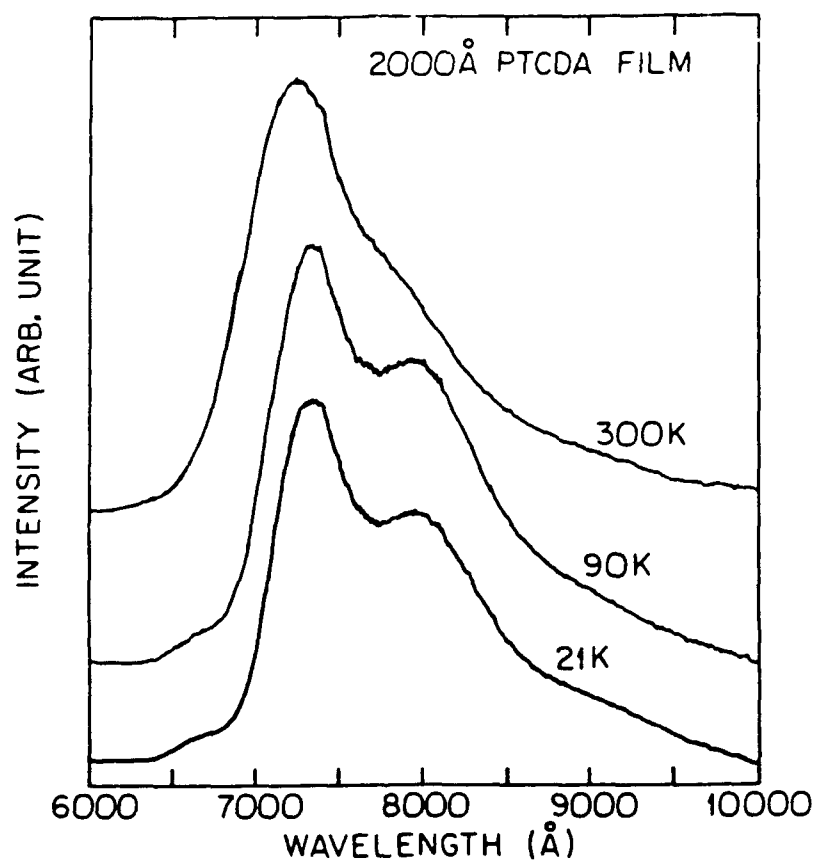


Fig. 5.8 Photoluminescence spectra of a 2000 Å thick PTCDA film as a function of temperature.

singlet state ( $S_1$ ) to the ground state ( $S_0$ ). As the temperature decreases, we observe sharpening as well as a red shift in the luminescence peak at 720 nm, and a shoulder appears at 670 nm. The sharpening of the luminescence spectrum at low temperatures is attributed to the decrease of phonon population.<sup>33</sup> On the other hand, as the temperature decreases, the crystal lattice contracts, resulting in an increase in  $\pi$ -orbital overlap. Due to the enhancement in intermolecular interaction, there is a red shift in the peak energy as the temperature decreases.<sup>34</sup>

Fig. 5.9 shows the luminescence spectra of several organic MQW samples taken at 21 K. The luminescence spectra are all due to PTCDA, since NTCDA is transparent to the 515 nm excitation. The total thicknesses of PTCDA in all MQW samples are the same (400 Å). The luminescence spectra of the MQW samples are similar to those of the bulk samples, except that there is a change in the relative intensities of the emission bands. We note that the luminescence intensity decreases by a factor of 7 as the layer thickness is decreased from 200 Å to 14 Å. Although the PTCDA/NTCDA multilayer structures are ordered, impurities and defects might still be present at the heterointerfaces, giving rise to non-radiative recombination paths. Hence, an increase in the number of heterointerfaces would lead to a reduction in luminescence efficiency, as observed. Also, there is a change in the relative peak intensity as the layer thickness is changed. As shown in Fig. 5.5, the luminescence (or fluorescence) in aromatic compound is related to  $\pi^*$ - $\pi$  electronic transitions from the lowest vibronic level in the  $S_1$  state to various vibronic levels in the  $S_0$  state. The presence of non-radiative recombination centers would affect the luminescence

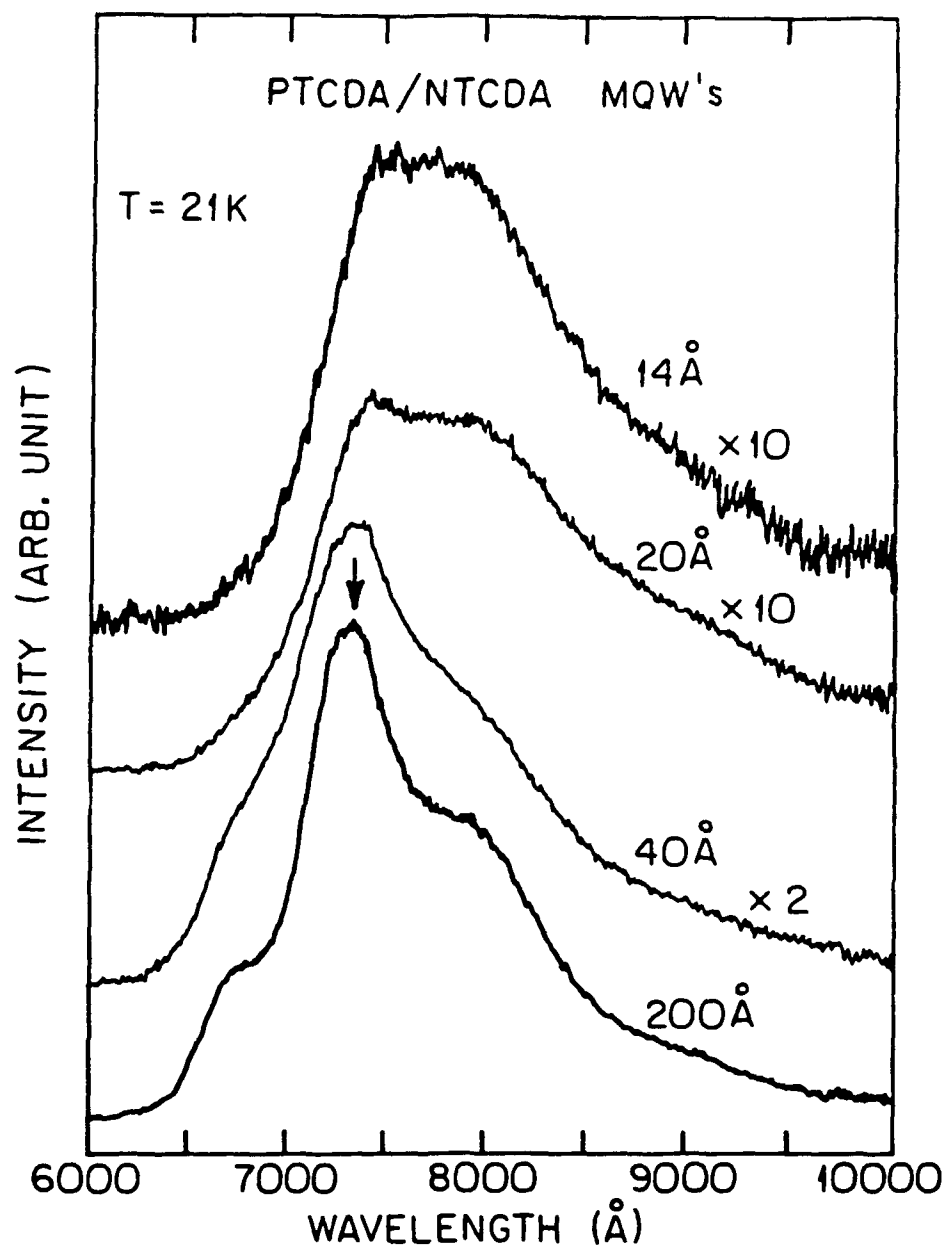


Fig. 5.9 Photoluminescence spectra for PTCDA/NTCDA multiple quantum well samples as a function of layer thickness.

efficiencies of the various vibronic transitions, and result in a change in relative peak intensity in the luminescence spectra.

### (C) Time-resolved Luminescence

Time-resolved photoluminescence measurements of organic quantum well samples were done at 20 K using a multi-line cw Ar ion laser (the most intense lines were at 488 nm and 515 nm) with a total output power of 400 mW. Laser pulses were generated using a Newport Electro-optic acousto-optic (AO) modulator with rise and fall times of less than 4 ns. The AO modulator was driven by an rf generator in conjunction with a function generator. The time decay of the monochromatic luminescence signal was measured using an S-1 photomultiplier tube with a Stanford SR430 multichannel photon counting averager. Deconvolution of the measured luminescence signal from the limited instrumental temporal response at the shortest times measured ( $\sim 5$  ns) has been carried out in all data analysis.

Time-resolved luminescence measurements were made by monitoring the time decay of the luminescence signal at 720 nm. The luminescence signal decay transients for two MQW samples obtained at 20 K are shown in the inset of Fig. 5.10. Here, the exponential decay over several decades in intensity of the transient is apparent. The luminescence signal has decay times of less than 12 ns, indicative of electronic transitions between singlet states. As shown in Fig. 5.10, the luminescence decay time is found to decrease as the layer thickness decreases. The exciton lifetime,  $\tau_{ex}$ , is found to be  $10.8 \pm 0.5$  ns for  $L_z = 200$  Å, decreasing to  $5.5 \pm 0.5$  ns for  $L_z = 10$  Å.

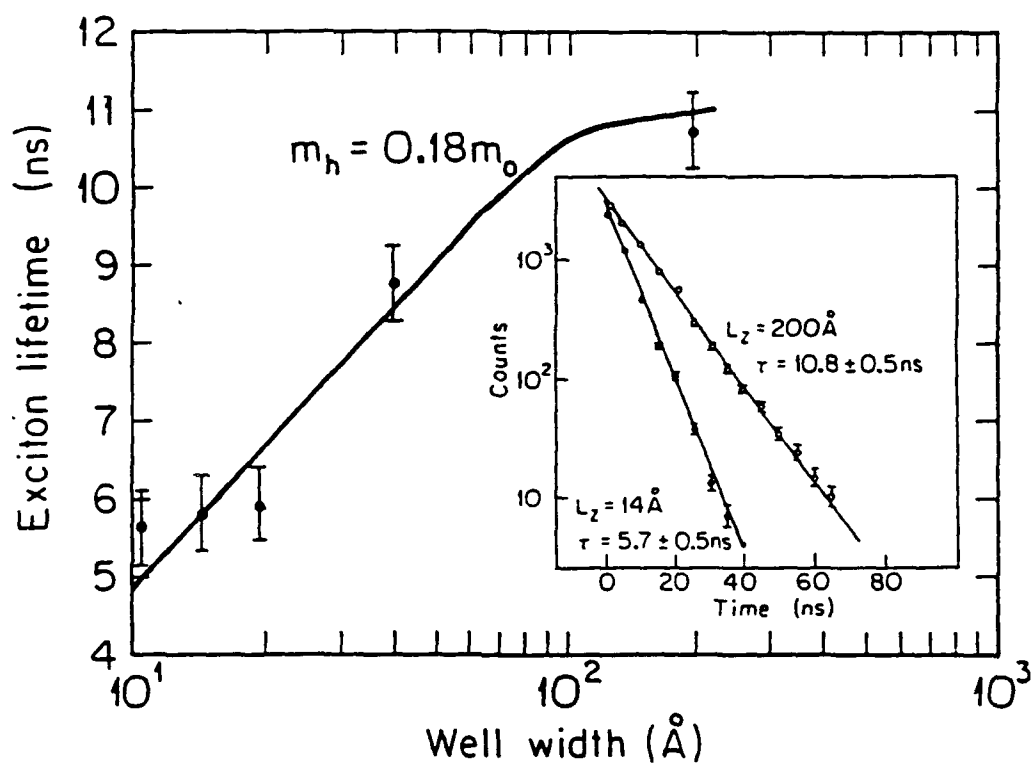


Fig. 5.10 Exciton lifetime,  $\tau_{ex}$ , as a function of well width. The solid line is the fit to the data based on the theory discussed in the text.



#### V.4 Discussion

##### (A) Franck-Condon shift in PTCDA

Both the absorption and luminescence spectra of an MQW sample are shown in Fig. 5.6. As previously discussed in Sec. V.3, the luminescence spectrum in the MQW sample is due only to PTCDA since NTCDA is transparent to the excitation from the Ar ion laser. From Fig. 5.6, the energy difference between the absorption and luminescence peaks of PTCDA is  $4050\text{ cm}^{-1}$ . The energy difference between the luminescence and the optical absorption peaks is known as the Franck-Condon shift.<sup>35</sup> As molecules in the crystal are excited, the non-equilibrium charge distribution in the excited molecules induces changes in electronic polarization of the lattice, thus causing a lattice distortion. The Franck-Condon shift ( $E_{\text{FC}}$ ) represents the lattice relaxation energy released due to these excitations. The magnitude of  $E_{\text{FC}}$  is related to the coupling strength between adjacent molecules in the lattice. A large value of  $E_{\text{FC}}$  implies strong coupling between molecules in the solid. Quantitatively,  $E_{\text{FC}}$  is related to the phonon frequency,  $\omega_0$ , in the solid,<sup>34</sup> and

$$E_{\text{FC}} = \lambda^2/\omega_0, \quad (5.2)$$

where  $\lambda$  is the exciton-phonon coupling constant. In general, the Franck-Condon shift in organic crystals varies from  $50\text{ cm}^{-1}$  in  $\text{H}_2\text{Pc}$ <sup>36</sup> to  $700\text{ cm}^{-1}$  in naphthalene.<sup>37</sup> Here, a very large Franck-Condon shift of  $4050\text{ cm}^{-1}$  in PTCDA is observed in MQW samples as well as in the bulk PTCDA crystal (see Fig. 5.6). To our knowledge, this is the largest value reported for a Franck-Condon shift in

organic crystals, and is indicative of an extremely strong exciton-phonon coupling along the tightly packed PTCDA molecular stacks. Lam and co-workers<sup>20</sup> have demonstrated theoretically that the key to large optical nonlinearities in the PTCDA/NTCDA MQW structures is related to the large Franck-Condon shift in PTCDA.

#### (B) Blue shift in optical absorption

There are two possible reasons for the observed blue shift in the singlet absorption peak in PTCDA as the layer thickness decreases. The first is due to changes in the molecular polarization energy due to the presence of NTCDA. Consider an exciton generated in the PTCDA layer. The presence of NTCDA molecules with a different dipole moment will cause a change in polarization energy of the exciton. The second possible explanation for the blue shift is due to quantum confinement of excitons in a quantum well structure. Quantum confinement of excitons has been observed in many inorganic semiconductor quantum well structures. In this section, we will analyze both the polarization and the quantum confinement models, and compare them with the experimental data.

##### B.1 Polarization effects

Consider an exciton with a Bohr radius  $a_0$  generated at point P in a PTCDA layer of thickness  $t$  sandwiched between two NTCDA layers with the same thickness, as shown in Fig. 5.11. The change of potential due to the presence of an NTCDA molecule at point N on the NTCDA surface is

$$\Delta\phi = \frac{\Delta\mu \cos\theta'}{\epsilon_p |\mathbf{R} - \mathbf{r}|^2}, \quad (5.3)$$

where  $\Delta\mu$  is the difference in dipole moment per unit volume between PTCDA and NTCDA,  $\epsilon_p$  is the dielectric constant of PTCDA,  $\mathbf{R}$  is a vector from the exciton at P to an NTCDA molecule at N,  $\theta'$  is the angle between  $\mathbf{R}$  and the normal to the NTCDA plane, and the charge density of the exciton is described by the spherical coordinates:  $r$ ,  $\theta$ , and  $\phi$ . Using Taylor's series expansion and dropping the higher order terms in Eq. (5.3), the change in potential is

$$\Delta\phi = \frac{\Delta\mu \cos\theta'}{\epsilon_p R^2} \left( 1 + \frac{2r}{R} \cos\theta \cos\theta' \right) \quad (5.4)$$

Assuming the ground state exciton wavefunction to be a hydrogenic 1s state and taking the first term in Eq. (5.4) to be proportional to the first order perturbation Hamiltonian, the first order polarization energy associated with this potential due to the NTCDA molecule at point N is:

$$E^{(1)} = \langle 1s | H^{(1)} | 1s \rangle = \frac{q\Delta\mu \cos\theta'}{\epsilon_p R^2} \quad (5.5)$$

On the other hand, assuming  $\psi_n$  is the excited state wavefunction and  $H^{(2)}$  is the second term in Eq. (5.4), then the second order energy is

$$\begin{aligned} E^{(2)} &= \sum_n \frac{|\langle n | H^{(2)} | 1s \rangle|^2}{E_n - E_{1s}} \\ &= \frac{1}{\Delta E} \left| \langle 2p | \frac{q\Delta\mu}{\epsilon_p R^3} 2r \cos\theta \cos^2\theta' | 1s \rangle \right|^2 + \dots \end{aligned} \quad (5.6)$$

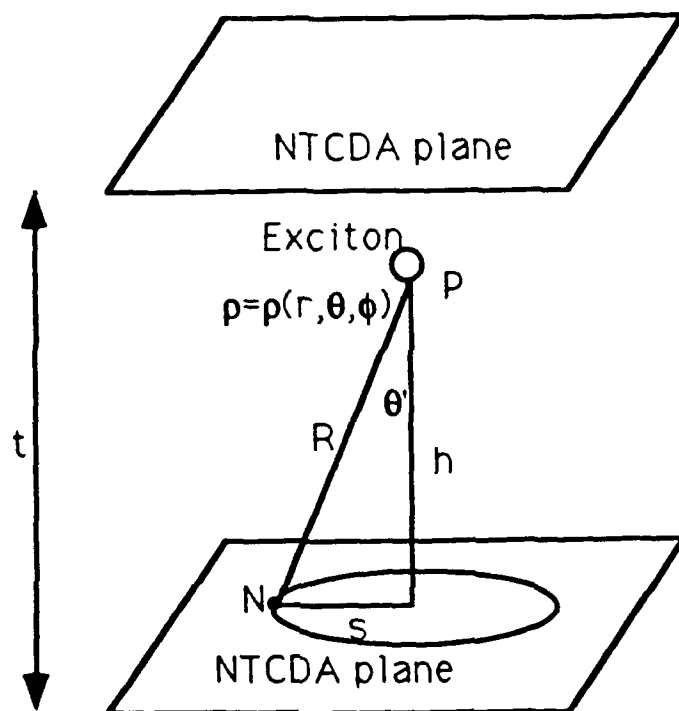


Fig. 5.11 An exciton generated in a PTCDA layer. The distance between the exciton and an NTCDA molecule is  $R$ , and the exciton is at a distance  $h$  above the NTCDA plane.

where  $\Delta E$  is the difference between the ground and excited state energies. Here, we neglect the higher order terms and consider the 2p state only (the 2s state is not allowed for dipole transitions). Substituting hydrogenic wavefunctions into Eq. (5.6) and evaluating the integral in Eq. (5.6) over all space, we get

$$E^{(2)} = \frac{A\Delta\mu^2 a_o^2}{\epsilon_p \Delta E^2} \left[ \frac{\cos^4 \theta'}{R^6} \right], \quad (5.7)$$

where  $A$  is a numerical constant. Now, we can integrate  $E^{(2)}$  over the entire NTCDA layer of thickness  $t$ , i.e.,

$$E_{\text{tot}}^{(2)} = \int_0^\infty \int_h^{h+t} 2\pi s ds E^{(2)} dy \quad (5.8)$$

where  $h$  is perpendicular distance between the exciton and the PTCDA/NTCDA interface plane, and  $s = h \tan \theta'$ . Hence, the integral in Eq. (5.8) can be evaluated by substituting  $\theta'$  for  $s$ . Finally, taking into consideration of the presence of the upper and lower NTCDA layers (see Fig. 5.11) we spatially average  $E_{\text{tot}}^{(2)}$  over the entire PTCDA layer, and therefore

$$\langle E_{\text{tot}}^{(2)} \rangle = \frac{1}{t} \left[ \int_\delta^{\delta+t} (E_{\text{tot}}^{(2)}(h) - E_{\text{tot}}^{(2)}(t-h)) dh \right] \quad (5.9)$$

where  $\delta$  is the thickness of the PTCDA/NTCDA interface. The above integral can be readily evaluated, and the second order energy is

$$\langle E_{\text{tot}}^{(2)} \rangle = \frac{A'}{t^4} \frac{\Delta\mu^2 a_o^2}{\epsilon_p} \delta, \quad (5.10)$$

where  $A'$  is a numerical constant. Similarly, the first order polarization energy can be evaluated using the same procedures, and we get

$$\langle E_{\text{tot}}^{(1)} \rangle = A'' \frac{\Delta\mu}{\epsilon_p} t \quad (5.11)$$

where  $A''$  is also a numerical constant. Therefore, the first order energy correction to the polarization energy due to the presence of the NTCDA layers increases linearly with  $t$ , and the second order term is proportional to  $t^4$ . As shown in Fig. 5.7, the observed thickness dependence is much weaker than even  $t^{-2}$ , and therefore the results of our polarization energy calculations are not consistent with the experimental results. Hence, polarization effects do not adequately explain the observed shift in the exciton line.

## B.2 Exciton quantum confinement

Alternatively, the exciton energy shift can be due the change in exciton binding energy as a result of quantum confinement. Here, the exciton in the potential well (PTCDA) layer is bounded by two energy barrier (NTCDA) layers. Exciton quantum confinement in inorganic quantum wells has been observed in GaAs/AlGaAs<sup>38</sup> and InGaAs/InP<sup>39</sup> systems. As the layer thickness decreases and approaches the exciton Bohr radius, the exciton motion becomes two-dimensional. The exciton is "squeezed" in the potential well formed in the PTCDA layer, resulting in an increase in exciton binding energy. In this model, the small band gap PTCDA layer is treated as a potential well bounded by the large band gap NTCDA layers in a Type I superlattice configuration. Thus, electrons and holes are confined in PTCDA layers of width  $L_z$  (in the  $z$ -

direction). To calculate the change of exciton binding energy due to quantum confinement, we use the variational calculations to evaluate the binding energy of an exciton in a quantum well structure. Here, PTCDA is considered as the well material, and the NTCDA is the potential barrier material.

Using cylindrical coordinates, the total Hamiltonian for an exciton in a quantum well is

$$H_{\text{tot}} = H_e + H_h + H_{xy}, \quad (5.12)$$

where

$$H_e = -\frac{\hbar^2}{2m_e} \frac{\partial^2}{\partial z_e^2} + V_e(z_e), \quad (5.13)$$

$$H_h = -\frac{\hbar^2}{2m_h} \frac{\partial^2}{\partial z_h^2} + V_h(z_h), \quad (5.14)$$

and

$$H_{xy} = -\frac{\hbar^2}{2\mu} \left[ \frac{1}{\rho} \frac{\partial}{\partial \rho} \rho \frac{\partial}{\partial \rho} + \frac{1}{\rho^2} \frac{\partial^2}{\partial \phi^2} \right] - \frac{q^2}{\epsilon_{xy} \sqrt{\rho^2 + \epsilon_z^2 z^2 / \epsilon_{xy}}}. \quad (5.15)$$

Here  $H_e$  and  $H_h$  describe the motion of electrons and holes along the  $z$ -axis in the quantum well, and  $H_{xy}$  describes the two-dimensional motion of excitons in the  $x$ - $y$  plane (parallel to the heterointerfaces) with reduced mass of  $\mu$ . Also,  $m_e$ ,  $z_e$ ,

$m_h$ , and  $z_h$  are the effective masses and positions in the  $z$ -direction for electrons(e) and holes(h). In Eq. (5.15),  $z = z_e - z_h$ , and  $\rho^2 = x^2 + y^2$ . In addition,  $\epsilon_{xy}$  is the dielectric constant in the  $x$ - $y$  plane, and  $\epsilon_z$  is the dielectric constant along the  $z$ -direction. The relative dielectric constant of PTCDA used in this calculation is 3.6, assuming the crystal is an isotropic dielectric continuum ( $\epsilon_{xy} = \epsilon_z$ ). While it is known that dielectric anisotropies in such films are large, the isotropic continuum model nevertheless has been found to provide a very accurate description of charge transfer exciton dynamics in similar organic crystals such as anthracene.<sup>21</sup> Finally, the electron and hole potentials are:

$$V_e(z_e) = \begin{cases} 0 & |z_e| < \frac{L_z}{2} \\ V_e & |z_e| > \frac{L_z}{2} \end{cases} \quad (5.16a)$$

and

$$V_h(z_h) = \begin{cases} 0 & |z_h| < \frac{L_z}{2} \\ V_h & |z_h| > \frac{L_z}{2} \end{cases} \quad (5.16b)$$

Here, we have chosen the origin of the coordinate system to be at the center of the quantum well.

The Schrodinger equation can then be solved by the variational principle using the following trial wavefunction:

$$\Psi_{\text{tot}} = \psi_e(z_e)\psi_h(z_h)\psi_{1s}(\rho, z) \quad (5.17)$$



where  $\psi_{1s}(\rho, z)$  is the hydrogen 1s-like wavefunction, and  $\psi_e(z_e)$  and  $\psi_h(z_h)$  are the exact solutions to the standard finite square well problem. Here,

$$\psi_e(z_e) = \begin{cases} \cos k_e z_e & |z_e| < \frac{L_z}{2} \\ B_e e^{-\kappa_e |z_e|} & |z_e| > \frac{L_z}{2} \end{cases} \quad (5.18)$$

with

$$k_e = \frac{\sqrt{2m_e E_e}}{\hbar} \quad (5.19a)$$

and

$$\kappa_e = \frac{\sqrt{2m_e (V_e - E_e)}}{\hbar} \quad (5.19b)$$

Here,  $E_e$  is the ground state energy of the electron in the potential well, and  $B_e$  can be determined by matching the boundary conditions of the wavefunction  $\psi_e$  at  $z = \pm L_z/2$ . Similar expressions can be written for the hole wavefunction. The values of  $E_e$  and  $E_h$  can be determined numerically by solving the following transcendental equations for the finite square well,

$$\left( \frac{E_e}{V_e} \right)^{1/2} = \cos \left[ \left( \frac{m_e E_e}{2\hbar^2} \right)^{1/2} L_z \right] \quad (5.20a)$$

and

$$\left( \frac{E_h}{V_h} \right)^{1/2} = \cos \left[ \left( \frac{m_h E_h}{2\hbar^2} \right)^{1/2} L_z \right] \quad (5.20b)$$

In Eq. (5.13), the hydrogen 1s-like wavefunction is assumed to have a form

$$\psi_{1s} = \exp \left[ - \left( \frac{\rho^2}{\alpha^2} + \frac{z^2}{\beta^2} \right)^{1/2} \right] \quad (5.21)$$

Also,  $\alpha$  is a variational parameter in the trial solution, and  $\beta$  is set equal to  $a_0$ , where  $a_0$  is the exciton Bohr radius in the bulk crystal.

It should be noted that the trial wavefunction used here is different from those used by others for inorganic quantum well structures. In earlier work by Bastard and co-workers,<sup>25</sup> they calculated the exciton binding energy in GaAs/GaAlAs quantum wells using both a two-dimensional ( $\beta \rightarrow \infty$ ) and spherically symmetric ( $\alpha = \beta$ )  $\psi_{1s}$  state. Shinozuka, et al.<sup>26</sup> have also calculated the exciton binding energy in a quantum well using two-dimensional variational calculations. They have found that for a spherically symmetric wavefunction,  $\alpha$  increases monotonically with decreasing well width, implying that the exciton Bohr radius increases as the well width decreases. This is inconsistent with the fact that carriers are localized due to quantum confinement, and hence the exciton Bohr radius should decrease as the well width decreases. Therefore, a spherical symmetric  $\psi_{1s}$  state does not seem to present a realistic picture. On the other hand, Shinozuka and co-workers<sup>26</sup> have also done the calculations using a 2-dimensional  $\psi_{1s}$ , and their results indicate a 2-D assumption is only valid in the regime where the exciton Bohr radius is larger than the well width. Thus, a 2-D wavefunction is not valid in organic MQWs where the exciton Bohr radius extends over only a few molecular layers and in most cases  $L_z \gg a_0$ . Hence, it is reasonable to assume an ellipsoidal trial wavefunction with  $\beta = a_0$ , and  $\alpha$  being the only variational parameter. Note that for very small well widths, the harmonic

part of the total trial wavefunction [see Eq. (5.17)] dominates the exciton z-dimension.

To calculate the exciton binding energy in a quantum well, the expectation value of the Hamiltonian can be evaluated using the wavefunction described in Eq. (5.12), following:

$$E = \frac{\iiint \Psi_{\text{tot}}^* H_{\text{tot}} \Psi_{\text{tot}} dz_e dz_h \rho d\rho}{\iiint \Psi_{\text{tot}}^* \Psi_{\text{tot}} dz_e dz_h \rho d\rho} \quad (5.22)$$

To solve the Schrodinger equation, the binding energy  $E$  in Eq. (5.22) is minimized as a function of  $\alpha$ . The results of the calculation of  $E$  as a function of  $L_z$  are shown by the solid line in Fig. 5.7. The parameters used in this model are listed in Table 5.2. Here, the sum of  $V_e$  and  $V_h$  is equal to the difference in energy gaps of PTCDA and NTCDA. Of all the parameters used in the calculation, the results are only sensitive to the choice of  $m_h$ . Using these parameters, a good fit to the experimental data is obtained for  $m_h = 0.18m_0$ , where  $m_0$  is the electron rest mass. Note that a small value of  $m_h$  and a relatively large value of  $m_e$  were chosen in the calculation. A large difference in electron and hole effective masses is common in organic crystals such as naphthalene and anthracene.<sup>40</sup> Indeed, it has been shown by Forrest and co-workers that PTCDA is a preferentially hole-transporting material,<sup>11</sup> indicating that  $m_h$  is substantially less than  $m_e$ . The effect of different values of  $m_h$  are also shown for comparison in Fig. 5.7, and indeed the results are very sensitive to the choice of  $m_h$ . Also note that our calculation implies that  $V_e \gg V_h$ . This is consistent with electrical characteristics of PTCDA/NTCDA heterojunctions that rectification was not

Table 5.2. Parameters used in the variational calculations

Parameters	Symbol	Unit	Value
Hole mass	$m_h$	$m_0$	0.18
Electron mass	$m_e$	$m_0$	10.0
Electron potential	$V_e$	meV	900
Hole potential	$V_h$	meV	50
Relative dielectric constant of PTCDA	$\epsilon_p$		3.6

observed in such devices from room temperature to about 90 K, indicating that the energy barrier to hole transport is less than 100 meV.

The calculated values of  $\alpha$ , as shown in Fig. 5.7, increase monotonically with increasing well width, and asymptotically approach the free exciton Bohr radius of 12 Å, indicating that the exciton is confined in the quantum wells. Such a variation of  $\alpha$  is different from the results obtained for a spherically symmetric  $\psi_{1s}$  state where  $\alpha (= \beta)$  *increases* monotonically with decreasing well width. The dependence of  $\alpha$  on  $L_z$  for the ellipsoidal exciton can be understood as follows: As the well width decreases,  $\psi_{1s}$  approaches a 2-D wavefunction, resulting in a decrease in its extent in the z-direction. On the other hand, since  $\psi_{1s}$  is a hydrogenic-like 1s state, the wavefunction maintains its spherical symmetry. Therefore, as  $L_z$  decreases, the effective Bohr radius ( $\alpha$ ) in the x-y direction also decreases. In the case of an extremely narrow well, the exciton is squeezed to the extent that its wavefunction is forced to deviate from spherical symmetry. When such an effect becomes significant, a  $p_x$ - or  $p_y$ -state instead of an s-state exciton wavefunction might be more stable.

We can also understand the variation of  $\alpha$  with  $L_z$  for the case of a spherical wavefunction ( $\alpha = \beta$ ) in terms of the symmetry argument given above. As the well width approaches the free exciton Bohr radius,  $\psi_{1s}$  of the exciton wavefunction approaches two-dimensional, i.e.,  $\beta \rightarrow \infty$ . At the same time, the Bohr radius in the x-y direction shrinks due to quantum confinement, resulting in a decrease of  $\alpha$  with decreasing  $L_z$ . Since  $\alpha = \beta$  in this trial wavefunction, the variations of  $\alpha$  and  $\beta$  compete, and the resulting *apparent* Bohr radius increases with decreasing well width.

### (C) Reduction of exciton lifetime

There are two reasons to cause a reduction of exciton lifetime ( $\tau_{ex}$ ) with decreasing well width. First, the change in exciton lifetime in the MQW samples could be due to traps at the NTCDA/PTCDA interface. The measured recombination rate ( $\tau$ ) can be written as

$$\frac{1}{\tau} = \frac{1}{\tau_r} + \frac{1}{\tau_{nr}} \quad (5.23)$$

where  $\tau_r$  is the exciton radiative lifetime and  $\tau_{nr}$  is the non-radiative recombination time. If nonradiative recombination is significant, then  $\tau_{nr} \leq \tau_r$  and the observed lifetime should decrease due to traps. The results of our time-resolved luminescence measurements show that the integrated luminescence intensity at  $\lambda = 720$  nm was found to be constant with sample layer thickness as shown in Fig. 5.12. This indicates that the measured signal is not affected by nonradiative recombination centers. Note that previously the difference in the cw luminescence intensity with layer thickness (see Fig. 5.9) measured has been attributed to the presence of non-radiative recombination centers, and the signal measured under this condition includes both fast ( $\sim 10$  ns) and slow ( $\sim 1$  ms) processes. Here, the fast process is due transitions from singlet states while the slow process is due to transition from triplet states. Therefore, the time-resolved luminescence results indicate the fast process is not affected by the presence of non-radiative recombination centers. Further, the exciton lifetime in molecular crystals due to traps is temperature dependent,<sup>41</sup> contrary to our time-resolved

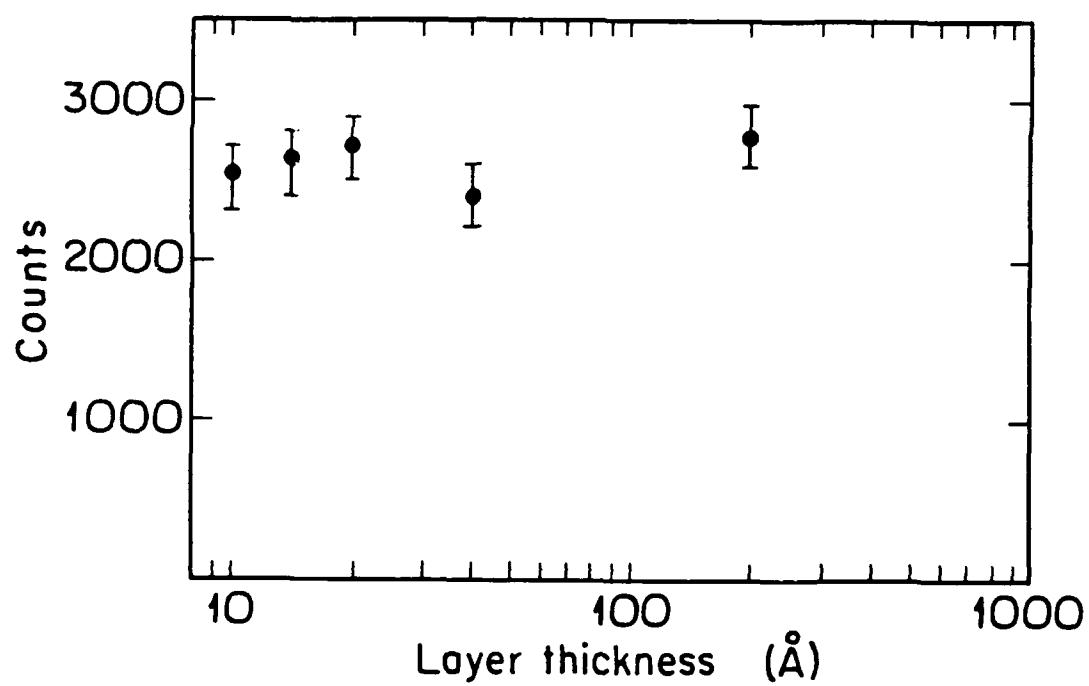


Fig. 5.12 Integrated luminescence intensity versus layer thickness.

measurements which show that the radiative decay time is independent of temperature from 20 K to 295 K. This is further evidence that the luminescence signal is not affected by traps.

The decrease of  $\tau_{\text{ex}}$  with decreasing  $L_z$ , therefore, can result from an increase in the spontaneous recombination rate due to an increase in the overlap of the electron and hole wavefunctions in the PTCDA potential well. A similar dependence of the exciton lifetime on well width has been observed in GaAs/GaAlAs quantum wells, and the enhanced recombination has been attributed to carrier localization.<sup>27,28</sup> For the hydrogenic 1s state, the spontaneous recombination rate,  $R_{\text{sp}}$ , can be shown to be proportional to the exciton volume,<sup>42</sup> i.e.,

$$R_{\text{sp}} \propto \int |\Psi_{\text{tot}}|^2 d^3\mathbf{r} \quad (3.24)$$

Note that this expression for exciton volume differs from that used in earlier work.<sup>27</sup> Previously, the exciton in an infinite square well was treated as two-dimensional, and the exciton volume is assumed to be cylindrical ( $= a_0^2 L_z$ ), where  $a_0$  is the exciton Bohr radius in the bulk. As we have discussed earlier, such an assumption is perhaps valid only in the regime where  $a_0 < L_z$ .

Using the results of the calculation of  $\alpha$  discussed above, the exciton volume in a quantum well is found to decrease with decreasing well width. The shrinkage of the exciton due to quantum confinement can thus account for the decrease in exciton lifetime. Based on the above analysis and using the parameters given in Table 5.2, the dependence of exciton volume, and hence  $\tau_{\text{ex}}$ , on well width are shown by the solid line in Fig. 5.10. The results of the



calculation are in good agreement with the exciton lifetime data, indicating the exciton quantum confinement model can quantitatively account for both the change in exciton binding energy and exciton lifetime using the set of parameters given in Table 5.2. Therefore, our results indicate organic MQWs are indeed similar to their inorganic counterpart in that there is an increase in exciton binding energy due to quantum confinement and a reduction in lifetime due to an increased overlap of the electron and hole wavefunctions.

#### V.5 Summary and Conclusions

In this chapter we have discussed the quasi-epitaxial growth of PTCDA/NTCDA organic multiple quantum well structures by organic molecular beam deposition. Both x-ray diffraction and birefringence measurements indicate that growth of ordered structures have been achieved even though the crystal structures of PTCDA and NTCDA are incommensurate. This is the first demonstration of the growth of multilayer structures using van der Waals solids.

PTCDA/NTCDA organic quantum well structures have been characterized by both optical absorption and time-resolved photoluminescence measurements. The exciton binding energy was found to increase with decreasing well width, whereas its lifetime is found to decrease with decreasing well width. The dependence of exciton binding energy and lifetime on  $L_z$  can both be understood in terms of confinement of molecular excitons in quantum wells. To our knowledge, these results provide the first evidence for exciton quantum confinement in organic MQW structures.

From the results of our variational calculations, the effective exciton Bohr

radius is 12 Å, indicating that the exciton wavefunction extends to 3 or 4 molecular layers in PTCDA, suggesting the excitons are Wannier-like. In general, excitons in molecular crystals are thought to be localized Frenkel excitons. However, Bounds and Siebrand<sup>21</sup> have calculated the binding energy of an electron-hole pair in anthracene, and have shown that the charge-transfer states can be treated as Wannier excitons. Therefore, their conclusions appear to be consistent with our analysis in this work.

The results from the present and previous chapters suggest the charge transport and optical properties of organic heterostructures are consistent with the band picture used to describe inorganic materials. As shown in the previous chapter, the energy barrier controls the charge flow across the organic heterojunction, similar to the charge flow mechanism in inorganic heterojunctions. The results from this chapter indicate there is sufficient charge carrier delocalization in organic MQW structures such that effects of quantum confinement can be observed. Quantum confinement results in an increase in exciton binding energy and enhancement in recombination with decreasing layer thickness. Due to the flexibility of van der Waals bonds in crystalline organic materials, it is possible to fabricate a variety of high quality organic quantum well devices without regard to lattice mismatch.

- <sup>1</sup> L. Esaki, IEEE J. Quantum Electron. **QE-22**, 1611 (1986)
- <sup>2</sup> J.P. Faurie, IEEE J. Quantum Electron. **QE-22**, 1656 (1986)
- <sup>3</sup> R. Hull, J.C. Bean, and C. Buescher, J. Appl. Phys. **66**, 5837 (1989)
- <sup>4</sup> R. Dingle, ed., *Semiconductors and Semimetals*, Vol.24 (Academic, New York, 1987).
- <sup>5</sup> W.T. Tsang, Appl. Phys. Lett. **39**, 134 (1981)
- <sup>6</sup> F. Capasso, W.T. Tsang, A.L. Hutchinson, and G.F. Williams, Appl. Phys. Lett. **40**, 38 (1982)
- <sup>7</sup> T.C. Sollner, W.D. Goodhue, P.E. Tannenwald, C.D. Parker, D.D. Peck, Appl. Phys. Lett. **43**, 588 (1983)
- <sup>8</sup> D.A.B. Miller, Appl. Phys. Lett. **54**, 202 (1989)
- <sup>9</sup> J.W. Matthews and A.E. Blakeslee, J. Cryst. Growth, **27**, 118 (1974)
- <sup>10</sup> M. Pope and C.E. Swenberg, *Electronic Processes in Organic Crystals* (Oxford University, New York, 1982)
- <sup>11</sup> S.R. Forrest, M.L. Kaplan, and P.H. Schmidt, J. Appl. Phys., **55**, 1492 (1984)
- <sup>12</sup> M.K. Debe, K.K. Kam, J.C. Liu, and R.J. Poirier, J. Vac. Sci. Technol. **A5**, 1914 (1987)
- <sup>13</sup> M. Mobus, M. Schrek, and N. Karl, Thin solid Films **175**, 89 (1989)
- <sup>14</sup> K. Saiki, K. Ueno, T. Shimada, A. Koma, J. Cryst. Growth, **95**, 603 (1989)

- <sup>15</sup> A. Koma, K. Saiki, and Y. Sato, Appl. Surf. Sci. **41**, 451 (1989)
- <sup>16</sup> A.J. Dann, H. Hoshi, and Y. Maruyama, J. Appl. Phys. **67**, 1371 (1990)
- <sup>17</sup> M. Hara, H. Sasabe, Y. Yamada, and A.F. Garito, Mat. Res. Soc. Symp. Proc. **159**, 57 (1990)
- <sup>18</sup> F.F. So, S.R. Forrest, Y.Q. Shi, and W.H. Steier, Appl. Phys. Lett., **56**, 674(1990)
- <sup>19</sup> D.-Y. Zang, Y.Q. Shi, F.F. So, S.R. Forrest, and W.H. Steier, Appl. Phys. Lett. **58**, 562 (1991)
- <sup>20</sup> J.F. Lam, S.R. Forrest, and G.L. Tangonan, Phys. Rev. Lett. **25**, 1614 (1991)
- <sup>21</sup> P.J. Bounds and Siebrand, Chem. Phys. Lett. **75**, 414(1980)
- <sup>22</sup> E.A. Silinsh, *Organic Molecular Crystals*, (Spring-Verlag, Heidelberg, 1980)
- <sup>23</sup> S.R. Forrest, L.Y. Leu, F.F. So, and W.Y. Yoon, J. Appl. Phys. **66**, 5908 (1989)
- <sup>24</sup> C.W. Tang, Appl. Phys. Lett. **48**, 183 (1986); C. Adachi, S. Tokito, T. Tsutsui, and S. Saito, Jpn. J. Appl. Phys. **27**, L713 (1988)
- <sup>25</sup> I.G. Bastard, E.E. Mendez, L.L. Chang, and Esaki, Phys. Rev., **B26** 1974(1982)
- <sup>26</sup> Y. Shinozuka and M. Matsuura, Phys. Rev., **B28**, 4878(1983)
- <sup>27</sup> E.O. Gobel, H. Jung, J. Kuhl, and K. Ploog, Phys. Rev. Lett. **51**, 1588(1983)

- <sup>28</sup> J. Christen, D. Bimberg, A. Steckenborn, and G. Wiemann, Appl. Phys. Lett. **44**, 84 (1984)
- <sup>29</sup> S.R. Forrest, M.L. Kaplan, and P.H. Schmidt, J. Appl. Phys. **56**, 543 (1984)
- <sup>30</sup> B.D. Cullity, *Elements of X-ray Diffraction*, (Addison-Wesley, Reading, 1978)
- <sup>31</sup> D.Y. Zang, F.F. So, and S.R. Forrest, To be published in Appl. Phys. Lett. (1991)
- <sup>32</sup> Y.J. Zhang and S.R. Forrest, Unpublished results.
- <sup>33</sup> H. Port, K. Mistelberger, and D. Rund, Mol. Cryst. Liq. Cryst. **50**, 11 (1979)
- <sup>34</sup> J.B. Birks and A.A. Kazzaz, Proc. Roy. Soc. **A304**, 291 (1968)
- <sup>35</sup> V.L. Broude, E.I. Rashba, and E.F. Sheka, *Spectroscopy of Molecular Excitons*, (Springer-Verlag, New York, 1985)
- <sup>36</sup> W.F. Kosonocky and S.E. Harrison, J. Appl. Phys. **37**, 4789 (1966)
- <sup>37</sup> J.D. Wright, *Molecular Crystals*, (Cambridge, New York, 1987)
- <sup>38</sup> R.C. Miller, D.A. Kleinman, W.T. Tsang, and A.C. Gossard, Phys. Rev. **B24**, 1134 (1981)
- <sup>39</sup> W. Stolz, J.C. Mann, M. Altarelli, L. Tapfer, and K. Ploog, Phys. Rev. **B36**, 4310 (1987)
- <sup>40</sup> W. Warta and N. Karl, Phys. Rev. **B32**, 1171 (1985)
- <sup>41</sup> A. Matsui and K. Mizuno, Chem. Phys. **113**, 111 (1987)
- <sup>42</sup> H. Barry Bebb and E.W. Williams, in *Semiconductors and Semimetals*, R.K. Willardson and A.C. Beer, eds., Vol.8 (Academic, New York, 1972)

## Chapter VI

### Conclusions and Future Work

#### VI.1 Conclusions

In conclusion, we have demonstrated quasi-epitaxial growth of crystalline organic thin films on a variety of substrate materials including inorganic semiconductors and glass by the process of organic molecular beam deposition (OMBD). This is an ultra-high vacuum growth technique similar to conventional molecular beam epitaxy. The key to such a growth technique is to keep the substrate temperature below 120 K. Due to the flexibility of the van der Waals bonds in the crystal, molecules have sufficient surface mobility to find their potential energy minima in the crystal surface even at very low temperatures. Hence, quasi-epitaxial growth enables us to grow high quality crystalline organic thin films without regard to the lattice mismatch. Further, we have also demonstrated the quasi-epitaxial growth of organic multiple quantum well structures based on two crystalline organic materials whose lattice structures are incommensurate. The ability to grow relatively defect-free crystalline organic thin films has allowed us to fabricate a variety of organic-on-inorganic (OI) and fully organic heterojunctions and multiple quantum well devices.

Similar to inorganic semiconductor heterojunctions, the charge transport across OI heterojunctions is controlled by the heterojunction energy barrier at the heterointerface. Using the temperature dependence of the forward-biased current-voltage characteristics and internal photoemission spectroscopy, for the first time

we directly measured the valence-band discontinuity energy of PTCDA/p-Si OI heterojunctions. Based on our studies of the electrical characteristics of organic/p-Si heterojunction devices, we found that in some (but not all) cases, the chemical interaction between the organic and inorganic semiconductors determines the magnitude of the energy barrier at the heterointerface. In particular, the interaction at the CuPc/p-Si interface results in a high density of interface states which pin the surface Fermi-level energy in the inorganic semiconductor band gap, thereby determining the magnitude of the OI barrier energy. Thus, for heterojunctions based on Pc compounds, OI energy barriers are similar to some metal-semiconductor Schottky barriers in that interface states play an important role in determining the barrier energy. On the other hand, chemical interactions at the heterointerface is not observed in heterojunctions based on dianhydride compounds, indicating in this case the OI energy barrier does not appear to depend on the defect states.

Carrier velocity in the organic film is another important parameter that determines the charge transport properties. We have calculated the carrier velocity in PTCDA thin films, and found that it varies from 100 cm/s under reverse bias to about  $10^5$  cm/s under forward bias. Such results are consistent with the transient response measured for OI photodetectors, and based on our analysis, the response of OI devices is limited by the carrier velocity in the organic film. By decreasing the organic layer thickness to below 100 Å, it is possible to fabricate OI devices with bandwidths  $> 1$  GHz. In addition, the potential distribution across the organic film was calculated considering both ohmic as well as space-charge-limited conduction regimes. Unlike metal-

semiconductor Schottky contacts, the majority carrier quasi-Fermi level in OI-HJ diodes is flat throughout the bulk of the inorganic semiconductor substrate due to the relatively low mean carrier velocity in the organic film under small bias voltage.

Fully organic p-P isotype heterojunctions have been grown and they are similar to inorganic heterojunctions in that the same charge transport theory for inorganic heterojunctions can be used to describe the characteristics of organic heterojunctions. In particular, the charge transport properties of organic heterojunctions are limited by thermionic emission of holes over the energy barrier at the heterointerface under low forward and reverse bias. The heterojunction energy barriers for three pairs of organic heterojunctions have been determined, and the results indicate that the band offsets for the three crystalline organic materials used follow a transitive relationship. Such a relationship indicates defect states at the heterointerfaces between materials in contact do not seem to affect the band offset energies.

Finally, we have grown organic multiple quantum well structures using PTCDA and NTCDA by organic molecular beam deposition. Both x-ray diffraction and birefringence data show that such structures are ordered, and that the growth is quasi-epitaxial in nature such that structural ordering exists even though the crystal structures of the two materials used are incommensurate. In addition, we have found that the energy of the exciton absorption line increases and the exciton lifetime decreases with decreasing layer thickness. These results can be understood in terms of confinement of Wannier-like molecular excitons in quantum wells. The results of our variational calculations indicate the absorption



and time-resolved luminescence data are consistent with the exciton quantum confinement model. Further, from the results of theoretical calculations, the effective exciton Bohr radius of PTCDA is found to be 12 Å, indicating the exciton wavefunction extends to 3-4 molecular spacings. This is also consistent with the Wannier-like exciton picture.

## VI.2 Future work

The area of heterojunctions and multiple quantum well structures based on crystalline organic materials is still a new field. Nevertheless, the present work has laid the ground work for further study of this new class of heterostructures. A thorough study of both the quasi-epitaxial growth of crystalline organic thin films and the electronic and optical properties of these organic heterostructures is anticipated to lead to many novel photonic device concepts.

### (A) Growth and structural properties

The analytical techniques used in the present work only give microscopic structural information. Analytical techniques with atomic resolution such as transmission electron microscopy (TEM) and scanning tunneling microscopy (STM) are desirable for the complete structural study of crystalline organic thin films. By employing the TEM lattice imaging technique, we can directly reveal how lattice matching takes place in the highly lattice-mismatched materials, and identify the nature of structural defects present in the organic heterostructures. On the other hand, in-situ STM provides another means to study the structural properties down to the molecular level without ever exposing the samples to the

atmosphere. This is important as the organic surface is free from any contamination, thus making it easier to interpret the STM data. A third analytical technique is reflection high energy electron diffraction (RHEED), which provides the capability of monitoring the surface crystal structure during growth. Such an in-situ technique is widely used to monitor the growth of inorganic semiconductor materials by molecular beam epitaxy, and it has been shown that RHEED<sup>1</sup> can also be useful for studying the growth mechanisms of quasi-epitaxial organic films. To gain a better understanding of the interactions between molecules in the lattice, Raman spectroscopy is also a useful tool.<sup>2</sup>

#### (B) OI heterojunctions

At present, the charge transport properties of OI heterojunctions (OI-HJs) is fairly well understood. However, there is still a basic issue which has not been resolved. That is, what determines the magnitude of the OI energy barrier? Is it an intrinsic or extrinsic process? The results of the present work indicate that in some cases the surface Fermi level of the inorganic semiconductor is pinned due to the high density of defect states at the OI heterointerface. However, Fermi-level pinning<sup>3</sup> is not observed in all OI-HJs, at least not in the heterojunctions based on dianhydride compounds. More experiments need to be done in order to provide an answer to this question. One such experiment is to do in-situ characterization of OI-HJs. This can be done using the new organic-inorganic molecular beam epitaxy (OIMBE) system described in this work. In this experiment, high quality inorganic semiconductor thin films can be grown in the gas-source MBE chamber, followed by the growth of organic thin films. These

procedures can ensure there will be no contamination at the OI heterointerface which might give rise to defect states. Next, metal contact dots to the organic film are evaporated onto the samples in the ultra-high vacuum connected e-beam chamber. Finally, the samples can be transferred into the analytical chamber for both electrical and optical characterization such as current-voltage (I-V), photocurrent-voltage ( $I_{ph}$ -V), and capacitance-voltage (C-V) measurements over a wide range of temperature (5K - 450K). By fabricating and testing the OI devices in vacuum, we can eliminate all extrinsic effects such as  $O_2$  adsorption<sup>4</sup>, and thereby gain a better understanding of the intrinsic charge transport mechanisms.

In terms of OI devices for optoelectronic applications, we have estimated that the bandwidth of OI devices with organic thin films of thickness less than 50 Å is  $> 1$  GHz. In the previous analysis, it was assumed that the charge transport is governed by thermionic emission over the energy barrier at the interface, and the speed is limited by the carrier mobility in the organic film. However, in the ultra-thin organic layer regime, it is expected that the predominant charge transport mechanism in OI devices changes from thermionic emission to tunneling.<sup>5</sup> Since ultra-thin organic films (thickness  $< 20$  Å) can be grown on inorganic substrates by OMBD techniques, the ultimate speed of response of OI devices can be tested. By carefully studying the I-V characteristics of devices with ultra-thin organic films as a function of temperature and frequency, the charge transport processes involved can be identified.

### (C) Non-linear optical properties of MQWs

It has been theoretically predicted by Lam and co-workers<sup>6</sup> that the quasi-epitaxially grown organic MQWs exhibit large optical non-linearities. In particular, they showed that the MQWs should have an intensity dependent absorption and index of refraction at relatively low pump beam intensities. These predictions can be directly tested by performing two wave mixing experiments over a wide temperature range (2K to 600K). In this experiment, both the pump beam (Ar laser light) and the probe beam (low intensity white light source from a quartz lamp) are mixed onto the surface of a MQW sample via illumination through an optical window of a liquid-helium cryostat. The absorption spectrum can then be measured using a Spex monochromator with a photon counter. Temporal response can also be measured using a multichannel photon counting averager.

One strong optical nonlinearity has already been observed in our studies. It was found that the lowest energy exciton emission peak in single layer PTCDA films is strongly blue shifted with very low pumping power densities ( $< 1 \text{ W/cm}^2$ ). Fig. 6.1 shows the luminescence spectra for  $0.4 \mu\text{m}$  PTCDA thin film sample under different pumping intensity, and Fig. 6.2 shows the peak shift as a function of Ar laser pumping intensity. While this process requires  $100 \mu\text{s} - 10 \text{ ms}$  to occur, the radiative recombination time is observed to be less than  $15 \text{ ns}$ . However, the luminescence peak shift is not observed in MQWs with very narrow well widths ( $L_z < 20 \text{ \AA}$ ).

We can gain an understanding of this phenomena in terms of the following picture. Consider a two-level system consisting of a singlet state (with  $\tau$

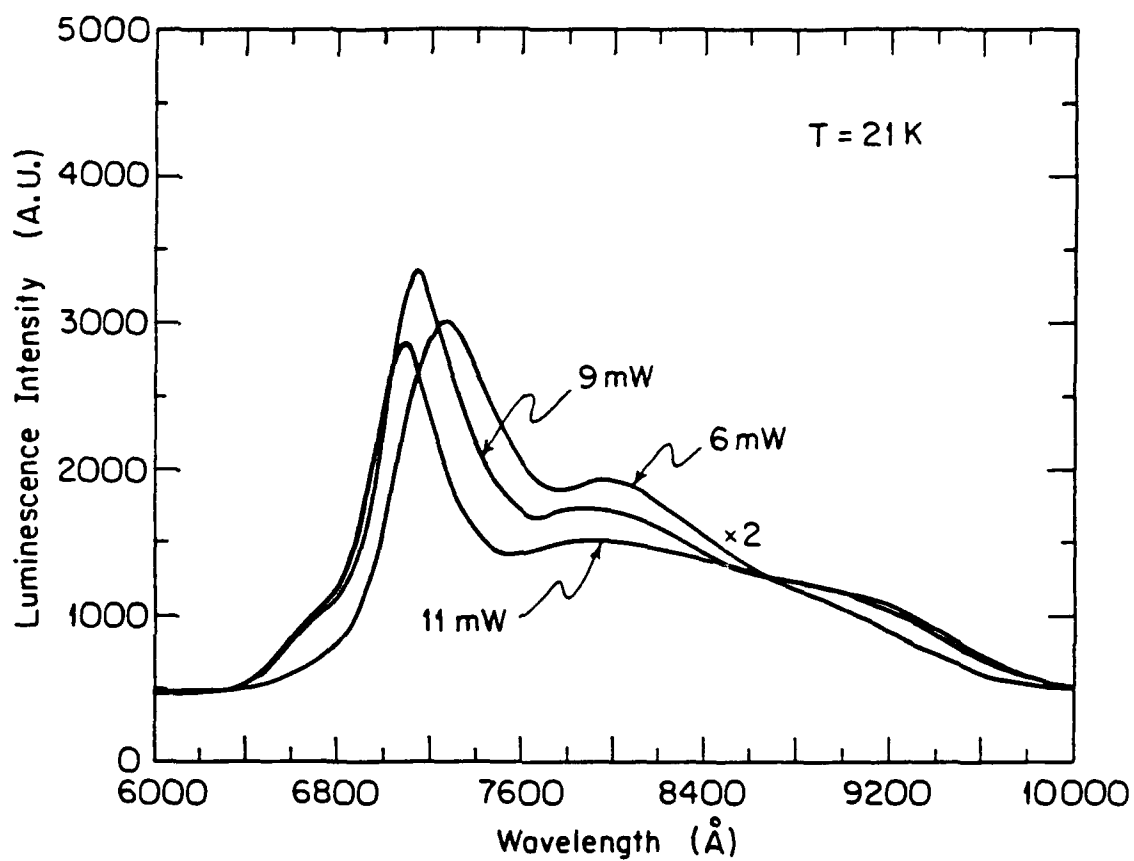


Fig. 6.1 Luminescence spectra of 0.4  $\mu\text{m}$  PTCDA thin film at 21 K under various pumping intensity.

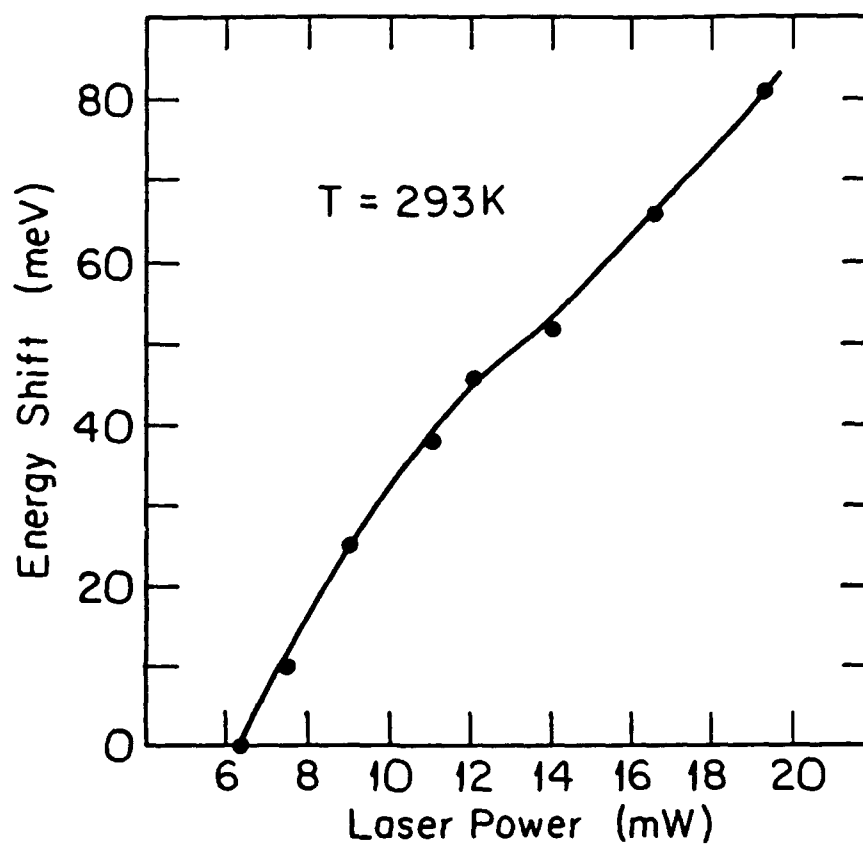


Fig. 6.2 Luminescence peak energy (at about 720 nm) shift of a 4000 Å PTCDA film as a function of the Ar laser pumping intensity.

~ 10 ns) and a triplet state (with  $\tau \sim 1$  ms) as shown in Fig. 6.3. During optical excitation, both the excited singlet and triplet ( $S_1$  and  $T_1$ ) states are filled. Transitions between the singlet ( $S_1$  and  $S_0$ ) states gives rise to the luminescence spectrum shown in Fig. 6.1. As the result of filling the triplet state due to the coulombic interaction with the triplet and singlet states, the energy of the  $S_1$ - $S_0$  transition is raised due to Coulomb repulsion. Using perturbation theory, the energy shift ( $\Delta E$ ) can be expressed in terms of a matrix element as:

$$M_{01} = \langle S_1 | q^2 / \epsilon r | S_0 \rangle \quad (6.1)$$

where  $q$  is the electronic charge,  $\epsilon$  is the dielectric constant, and  $r$  is the average distance of separation between two excitons. Here, we attempt to gain a qualitative understanding based on the model described by Fig. 6.3. For a given pumping intensity, the exciton density generated is constant, hence  $r$  is constant in Eq. (6.1). Consider a pump beam incident normal to the sample with excitons generated in the sample plane. The two-dimensional exciton density is proportional to the pump intensity ( $I$ ), and hence  $I^{1/2}$  is proportional to  $1/r$ . Therefore, the energy shift ( $\Delta E$ ) should be proportional to the square root of the light intensity ( $I$ ). Here, the data in Fig. 5.2 indicates  $\Delta E \sim I^{0.4 \pm 0.1}$ , indicating that above model based on Eq. (6.1) is plausible. For more exact calculations of the dependence of the energy shift with pumping intensity, the matrix element in Eq. (6.1) must be summed over all initial and final states at all molecular sites.

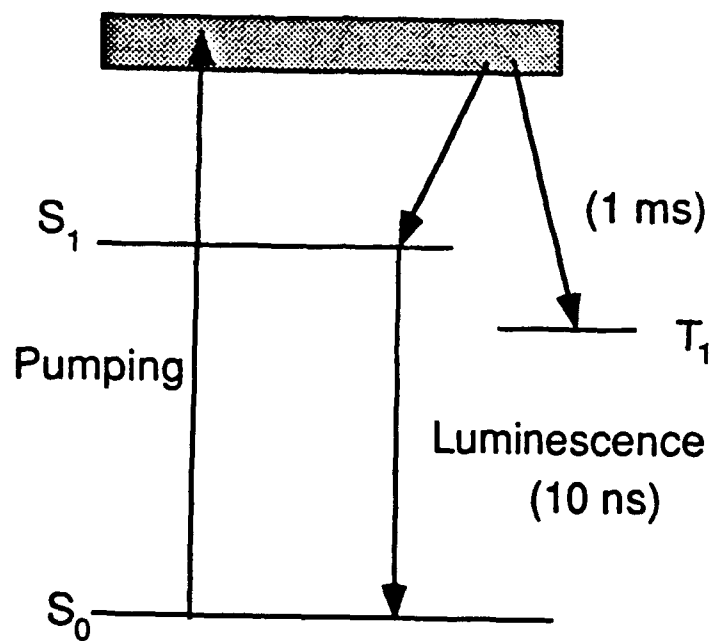


Fig. 6.3 Schematic diagram showing the two-level model.  $S_0$  is the ground state energy, and  $S_1$  and  $T_1$  are the excited singlet and triplet states.



## References

- <sup>1</sup> M. Hara, H. Sasabe, Y. Yamada, and A.F. Garito, Mat. Res. Soc. Symp. Proc. **159**, 57 (1990)
- <sup>2</sup> K. Akers, R. Aroca, A. Hor, and R.O. Loutfy, J. Phys. Chem. **91**, 2954 (1987)
- <sup>3</sup> W.E. Spicer, I. Lindau, P. Skeath, C.Y. Su, and P. Chye, Phys. Rev. Lett. **44**, 420 (1980)
- <sup>4</sup> J. Simon and J.J. Andre, *Molecular Semiconductors* (Springer, Berlin, 1985)
- <sup>5</sup> S.M. Sze, J. Appl. Phys. **38**, 2951 (1967)
- <sup>6</sup> J.F. Lam, S.R. Forrest, and G.L. Tangonan, Phys. Rev. Lett. **25**, 1614 (1991)

## Appendix A Dielectric measurements of PTCDA thin films

### A.1 Dielectric constants

To measure the dielectric constants of PTCDA thin films along different film directions, capacitors consisting of PTCDA thin films sandwiched between two metal contacts were fabricated on quartz substrates. For measuring the dielectric constant along the in-plane direction, interdigitated patterns of Cr-Au contacts were employed. Here, a thin layer of Cr (150 Å) was deposited, followed by a 0.7  $\mu\text{m}$  thick Au layer. These contacts were then patterned by lithographic technique into 2mm long interdigitated electrodes with 2  $\mu\text{m}$  spacing and finger width. In addition, some electrode sets were oriented perpendicular to other sets to determine if there were significant asymmetries in the capacitance in the two in-plane directions. Next, a PTCDA thin film of thickness 0.9  $\mu\text{m}$  was deposited, filling the spaces between the electrode fingers, as well as being deposited onto the electrode top surface. Here, PTCDA was deposited using the process of organic molecular beam deposition (OMBD) onto the quartz substrate which was maintained at a temperature of approximately 90 K during film growth. As has been discussed previously, deposition under these conditions ensures that the resulting film is single crystalline.

The capacitance measured between 100 Hz and 10 MHz for one set of electrode pairs using this in-plane geometry is shown in Fig. A.1. The capacitance is independence of frequency over the measurement range, indicating that the

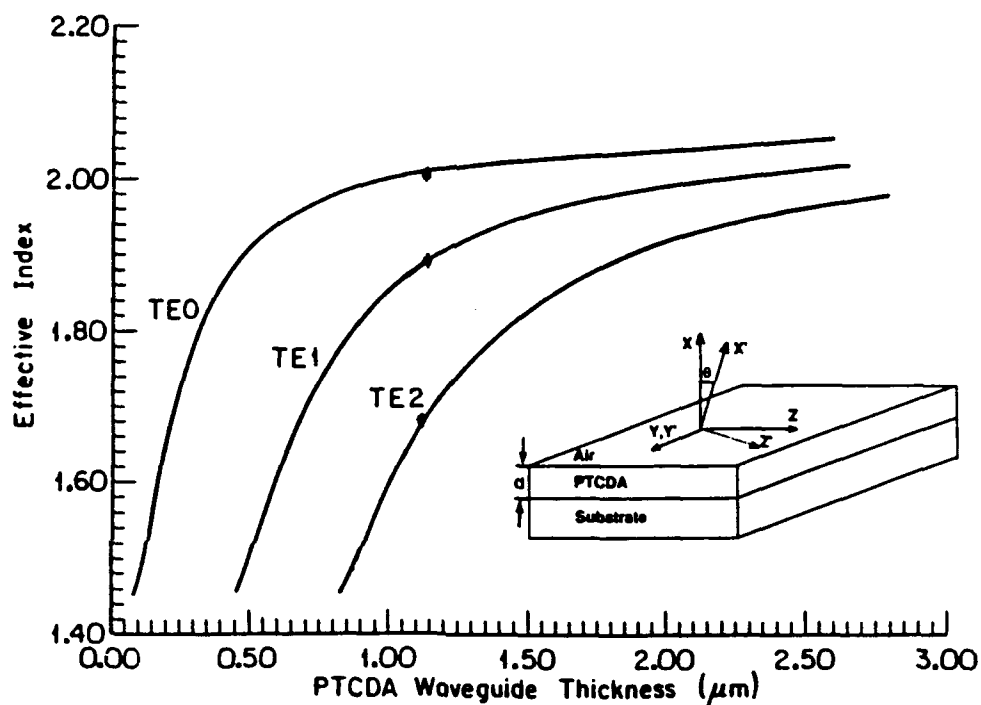


Fig. A.1 Calculated effective indices at  $\lambda = 1.064 \mu\text{m}$  vs PTCDA waveguide thickness. Data points represent the measured values. The PTCDA guide has a thickness of  $1.05 \mu\text{m}$ , and is on a fused quartz substrate.

Inset: Coordinate system for a PTCDA waveguide. The Z-axis is the propagation direction, and the Y-axis lies along the PTCDA b-crystallographic axis.

films are free of traps. Traps tend to affect the capacitance when their emission rate is comparable to the test frequency.

The capacitance of a co-planar strip line lying on a quartz substrate with dielectric constant  $\epsilon_s$  is given by<sup>1</sup>:

$$C = (\epsilon_s + \epsilon_F)\epsilon_0[FK(\kappa)]l/2 \quad (A1),$$

where  $\epsilon_0$  is the permittivity of free space,  $\epsilon_s$  is the dielectric constant of the quartz substrate,  $l$  is the finger length,  $F = 16$  is the number of finger pairs,  $K$  is the ratio of two complete elliptic integrals of the first kind, and  $\kappa$  is a geometrical parameter related to the finger width and spacing. Here, we assume quartz fills one half plane, and a material (i.e. PTCDA) with dielectric constant  $\epsilon_{||}$  the other. The ratio of capacitances of the pattern measured before ( $C_{w0}$ ) and after ( $C_w$ ) deposition of the PTCDA film is then simply:

$$C_{w0}/C_w = (\epsilon_s + 1)/(\epsilon_s + \epsilon_{||}) \quad (A.2).$$

We note that a small amount of electric field penetration above the PTCDA film can lead to deviations from Eq. (A.2). However, since the PTCDA thickness was larger than that of the contact finger, this error is expected to lead to an insignificant underestimate of  $\epsilon_{||}$ . In this way, we obtain the in-plane dielectric constants for PTCDA of  $\epsilon_{||} = 4.6 \pm 0.2$  and  $4.3 \pm 0.2$  for the two perpendicular orientations of the patterns. Since these values are within each other's error limits, we assume that the dielectric constants along the two directions is not significantly different, leading to  $\epsilon_{||} = 4.5 \pm 0.2$ .

To measure  $\epsilon_{\perp}$ , a parallel plate geometry was used, where the back contact was formed using a broad Cr-Au contact deposited on glass. This was followed by deposition of a 0.9  $\mu\text{m}$  thick layer of PTCDA by OMBD. Top

contact to the PTCDA layer was made using circular Au pads of area  $2.5 \times 10^{-4} \text{ cm}^2$ . Using this geometry, it is found that  $\epsilon_{\perp} = 1.9 \pm 0.1$  over the same frequency range as that used to measure  $\epsilon_{\parallel}$ . From these data we obtain  $(\epsilon_{\perp} - 1)/(\epsilon_{\parallel} - 1) = 0.26$  which is close to the theoretical estimate of 0.22 for perfectly oriented crystalline films.

## A.2 Indices of refraction

### (a) In-plane index of refraction

PTCDA is a biaxial crystal with three refractive indices:  $N_1$ ,  $N_2$  and  $N_3$  along its principal axes. For PTCDA thin films grown by OMBD, the molecules form stacks such that the crystallographic b-axis lies in the substrate plane<sup>2</sup>, one of the PTCDA principle axes must also lie in the substrate plane coinciding with the b-axis<sup>3</sup>.

PTCDA slab waveguides on fused quartz substrates were used to measure the refractive index of PTCDA parallel to the substrate plane ( $n_{\parallel}$ ). Modal solutions of optical waves propagating in an anisotropic crystal slab waveguide have shown that uncoupled transverse electric (TE) or transverse magnetic (TM) modes can exist only if the polarization direction of the guided wave is parallel to one of the principal axes of the crystal, or if the crystal optical axis lies in a plane containing the waveguide normal and the propagation direction.<sup>4</sup> Otherwise, the waveguide can only support hybrid (TE-like or TM-like) modes, where the TE and TM modes are coupled. Thus, for a PTCDA slab waveguide shown in the inset in Fig. A.2, the Y-axis coincides with the b-axis, and the Z-axis lie in the propagation direction to obtain uncoupled modes. The coordinates ( $X'$ ,  $Y'$ , and

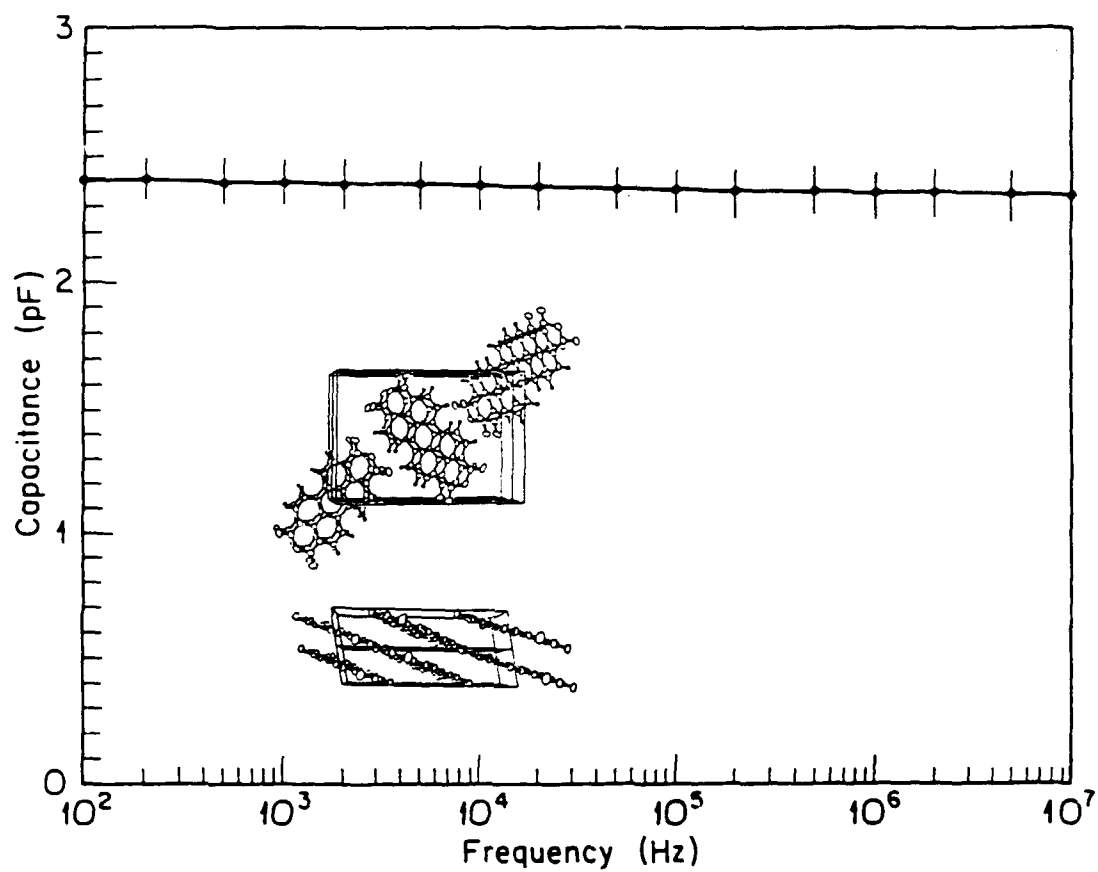


Fig. A.2 Capacitance measured versus frequency for a horizontal, interdigitated capacitor with PTCDA serving as the dielectric.

Z') represent the PTCDA principal axes with corresponding principal indices  $N_1$ ,  $N_2$ , and  $N_3$ , respectively.

Next, The orientation of the PTCDA principal optic axis was determined using birefringence measurements as follows: First, a PTCDA thin film sample (deposited on a quartz substrate) was inserted between two crossed polarizers. With a He-Ne laser ( $\lambda = 633 \text{ nm}$ ) as a light source and the beam incident normal to the sample, the birefringence was obtained by measuring the transmitted intensity variation while the sample plane was rotated about its normal axis. Then, the principle optical axis of PTCDA was determined by tilting the sample normal axis with respect to the beam, and observing the orientation at which no birefringence was observed.

Having determined the principle axis of PTCDA, the incident light from a YAG laser ( $\lambda = 1.064 \text{ }\mu\text{m}$ ) was coupled into a waveguide sample via a grating, with the polarization along the principle axis in order to excite uncoupled TE modes. Accordingly, the dispersion relationship for TE modes in a slab waveguide is given by<sup>5</sup>:

$$(k^2 n_{py}^2 - \beta^2)^{1/2} d = \tan^{-1} \left( \frac{\beta^2 - k^2 n_t^2}{k^2 n_{py}^2 - \beta^2} \right)^{1/2} + \tan^{-1} \left( \frac{\beta^2 - k^2 n_s^2}{k^2 n_{py}^2 - \beta^2} \right)^{1/2} + m\pi \quad (\text{A.3})$$

where  $k$  is the wave vector in vacuum,  $\beta$  is the propagation constant which equals  $kn_{\text{eff}}$  ( $n_{\text{eff}}$  is the effective index),  $m$  is an integer which identifies the mode number, and the subscripts  $t$ ,  $p$  and  $s$  refer to the top layer, the PTCDA film, and the substrate, respectively.

The relationship between the effective index and the grating coupling angle for a fixed optical wavelength is then given by:

$$n_{\text{eff}} = g \lambda / \Lambda + \sin \theta_c \quad (\text{A.4}),$$

where  $g$  is the grating order,  $\lambda$  is the wavelength of the incident light ( $1.064 \mu\text{m}$ ) in vacuum,  $\Lambda$  is the grating periodicity, and  $\theta_c$  is the coupling angle which is defined as the angle between the incident light beam and the normal to the grating. When the coupling angle satisfies Eq. (A.4), a maximum light intensity from the incident light beam can be coupled into the waveguide mode.

The resonant coupling angles defined in Eq. (A.4) were readily found by carefully scanning the coupling angle. Three TE modes were observed from a sample with a PTCDA thickness of  $1.05 \mu\text{m}$ . The resonant coupling angles for the  $\text{TE}_0$ ,  $\text{TE}_1$ , and  $\text{TE}_2$  modes were  $23.75^\circ$ ,  $16.58^\circ$ , and  $4.58^\circ$ , respectively. This corresponds to effective indices of  $1.979 \pm 0.002$ ,  $1.861 \pm 0.002$ , and  $1.656 \pm 0.002$  obtained from Eq. (A.4). The measured effective indices are shown in Fig. A.2, together with the theoretical calculations based on Eq. (A.3). The experimental results fit the theoretical calculations within the experimental accuracy for a film index parallel to the substrate ( $n_{\parallel}$ ) of  $2.017 \pm 0.005$ .

(b) Index of refraction normal to the substrate plane

Determination of  $n_{\perp}$  proceeds by measuring the reflectivity from the PTCDA thin film as a function of beam incident angle using several film thicknesses and light wavelengths. Consider an isotropic homogeneous thin film sandwiched between two-infinite media. The total reflectivity is given by<sup>6</sup>:



$$R = \frac{r_{12}^2 + r_{23}^2 + 2r_{12}r_{23} \cos 2\alpha}{1 + r_{12}^2 r_{23}^2 + 2r_{12}r_{23} \cos 2\alpha} \quad (\text{A.5})$$

where  $\alpha = 2\pi n_2 t \cos \theta_2 / \lambda$ . Here,  $n_2$  is the refractive index measured along the refractive angle  $\theta_2$  in the thin film of thickness,  $t$ . Also,  $r_{12}$  ( $r_{23}$ ) is the reflectivity at the interface between medium 1 (3) and medium 2. The reflectivity maxima and minima for a given index,  $n_2$ , occurs at angles  $\theta_2$  which satisfy  $n_2 t = m\lambda/4\cos\theta_2$ , where  $m$  is the integer order of the extremum. If the film thickness is accurately determined, the refractive index can thence be obtained by measuring the angles corresponding to the reflectivity extrema as predicted by the above equations.

To extend this technique to anisotropic thin films, the incident light polarization is made parallel to the plane of incidence, the propagating field has a component along the TM polarization direction. Furthermore, using birefringence measurements discussed previously, the  $b$ -axis is located, and is also oriented parallel to the incident light polarization vector. When the incident angle of the beam to the film is changed, this is equivalent to a rotation of the angle  $\theta_2$  in an index ellipsoid with axes of length  $n_{||} = n_b$  and  $n_{\perp}$ , as shown in the inset in Fig. A.3. Here,  $n_b$  is the index along the  $b$ -axis. From this figure, it can be shown that the index measured using this technique is simply given by:

$$n_2^2 = n_{||}^2 + (1 - n_{||}^2/n_{\perp}^2)\sin^2\theta_1 \quad (\text{A.6})$$

from which  $n_{\perp}$  is easily extracted since  $n_{||}$  is already known. Here,  $\theta_1$  is the incident angle.

A typical measurement result together with a theoretical calculation using the above treatment is shown in Fig. A.3. Here, the measurement is made at  $\lambda =$

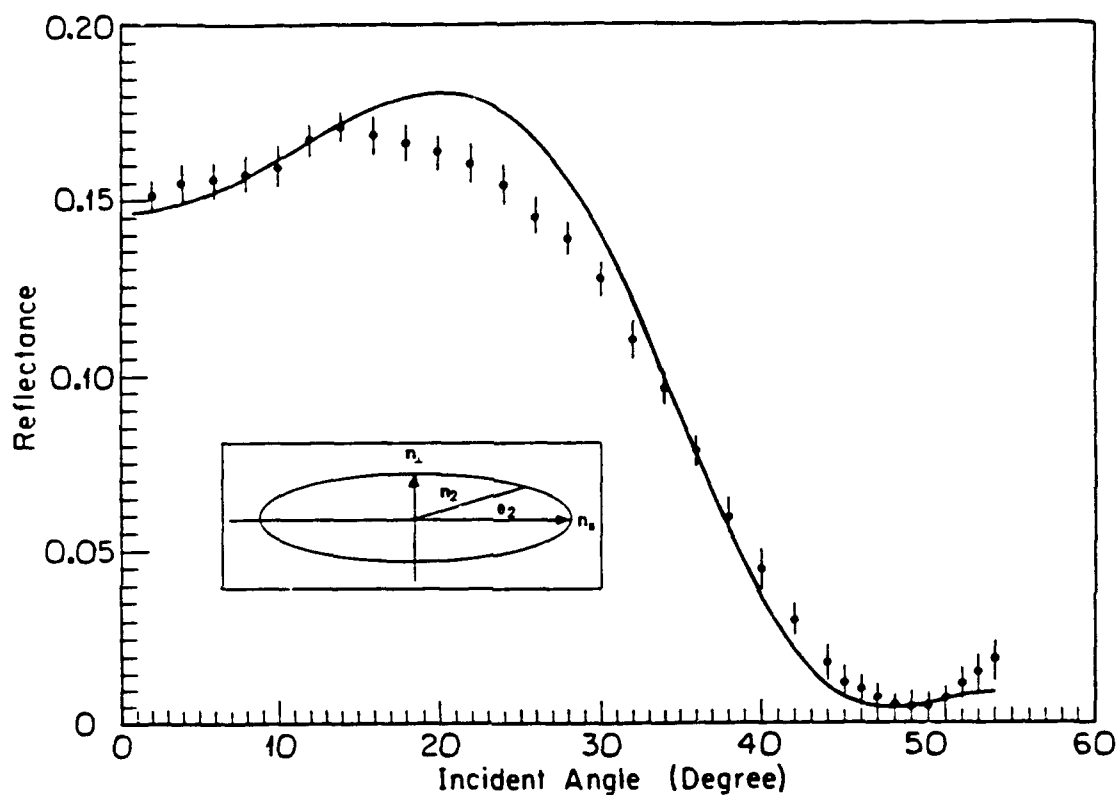


Fig. A.3 Reflectance at  $\lambda = 1.064$  mm versus incident beam angle for a 1.25 mm thick film on a quartz substrate. Data are shown as closed circles, and theory is shown as a solid line.

Inset: Index of refraction ellipsoid for PTCDA showing the relationship between the indices along different thin film directions.

1.064  $\mu\text{m}$  for a PTCDA film with  $t = 1.25 \mu\text{m}$ . The experimental setup consists of a YAG laser providing the incident beam. A large area detector is positioned near the top film surface to measure the reflected light intensity. The PTCDA is deposited on a quartz substrate by organic molecular beam deposition to achieve good crystalline order. Also, the back surface of the quartz is frosted to minimize reflections from the quartz/air interface. It can be seen that the positions of the theoretical extrema can be made to match those obtained experimentally, although the magnitude of the reflected signal is sometimes different than predicted due to unwanted reflections from surface imperfections and the quartz/air interface. A similar fit is obtained for a film thickness of 1.13  $\mu\text{m}$ , and at  $\lambda = 1.3 \mu\text{m}$ , and the data are listed in Table A.1. From these data, we obtain  $n_{\perp} = 1.36 \pm 0.01$  at  $\lambda = 1.064 \mu\text{m}$ . Very little dispersion is observed in  $n$  measured at  $\lambda = 1.064 \mu\text{m}$  and 1.3  $\mu\text{m}$ , as indicated by the data in Table A.1.

Table A.1 Reflectivity data for PTCDA thin films.

Wavelength ( $\mu\text{m}$ )	Film thickness ( $\mu\text{m}$ )	Incident Angle*	$n_{\perp}$ value (calculated)
1.064	1.13	29°	1.354 (m = 8)
	1.25	47°	1.364 (m = 8)
1.319	1.13	41°	1.343 (m = 6)
	1.25	55.5°	1.346 (m = 6)

\* Corresponding to the reflectivity minimum.

## References

- <sup>1</sup> W.R. Smythe, *Static and Dynamic Electricity*, (McGraw Hill, NY, 1950)
- <sup>2</sup> A.J. Lovinger, S.R. Forrest, M.L. Kaplan, P.H. Schmidt, and T. Venkatesan, *J. Appl. Phys.*, 55, 476 (1984)
- <sup>3</sup> N.H. Hartshorne and A. Stuart, *Crystals and the Polarizing Microscope*, (E. Arnold, London, 1969), pp.131
- <sup>4</sup> W.K. Burns and J. Warner, *J. Opt. Soc. Am.* 64, 441 (1974)
- <sup>5</sup> R.G. Hunsperger, *Integrated Optics: Theory and Technology*, (Springer-Verlag, New York, 1985)
- <sup>6</sup> M. Born and E. Wolf, *The Principles of Optics*, (Pergamon Press, Oxford, 1980)